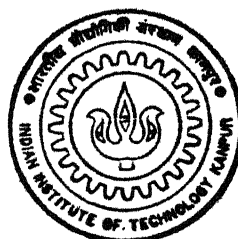


9116974

HYDROGEN IN KDP, DLC & DIAMOND FILMS, Si AND OTHER MATERIALS: STUDY OF ION INDUCED AND THERMAL EFFECTS BY ERDA USING MeV He⁺ BEAM

by
TAPOBRATA SOM

6 ✓
TH
PHY/1998/P
So 51A



DEPARTMENT OF PHYSICS

Indian Institute of Technology, Kanpur

JULY, 1998

HYDROGEN IN KDP, DLC & DIAMOND FILMS,
Si AND OTHER MATERIALS: STUDY OF ION
INDUCED AND THERMAL EFFECTS BY ERDA
USING MeV He⁺ BEAM

A Thesis Submitted
in Partial Fulfillment of the Requirements
for the Degree of
Doctor of Philosophy

by
TAPOBRATA SOM

to the
DEPARTMENT OF PHYSICS
INDIAN INSTITUTE OF TECHNOLOGY, KANPUR
July, 1998

20 JUL 1999/PHY

CENTRAL LIBRARY
I. I. T., KANPUR

Inv. No. A 128585

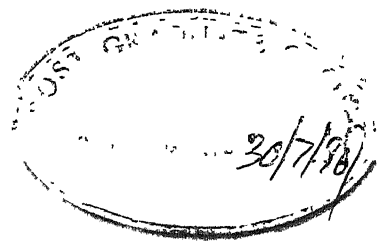
TH
PHY/1998/P
So 31/6



A128585

A humble offering to
my parents & teachers

The important thing in science is not so much
to obtain new facts as to discover new
ways of thinking about them.
- William Lawrence Bragg



CERTIFICATE

It is certified that the work contained in this thesis entitled *HYDROGEN IN KDP, DLC & DIAMOND FILMS, Si AND OTHER MATERIALS: STUDY OF ION INDUCED AND THERMAL EFFECTS BY ERDA USING MeV He⁺ BEAM* by *Tapobrata Som* has been carried out under my supervision and that this work has not been submitted elsewhere for a degree.

A handwritten signature in black ink, which appears to read "V. N. Kulkarni".

V. N. Kulkarni
Department of Physics
Indian Institute of Technology
Kanpur

July, 1998

Acknowledgements

Writing this part is not going to be easy for me at all. This is because so many people helped me during my Ph.D. days that I am afraid I should not fail to acknowledge them. However, with due respect to each and every help being rendered to me, I want to convey special thanks to some persons whose contributions in this thesis work will be remembered by me for years to come.

First of all, I must convey my “Guru Pranam” to my thesis supervisor Dr. V.N. Kulkarni. I am indebted to him for introducing me with the research field of ion-beam physics and more precisely with the world of hydrogen in materials. It is the sincere effort, patient guidance and incessant encouragement of Dr. Kulkarni that could result in the development of the low energy accelerator based hydrogen detection facility during my thesis work. I express my profound gratitude to him for bearing with my smoggy ideas on number of occasions and then to show me the right path which will forever remain invaluable to me. I have learnt many valuable experimental and theoretical aspects for pursuing my research work in the research field of material-hydrogen systems. No words will be sufficient on behalf of me to thank him for stressing on the work culture based on independent thinking and working. I have also realized the importance of liberty in scientific research through Dr. Kulkarni and shall be glad enough to maintain this spirit throughout my future years of research. Moreover, my seven years of work experience with him was always more than a research supervisor and this had helped in solving many of my personal problems during my stay at IIT Kanpur.

I take this opportunity to express my gratitude to Dr. Satyendra Kumar for providing me the diamondlike carbon films for my thesis work. I have learnt many important lessons from him also during several enlightening discussions in the last few years. His constant encouragement and ‘never-say-no’ helping attitude will be remembered by me for a long time.

I am indebted to Prof. H.D. Bist for extending me his help to perform the micro Raman measurements at the Modern Laser Raman Laboratory at IIT Kanpur. I am also thankful to him for many useful discussions on Raman spectroscopy.

I remain grateful to Dr. Debasis Kundu, Department of Mathematics, IIT Kanpur for

providing me much needed mental boost from time to time. I am really indebted to him for his very timely help in the statistical part of the phenomenological modelling used in my thesis work.

Thanks are due to Dr. D.K. Setua and Mr. A.K. Saxena for kindly extending the Fourier transform infrared facility at Defence Materials & Stores Research & Development Establishment (DMSRDE), Kanpur.

I am thankful to Dr. P. Gupta-Bhaya for providing me the biological samples studied in this work. Many hours of delightful discussion with him helped me in experiencing some glimpses of biophysics.

Thanks are due to Dr. M. Aslam, Michigan State University, USA for providing the CVD diamond films.

I would also like to express my thanks to Dr. Y.N. Mohapatra for sparing time for me from his busy schedule for valuable discussions and suggestions at various stages of this work.

I would like to acknowledge the help and constant encouragement from Prof. R.M. Singru, Dr. S.K. Saha, Prof. Y.R. Waghmare, Prof. V.A. Singh and Dr. H.C. Verma.

I am indebted to Dr. Sankar Dhar for his untiring help in teaching me many basic things during my initial days in the laboratory. It is my privilege to work with him as a junior colleague in the laboratory since he is the person who has shown me the right direction in innumerable cases. I have enjoyed each and every moment in the laboratory and in the campus during our stay at IIT Kanpur.

I am indebted to Mrs. Bishakha Bhattacharyya for providing me some valuable samples and extending immense help at a crucial stage of my thesis work which will forever remain with me with some special meaning.

My sincere thanks are due to Dr. M.S. Navati, Modern Laser Raman Laboratory, IIT Kanpur for his unique help and untiring company at the final stage of this thesis. His active participation during the micro Raman experiments and analysis of those spectra have helped me to a great extent. We had spent hours together in the laboratory which will be a fond memory for me in the many years to come.

Thanks are due to Dr. Manju Malhotra for preparing the DLC samples and Mr. Tapan Kumar Khan for helping me in preparing the biological films.

Thanks are due to Dr. Sandeep Singh for helping me in some of the important measurements described in this work. Thanks are also due to Dr. S.B. Majumder for helping me

in learning many things during my stay at IIT Kanpur. I am specifically thankful to Mr. Swapan Chakraborty, Mr. Anirban Mitra, Mr. Anirban Bhattacharyya, Mr. Narasimhan, Mr. Ashutosh Mishra, Mr. Amit Ranjan, Mr. Akash Singh, Mr. Kousik Nandy, and Dr. GDM for their immense help rendered to me during my thesis preparation.

I would like to take this opportunity to express my sincere thanks to other lab colleagues Dr. Nobin Banerji, Paritosh Chowdhury, Kalyan Raman Ramakrishnan, Bishakha Bhattacharyya, Roy Paily. Rajnish Gupta, Amit Ranjan, Arvind Shukla, Shiraz N. Minwalla, S. Balaji, Abhijit Bhattacharyya, Rajesh Kumar, Bivash Ranjan Dasgupta, Shreos Roychowdhury, Rajib Rakshit, Dr. Debashis Bondyopadhyay and Dr. Bidyut Halder for helping me at different times.

No words will be sufficient for Mr. M. M. Gupta, Mr. K. Masood, and Mr. R. S. Rajput the technical staff members of the Van de Graaff laboratory, for their ungrudging help and sincere co-operation (even on holidays) throughout the course of this work. At this point I wish to extend my sincere thanks to Mr. Shivprakash (Babuji) for his help in getting liquid nitrogen throughout this work. I am also grateful to Mr. A. K. Srivastava and Mr. S.L. Kanaujia for making my stay cheerful. I shall surely miss their company when I won't be here at IIT Kanpur.

Special thanks are due to Mr. Arun Kumar Ganguly for preparing neat drawings. I must appreciate their (Mr. and Mrs. Ganguly) encouragement. I remain grateful to Mr. and Mrs. D.C. Banerjee for their caring attitude during my long stay at Kanpur.

I am thankful to Mrs. Anjali Kulkarni, Mrs. Shraddha Mohapatra and their children - Sai, Apoorva and Stuti for their friendly as well as homely association.

I wish to extend my sincere thanks to the technical staff of physics workshop Mr. R. Singh, Mr. Bahadur Singh, Mr. S.N. Gosain, Mr. R.M. Singh, Mr. Bhagawandeen Sharma, and Mr. Dubey for their sincere and hard work in making different experimental apparatus used in this work.

I am very much indebted to Mr. Khalid Masood and Bhabhiji for their friendly and caring attitude especially during my tough days at IIT Kanpur. I would also like to thank their children Shazeb, Shazad, and Sumaiya for creating a homely association.

Let me thank Mr. Manmohan Gupta separately for his constant encouragement during our lunch time.

Special thanks are due to Indrani, Supriti, Suneeta, Sangita, Sudiptoda, Antara, Biswajit,

Boudi, Masima and Mesomasay for making my stay cheerful at IIT Kanpur.

I am indebted to all my beloved C-TOP family members. However, special thanks are due to Bhargab, Bappa, Deba, Tapan, Subit, Sankarda, Manoj, Prasen, Sinha, Pal, Sumanta, Kali, Samudra, Pradip, Naru, Sujay, Dinuda, Santi, Atanu, Arun, Pradipta, Rajib, Bivash, Pushan, Jethu, Goyal, and Maku. Alope, Kaushik Basak, Kamalesh, Kausik Biswas, and Kousik Nandy - I shall remember you five for your brotherly attitude and many situations which I cannot share with anybody else apart from you.

My heartfelt thanks are due to Debuda who is not only my colleague but like my elder brother and special thanks are due to Ani for his meticulous help whenever I needed. I wish he were my brother. Swapan, it will be difficult for me to compensate your absence! Girida and Abirda both of you are missed by me very much!

I would like to thank to all of my friends and departmental colleagues who had helped me from time to time and also made the stay a memorable one.

I would like to thank all of my childhood friends. However, I would like thank Debajit specially who is a dream friend of mine! He knows what friendship is and also knows how to nurture it. Bravo Pana, for your constant boosting!

Special acknowledgement to Mr. Balai Chandra Gol and Mr. Bani Kumar Mukhopadhyay who have taught me and always cared for me.

At last but not the least, my deepest gratitude to my parents for their constant inspiration and silent acceptance of my long absence from home.

Tapobrata Som

Synopsis

Hydrogen is a major reactant with solids because of its strong chemical activity, high lattice mobility and wide occurrence as H_2 and constituent of molecular gases and liquids. The presence of hydrogen affects the physical, chemical, mechanical and electrical properties of many materials like metals, semiconductors, insulators, superconductors, etc. Therefore, detection and analysis of hydrogen play an important role in many scientific and technical problems, and hydrogen-material system has emerged as an area of special interest in present-day condensed matter physics. Indeed, the research field of hydrogen touches upon many classical problems, viz. chemical bonding, electronic structure, lattice structure, optical properties, defects, magnetism, phase transition, isotope effect, diffusion, segregation, chemisorption, electrochemistry, surface chemistry, etc. It may be noted that in many cases it is only necessary to study the behaviour of hydrogen in the near-surface region (up to $1\ \mu m$).

The present thesis work deals with the detection of hydrogen and its depth profiling by elastic recoil detection analysis (ERDA) using MeV $^4He^+$ ions in wide class of materials, viz. potassium dihydrogen phosphate (KH_2PO_4 or KDP), diamondlike carbon (DLC) and diamond films, Si, etc. The importance of hydrogen in variety of ^{materials} and the different techniques for its detection have been briefly discussed below followed by the objectives of the thesis and a summary of the contents of the thesis.

In metallic systems, the formation of hydride phases has been extensively investigated as a means to store H fuel. On the other hand, moisture-induced hydrogen leads to material embrittlement which is an important cause of environmental degradation of structural alloys. In case of semiconductors, atomic hydrogen has an important role to play since it can passivate the electrically active dangling bonds and neutralize the effect of shallow acceptors and donors. It has been observed that atomic hydrogen is a key stabilizing species in the growth

of chemical vapour deposited (CVD) diamond films as it selectively etches non-diamond-bonded material, thereby reducing the incorporation of graphitic component in the films. Similarly, the role of hydrogen in DLC films is of particular interest since hydrogen concentration and the way it is incorporated in this material are closely related to the mechanical, electrical and optical properties of these films. In case of high- T_c superconductors, it has been observed that incorporation of hydrogen leads to alter their structural, electrical and magnetic properties. In KDP-type ferroelectric phosphate materials, owing to the strong H-bond formation, hydrogen plays a crucial role in phase transition and determining the optical properties of these materials. Moreover, hydrogen is a major constituent of all the biological systems which have tremendous application potential in biotechnology and other related fields like molecular bioelectronics and solid state electrochemistry

Hydrogen may get incorporated in materials in several ways. These may be classified into two distinct groups: (i) methods in which hydrogen is introduced in an intentional and controlled manner, such as exposure to plasma or by direct implantation, and (ii) the methods in which hydrogen is injected into the materials in an uncontrolled and unintentional way. Examples of the latter include sample preparation, cleaning and fabrication processes such as boiling in water, wafer polishing in the presence of H-containing reagents, heat treatments in molecular hydrogen, exposure to humid atmosphere etc.

The available experimental tools, for investigating H related problems, may be arranged into two categories: (i) experiments, which probe the change in the material properties due to the presence of H in the system and (ii) experiments, which directly probe hydrogen itself, in the materials. Experiments belonging to the first group include measurements of changes in the electrical and optical properties, study of absorption isotherms, etc. On the other hand, experimental methods belonging to the second group are mainly nuclear techniques like nuclear reaction analysis (NRA), ERDA, and other methods like secondary ion mass spectroscopy (SIMS) which use energetic ion-beams and detection of the secondary ions.

The group (ii) experiments, as mentioned above, are generally known as ion-beam analysis (IBA) techniques. During irradiation, interaction occurs with nuclei of the host material as well as with hydrogen present in it. Indeed, the possibility of identifying the events corresponding to reaction with hydrogen is conditioned by the choice of the type and energy of the bombarding particles. The participation of charged particles in such nuclear interactions

allows one to perform the depth profiling of hydrogen where the interaction products are detected by suitable detectors. Some of these methods use only the total number of particles that appear as a result of nuclear reactions with hydrogen, while others utilize their energy spectrum.

Hydrogen depth profiling made considerable advances with the introduction of ^{15}N method in 1976. This nuclear resonance reaction $^1\text{H} (^{15}\text{N}, \alpha\gamma) ^{12}\text{C}$ offers outstanding depth resolution due to small resonance width of the reaction, very good detection sensitivity and a good analyzable depth of $\sim 1\text{ }\mu\text{m}$. However, the ^{15}N method (and other resonance reactions) is strictly restricted to the particular H isotope in a single run. In contrast, ERDA allows simultaneous depth profiling of all the three isotopes of hydrogen in a non-destructive fashion. Although, this technique was first demonstrated by L'Ecuyer *et al.*[1] by using a ^{35}Cl beam at 30 MeV. lateron, Doyle and Peercy[2] had shown the successful use of ERDA technique for measuring ^1H depth distributions using a ^4He beam from a 2.5 MeV Van de Graaff accelerator.

In the past two decades ERDA with low energy (1-2 MeV) He^+ ions gained more and more attention. At the same time, desorption of hydrogen from some materials by bombardment of energetic ions (during ERD analysis) was recognized[3, 4]. Hydrogen desorption is interesting in itself but is also a problem when it is induced by the analyzing beam. This phenomenon leads to alter the measured depth profiles and the total hydrogen concentrations are underestimated. However, it is possible, in principle, to have the original total hydrogen concentration by extrapolating the measured H concentration versus ion fluence curve to zero fluence. The accuracy of extrapolation then depends upon the precision of the curve and on the adequacy of the fitting equation. This necessitates understanding of the processes occurring during ERDA (viz. bond-breaking, hydrogen molecule formation, etc.) on the basis of ion-solid interaction phenomena. Several research groups have put efforts in this direction and in doing so they have proposed phenomenological models to explain ion induced H-depletion from materials. However, study of H depth distributions in *wide class* of materials by ERDA, identification of hydrogen depletion amongst these and the attempt of fitting such hydrogen depletion data by a generalized model still remains an area which is yet to be completely explored .

The main objectives of this work are: (i) to develop and standardize a low energy ERDset-up using the 2 MV Van de Graaff accelerator for analysis of hydrogen and its isotopes in materials using $^4\text{He}^+$ ions, (ii) to study He^+ ion-beam induced hydrogen loss occurring

from inorganic material like KDP and biomaterial like phospholipid ($C_{83}H_{152}O_{17}P_2$) where hydrogen is a natural constituent, (iii) to analyze hydrogen in DLC and diamond films where hydrogen gets incorporated in an uncontrolled manner during film growth and to study the effects of thermal treatment and $^4\text{He}^+$ ion bombardment in these films, (iv) to develop a plasma source ion implantation (PSII) facility for implantation of low energy (few keV) ions of gaseous species in materials and to study the thermal and ion induced changes occurring in the implanted hydrogen profiles from single crystalline Si and GaAs samples, (v) to understand the mechanism responsible for hydrogen depletion from materials under ion irradiation and to develop a formalism in terms of energy deposition by incident He^+ beam through electronic energy loss, and (vi) to correlate He^+ ion-beam induced hydrogen evolution with the physico-chemical changes occurring in the samples as measured by Fourier transform infrared (FTIR) analysis and micro Raman analysis, respectively.

There are seven chapters in the present thesis. Chapter 1 provides a brief introduction to the importance of hydrogen in materials, methods of its incorporation, and its various detection techniques. Among these, ERDA has been singled out due to its unique capability of detecting hydrogen and its isotopes in a simultaneous fashion using a low energy accelerator.

Chapter 2 describes the experimental techniques used in this thesis work. ERDA facility was developed using the 2 MV Van de Graaff accelerator for analysis of hydrogen in materials. Rutherford backscattering spectrometry was employed for compositional analysis. Techniques like FTIR and micro Raman analysis have also been described for their use to study the physico-chemical changes occurring in the materials, under investigation, due to ion induced and thermal effects.

Chapter 3 presents a review and the formalism of ERDA, influence of various system parameters on ERDA measurements and the way to optimize these parameters. The problem of the scattering cross section which deviates from the Rutherford cross section value has been dealt in detail. A linear fit to the published cross section data[5] was made. These parameters were used for the analysis of hydrogen recoil spectra using the 'RUMP' code[6]. This chapter also describes the method of standardizing an ERDA set-up and the methodology for quantitative analysis of H recoil spectra.

The experimental results and analysis of hydrogen from several technologically important materials are presented in Chapters 4,5, and 6 respectively. These chapters deal with the consequences of ion induced and thermal changes brought into the materials, under

investigation.

Chapter 4 describes the results of hydrogen analysis and its depletion from three different category of samples, viz. single crystalline inorganic potassium dihydrogen phosphate (KDP), DLC films deposited on Si under various conditions by dc glow discharge technique, and organic phospholipid (cardiolipin) thin films deposited on Si by spin coating technique. The importance of these materials and various steps of sample preparation have also been described in the respective sections. An attempt has been made to look into the physico-chemical changes occurring in the samples by using Fourier transform infrared (FTIR) and micro Raman spectroscopy.

In this work, based on statistical arguments, the number of terms selection has been justified for fitting the H-depletion curves, obtained from KDP, DLC and phospholipid samples, with a multiple-term inverse exponential model. Suitable physical arguments have been given to explain the fitting parameters on the basis of energy deposition along the trajectory of the incident ion-beam, its consequence on the chemical reconstruction process and atomic migration through the ion track. To be more specific, a model has been adopted in which molecular bond cleavage due to electronic energy loss by the projectile leads to the liberation of H atoms. The combined mechanisms of direct recombination within a characteristic volume and the formation of H₂ molecule by diffusing H radicals has been used to describe the H loss from the above mentioned materials. The predictions of this model, in terms of molecular hydrogen release cross section, are well within the reported framework of H₂ molecular release cross section versus projectile energy loss curve. It is demonstrated that this model would be applicable for accurate prediction of initial hydrogen content from important class of materials showing hydrogen depletion during ERD analysis.

Chapter 5 presents the importance of diamond and application of ERDA technique to study the hydrogen depth distributions from CVD diamond films grown on Si. Surprisingly, MeV He⁺ ion induced delamination of diamond films were observed at room temperature during ERD analysis. Since diamond films contain very less amount of hydrogen, hydrogen depth distribution from the film and film/substrate interface has played a crucial role as that of a 'marker' to determine the threshold fluence at which the delamination occurs. The nature of as-deposited and delaminated diamond films was investigated using scanning electron microscopy (SEM). On the basis of these observations and micro Raman spectroscopic measurements, it has been proposed that the residual film stress gets enhanced under He⁺

ion bombardment leading to stress saturation condition which causes the delamination of diamond films.

Chapter 6 describes the importance of hydrogen in crystalline semiconductors and its various methods of incorporation in these materials. It also describes the importance of the PSII technique and the development of such a low energy dc PSII set-up for studying migration of hydrogen in crystalline semiconductors, viz. Si and GaAs. ERDA has been extensively used to study the changes occurring in the implanted hydrogen profile due to vacuum annealing in the temperature range of 300 to 800° C. ERDA studies reveal outdiffusion of hydrogen for both Si and GaAs beyond 400° C. Exponential fitting of retained amount of hydrogen as a function of annealing temperature has been employed to determine the activation energy for hydrogen outdiffusion from Si.

Chapter 7 presents the summary and conclusions of this work. Also, the scope of further work has been mentioned which may enable one to undertake such studies in different technologically important materials which contain hydrogen.

Bibliography

- [1] J. L'Ecuyer, C. Brassard, C. Cardinal, J. Chabbal, L. Dêschenes, J.P. Labrie, B. Terrault, J.G. Martel and R. St.-Jacques, *J. Appl. Phys.* 47 (1976) 881.
- [2] B.L. Doyle and P.S. Peercy, *Appl. Phys. Lett.* 34 (1979) 811.
- [3] D. Boutard, B.M.U. Scherzer, and W. Möller, *J. Appl. Phys.* 65 (1989) 3833.
- [4] M.P. de Jong, A.J.H. Maas, L.J. van Ijzendoorn, S.S. Klein, and M.J.A. de Voigt, *J. Appl. Phys.* 82 (1997) 1058.
- [5] V. Quillet, F. Abel, and M. Schott, *Nucl. Instr. Meth. B* 83 (1993) 47.
- [6] L.R. Doolittle, *Nucl. Instr. Meth. B* 9 (1985) 344.

List of Publications

International Journals

1. ¹ “MeV He⁺ ion induced delamination of diamond films” – T. Som, S. Bhargava, M. Malhotra, H.D. Bist, V.N. Kulkarni and S. Kumar, *Appl. Phys. Lett.* 72 (1998) 3014.
2. ¹ “Stress distribution around the ion induced channels in CVD diamond films; A micro Raman study” – P.S. Dobal, M.S. Navati, H.D. Bist, T. Som and V.N. Kulkarni, *J. Raman Spectroscopy* (in press).
3. ¹ “Study of low energy plasma ion implanted hydrogen in GaAs” – T. Som, S. Dhar and V.N. Kulkarni, *Rad. Phys. Chem.* 51 (1998) 683.
4. “MeV ion beam mixing of Au in Fe₇₈B₁₃Si₉ amorphous metallic alloy” – S. Dhar, T. Som, H.C. Verma and V.N. Kulkarni, *Rad. Phys. Chem.* 51 (1998) 539.
5. “Ion-induced room temperature synthesis of low resistive nickel germanide phase” – S. Dhar, T. Som and V.N. Kulkarni, *J. Appl. Phys.* 83 (1998) 2363.
6. ¹ “Hydrogen depletion from KH₂PO₄ under He⁺ ion bombardment” – T. Som, S. Dhar, S.N. Minwalla and V.N. Kulkarni, *Nucl. Instr. Meth. B* 122 (1997) 244.
7. “Ar ion induced copper germanide phase formation at room temperature” – S. Dhar, T. Som, Y.N. Mohapatra and V.N. Kulkarni, *Bull. Mater. Sci.* 20 (1997) 420.
8. ¹ ERD facility for analysis of hydrogen and deuterium in materials – T. Som, S. Dhar, N. Banerji, K. Ramakrishnan and V. N. Kulkarni, *Bull. Mater. Sci.*, 19 (1996) 73.
9. ¹ “A study of hydrogen in diamondlike carbon films” – M. Malhotra, T. Som, V. N. Kulkarni and S. Kumar, *Vacuum* 47 (1996) 1265.
10. “Room temperature synthesis of copper germanide phase by ion beam mixing” – S. Dhar, T. Som, Y.N. Mohapatra and V. N. Kulkarni, *Appl. Phys. Lett.* 67 (1995) 1700.

¹Article is based on this thesis work.

11. ¹“Ion-beam analysis of phospholipid thin film deposited on Si” – T. Som, T.K. Khan, P. Gupta-Bhaya, S. Kumar and V.N. Kulkarni (communicated to *Nucl. Instr. Meth. B*).

International Conferences/Symposia

1. ² “Study of hydrogen content and physical properties of YBCO pellets exposed to humid atmosphere” – T. Som, S. Dhar S. Singh and V.N. Kulkarni, in “High Temperature Superconductivity - Ten Years after its Discovery” eds. K.B. Garg and S.M. Bose (Narosha, New Delhi, 1998) p. 285.
2. ²“Study of plasma ion implanted hydrogen in semi-insulating GaAs” – T. Som, S. Dhar, Y.N. Mohapatra and V.N. Kulkarni, in “Physics of Semiconductor Devices”, eds. Vikram Kumar and S.K. Agarwal (Narosha, New Delhi, 1998) p. 369.
3. “Cu₃Ge, a novel contact material for semiconductor device technology: Room temperature synthesis by ion beam mixing” – S. Dhar, T. Som, Y.N. Mohapatra and V.N.Kulkarni, in *Semiconductor Devices*, Ed. Krishan Lal (Narosa, New Delhi, 1996) p. 502.

National Conferences/Symposia

1. “Quantitative analysis of hydrogen in YBCO pellets using Elastic Recoil Detection Analysis” – T. Som, N. Banerji, K. Ramakrishnan and V.N. Kulkarni, Proc. DAE SSP Symp. 37C (1994) 76.
2. “Mixing of Au in a-SiO₂ by Kr ion beam” – S. Dhar, T. Nigam, T. Som, K. Ramakrishnan and V.N. Kulkarni, Proc. DAE NP Symp. 37B (1994) 521.
3. “Study of hydrogen diffusion in silicon by Elastic Recoil Detection Analysis” – T. Som, S. Dhar and V.N. Kulkarni, in “Semiconductor Materials and Devices”, eds. O.P. Agnihotri and V.K. Jain (Narosa, New Delhi, 1997) p. 148.

²Article is based on this thesis work.

4. "Degradation of physical properties of Indium Tin Oxide films on glass plate due to interaction with water" – **T. Som**, S. Dhar and V.N. Kulkarni, Proc. of National Conference, CRYOVAC-95, VECC, Calcutta, 1995.
5. "Hydrogen depletion from KH_2PO_4 due to interaction with helium" – **T. Som**, S. Minwalla, S. Dhar and V.N.Kulkarni, Proc. DAE SSP Symp., 38C (1995) 395.
6. "Ion beam mixing study of Si-Ge system" – P. Choudhuri, S. Dhar, **T. Som**, Y.N. Mohapatra, and V.N. Kulkarni, Proc. DAE SSP Symp., 38C (1995) 175.
7. "Low energy DC H and D Plasma Source Ion Implantation facility at IIT, Kanpur" – **T. Som**, S. Dhar and V.N. Kulkarni, Proc. Natl. Symp. on Plasma Science, ed. P.K. Ghosh (Prentice-Hall, New Delhi, 1996) p. 103.
8. "Channeling study of low energy DC plasma ion implanted N in Si and GaAs"– **T. Som**, R. Paily, S. Dhar, Y.N. Mohapatra and V.N. Kulkarni, Proc. DAE SSP Symp., 39C (1996) 225.
9. "Ion induced synthesis of low resistive metal germanide phases" – S. Dhar, P.K. Giri, **T. Som**, Y.N. Mohapatra and V.N. Kulkarni, Proc. DAE SSP Symp. 39C (1996) 374.
10. "Reduction of hydrogen depletion from KH_2PO_4 due to interaction with He^+ at low temperature" – **T. Som** and V.N. Kulkarni, Proc. DAE SSP Symp. 40C (1997) 56.

Contents

Acknowledgments	vii
Synopsis	xi
List of Publications	xviii
List of Tables	xxv
List of Figures	xxvii
1 Introduction	1
1.1 Preamble	1
1.2 Hydrogen in materials	2
1.3 Methods of H incorporation	4
1.4 Hydrogen detection	5
1.5 Motivation and objectives of this work	8
1.6 Organization of the thesis	9
2 Experimental	13
2.1 Introduction	13
2.2 Sample processing	14
2.3 Van de Graaff accelerator facility	14
2.4 Elastic recoil detection analysis	17
2.5 ERDA set-up	17
2.5.1 The beam line	17
2.5.2 Pulse shaping electronics and multichannel analyzer	19
2.6 Rutherford backscattering spectrometry	19

2.7	RBS set-up	20
2.7.1	RBS Spectra analysis	22
2.8	RBS-channeling	25
2.9	Infrared spectroscopy	28
2.10	Raman Spectroscopy	29
2.11	Mass spectroscopic thermal effusion	29
2.12	X-ray Diffraction	30
2.13	Scanning Electron Microscopy	31
3	Elastic recoil detection: Formalism and analysis	34
3.1	Introduction	34
3.2	ERDA Fundamentals	35
3.2.1	Kinematics	35
3.2.2	Cross Section	37
3.2.3	Energy Loss	41
3.2.4	Energy straggling	46
3.3	Influence of various parameters and their optimization	48
3.3.1	Mass resolution	48
3.3.2	Sensitivity	49
3.3.3	Depth resolution	50
3.3.4	Depth of analysis	52
3.4	Analysis of H recoil spectra	52
3.4.1	System calibration	52
3.4.2	Hydrogen quantification	56
3.5	Summary	60
4	Hydrogen depletion during ERDA: Experimental results and modelling	66
4.1	Introduction	66
4.2	Ion induced hydrogen depletion	67
4.2.1	KDP system	67
4.2.2	DLC system	83
4.2.3	Phospholipid system	104
4.3	Determination of initial hydrogen concentration	117

4.4	Phenomenological/empirical models	119
4.4.1	Review of the existing models	119
4.4.2	Model of Adel <i>et al.</i>	125
4.4.3	de Jong <i>et al.</i> 's model	126
4.4.4	Comparison with experimental results	130
4.5	Summary	137
5	Role of hydrogen to study ion induced delamination of CVD diamond	144
5.1	Introduction	144
5.2	Experimental	146
5.3	Results and discussion	146
5.3.1	RBS	146
5.3.2	SEM	147
5.3.3	Irradiation and ERDA	147
5.3.4	Effects of irradiation	152
5.3.5	Micro Raman spectroscopy	155
5.4	Conclusions	160
6	Out-diffusion of H from Si and GaAs	165
6.1	Introduction	165
6.2	Techniques for hydrogen incorporation in semiconductors	166
6.2.1	Hydrogen plasma exposure	167
6.2.2	Broad beam ion implantation	167
6.2.3	Plasma source ion implantation	168
6.3	Shallow impurity passivation by hydrogen	168
6.4	Hydrogen diffusion	170
6.5	Experimental	170
6.5.1	PSII set-up and H implantation	170
6.5.2	ERDA measurements	171
6.6	Results and discussion	173
6.6.1	Si:H system	173
6.6.2	GaAs:H system	176
6.7	Summary and conclusions	180

7	Summary and conclusions	187
---	-------------------------	-----

List of Tables

3.1	Summary of reported hydrogen and deuterium recoil cross section data. . . .	44
3.2	Slab analysis to calculate stopping of hydrogen in a 6 μm mylar foil.	53
3.3	Comparison of hydrogen energy loss in a 5 μm mylar foil as calculated from single layer and slab analysis.	55
4.1	Observed infrared frequencies (400-2000 cm^{-1}) and their assignments for as obtained KDP at room temperature.	76
4.2	Different KDP Raman peak wavenumbers (ν in cm^{-1}), FWHM's ($\Delta\nu_{1/2}$ in cm^{-1}) and intensities (I in a.u.) along with respective peak assignments. A, B and C refer to the three different irradiated regions corresponding to fluences of 8.9×10^{14} , 1.78×10^{15} and 3.56×10^{15} He^+/cm^2	78
4.3	Growth parameters and some of the physical properties of the samples on which hydrogen and microstructural analysis have been presented in this section[44].	85
4.4	Observed infrared bands (in cm^{-1}) and their assignments (in cm^{-1}) for DLC 51, DLC 33, and DLC 18 films.	98
4.5	Results of micro Raman analysis obtained from a film DLC 33.	100
4.6	Results of micro Raman analysis obtained from annealing of the sample DLC 49.	100
4.7	Comparison of carbon, oxygen and phosphorous contents of cardiolipin film ($\#TK - 2$), as obtained from RBS.	110
4.8	Comparison of thickness and composition of <i>cardiolipin</i> film ($\#TK-2$) for two different He^+ ion fluences, as obtained from ERDA.	112
4.9	Peak positions and various bonding configurations observed in infrared spectra of phospholipid films.	113

4.10 Raman peak positions and respective FWHMs obtained from phospholipid samples. 115

4.11 Initial H/C ratios for different DLC films obtained from the method of extrapolation proposed in this work. 119

4.12 Explanation of the quantities in the table: E_0 is the beam energy used in the experiment, $A\xi^2$ is extracted from the fitting of H-depletion data, A is the effective ion track area, ξ is the bond-breaking probability in the ion track, and N_δ is the number of secondary electrons emitted per unit length. 134

4.13 Comparison of recombination volume (V) and ratio of reaction rates (k_1/k_2) for all the samples studied in this work. 136

6.1 Results of RUMP simulation. 180

List of Figures

1.1	Comparison of various surface analysis techniques	7
2.1	Layout of the Van de Graaff facility.	15
2.2	Photographs of (a) the Van de Graaff accelerator and (b) the analyzing magnet.	16
2.3	Schematic representation of an elastic collision process in laboratory frame. Target of mass M is initially at rest.	21
2.4	Block diagram of RBS and ERDA experimental chamber alongwith target, detector and other accesories.	23
2.5	RBS calibration spectra of pure Al and Au film deposited on Al.	24
2.6	Typical RBS spectrum of a Si sample along with its RUMP simulation. . . .	26
2.7	Schematic diagram of the sample manipulator for RBS-channeling experiment.	27
3.1	Schematic diagram showing the ERDA process.	36
3.2	Kinematic factor (for recoiled particles) versus (M_r/M_p)	38
3.3	Projectile energy as a function of the projectile atomic number.	40
3.4	Experimental and Rutherford recoil cross section data for H plotted against inverse square of the projectile energy : (a) $\theta_r = 10^\circ$, (b) $\theta_r = 20^\circ$, and (c) $\theta_r = 30^\circ$	42
3.5	Experimental and Rutherford recoil cross section data for D plotted against inverse square of the projectile energy : (a) $\theta_r = 10^\circ$, (b) $\theta_r = 20^\circ$, and (c) $\theta_r = 30^\circ$	43
3.6	A monoenergetic beam of energy E_0 loses energy ΔE in traversing a thin film of thickness ΔX . Simultaneously, energy straggling broadens the energy profile.	47
3.7	H recoil spectrum obtained from Si implanted with hydrogen.	54
3.8	ERDA spectra obtained from KDP at 130 K : (o) experimental and (-) simul- tation.	58

3.9	H coil spectra from high- T_c YBCO pellets : before and after exposure to humid atmosphere. The experimental parameters are : $E_0 = 1.43$ Mev, $Q = 10 \mu\text{C}$, $\Omega = 0.865$ msr, and $\theta_r = 25^\circ$. The arrow indicates the surface position of recoiled hydrogen.	59
3.10	As implanted H and D recoil spectra (along with simulation) from Al:H:D sample. The experimental parameters are : $E_0 = 1.7$ Mev, $Q = 10 \mu\text{C}$, $\Omega = 0.468$ msr, and $\theta_r = 30^\circ$. The arrows indicate the sample the surface position of H and D.	61
4.1	Experimental and simulated RBS spectra obtained from KDP/Au(60 Å) sample.	70
4.2	1.5 Mev He^+ induced hydrogen recoil spectra obtained from different sample configurations: (a) KDP/Au(60 Å), (b) KDP/Au(30 Å) and (c) bare KDP samples.	71
4.3	Variation in the hydrogen composition as a function of incident He^+ -dose obtained from different sample configurations.	72
4.4	Growth of the surface hydrogen peak as a function of He^+ irradiation dose. The solid line is a best fit to the experimentally obtained points. Each point represents the area under the surface H peak which has been obtained by subtracting the contribution of the flat portion of recoil spectra (see Fig.4.2).	73
4.5	Infrared spectrum obtained from as obtained KDP.	74
4.6	Deconvoluted micro Raman spectrum for as obtained KDP.	75
4.7	Overlapped Raman spectra from various irradiated regions of KDP.	79
4.8	Variation in Raman peak intensity corresponding to (a) $\nu_1(\text{PO}_4)$ and (b) $\nu_3(\text{PO}_4)$ modes as a function of He^+ ion fluence.	80
4.9	Variation in Raman peak shift corresponding to (a) $\nu_1(\text{PO}_4)$ and (b) $\nu_3(\text{PO}_4)$ modes as a function of He^+ ion fluence.	81
4.10	Variation in FWHM corresponding to (a) $\nu_1(\text{PO}_4)$ and (b) $\nu_3(\text{PO}_4)$ modes as a function of He^+ ion fluence.	82
4.11	ERDA depth versus concentration profiles for various DLC samples studied in this work. All the spectra correspond to an integrated He^+ charge of $5 \mu\text{C}$.	87
4.12	ERDA spectra obtained from DLC 33: (o) $8.9 \times 10^{14} \text{ He}^+/\text{cm}^2$, (●) $6.2 \times 10^{15} \text{ He}^+/\text{cm}^2$, (-) simulated spectra.	88

4.13 ERDA spectra obtained from DLC 51: (o) 1.8×10^{14} He ⁺ /cm ² , (●) 4.4×10^{15} He ⁺ /cm ² , (-) simulated spectra.	89
4.14 ERDA spectra obtained from DLC 18: (o) 1.8×10^{14} He ⁺ /cm ² , (●) 6.2×10^{15} He ⁺ /cm ² , (-) simulated spectra.	90
4.15 Dependence of bulk hydrogen content on analyzing ion fluence for various DLC samples studied in this work. Solid lines are guide to the eye.	91
4.16 ERDA spectra obtained from DLC 49: (a) as deposited film: (o) 1.8×10^{14} He ⁺ /cm ² , (●) 6.2×10^{15} He ⁺ /cm ² , (-) simulated spectra; (b) annealed film (600 ^o C): (o) 1.8×10^{14} He ⁺ /cm ² , (●) 6.2×10^{15} He ⁺ /cm ² , (-) simulated spectra.	92
4.17 IR transmission spectra for three different DLC films, viz DLC 18, DLC 33 and DLC 51.	94
4.18 FTIR spectra obtained from DLC 18 before and after He ⁺ irradiation corresponding to an ion fluence of 6.2×10^{15} ions/cm ²	95
4.19 FTIR spectra obtained from DLC 49 before and after annealing at 600 ^o C.	96
4.20 Thermal effusion spectra obtained from DLC 49: (a) 600 ^o C, (b) 1000 ^o C.	99
4.21 Micro Raman spectra recorded from DLC 33 before and after He ⁺ irradiation corresponding to an ion fluence of 6.2×10^{15} ions/cm ²	101
4.22 Micro Raman spectra recorded from DLC 49 after annealing at: (a) 600 ^o C and (b) 1000 ^o C.	102
4.23 Structure of <i>cardiolipin</i>	107
4.24 (a) Random and (b) aligned RBS spectra of a <i>cardiolipin</i> film (#TK-2), collected after He ⁺ cumulated charge of 40 μC.	109
4.25 ERDA spectra of a <i>cardiolipin</i> film (#TK-2), collected after cumulated He ⁺ charge collection of 1 μC and 40 μC. The arrow indicates the surface position of H. The inset depicts ion-induced desorption of hydrogen from phospholipid films as a function of the cumulated dose during irradiation by He ⁺ ions of 1.23 MeV, used for ERDA. The solid line is a guide to the eye.	111
4.26 IR spectrum of as deposited phospholipid film on Si (100) substrate.	114
4.27 Raman spectra of phospholipid film obtained from: (a) as deposited and (b) He ⁺ irradiated spot.	116

4.28	Determination of initial hydrogen concentration of KDP by extrapolation method. Experimental data points (●) have been best fitted as indicated by the solid lines.	120
4.29	Determination of initial hydrogen concentration of porphyrin by extrapolation method. Experimental data points (●) have been best fitted as indicated by the solid lines. It may be noted here that initial three data points of the actual depletion curve has not been considered here for extrapolation.	121
4.30	Determination of initial hydrogen concentration of phospholipid by extrapolation method. Experimental data points (●) have been best fitted as indicated by the solid lines.	122
4.31	Determination of initial hydrogen concentration of DLC films: (a) DLC 18, (b) DLC 40, (c) DLC 33 and (d) DLC 51 by the method of extrapolation. Experimental data points (●) in all four cases have been best fitted as indicated by the solid lines.	123
4.32	Schematic diagram of an ion track and possible mechanism of H ₂ molecule formation on it.	127
4.33	Fitted H-depletion curve for KDP: (●) extrapolated H composition at zero analyzing fluence, (o) experimental data points, (–) fitted curve using Eqn. 4.10131	
4.34	Fitted H-depletion curve for different DLC films: (a) DLC 18, (b) DLC 40, (c) DLC 33 and (d) DLC 51. The experimental data points (o) have been fitted (–) curve using Eqn. 4.10. [In all the four cases extrapolated H/C ratio at zero analyzing fluence (●) has also been included.]	132
4.35	Fitted H-depletion curve for phospholipid: (●) extrapolated H/C ratio at zero analyzing fluence, (o) experimental data points, (–) fitted curve using Eqn. 4.10133	
4.36	$A\xi^2$ versus electronic energy loss $\left[\left(\frac{dE}{dx}\right)_e\right]$ plot for all the samples studied in this work alongwith literature repored data. Reported data were fitted using Eqn. 4.10 in order to extract the $A\xi^2$ values.	135
5.1	X-ray diffractogram of an as-deposited CVD diamond film grown on Si. . . .	148
5.2	SEM micrograph of the as-deposited diamond film on crystalline Si.	149

5.3	SEM photographs of He ⁺ ion irradiated diamond film: (a) three different ion irradiated regions on the film corresponding to three different target current densities; (b) propagation of the ion induced cracking of diamond film; and (c) close view of a delaminated spot on the diamond film corresponding to a target current density of 1 $\mu\text{A}/\text{cm}^2$	150
5.4	SEM micrograph obtained from one of the delaminated spots.	151
5.5	1.5 MeV He ⁺ induced ERDA spectra corresponding to different ion fluences: 5.2×10^{15} ions/cm ² (●), 1.0×10^{16} ions/cm ² (○), and 3.6×10^{16} ions/cm ² (×). The inset depicts the variation in surface H content (at.%) with He ⁺ ion fluence.	153
5.6	Micro Raman spectra of diamond films on Si from: (a) as deposited region and (b) periphery of the delaminated region.	157
5.7	The trace of an ion beam induced channel taken from TV screen assisted with Raman microprobe and a video camera. OC's, IC's and J's are different spots where Raman spectra were excited. The circle around each spot shows the apparent size (2 μm) of focused laser beam.	158
5.8	Room temperature Raman spectra recorded from natural diamond and from various spots in and around Channel-A under 514.5 nm excitation.	159
5.9	514.5 nm excited room temperature Raman spectra from the spots OC1, OC2, IC1, and IC2 of Channel-C.	161
6.1	Schematic diagram of dc plasma source ion implantation set-up.	172
6.2	H recoil spectrum obtained from as implanted Si.	174
6.3	Variation in the retained hydrogen fraction in Si after vacuum anneal at different temperatures. Solid lines are guide to the eye.	175
6.4	Time constant for hydrogen evolution (τ) from Si as a function of inverse temperature.	177
6.5	1.38 MeV ERDA spectra of n ⁺ -GaAs(Si):H samples.	178
6.6	Variation in integrated fraction of remaining H, (N/N_0).	179
6.7	ERDA spectra and their simulations for SI-GaAs:H samples.	181
6.8	Variation of the peak width of hydrogen distribution in SI-GaAs as a function of temperature.	182

Chapter 1

Introduction

1.1 Preamble

Hydrogen is the most prevalent element of the cosmos. It is present in inorganic, organic and biologic matters alike. There are three isotopes, ^1H , ^2H and ^3H , having atomic masses of 1.00797, 2.04100 and 3.01605 respectively. Since the relative mass differences are the biggest encountered throughout the periodic table, chemical isotope effects are well pronounced. Consequently, the hydrogen isotopes are distinguished by extra-names and extra-symbols: protium H (^1_1H), deuterium D (^2_1H) and tritium T (^3_1H). The positive ions are called proton, deuteron and tritium and with reference to particle beams their symbols are p, d and t, respectively. The natural abundance of protium is 99.985% and 0.015% is of deuterium. Tritium is unstable and decays by emission of β particles, having a maximum energy of 18.61 keV: $^3_1\text{H} \rightarrow ^3_2\text{He} + {}_{-1}e^0 + \bar{\nu}$; $\tau = 12.26$ years.

Hydrogen is a major reactant with solids as a result of its strong chemical activity, high lattice mobility and wide occurrence as H_2 and a constituent of molecular gases and liquids. The presence of hydrogen may have important effects on physical, chemical, mechanical and electrical properties[1–3] of many materials like metal, semiconductor, insulator, superconductor and so on and so forth. Therefore, detection and analysis of hydrogen play important role in many scientific and technical problems, and hydrogen-material system has emerged as an area of special interest in present-day condensed matter physics. Indeed, the research

field of hydrogen touches upon many classical problems, viz. chemical bonding, electronic structure, lattice structure, optical properties, defects, magnetism, phase transition, thermodynamics, isotope effect, diffusion, segregation, chemisorption, electrochemistry, surface chemistry, etc. This chapter describes the importance of hydrogen in materials, methods of hydrogen incorporation and its detection. It also describes the motivation and objectives for this work and the organization of the thesis.

1.2 Hydrogen in materials

In metallic systems, the formation of hydride phases has been extensively investigated as a means to store H fuel[4]. The hydrogen concentration in a hydride ($\sim 240 \text{ kg/m}^3$) is often more than 3 times higher than that for liquid hydrogen ($\sim 70 \text{ kg/m}^3$). This feature makes hydrogen storage in metals a practical proposition. On the other hand, moisture-induced hydrogen leads to material embrittlement which is an important cause of environmental degradation of structural alloys. For example, the estimated hydrogen diffusivity in single crystal of Fe-Al (40 at.%) intermetallic alloy at room temperature is about $10^{-9} \text{ cm}^2/\text{sec}$ [5]. It is revealed that hydrogen can be trapped in a vacancy or bonded inside the lattice which reduces the bond strength. Grain boundaries also act as a hydrogen condensation sites and hydrogen in grain boundaries possesses higher stability than in the vacancy.

In electronic materials hydrogen plays many roles, both beneficial and detrimental. It is incorporated into amorphous Si at elevated concentrations to passivate dangling bonds[6] which leads to the fabrication of devices. In crystalline semiconductors, viz. Si, Ge, GaAs, etc., it is emerging as an important reactant with imperfections to passivate both shallow and deep level acceptors and donors[3]. Parallely, H induced donor/acceptor levels have also been observed in the crystalline Si. It serves to passivate interfacial charge traps in SiO_2 on Si and also mediates the radiation sensitivity of these structures[7]. Presence of H in silicon oxynitride is a major cause of their instabilities, because of its capability to diffuse in these materials at relatively low temperatures[8]. Chemisorbed hydrogen has now been recognized to enhance the oxidation resistance of the Si surface, thereby facilitating processing[9]. A variety of H-containing molecular species are used for layer growth on semiconductors, resulting in important H-solid interactions which are not completely understood[10].

In recent years, diamond films have been proved to have tremendous applications as hard

wear resistant coatings for cutting tools, impact resistant coatings for high density computer disks, protective layer for solar cells used in space applications, heat sinks for high frequency and high power devices, etc. It has been observed that atomic hydrogen is a key stabilizing species in the growth of chemical vapour deposited diamond films as it selectively etches non-diamond-bonded material, thereby reducing the incorporation of graphitic component in the films. It also leads to the stabilization of diamond nuclei, hydrogenation of unsaturated hydrocarbon compounds on the substrate surface, and helps in abstraction of hydrogen from surface hydrocarbons[11].

Similarly, the role of hydrogen in amorphous hydrogenated carbon films (or diamond-like carbon (DLC)) is of particular interest since hydrogen concentration and the way it is incorporated in this material are closely related to the mechanical, electrical and optical properties of these films[12]. For example, low hydrogen containing films ($\sim 9-10$ at.%) having sp^2 carbon content of more than 50% are termed as graphitic and they have the optical band gap of ~ 1 eV. On the other hand, films having high hydrogen content (15-35 at.%) have been observed to have optical band gaps in the range of 1.8-2.2 eV. These films are rich in sp^3 C-C bonding between 40-65% and are typically termed as DLC's. There is another category viz. tetrahedrally bonded α -C:H films having low hydrogen content (~ 10 at.%) but is found to have a high optical band gap of ~ 2.8 eV. It is also observed that the films with high hydrogen content are usually soft whereas low hydrogen containing films are hard and have compact microstructures. These materials are used as protective layers and hard coatings and hence the study of H in DLC films has proved to be immensely important, both from scientific and technological view points.

Ever since the discovery of high- T_c superconductors, it has been observed by many researchers that incorporation of H leads to alter their several properties[13]. These include structural, electrical and magnetic properties. For example, hydrogen leads to a transition from orthorhombic to tetragonal structure for a composition of $H_{1.05}YBa_2Cu_3O_{6.91}$ [14]. It has led to increase the superconducting transition temperature (T_c) up to 95.7 K for a composition of $H_{1.7}YBa_2Cu_3O_7$ in comparison to the hydrogen free samples having a T_c of 94.6 K[15].

Hydrogen being a natural constituent, is also important for ferroelectric oxide material like KH_2PO_4 (KDP). KDP is a nonlinear optical material and is being used as the second harmonic generator in optoelectronics technology[16]. It has two correlated phase transitions

- the lower transition point was identified as the Curie point (123 K) and the higher one (353 K) was suggested to be the melting or dissociation point, where some of the H-bonds break. Since the prediction of high temperature phase transition, a lot of interests have been developed in the study of phase transition in hydrogen bonded solids of KDP-type materials[17].

Recently, biomaterials have attracted the attention of many researchers due to their potential application in biosensor technology. Hydrogen is a major constituent of all the biological systems which have tremendous applications in biotechnology and many other related fields. Amongst many such applications, molecular bioelectronics and solid state electrochemistry are emerging very fast. It has been identified that thin films of lipids have a great potential in the fabrication of immunochemically sensitive field-effect transistor. The interfaces of lipid films with Si, Au, and other inorganic substances form the basis of many electronic and biotechnological applications[18]. However, most of these problems are at their initial stages of development and require immense research efforts before making them viable for applications.

In summary, hydrogen plays important roles in altering various properties in wide class of technologically important materials. In addition, it plays important role in the fabrication of novel materials like DLC and diamond films. Besides, in many applications it becomes very important to study various aspects of hydrogen-material system in the near-surface region (few thousand Å to μm depth). As a consequence, it is important to investigate: (i) Depth distribution of H concentration in the near-surface region of materials, (ii) thermal diffusion of H, (iii) H related chemical bonds, (iv) correlation of H depth distribution with sample microstructure, etc. These should enable one to correlate the change in properties of the materials as a function of H content and should serve as a feed back in developing novel materials, fabricating devices etc.

1.3 Methods of H incorporation

There are several ways available for incorporating H in materials. These may be classified into two distinct groups- methods in which hydrogen is introduced in an intentional and controlled manner, such as exposure to plasma[19] or by direct implantation[20], and those methods in which hydrogen is injected into the materials in an uncontrolled and unintentional way.

Examples of the latter include sample preparation[21], cleaning and fabrication processes such as boiling in water, wafer polishing in the presence of H-containing reagents, heat treatments in molecular hydrogen, exposure to humid atmosphere etc.

1.4 Hydrogen detection

The available experimental tools, for investigating H related problems, may be arranged into two categories:

- i) Experiments, which probe the change in the material properties due to the presence of H in the system.
- ii) Experiments, which directly probe H itself, from the materials.

Experiments of group (i) include electrical conductivity measurements, study of absorption isotherms, etc. On the other hand, experimental methods belonging to group (ii) are based on the use of energetic beams obtained from particle accelerators. Some of the examples are secondary electron mass spectroscopy (SIMS)[22], nuclear reaction analysis (NRA)[23], elastic recoil detection analysis (ERDA)[24], etc.

The group (ii) experiments, as mentioned above, are called instantaneous or rapid nuclear analysis as the measurements are made simultaneously with irradiation. Also, these are known under the general name of ion-beam analysis (IBA) techniques. During irradiation interaction occurs with nuclei of host material as well as with H in it. However, the possibility of identifying the events corresponding to reaction with H is conditioned by the choice of the type and energy of the bombarding particles. In fact, participation of charged particles in a nuclear interaction allows one to perform the concentration depth profiling of H where the interaction products i.e., γ -rays, neutrons and charged particles are detected by scintillation and semiconductor detectors. Some methods use only the *total number* of particles that appear as a result of nuclear reactions with H, while others utilize their energy spectrum.

In case of SIMS, a low energetic heavy ion beam is incident on the target and surface layers are eroded by the sputtering process and hence the relative abundance of the ionized sputtered species (secondary ions) provide a direct measure of the composition of the layer that has been removed. SIMS has a very good depth resolution and detection sensitivity and is commonly used for detection and measurement of low concentrations of H atoms present in solids. However, it is naturally destructive and suffers from lack of discrimination between

different concentrations. Besides, radiation damage introduced during SIMS analysis seems to change the lattice structure at the surface. These disadvantages are thus responsible for the restricted usefulness of SIMS for studying H in materials.

On the other hand, among the experimental tools using MeV ions, only a few papers dealt with H profiling till the end of 1973[23, 25–27]. Cohen *et al.*[25] employed the p - p scattering technique for monitoring the hydrogen concentration profiles (detection limit of 1 ppm of H) across a 67 μm thick pile of mylar foils alternating with three Fe foils. In 1973, Leich *et al.*[23, 27] established the *resonant nuclear reaction* $^1\text{H}(^{19}\text{F}, \alpha\gamma)^{16}\text{O}$ for measuring hydrogen depth profiles in solids (lunar samples). Of course, hydrogen depth profiling made considerable advances with the introduction of ^{15}N method[28–30] in 1976. This nuclear resonance reaction $^1\text{H}(^{15}\text{N}, \alpha\gamma)^{12}\text{C}$ offers outstanding depth resolution due to small resonance width of the reaction, very good detection sensitivity and fairly good analyzable depth of $\sim 1 \mu\text{m}$. However, the ^{15}N method (and other resonance reactions) is strictly restricted to the particular H isotope-in a single run. In contrast, elastic recoil detection analysis (ERDA)[24] allows the simultaneous depth profiling of all the three isotopes of H and other light elements in a non-destructive fashion. The principle behind ERDA will be described in the next chapter. This technique was first applied by J. L'Ecuyer *et al.*[31] who used a ^{35}Cl beam at 30 MeV. Later on, Doyle and Peercy[32] had adopted the ERDA technique for measuring ^1H depth distributions using a ^4He beam from a 2.5 MeV Van de Graaff accelerator. Till then ERDA studies of hydrogen containing materials using low energy (1-2 MeV) He^+ ions have been proved to be very efficient from various aspects.

Fig.1.1 summarizes the details of several surface analysis techniques for the detection of hydrogen in materials characterization of materials. Although, ERDA has the unique capability of simultaneous depth profiling of H and its isotopes in a non-destructive fashion, in some cases, ion-beam induced H loss has been observed from materials during ERDA measurements from variety of materials[33–35].

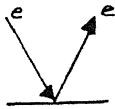

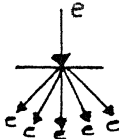
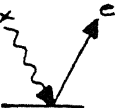
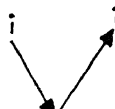
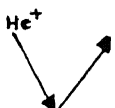

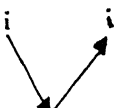
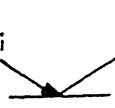
Method	Particle Measured	Process	Information
Auger Emission Spectroscopy (AES)	Auger Electron		-Elements Li.U
Scanning Electron Microscopy- Energy dispersive X-Ray (SEM-EDX)	X-Rays		-Elements Na.U
Transmission Electron Microscopy (TEM)	Diffacted Electrons		-Compound identification
X-Ray Photo Electron Spectroscopy (XPS or ESCA)	Photo Electrons		-Elements Li.U - Chemical Bonding
Secondary Ion Mass Spectrometry (SIMS)	Sputtered Ions		-Elements H.U
Rutherford Backscattering Spectrometry (RBS)	Scattered Ions (H^+ , He^+)		-Elements Be.U
Particle Induced X-Ray Emission (PIXE)	X-Rays		-Elements Na.U
Nuclear Reaction Analysis (NRA)	Light Ion Reaction Product		-Light Elements (H, Be, B, C, O, F...)
Elastic Recoil Detection Analysis (ERDA)	Recoiled Ions (H^+ , D^+ , T^+ etc.)		-Light Elements (H-O)

Figure 1.1: Comparison of various surface analysis techniques

1.5 Motivation and objectives of this work

It is now well recognized that ERDA can be used as a sensitive and useful method to study H and its isotopes in materials. In the past two decades ERDA with He^+ ions has gained more and more attention. This is beneficial as: (i) less energy is deposited in the target to obtain a profile so that less beam-induced damage is expected and (ii) H profiling can be performed in a low-energy accelerator laboratory. However, ion induced H evolution during ERDA measurements is a striking feature from materials and needs more attention to justify its non-destructive nature. Thus, the main objectives of this work have been summarized below:

- To develop and standardize a low energy ERDA set-up using the 2 MeV Van de Graaff accelerator for analysis of hydrogen and its isotopes in materials using $^4\text{He}^+$ ions. Development of a low energy plasma source ion implantation (PSII) facility for implantation of low energy gaseous species in materials.
- To study He^+ ion-beam induced hydrogen loss occurring from materials like KDP (KH_2PO_4) and phospholipid ($\text{C}_{81}\text{H}_{152}\text{O}_{17}\text{P}_2$) where hydrogen is a natural constituent.
- To analyse hydrogen in DLC and diamond films where hydrogen gets incorporated in an uncontrolled manner during film growth and to study the effects of thermal treatment and $^4\text{He}^+$ ion bombardment in these films.
- To study the thermal and ion induced changes occurring in the hydrogen concentrations of Si:H and GaAs:H where hydrogen has been incorporated in a controlled fashion during sample processing by low energy PSII.
- To understand the mechanism responsible for hydrogen depletion from materials under ion irradiation and to develop a formalism in terms of energy deposition by incident He^+ beam through electronic energy loss.
- To correlate He^+ ion-beam induced hydrogen evolution with the physio-chemical changes occurring in the samples as measured by Fourier transform infrared (FTIR) analysis

and micro Raman analysis, respectively.

1.6 Organization of the thesis

There are *seven* chapters in the present thesis. The present chapter (Chapter 1) gave a brief introduction to the importance of hydrogen in materials and its various detection techniques. Chapter 2 describes the experimental techniques used in this thesis work. It also describes the ERDA facility developed using the 2 MeV Van de Graaff accelerator for analysis of hydrogen in materials. Chapter 3 presents the formalism of ERDA, influence of various system parameters on ERDA measurements and their optimization. This chapter also describes the method of standardizing an ERDA set-up and the methodology for quantitative analysis of H recoil spectra. Chapter 4 describes the results of hydrogen analysis and its depletion from three different category of materials, viz. single crystalline inorganic potassium dihydrogen phosphate (KDP), DLC films deposited on Si under various conditions by dc glow discharge technique, and thin films of biological fluid - phospholipid (cardiolipin) deposited on Si by spin coating technique. An attempt has been made to look into the physico-chemical changes occurring in the samples by using Fourier transform infrared (FTIR) and micro Raman spectroscopy. Suitable physical arguments have been given to explain the fitting parameters on the basis of energy deposition along the trajectory of the incident ion-beam, its consequence on the chemical reconstruction process and atomic migration through the ion track. Chapter 5 presents the importance of diamond and application of hydrogen depth profiling by ERDA technique to determine the threshold fluence for MeV He^+ ion induced delamination of diamond films at room temperature. Based on micro Raman spectroscopic measurements, it has been proposed that the residual film stress gets enhanced under He^+ ion bombardment leading to stress saturation condition which causes the delamination of diamond films. Chapter 6 describes the importance of hydrogen in crystalline semiconductors. It also describes the importance of the plasma source ion implantation (PSII) technique and the development of a low energy dc PSII set-up for implanting hydrogen in crystalline semiconductors, viz. Si and GaAs. ERDA has been employed to study the thermal out-diffusion of hydrogen from these materials. Finally, chapter 7 presents the summary and conclusions of this work and the scope of future work.

Bibliography

- [1] *Hydrogen in Metals I* Eds. G. Alfeld and J. Völkl (Springer-Verlag, Heidelberg, 1978).
- [2] Y. Lifshitz, S.R. Kasi, and J.W. Rabalais, in *Properties and Characterization of Amorphous Carbon Films*, Eds. J.J. Pouch and S.A. Altervoitz, Vol. 52&53 of *Material Science Forum* (Trans. Tech. Publications, Switzerland, 1989).
- [3] S.J. Pearton, J.W. Corbett and M. Stavola, *Hydrogen in Crystalline Semiconductors* (Springer-Verlag, Heidelberg, 1992).
- [4] R. Kirchheim, E. Fromm and E. Wicke, Eds. *Proc. International Symposium on Metal-Hydrogen Systems: Fundamentals and Applications*, *Z. Phys. Chem. [NF]* 163-164 (1989).
- [5] Y. Yang and S. Hanada, *Scripta Metall. Mater.* 32 (1995) 1719.
- [6] M. Paesler, S.C. Agarwal and R. Zallen, Eds. *Proc. of the 13th International Conference on Amorphous and Liquid Semiconductors*, *J. Non-Cryst. Solids* 114 (1989).
- [7] E.H. Poindexter, Ed. *Metal-Oxide-Semiconductor Structures*, *Semicond. Sci. Technol.* 4 (1989) 970.
- [8] W.M. Arnoldbik, C.H.M. Marée, A.J.H. Mass, M.J. van den Boogaard, F.H.P.M. Habraken, and A.E.T. Kuiper, *Phys. Rev. B* 48 (1993) 5444.
- [9] G.S. Higashi, Y.J. Chabal, G.W. Trucks and K. Raghavachari, *Appl. Phys. Lett.* 56 (1990) 656.
- [10] K.K. Schuegraf, Ed. *Handbook of Thin-Film Deposition Processes and Techniques* (Noyes, Park Ridge, NJ, 1988).

- [11] L.S.G. Plano, in *Diamond: Electronic Properties and Applications*, Eds. L.S. Pan and D.R. Kania (Kluwer Academic, Massachusetts, 1995), p.64.
- [12] J.C. Angus, P. Koidl and S. Dominitz, in *Plasma Deposited Thin Films*, Eds. J. Mort and F. Jansen (Chemical Rubber Co., Boca Raton, FL, 1986) ch. 4.
- [13] T. Hirata, *Phys. Stat. Sol. (a)* 156 (1996) 227.
- [14] V.V. Sinitsyn, I.O. Bashkin, E.G. Ponyatovskii, V.M. Prokopenko, R.A. Dilanyan, V. Sh. Shekhtman, M.A. Nevedomskaya, I.N. Kremenskaya, N.S. Sidorov, R.K. Nikolaev, and Zh. D. Sokolovskaya, *Sov. Phys. Solid State* 31 (1989) 2056.
- [15] J.J. Reilly, M. Suenaga, J.R. Johnson, P. Thompson A.R. Moodenbaugh, *Phys. Rev. B* 36 (1987) 5694.
- [16] M. Vallade, *Phys. Rev. B* 12 (1975) 3755.
- [17] R.S. Viswanath and P. Miller, *Solid State Commun.* 29 (1979) 163.
- [18] C. Nicolini and F. Nazza, *Thin Solid Films* 284 (1996) 1.
- [19] K. Kohler, J.W. Coburn, D.E. Horne, E. Kay and J.H. Keller, *J. Appl. Phys.* 57 (1985) 59.
- [20] C. Ji, T.S. Shi and P. Wang, *Nucl. Instr. Meth. B* 12 (1985) 486.
- [21] J.C. Angus, *Diam. Relat. Mater.* 1 (1991) 61.
- [22] C.W. Magee and C.P. Wu, *Nucl. Instr. Meth.* 149 (1978) 529.
- [23] D.A. Leich and T.A. Tombrello, *Nucl. Instr. Meth.* 108 (1973) 67.
- [24] J. L'Ecuyer, C. Brassard, C. Cardinal, J. Chabbal, L. Dêschenes, J.P. Labrie, B. Terrault, J.G. Martel and R. St.-Jacques, *J. Appl. Phys.* 47 (1976) 881.
- [25] B.L. Cohen, C.L. Fink and J.H. Degnan, *J. Appl. Phys.* 43 (1972) 19.
- [26] R.S. Blewer, *Appl. Phys. Lett.* 23 (1973) 593.
- [27] D.A. Leich, T.A. Tombrello and D.S. Burnett, *Geochim. Cosmochim. Acta* 2 (1973) 1597.

- [28] W.A. Lanford, H.P. Trautvetter, J.F. Ziegler and J. Keller, *Appl. Phys. Lett.* 28 (1976) 566.
- [29] W.A. Lanford, *Science* 196 (1977) 975.
- [30] W.A. Lanford, *Nucl. Instr. Meth.* 149 (1978) 1.
- [31] J. L'Ecuyer, C. Brassard, C. Cardinal and B. Terrault, *Nucl. Instr. Meth.* 149 (1978) 271.
- [32] B.L. Doyle and P.S. Peercy, *Appl. Phys. Lett.* 34 (1979) 811.
- [33] D. Boutard, B.M.U. Scherzer, and W. Möller, *J. Appl. Phys.* 65 (1989) 3833.
- [34] C. Godet, R. Etemadi, and C. Clerc, *Appl. Phys. Lett.* 69 (1996) 3845.
- [35] M.P. de Jong, A.J.H. Maas, L.J. van Ijzendoorn, S.S. Klein, and M.J.A. de Voigt, *J. Appl. Phys.* 82 (1997) 1058.

Chapter 2

Experimental

2.1 Introduction

The study of hydrogen in different materials, presented in this thesis, typically involved the following experimental steps: (i) sample processing and cleaning, (ii) compositional analysis by Rutherford Backscattering Spectrometry (RBS), (iii) hydrogen analysis by Elastic Recoil Detection Analysis (ERDA), (iv) chemical analysis by Fourier Transform Infrared Spectroscopy (FTIR), and (v) structural analysis by micro Raman Spectroscopy. In some cases samples were also characterized by mass spectroscopic thermal effusion technique, X-ray diffraction technique, and scanning electron microscopy (SEM). For semiconducting samples, a dc plasma ion implantation set up was developed for hydrogen implantation in the range of 1-10 kV. These samples were thermally annealed in high vacuum up to 700° C.

The 2 MV Van de Graaff accelerator at Central Nuclear Laboratories, IIT Kanpur was used for ERDA and RBS measurements using He^+ ions. This chapter describes the experimental steps mentioned above alongwith the description of the accelerator facility.

2.2 Sample processing

As has been mentioned in Chapter 1, H may be present in materials for various reasons[1]. It can either be a constituent element of a material or can be incorporated in a material by some external means. External incorporation is possible during sample preparation/cleaning. due to exposure in hydrogen rich (humid) atmosphere or by the controlled process like ion implantation. Since this thesis deals with a wide class of materials, the source of hydrogen in all these cases are also different. As a result of this, each individual case has been described separately in the respective chapters.

2.3 Van de Graaff accelerator facility

The Van de Graaff accelerator is the most widely used among the commonly available accelerators. A schematic diagram of the accelerator system is shown in **Fig.2.1** and photographs of the same are presented in **Fig.2.2(a)** and **Fig.2.2(b)**. The accelerator (Model AN-2000), High Voltage Engineering Corporation make USA, is a precision to 2 MV high intensity source of positive ions. The accelerator produces a beam of ions which is homogeneous, stable and controllable over a wide range of energies. It is provided with three gas bottles and presently they are filled with three different gases He, Ar and Kr. An rf ion source is used to produce positive ions.

The mass and energy analysis of the accelerated ion beam is done by an analysing and switching magnet which is a 16 K Gauss electromagnet having a dc regulated (0-30 V) power supply which has a capability of supplying current upto 250 A[2]. During operation, the magnet is cooled to 10° C by circulating demineralised water through the coils. However, to operate the magnet at currents less than 140 A, air cooling is done by passing compressed (60 psi), chilled air instead of water through the tubular aluminium coils. The stainless steel switching chamber has five ports at angles 0°, $\pm 20^\circ$ and $\pm 45^\circ$. At present, the ports are utilized for performing experiments using the energy and mass analysed beam. The port at $+45^\circ$ is used to direct the beam into the experimental chamber for ERDA or RBS and channelling analysis while the beam of heavy ions are deflected through a small angle of 5° utilizing the 0° port. In the experimental chamber mounted on this port, experiments related to heavy ion irradiation can be performed.

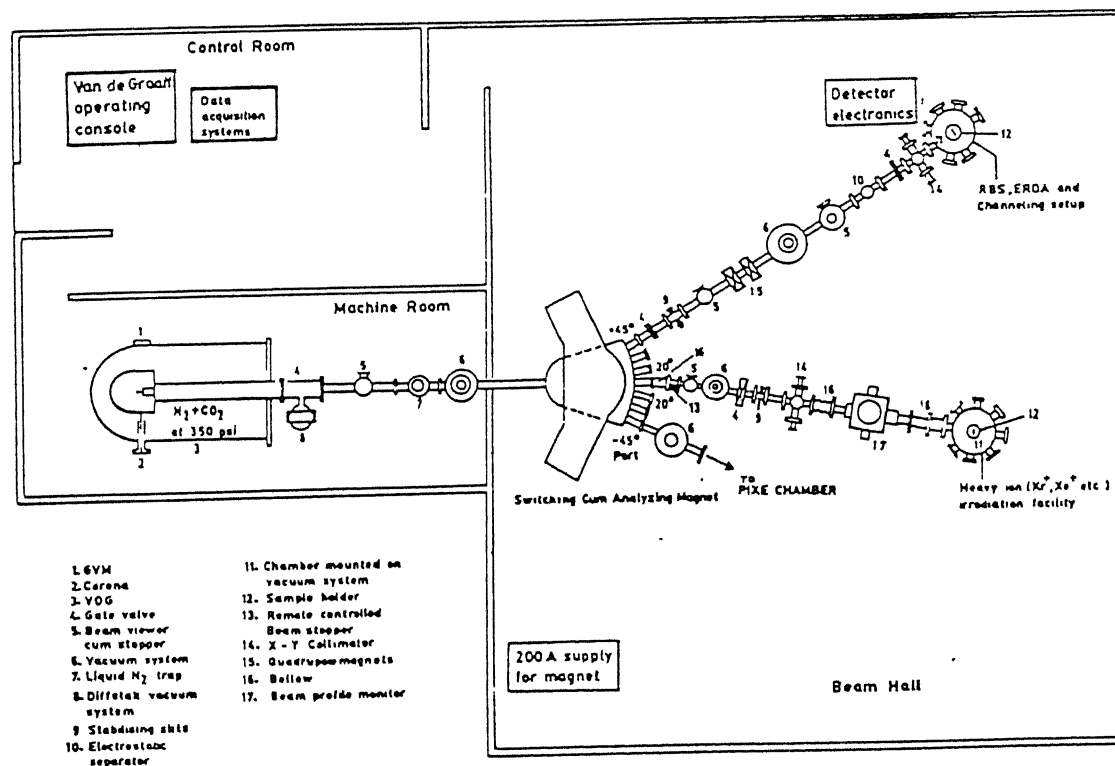


Figure 2.1: Layout of the Van de Graaff facility.

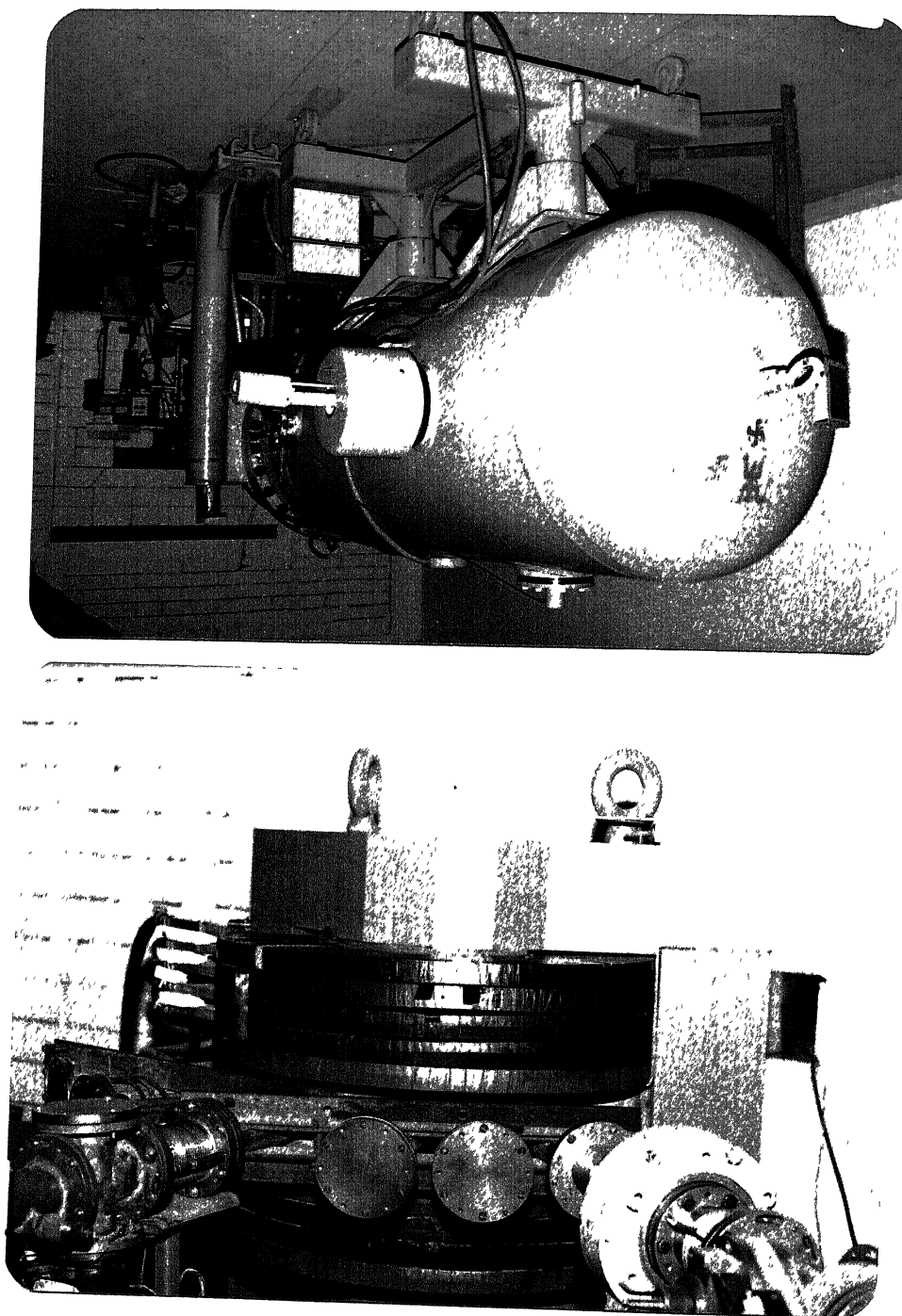


Figure 2.2: Photographs of (a) the Van de Graaff accelerator and (b) the analyzing magnet.

2.4 Elastic recoil detection analysis

The formalism of elastic recoil detection analysis (ERDA) and the methodology for analysis of ERDA spectra will be discussed at length in Chapter 3. Here, the experimental arrangement, especially set up for the present work has been described along with the details of ancillaries such as sample manipulators, beam viewer, beam defining slits, beam stopper, adjustable detector bench, etc. Some of these components were designed and fabricated for performing ERDA experiments under different conditions.

2.5 ERDA set-up

The complete ERDA set-up used in the present study consists of the following main stages:

1. Production of ions and acceleration using the 2 MV van de Graaff accelerator.
2. Mass and energy analysis of the accelerated ions using electromagnet.
3. Focusing of the energy analysed beam and separation of the O^{++} from He^+ ions of the same energy.
4. Final 'complete' set-up for ERD analysis.

2.5.1 The beam line

The ERDA set-up has been facilitated in a scattering chamber which is located at the 17° beam port. After deflection, the beam passes through energy stabilizing slits and quadrupole magnets. This focused and collimated ion-beam then passes through an uniform electric field generated by parallel plates (electrostatic beam separator) in order to separate out O^{++} from the He^+ beam[3] of the same energy. The ion-beam collimating unit is placed between the scattering chamber and the ion-beam separator, ^{which} has horizontal and vertical slits, which define the beam size, so that a beam spot of required dimension ^{is} available on the target (Fig.2.3). Beam viewers and beam stoppers have been positioned along the beam path to see the ion-beam for diagnosing the beam alignment problem and to block the ion-beam from entering the chamber as and when required. The scattering chamber used in this work has

six ports as shown in **Fig.2.4**. The important components of the ERD set-up are: (i) holder for accurate positioning and orientation of the sample, (ii) secondary electron suppressor, (iii) arrangement to measure integrated charge, (iv) arrangement to mount and cool the detector, and (v) mylar foil to stop the scattered primaries from reaching the detector. The ERD detector can be accurately positioned to make an angle varying from 20° to 40° with respect to the incident beam direction in a horizontal plane containing the incident beam. For ERDA experiments, the sample holder is a plate of dimensions $120\text{ mm} \times 25\text{ mm} \times 2.5\text{ mm}$. and five to six samples can be mounted on it at a time. It can be moved in the vertical direction, such that the region of interest of a sample can be brought in front of the incident beam for analysis, with an accuracy of $\pm 0.5\text{ mm}$. In this way several measurement on different regions of the same sample and measurements on various samples are possible without breaking vacuum. The sample holder, in this case, is rotated to a position such that the incident beam impinges on the target at an angle of 15° with respect to the sample surface. An aluminium grid is placed around the holder (inside the chamber) and a negative voltage of -260 V is applied to it, to suppress the secondary electrons emitted from the samples due to the primary ion-beam. Beam currents of $5\text{-}10\text{ nA}$ were utilized for the present analysis. Currents more than 10 nA may increase the detector dead time and pulse pile up effect, and hence it was maintained at all times to obtain the total fluence or charge (which^{is} related the number of incident He^+ ions incident on the target) using a current integrator (ORTEC, Model-401). For this purpose, the scattering chamber itself is used as a Faraday cup. The partially passivated ion implanted surface barrier detector is placed on a detector bench and the recoil angle (θ_r) can be varied from 20° to 40° with respect to the transmitted beam. This corresponds to a maximum uncertainty on the scattering angle of 0.5° which, however, is a significant value for the grazing incidence of the He^+ ions. The experimental geometry of ERDA is schematically shown in the inset of **Fig.2.4**. For a better depth resolution, a small aperture was used which subtends a solid angle of 0.865 msr . However, for higher sensitivity, the solid angle can be made up to 5 msr which is limited by the detector area and the minimum allowable distance.

2.5.2 Pulse shaping electronics and multichannel analyzer

The recoiled hydrogen signals from ERDA experiments are initially amplified by a charge sensitive preamplifier (ORTEC Model-142). The bias circuit (in the preamplifier), for the detector is dc coupled as it has very high resolution. The preamplifier is specially designed to accept the detector signal and amplify it with some shaping so as to preserve the maximum signal-to-noise ratio. In case of ERDA, the useful information in the preamplifier output signal is the amplitude of each pulse. The subsequent main amplifier (ORTEC Model-572) amplifies this signal creating a suitable pulse shape (having a rise time of 1 μ sec) thus optimizing resolution and count rate capability. The pulse shaping is done to avoid pulse pileup and to enhance the signal-to-noise ratio. Each individual detector signal has to be terminated in a time shorter than that compared to the time interval between two pulses. Otherwise pulses will overlap causing pulse pileup, which leads to erroneous amplitude measurements.

The CR-RC (differentiating-integrating) pulse shaping circuit of the amplifier operates with time constants much shorter than the decay of the preamplifier signal and much longer than its rise time. This effectively removes the slow component of the preamplifier signal preventing the pileup error. It also removes the low and high frequency signals and noise components thereby significantly enhance the signal-to-noise ratio. Hence the amplifier finally produces individual pulses whose amplitudes convey the quantity of interest, i.e., the energy of the detected particles. The output signal from the main amplifier is then fed to a biased amplifier (ORTEC Model-444). With the help of this the amplifier signals are either compressed or stretched and the edges are cut off as desired, for more efficient analysis in the multichannel analyzer (MCA). The signals from the biased amplifier are then collected, either in the MCA (Nuclear Data Inc. Model-ND65). The MCA has two distinct data analysis modes: the pulse height analysis (PHA) and the multichannel scaling (MCS) mode. The PHA mode is exclusively used for the ERDA measurements.

2.6 Rutherford backscattering spectrometry

Rutherford backscattering spectrometry (RBS) is a well established method for determining the composition of thin films on the near-surface region of the bulk samples especially when the sample contains atoms of heavier species. It is based on the frame work of the discoveries

by Rutherford (1911) and Geiger and Marsden (1913). In general H^+ , He^+ , etc. ions in the range of 0.5 to 3 MeV are used for RBS. The well collimated ion-beam of size 1 mm^2 is made to impinge on the surface of the sample making a suitable angle with the surface normal as shown in Fig.2.4. The backscattered particles are detected using an ion implanted semiconductor detector subtending a small solid angle. The signals are energy analyzed using conventional nuclear electronics. The frequency of occurrence of the scattering event as a function of energy of the backscattered particles, known as “spectrum”, is recorded by using a multichannel analyzer. The basic physical phenomena occurring at the target are:

- The process of energy transfer from the projectile to the target nucleus in an elastic collision. This leads to the concept of kinematic factor (K_e) and the capability to determine the mass of the target nucleus.
- The process of probability of occurrence of a two-body collision, which leads to the concept of scattering cross section (σ) and the capability to quantitatively analyze the atomic composition of the target.
- The process of average energy loss of the projectile ions through the target, leading to the concept of stopping cross section (ϵ) and to the capability of depth perception.
- The process of statistical fluctuations in the energy loss of the projectile in the target. This phenomenon leads to the concept of energy straggling (Ω') and to a limitation in the ultimate mass and depth resolution of backscattering spectrometry.

The RBS measurements are usually carried out in the high vacuum ($1\text{--}2 \times 10^{-6}$ mbar). An ultrahigh vacuum may be needed if the prolonged measurement on the same spot (to prevent carbon build up on the target due to the breaking of residual hydrocarbons in the chamber under ion bombardment) is required. The method has been described in detail by Chu *et al.*[4].

2.7 RBS set-up

The ERDA set-up described in section 2.5 is also utilized for elemental analysis using RBS. However, certain differences exist in the principles of these two techniques and hence the

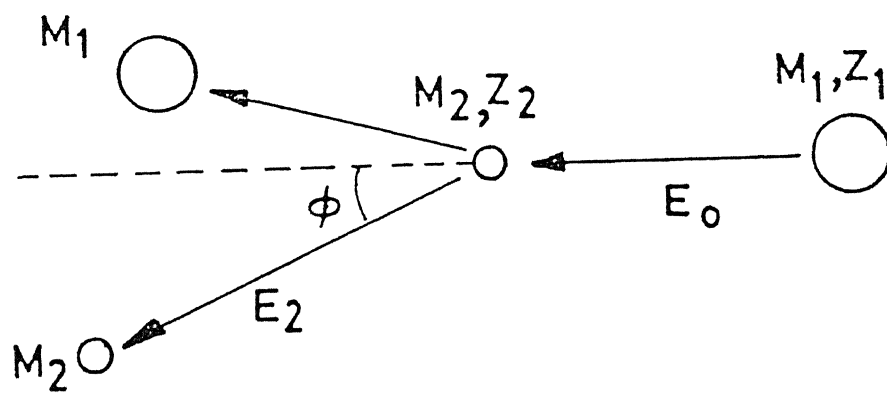


Figure 2.3: Schematic representation of an elastic collision process in laboratory frame. Target of mass M_2 is initially at rest.

geometric considerations are differed in comparison to the ERDA experiments. The RBS geometry has also been schematically shown in the inset of Fig.2.4. The sample holder is mounted on the top of a flange in such a way that the ion-beam entering from one of the ports is incident perpendicularly on the sample surface. The RBS detector is placed at a scattering angle (θ) of 150° with respect to the incident beam and is fixed at one of the chamber ports. The detector surface area is decreased by about 80% by inserting a plate having a small aperture in front of the detector. The detector to sample distance was approximately 10 cm. The solid angle of 2.57 msr subtended by the detector was measured by taking several RBS spectra from various standard samples.

2.7.1 RBS Spectra analysis

In case of RBS, backscattering spectra of pure elements (or calibration samples) are taken in every run. A set of calibration spectra are depicted in Fig.2.5, for thin film of pure Au on pure Al substrate and for pure Al. In these spectra, the surface position of Au is at channel number 494 and that of Al is at 278 corresponding to an incident He^+ energy of 1.34 MeV. The backscattered energy $E_{1,e}$ for each of these elements (e) is calculated as follows:

$$E_{1,e} = K_{1,e} \times E_o \quad (2.1)$$

where $K_{1,e}$ is the kinematic factor of the element e and E_o is the incident energy of He^+ beam (in the case 1.34 MeV). The calibration factor for the MCA can be calculated from the following equation:

$$\delta E = \frac{(K_{1,e} K_{2,e}) E_o}{(ch_1 ch_2)} \text{ keV/ch.} \quad (2.2)$$

Once the calibration factor for the MCA is determined, the RBS spectra are analyzed by using the RUMP simulation package[5]. One of the important features of RUMP is that it is an extremely powerful tool for understanding complex spectra involving overlap of numerous elements and that it also takes into account the detector resolution as well as energy straggling of the ions. Fig.2.6 shows the typical RBS spectrum along with its RUMP simulation, as obtained from a $c\text{-Si}$ sample. The x-axis corresponds to the He^+ backscattered energy and the y-axis corresponds to the normalized backscattering yield.

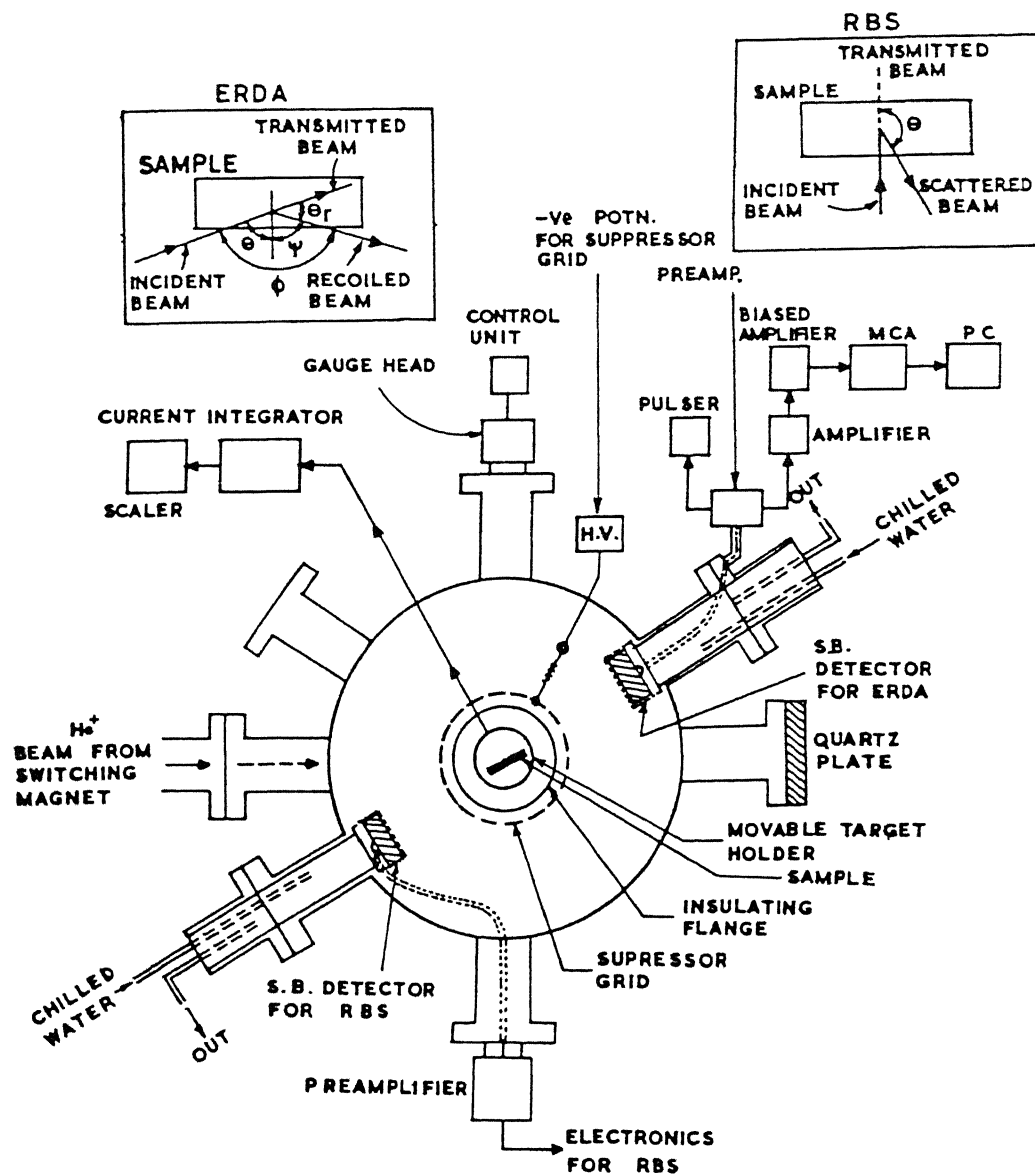


Figure 2.4: Block diagram of RBS and ERDA experimental chamber alongwith target, detector and other accesories.

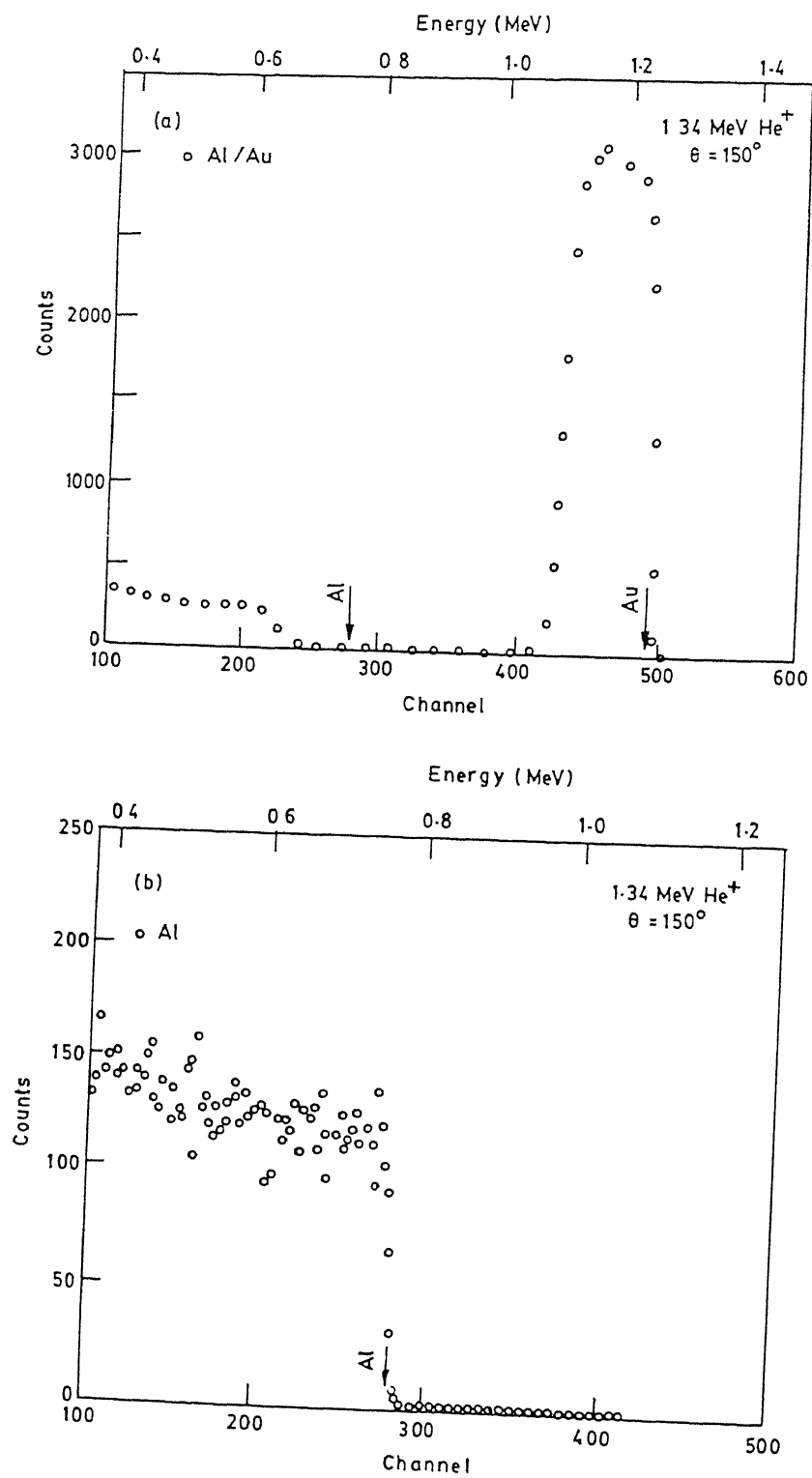


Figure 2.5: RBS calibration spectra of pure Al and Au film deposited on Al.

The arrow indicates the surface position of Si whereas the simulated spectrum has been indicated by the continuous line.

2.8 RBS-channeling

One of the important effects available in ion-solid interactions, viz. the perception of structural and crystalline order by use of channeling effects. The channelling effect arises because rows or planes of atoms can “steer” energetic ions by means of a correlated series of gentle, small-angle collisions. In terms of backscattering spectrometry, channelling effects produce strikingly large changes in the yield of backscattered particles as the orientation of the single-crystalline target is changed with respect to the incident ions. Channelling effect measurements have had three major applications in backscattering analysis: (1) amount and depth distribution of lattice disorder, (2) location of impurity atoms in the lattice sites, and (3) composition and thickness of amorphous surface layers. RBS-channelling technique has been utilized to improve the detection sensitivity[4] of the film constituents, viz. C, O, and P from thin amorphous phospholipid layer deposited on *c*-Si.

In order to align a sample with respect to the incident He^+ beam, we used a 3-axes goniometer (High Voltage Engineering Europa, B.V.) which is specially designed for ultra high vacuum systems. The schematic diagram of the sample manipulator has been shown in Fig.2.7. This can rotate a sample around three independent axes by means of two linear movements, and one rotatory movement, driven by stepper motors. The three axes of rotation intersect at one point on the surface of the sample. The sample can be rotated by a complete cycle (360°) around the axis of the goniometer (R_1) with a precision of 0.018° , 180° around the axis of the incident ion-beam (R_2) with a precision of 0.0125° . and can be tilted around the vertical axis perpendicular to both R_1 and R_2 with a precision of 0.0071° . In addition to the rotations there are provisions for shifting the sample by ± 10 mm along x,y, and z-axes with a resolution of 0.01 mm. The multiport goniometer chamber is coupled with a diffstack pumping system and is equipped with secondary electron suppressor and an ion implanted semiconductor detector kept at 150° with respect to the incident beam.

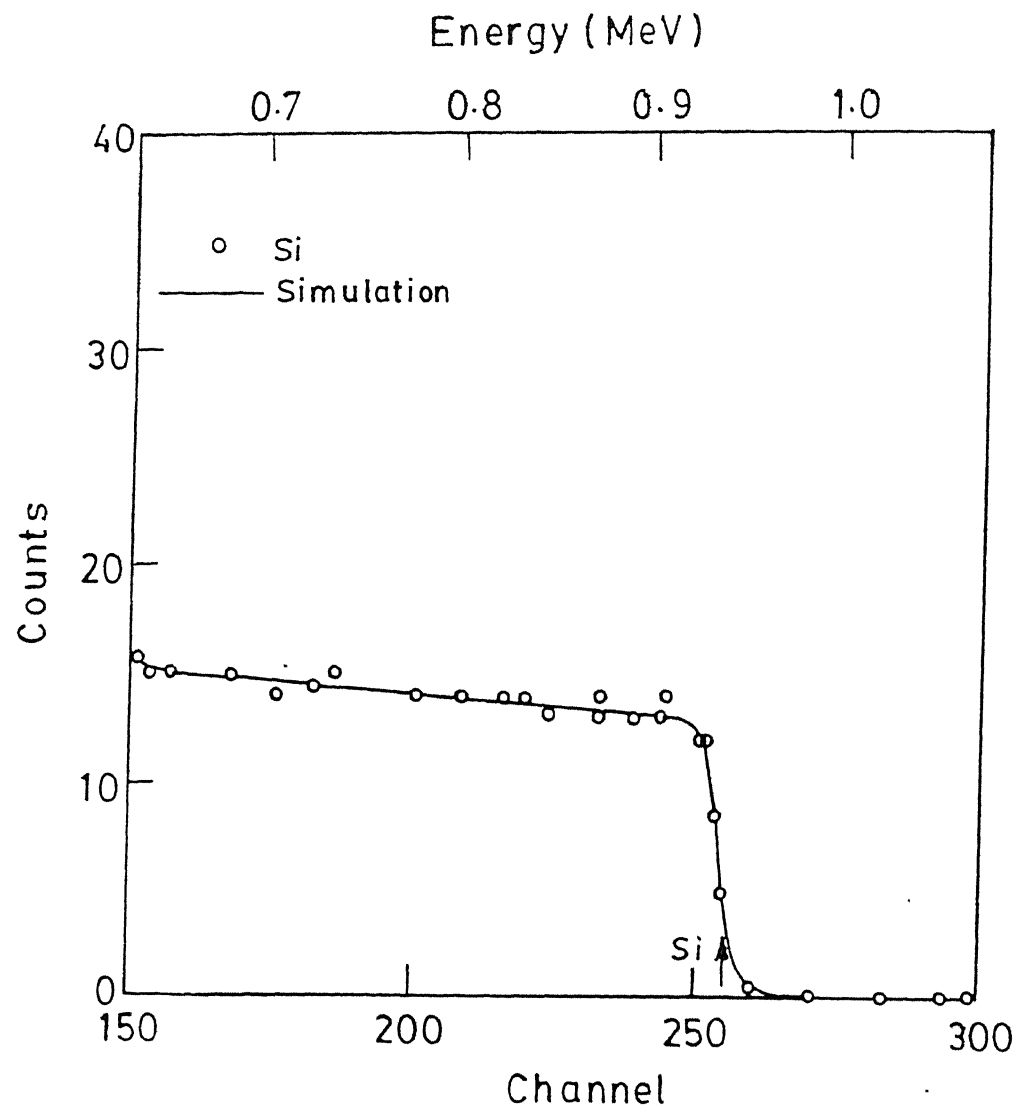


Figure 2.6: Typical RBS spectrum of a Si sample along with its RUMP simulation.

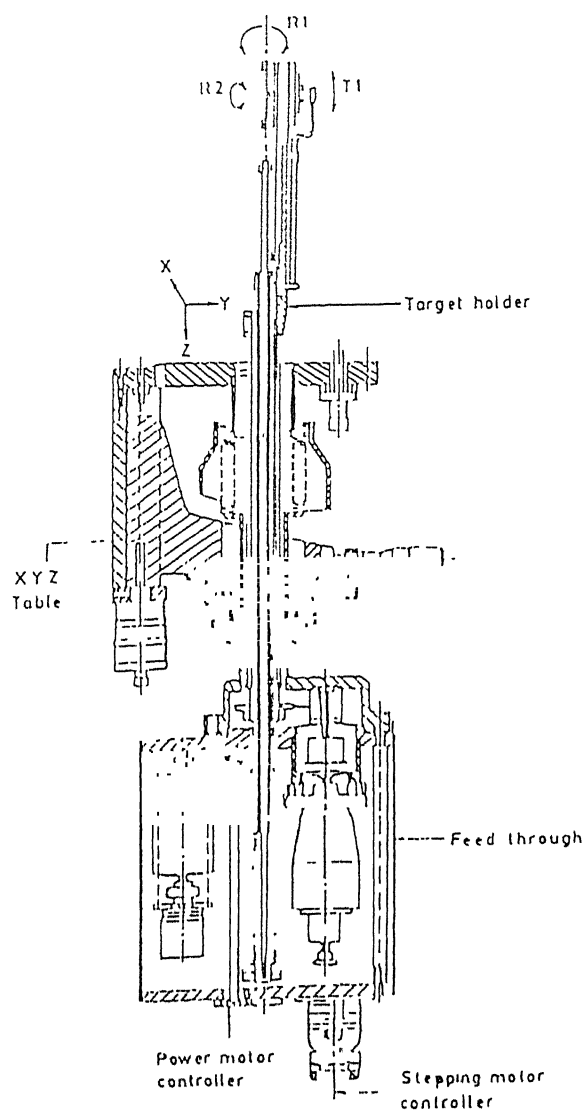


Figure 2.7: Schematic diagram of the sample manipulator for RBS-channeling experiment.

2.9 Infrared spectroscopy

The transmission spectra of α -C:H films deposited on Si, phospholipid thin films deposited on Si and KH_2PO_4 samples were recorded in the range of 400-4000 cm^{-1} using a Nicolet FTIR spectrometer. The measurements were performed at BECPRL, National Physical Laboratory, New Delhi and Defence Materials & Stores Research & Development Establishment (DMSRDE), Kanpur.

To convert the % transmission (T) to the absorption coefficient (α), for α -C:H films, the interference free transmission is approximated by

$$T = \left[\frac{(1 - R)^2 \exp(-\alpha d)}{(1 - R)^2 \exp(-2\alpha d)} \right], \quad (2.3)$$

where α is the absorption coefficient, d the film thickness, and R an empirically determined interface multiple reflection loss. R was determined by setting $T=T_o$ (experimentally measured) when $\alpha=0$. Eqn. 2.4 then becomes[6]:

$$T = \left[\frac{4T_o \exp(-\alpha d)}{[(1 + T_o)^2 - (1 - T_o)^2 \exp(-2\alpha d)]} \right], \quad (2.4)$$

which can be solved for α in terms of the measured T values.

For the α -C:H samples, the absorption band around 2800-3100 cm^{-1} was analyzed more carefully for the individual contributing peaks to the stretching bands. Experimental spectrum was fitted using Gaussian peaks after background corrections. PEAKFIT, from the Jandel Scientific[7] utilizing the Lovenberg-Marquardt algorithm to find a global minimum in sum of squares[8] was used. The software first needs a mannual approximation. In general, two constraints were imposed on each Gaussian peak. Firstly, the peak position had to correspond to a known vibration frequency within $\pm 10 \text{ cm}^{-1}$. A component not indicated in the spectra by a hump or a shoulder was introduced only in those cases where the repeated trials failed by large margins and there were other spectral evidence for the existence of such a component. For a sharp band, the fitting procedure produces same peak characteristics with a high accuracy even if all the parameters were left free. However, in case of very broad convoluted bands the uncertainty in position and width may be as large as $\pm 5 \text{ cm}^{-1}$.

2.10 Raman Spectroscopy

The inelastic scattering of light is a sensitive spectroscopic tool to investigate structure and symmetry properties of solids, liquids and gases[9]-[13]. Raman spectroscopy was used for the characterization and identification of the various phases and the respective changes occurring in them due to He^+ ion bombardment or thermal annealing in vacuum.

The Raman scattering measurements were carried out at the Modern Laser Raman Laboratory at IIT Kanpur. The experimental set up used to record the micro Raman spectrum mainly consists of a Spectra Physics 5 and 15 Watt Ar^+ lasers as the excitation source, chilling plants for cooling the laser head, and the electronics. The Raman spectra from films were recorded at room temperature with 514.5 nm line of Ar^+ laser in the backscattering geometry with a laser power of ~ 4 mW on the sample. The scattered light is dispersed by 1200 gr/mm grating. The spectra were recorded with a Spex Triplemate equipped with a liquid nitrogen cooled Charge Coupled Detector (CCD). The instrument slit width was 10 cm^{-1} . A natural diamond was used for calibration of the spectra[14]. The spectra obtained from different spot of the samples, were analyzed for peak positions and half widths. A non-linear curve fitting software PEAKFIT (as described in section 3.8) was used to deconvolute the spectra. Raman spectroscopy is useful for detecting sp^2 carbon atoms. The scattering efficiency of graphitic phonons is much higher than those of diamond. The phases present in the films and the bulk materials (as studied in this thesis) have been identified by carefully comparing the peak positions with the known assignments from the literature[11]-[14].

2.11 Mass spectroscopic thermal effusion

A computer controlled mass spectroscopic thermal effusion (MSTE) system was used to detect the effusion of gases from materials[15]. The sample is inserted into a quartz tube and the system is evacuated by a turbomolecular pump to a base vacuum of better than 10^{-8} Torr. Quartz tube is heated by a tubular furnace, made of alumina muffle and with number 22 kanthal heater wire. A chromel-alumel thermocouple is placed in contact with the quartz tube to sense the sample temperature. The tube temperature was calibrated with the temperature measured directly on the samples inside the tube in a dummy run. Prior to each experiment, the quartz tube is cleaned by baking it to 600°C to remove molecules

absorbed at the inner walls of the tube. Quadruple mass analyzer (Ametek, Dycor Model MA 2000) was used for partial pressure detection.

While heating the sample, temperature of it and the partial pressure of evolved gases are continuously recorded through a computer. Gas analyzer can be used to display the data in three different modes and is highly sensitive. H effusion from a diamond film containing less than 1 at.% H could be detected using this set up. In fact, twelve mass numbers could be simultaneously monitored as a function of temperature. Design considerations for higher sensitivity involves low volumes ($\sim 230 \text{ cm}^3$) of the sample holder attachment and low leak rate ($< 10^{-4} \text{ Torr-lit./sec}$).

2.12 X-ray Diffraction

The crystallographic structure and composition of phases of the c-Si, KH_2PO_4 , diamond films and some other systems, studied in this thesis were analysed by X ray diffraction (XRD) technique. The amorphous nature of our *a*-C:H and phospholipid films were also confirmed by XRD. XRD experiments were performed by using a X ray diffractometer (RICH and Seifert ISO Debye Flex 2002). The geometry used is of the conventional Bragg-Brentano ($\theta - 2\theta$) geometry. Monochromatic Cu-K_α ($\lambda = 1.5418 \text{ \AA}$) radiation obtained from a Cu target was made to fall on a sample at an angle θ . Diffracted angle 2θ was scanned by the detector in the range of 20° to 140° at a scan speed of $3^\circ / \text{min}$. The other recording conditions were (i) Counts per minute = 5 K to 20 K, (ii) accelerating voltage/current equal to 30 kV/20 mA, (iii) time constant equal to 10 sec and chart speed equal to 3.0 cm/min. Another target of Fe ($\lambda = 0.711 \text{ \AA}$) was also employed to access lower Bragg angles.

The inter planar spacing d was determined from the Bragg relation[16]. Intensity and the inter planar spacing of the dominant peaks were used for matching with the standard ASTM data card[17] values to ascertain the crystallographic present in the various samples. The lattice parameters for different samples were calculated by indexing the XRD patterns[16].

2.13 Scanning Electron Microscopy

In electron beam techniques electrons can be absorbed, emitted, reflected or transmitted. Scanning and transmission electron microscopy (SEM) is widely used to study the surface topography of the materials. In SEM, a finely focused electron beam is scanned over the surface of the specimen. The secondary electrons emanated from 10 Å from the film surface are extracted by a high potential applied to a scintillator-Detector system. Secondary electron images are generated by synchronising the output of the detector system with faster of the electron probe across the sample.

SEM was performed using JEOL 840 JSM Scanning Electron Microscope[18] at IIT Kanpur. The morphologies of the diamond films: shape and the size of the diamond crystallites and other important features were studied by SEM. Features developed as a result of MeV He⁺ bombardment have been nicely distinguished in case of diamond films.

Bibliography

- [1] S. J. Pearton, J.W. Corbett, and M. Stavola, in “*Hydrogen in Crystalline Semiconductors*” (Springer Verlag, Heidelberg, 1992) ch.1.
- [2] G. K. Mehta *et al.*, *Technical Report*, IIT Kanpur, VDG/13/1976.
- [3] V. N. Kulkarni and R. M. Singru, *Technical Report*, IIT Kanpur, TR/CNF/1987.
- [4] W.-K. Chu, J. W. Mayer, and M.-A. Nicolet, “*Backscattering spectrometry*” (Academic press, New York, 1978).
- [5] L. R. Doolittle, *Nucl. Instr. Meth. B9* (1985) 344.
- [6] M. H. Brodsky, M. Cardona, and J. J. Cuomo, *Phys. Rev. B* 16 (1977) 3556.
- [7] Reference Manual, “*PEAK FIT*”, version 3 (Jandel Scientific, USA).
- [8] W. H. Press, B. P. Flannery, S. A. Teukolsky and W. T. Vetterling, “*Numerical Recipes The Art of Scientific Computing*” (Cambridge University press, 1989) p. 52.
- [9] J. C. Grasseli, M. K. Snavely, and V. J. Bukin, *Phys. Rep.* 65, (1980) 231.
- [10] “*Recent Trends in Raman Spectroscopy*”, Eds. Banerjee and S.S. Jha (World Scientific, Singapore, 1989).
- [11] D.S. Knight and W.B. White, *J. Mater. Res.* 4 (1990) 38.
- [12] A.R. Badzian, P.K. Bachmann, T. Harnett, T. Badzian, and R. Messier, *Proc. E-MRS Symp.* 15 (1987) 63.
- [13] D. Beeman, J. Silverman, R. Lynds, and M.R. Anderson, *Phys. Rev. B* 30 (1984) 870.

- [14] N. Fukuta, S. Sasaki, K. Murakami, K. Ishioka, M. Kitajima, S. Fujimura, and J. Kikuchi, *Jpn. J. Appl. Phys.* 35 (1996) L1069.
- [15] M. Malhotra, *Ph.D. Thesis*, Indian Institute of Technology Kanpur, 1996.
- [16] B.D. Cullity in “*Elements of X-ray Diffraction*” (Addison-Wesley Publishing Co., USA, 1978).
- [17] “*Powder Diffraction File*”, Joint Committee on Powder Diffraction Standards, International Center for Diffraction Data, 1601, Park Lane, Swarthmore, Pennsylvania, USA, 1981.
- [18] “*Instruction Manual*”, Scanning Electron Microscopy, Model JSM 840, JEOL, Japan.

Chapter 3

Elastic recoil detection: Formalism and analysis

3.1 Introduction

Importance of hydrogen and the methods used for detection and analysis of hydrogen have been briefly described in Chapter 1. The detection of hydrogen is difficult by the conventional tools routinely used for elemental analysis, viz. Auger electron spectroscopy (AES), energy sensitive chemical analysis (ESCA), energy dispersive X-ray analysis (EDX), electron microprobe analysis (EPMA), etc. Most of these methods rely on the principles based on the detection of either photons or electron of energies few keV (due to radiative or nonradiative transition of electrons from excited states). Therefore, these methods are not useful for detection of hydrogen as it contains only one electron. However, with the advent of nuclear physics techniques (viz. NRA, SIMS, ERDA, etc.) accurate determination of hydrogen in materials became possible with high sensitivity. It has been mentioned in Chapter 1 that one of the main objectives of the present work was to develop an ERDA facility using the 2 MV Van de Graaff accelerator facility at IIT Kanpur for analysis of hydrogen. The details of the experimental set up have been already described in Chapter 2. This chapter describes the formalism of ERDA and the methodology for quantification of hydrogen by this technique.

The cross section data reported in the literature was compiled and parametrized for the analysis of hydrogen profiles using the simulation program.

In case of ERDA, an energetic projectile impinges on a target at a grazing incidence and as a result of the elastic scattering, the lighter nuclei get recoiled in the forward direction and are detected by a detector. ERDA depends mainly on the following four physical concepts:

- The kinematic factor which describes the energy transfer from a projectile to a target nucleus in an elastic two-body collision.
- The differential scattering cross section which gives the probability for the scattering event to occur.
- The stopping powers which give the average energy loss of the projectile and the recoiled target atom as they traverse through the sample.
- The energy straggling which gives the statistical fluctuation in the energy loss.

By applying these four physical concepts, the elastic recoil spectrum can be transformed into a concentration versus depth profile in order to obtain quantitative information.

3.2 ERDA Fundamentals

3.2.1 Kinematics

A schematic of ERDA process is depicted in Fig.3.1. It is seen that a projectile with energy E_0 , charge Z_p and mass M_p is made incident on the sample at an angle of θ with respect to the surface normal. Consequently, at depth x , an atom of mass M_r and charge Z_r is recoiled out of the target at an angle of $\theta_r (= \pi - (\theta + \psi))$ whose energy is now E'_0 . Although, the recoil ion initially has an energy E_1 (say), its exit energy is E_2 .

Applying the laws of conservation of energy and momentum, the energies of the particle after elastic scattering can be expressed as follows[1]:

$$E_1 = K_r E_0 \quad (3.1)$$

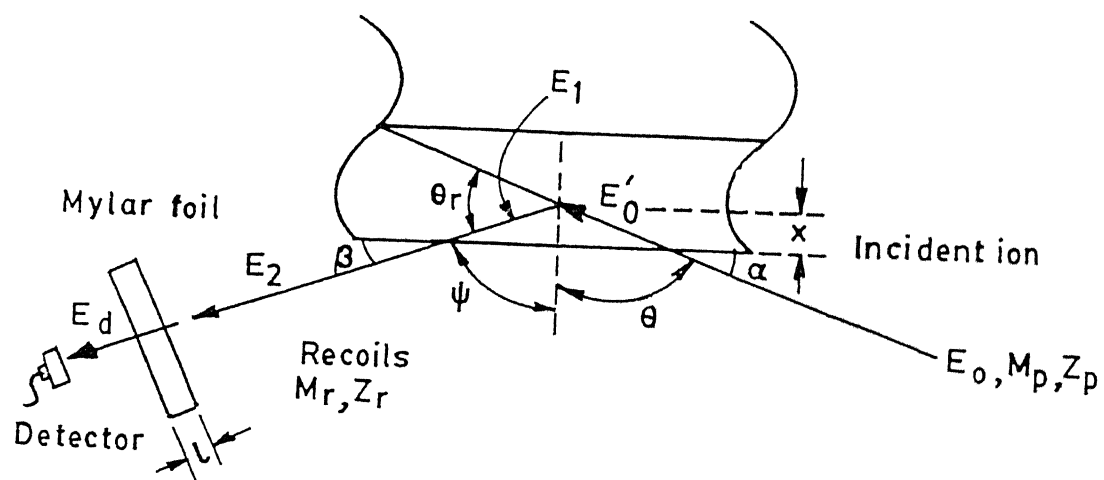


Figure 3.1: Schematic diagram showing the ERDA process.

where E_1 denotes the energy of the recoiling particles immediately after the scattering event and K_r is the proportionality constant, known as “kinematic factor”. Kinematic factor gives the fraction of energy transferred to the recoiling particles. This is a function of the projectile and the target atom masses and the recoiling angle. It can be expressed as follows:

$$K_r = \left[\frac{4M_p M_r \cos^2 \theta_r}{(M_p + M_r)^2} \right]. \quad (3.2)$$

The maximum value is achieved for $M_p = M_r$ for which K_r will be $\cos^2 \theta_r$ ($=1$, for $\theta_r = 0^\circ$). It is observed that K_r is a function of the mass ratio M_r/M_p and the angle θ_r . It appears that the energy of the recoiled particle achieves a maximum when $M_p = M_r$ (see). In order to show the capability of detecting different recoiling masses, the kinematic factor K_r has been plotted against M_r/M_p in Fig.3.2. From this figure one can infer that particles moving towards a detector, located at an angle smaller than 90° (with respect to the incident beam direction), have larger energies when they originate from a scattering process involving heavier target nuclei. For $M_r/M_p < 1$, the largest energy is carried by the heaviest recoils.

3.2.2 Cross Section

The concept of cross section is useful to know the probability of the recoil events which in turn gives an idea about the total number of atoms present in a specimen. It can be derived by transforming the equation for Rutherford type scattering process from the centre-of-mass (COM) frame of reference to the laboratory frame as suggested by Marion and Young[2] in 1968 and is given by

$$\sigma_r^{Ruth}(E'_0, \theta_r) = \left[\frac{Z_p Z_r e^2 (M_p + M_r)}{(2 M_r E'_0)^2 \cos^3 \theta_r} \right] \quad (3.3)$$

where $(e^2/E'_0)^2 = 0.020731$ barn for $E'_0=1$ MeV, and 1 barn= 10^{-24} cm². The above equation holds true strictly for the cases where the scattering process is assumed to involve two nuclei with charge $Z_p e$ and $Z_r e$ while the interaction potential is given by Coulomb's law. In certain experimental situations the actual cross section may deviate from the one given by Eqn.

3.3. If the energy of the primary particles is too low to penetrate sufficiently inside the inner shell orbitals, screening effects due to the electron clouds will occur. This is a common case for high Z projectiles at low energies. Similarly, deviations from Rutherford recoil cross sections resulting from Coulomb barrier penetration occur most often for low Z projectiles

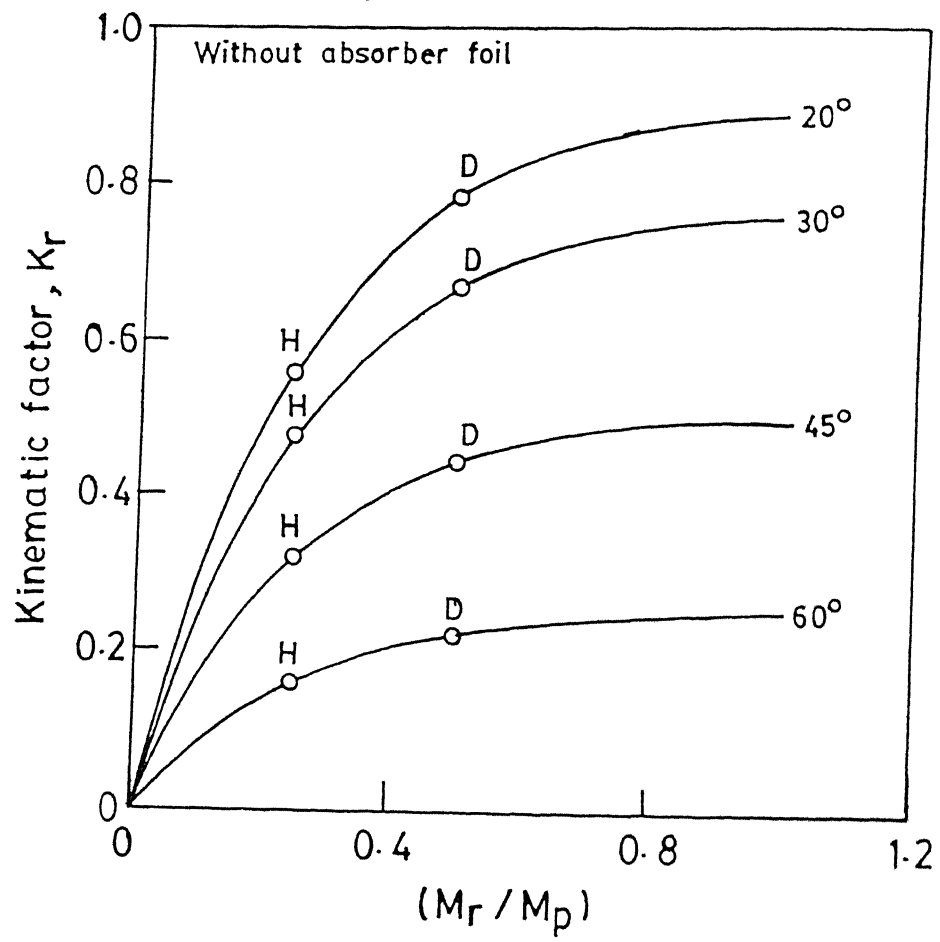


Figure 3.2: Kinematic factor (for recoiled particles) versus (M_r / M_p) .

at high energies. Bozonian *et al.*[3] have modelled the case of Coulomb barrier penetration and determined the energies where the cross sections may become non-Rutherford. In the laboratory reference frame and for a recoil angle of 30° , their formulation of this energy boundary is given by

$$E \text{ (MeV/amu)} = \left[\frac{-1.1934(Z_p Z_r)(M_p + M_r)}{M_p M_r A_p^{1/3} \ln(0.001846 Z_p A_r / Z_r)} \right] \quad (3.4)$$

where A_p and A_r are the respective mass numbers of the projectile and the recoiling species. Further, Andersen *et al.*[4] have modeled the case where screening effects cause significant deviations from the Rutherford formula and in the laboratory reference frame, for 1% screening effect (i.e., $\sigma/\sigma_x^{Ruth} = 0.99$), the energy boundary is given by

$$E \text{ (MeV/amu)} = 99 V_{LJ} \left(\frac{M_p + M_r}{M_p M_r} \right) \quad (3.5)$$

where $V_{LJ} = 48.73 Z_p Z_r \sqrt{(Z_p^{2/3} + Z_r^{2/3})}$ is the Lenz-Jensen potential.

The determination of projectile energy boundaries for non-Rutherford scattering are shown in **Fig.3.3** as a function of the projectile atomic number. For example, the regions corresponding to the use of 1.5 MeV He ERDA, 28 MeV Si ERDA and 12 MeV Au ERDA are also given in this figure. The use of a He ion beam for ERDA is nearly always (maximum energy is limited by the threshold of nuclear reactions) in the region where penetration of the Coulomb barrier can occur, and the use of Au is nearly always in the region where significant screening effects can occur. The use of a 28 MeV Si beam for ERDA is close to the boundary where Coulomb barrier penetration may occur, but in practice, significant deviations from the Rutherford formula, σ_r^{Ruth} have not been measured. When projectile energies lying outside the Rutherford region (in **Fig.3.3**) have to be used for ERDA, an accurate determination of their scattering cross sections should be made.

In the present study, He^+ beam has been utilized for hydrogen analysis. A detailed survey of the experimental cross section measurements was done for utilization in the analysis. *Table-3.1* shows the summary of $(d\sigma^H/d\Omega)$ and $(d\sigma^D/d\Omega)$ measurements as reported in the literature. However, the ERDA cross section measurements available in the literature (for

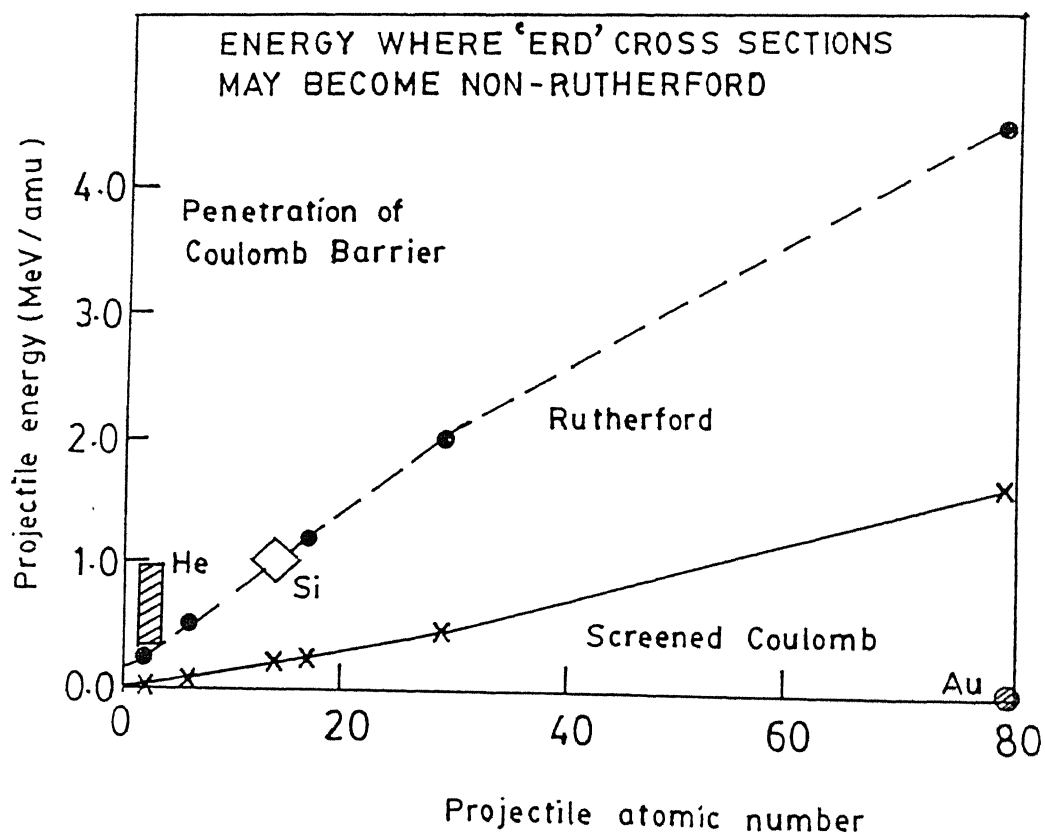


Figure 3.3: Projectile energy as a function of the projectile atomic number.

hydrogen and deuterium) are often in poor agreement or of low accuracy. Quillet *et al.*[5] determined the accurate absolute values of $(d\sigma^H/d\Omega)$ over the whole ^4He energy range (1 to 2.5 MeV) generally used in ERDA and had fitted in the following form:

$$\left(\frac{d\sigma^H}{d\Omega}\right) = \left(\frac{d\sigma^H}{d\Omega}\right)_{Ruth} + \frac{a}{(E - E_0)^2 + b} \quad (3.6)$$

such that $E_0 = 8050$ keV yields a very good fit to the data. Quillet *et al.* also obtained the values for the fitting parameters, a and b to find out $(d\sigma^H/d\Omega)$ values for different projectile energies. On the other hand, the adopted $(d\sigma^D/d\Omega)$ values in this thesis were obtained by Besenbacher *et al.*[22]. These reported experimental recoil cross section data for H[5] and D[22] have been plotted in Figs.3.4 and 3.5, respectively[23].

Linear fits to the H and recoil spectra were obtained especially for use in the H and D recoil spectra analysis using the RUMP simulation code which requires the cross section in this particular form (see section 3.5.2).

3.2.3 Energy Loss

It has been observed that the scattered particles typically have a higher energy than the recoils. since the particles lose energy while moving in the target, scattering from substrate atoms at different depth produces a continuum and the contributions of scattering and recoiling atoms to the energy spectrum will tend to overlap. To avoid this problem, usually an absorber foil is placed in front of the detector. The following formalism helps determining the relationship between the energy of the detected recoils and the depth of the sample from which it originated.

Assuming that the stopping powers, $\left(\frac{dE}{dx}\right)^{He}$ and $\left(\frac{dE}{dx}\right)^r$, of both projectile and the recoils are constant, the detected energy of the recoiling particles can be obtained as follows:

$$E'_0 = E_0 - \int_0^{x/\sin \alpha} \left(\frac{dE}{dx}\right)^{He} dx \quad (3.7)$$

$$E_1 = K_r E'_0 \quad (3.8)$$

$$E_2 = E_1 - \int_0^{x/\sin \beta} \left(\frac{dE}{dx}\right)^r_s dx \quad (3.9)$$

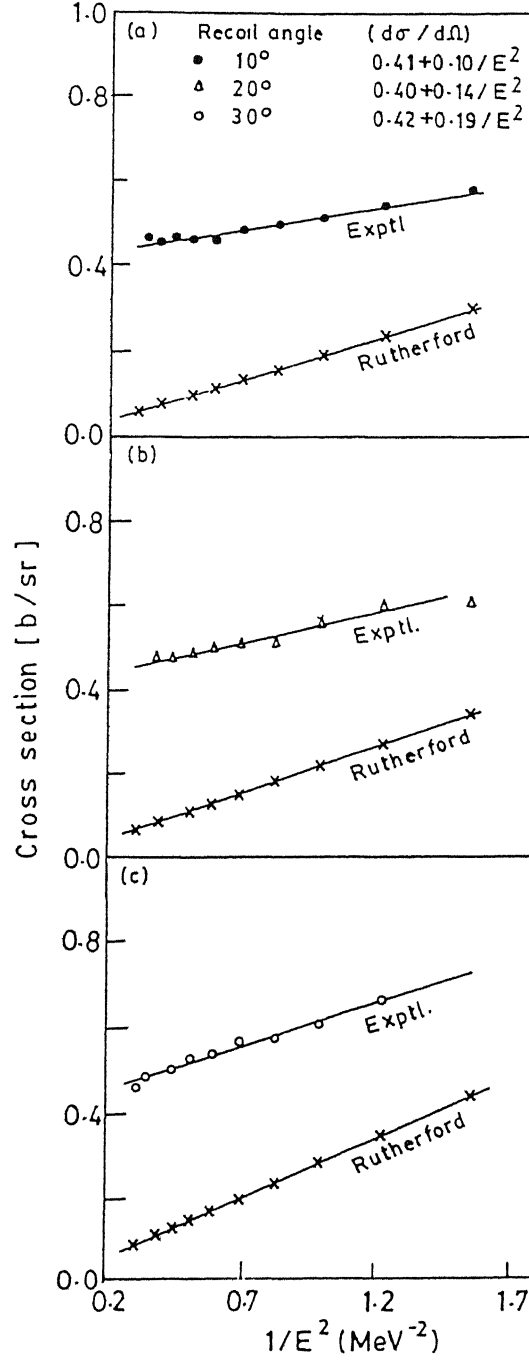


Figure 3.5: Experimental and Rutherford recoil cross section data for D plotted against inverse square of the projectile energy : (a) $\theta_r = 10^\circ$, (b) $\theta_r = 20^\circ$, and (c) $\theta_r = 30^\circ$.

Hydrogen			Deuterium			Ref.
θ_r [deg]	Energy [MeV]	Error	θ_r [deg]	Energy [MeV]	Error	
6 to 35	3 to 7	$\pm 3\%$				[6]
10, 40	8 to 44	$\pm 2\%$				[7]
6 to 40	2 to 12	$\pm 6\%$				[8]
21.5, 31.5, 41.5	1.9 to 3	$\pm 5\%$				[9]
30	1.6 to 4.5	–				[10]
21.3, 31.3, 41.5	1.5 to 3	$\pm 20\%$	21.5, 31.5, 41.5	1.9 to 3	$\pm 20\%$	[11]
23	2 to 3.5	–	30	1.6 to 3	–	[12]
10, 20, 30	1.3 to 2.1	$\pm 12\%$				[13]
0, 10, 20, 20, 40	1 to 8	calculation				[14]
0, 10, 20, 20	1 to 8	calculation				[15]
16, 18, 21, 23, 26, 31, 36, 41	1 to 3.5	$\pm 10\%$				[16]
0, 5, 10, 15, 20, 30	1 to 2.5	calculation				[17]
20, 25, 30, 35	1 to 2.9	$\pm 5\%$				[18]
20, 25, 30, 35	1 to 2.9	$\pm 5\%$				[19]
			10 to 41	4, 5, 7	$\pm 3\%$	[20]
			3.2	1.3 to 9	$\pm 3\%$	[21]
			6, 15.2, 19.6			
			24.4, 27.7	1.8 to 2.5	$\pm 3\%$	
			0 to 35	0.9 to 2.3	$\pm 5\%$	[22]

Table 3.1: Summary of reported hydrogen and deuterium recoil cross section data.

and

$$E_d = E_2 - \int_0^l \left(\frac{dE}{dx} \right)_f^r dx \quad (3.10)$$

Here $(dE/dx)^r$ corresponding to the recoiling species has two subscripts in Eqns. 3.9 and 3.10 depending on its energy loss in the sample (s) or absorber foil (f). These integrals should be calculated along the actual trajectory and can be evaluated numerically. Eqn. 3.10 can be expressed in a simple form like:

$$E_d = K_r E_0 - [S] x - \Delta E_f \quad (3.11)$$

where $[S]$ is the energy loss factor given by

$$[S] = \left[\left(\frac{K_r \left(\frac{dE}{dx} \right)^{He} E_0}{\sin \alpha} \right) + \left(\frac{\left(\frac{dE}{dx} \right)_s^r (K_r E_0)}{\sin \beta} \right) \right] \quad (3.12)$$

or

$$[S] = \left[\left(\frac{K_r \left(\frac{dE}{dx} \right)^{He} E_0}{|\cos \theta|} \right) + \left(\frac{\left(\frac{dE}{dx} \right)_s^r (K_r E_0)}{|\cos (\theta + \theta_r)|} \right) \right] \quad (3.13)$$

where x is the penetration depth and ΔE_f is the energy lost by the recoiled particles in the absorber foil. The stopping powers are tabulated by Ziegler[24]. However, for larger depths, $[S]$ must be evaluated by numerical methods, similar to RBS[25].

The derivative of Eqn. 3.13, (dE_d/dx) is also important in determining the depth resolution, as will be discussed later, and can be written as

$$\left(\frac{dE_d}{dx} \right) = R[S] \quad (3.14)$$

where R is the ratio of the recoiled ion's stopping power in the foil at energies E_d and E_2 , i.e.,

$$R = \frac{\left[\left(\frac{dE}{dx} \right)_{E_d}^r \right]^f}{\left[\left(\frac{dE}{dx} \right)_{E_2}^r \right]^f} \quad (3.15)$$

Using the universal scaling suggested by Ziegler[26] and the empirical H stopping powers tabulated by Anderson and Ziegler[27], R values have been calculated by Doyle and Peercy[28] for several beams at 1 MeV/amu. Calculations show that the factor R is not

very important except for the case of He beams. This is largely due to the fact that much less energy is imparted to H in the ^4He collisions and hence the relative energy loss in the stopper foil is significantly greater for the ^4He projectile.

At this point, one may calculate the H concentration (at./cm²) at a depth x in the sample from the following equation:

$$N(x) = \left[\frac{Y(E_d)}{Q \left(\frac{d\sigma}{d\Omega} \right) \Omega \left(\frac{\delta E}{R[S] \sin \alpha} \right)} \right] \quad (3.16)$$

where Y is the yield of recoiling particles per channel at energy E_d , Q is the total number of incident ions on the sample during the data acquisition time, δE is the detected energy window per channel, $\left(\frac{d\sigma}{d\Omega} \right)$ is the differential elastic recoil cross section. Ω is the solid angle subtended by the detector and α is the grazing angle at which the incident beam impinges the surface as shown in **Fig.3.1**.

3.2.4 Energy straggling

An energetic particle while moving through a medium, loses its energy via many individual encounters. Such a quantized process is subject to statistical fluctuations. As a result, identical energetic particles, which all have the same initial velocity, do not have exactly the same energy after traversing a certain thickness in a homogeneous medium. The phenomenon sketched in **Fig.3.6** is called *energy straggling*. Energy straggling puts a finite limit for the precision with which energy losses and depths can be resolved by ERDA. Hence, it is important to have quantitative information on the magnitude of the energy straggling for any given combination of energy, target material, target thickness and the projectile. Light particles such as ^1H or ^4He in the megaelectron volt range lose energy primarily by encounters with the electrons in the target. It is thus expected that the dominant contribution to energy straggling is the consequence of these electronic interactions. Bohr in 1915, was first to derive the energy straggling with the help of some simple classical models. It is referred to as the *Bohr value* Ω_B^2 of energy straggling. For a layer of thickness t , Bohr straggling is given by

$$\Omega_B^2 = 4 \pi (Z_p e^2)^2 N Z_s t. \quad (3.17)$$

Later, Chu[29] modified the Bohr straggling for protons and α -particles to yield:

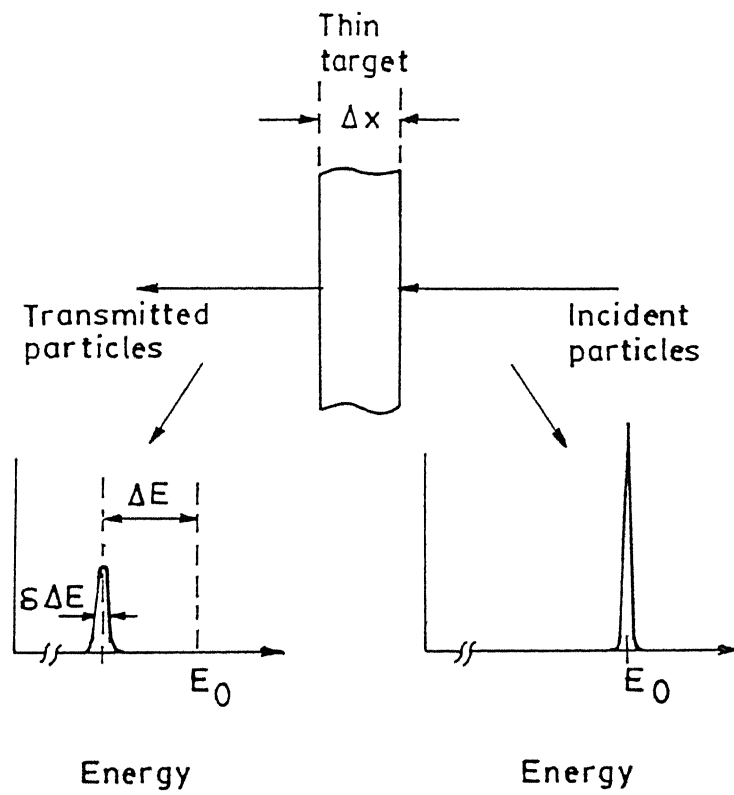


Figure 3.6: A monoenergetic beam of energy E_0 loses energy ΔE in traversing a thin film of thickness ΔX . Simultaneously, energy straggling broadens the energy profile.

$$\Omega^2 = \Omega_B^2 \overline{H}(\tilde{E}, Z_s) \quad (3.18)$$

where $\tilde{E} = E/M_p$ and $\overline{H}(\tilde{E}, Z_s)$ is Chu's correction, that takes into account the deviation from Bohr straggling caused by the electron binding in the target.

3.3 Influence of various parameters and their optimization

In the previous sections the formalism of ERDA, with an absorber foil in front of the detector, has been described. The system and sample parameters which affect the mass resolution, sensitivity, depth resolution and depth of analysis include type of ion-beam, projectile energy, angle of incidence, recoiling angle, the type of absorber foil and its thickness, and the smoothness of the sample surface. The influences of various parameters and the optimal measurement conditions will now be discussed separately in the following subsections.

3.3.1 Mass resolution

In case of a conventional ERDA set-up with the use of an absorber foil, mass resolution is the ability to separate the signal from different recoiled atoms in the spectrum along the energy axis. The selectivity for different masses is determined by the kinematic factor, K_r , given in Eqn. 3.2, and the effect of stopping in the absorber foil. In the absence of an absorber foil, the detected energy would increase continuously for increasing M_r . However, the necessity of using an absorber foil drastically modifies the energy of the recoils in the detector. This has been demonstrated by L'Ecuyer *et al.* for recoils ejected from the surface by various ion-beams[30]. Since the absorber is just thick enough to stop the scattered incident ions, it is clear that recoils with mass, and therefore energy, close to that of the incident ions will lose most of their energy in the absorber. Accordingly, the energy of the recoils will go through a maximum. The height and position of this maximum for a given incident ion-beam depend on the recoil angle and the absorber thickness. For example, the mass resolution between H and D corresponds to an energy difference of approximately 0.8

MeV when using a 4 MeV ^4He projectile, but the mass resolution increases giving an energy difference of $\simeq 2.5$ MeV when using a 28 MeV ^{28}Si projectile. Thus, mass resolution increases with increasing projectile energy and mass. The highest projectile energy is limited by the onset of nuclear reactions while the projectile mass is limited by the radiation damage - it creates in the material.

3.3.2 Sensitivity

One possible definition for sensitivity is a measure of the smallest detectable areal density (at./cm²). In principle, the areal density (A) of hydrogen over a thickness t , is given by (from Eqn. 3.16)

$$A = \int_0^t N(x) dx = \left(\frac{\sin \alpha}{Q \Omega} \right) \int_0^t \frac{R[S]}{\left(\frac{d\sigma}{d\Omega} \right) \delta E} Y(E_d) dx = \left(\frac{R \sin \alpha}{Q \Omega} \right) \int_{E_d(0)}^{E_d(x)} \frac{Y(E_d)}{\left(\frac{d\sigma}{d\Omega} \right) \delta E} dE_d \quad (3.19)$$

In practice, the final integral of Eqn.3.19 is evaluated as a summation. For a surface peak, the cross section is evaluated at the specific energy (E_0) to give

$$A = \frac{R \sin \alpha}{Q (d\sigma/d\Omega) \Omega} \sum_{channel(E_d(0))}^{channel(E_d(x))} Y(channel)$$

i.e.,

$$\sum Y = \left[\frac{A \left(Q \left(\frac{d\sigma}{d\Omega} \right) \Omega \right)}{R \sin \alpha} \right] \quad (3.20)$$

In order to maximize the sensitivity, $\sum Y$ may be maximized by increasing Ω , Q , $(d\sigma/d\Omega)$ or by decreasing R or α . It can be mentioned here that the use of lower energies help in increasing the $(d\sigma/d\Omega)$ (as seen from Fig.3.4). So far lower value of α is concerned, it requires a wide sample or a small beam size, since the effective sample width seen by the incident beam includes the $\cos \alpha$ term. However, this causes a lower counting efficiency as well as larger heat load to the sample. Actually, the count rate of recoil hydrogen atoms is proportional to the beam current and the detector solid angle. So increase in these two

parameters result in a shorter counting time. These parameters are however limited by the maximum count rate of the detector otherwise causing the pulse pile up problem. In addition to this limitation, the beam current and the analysis fluence are set to optimum values such that the irradiation effects are minimum. There is no universal optimum value of the beam current which can be employed in all cases. In the case of hydrogen analysis by MeV He^+ ions typical beam current of 10 to 20 nA can be utilized. So far the solid angle is concerned, too small a value causes poor sensitivity. Thus, being mutually dependent, these two parameters can be optimized to obtain the best possible sensitivity in a given geometry. In this work, the typical H-detection sensitivity was found to be ~ 0.1 at. %.

3.3.3 Depth resolution

Depth resolution is the ability to separate, in the spectrum along the energy axis, the signal coming from the recoiled atoms at different depths in the sample. The depth resolution Δx is determined by the energy spread ΔE and the effective stopping power (dE_d/dx):

$$\Delta x = \frac{\Delta E}{dE_d/dx} \quad (3.21)$$

There are several factors contributing to ΔE [31]. Particles originating from depth x , recorded by a detector with mean energy $E(x)$, show energy fluctuations due to statistical effects characterizing the incoming particles, the detection and the slowing down process, i.e., energy straggling and multiple scattering of particles as they traverse the material. Following are the factors which affect the energy resolution:

- (i) *Geometrical broadening*, ΔE_g , arising from the finite size of the beam spot on the sample and the detector acceptance angle.
- (ii) *Energy straggling contributions* for the in-going and out-going paths in the sample- ΔE_s^i and ΔE_s^o , respectively.
- (iii) *Multiple scattering contributions* for the in-going and out-going trajectories- ΔE_{ms}^i and ΔE_{ms}^o , respectively.
- (iv) The straggling contribution of the absorber foil comprises of the contributions due to electronic stopping ΔE_s^f , the contribution from the scattering of recoils on the absorber nuclei ΔE_n^f .

Other contribution can be due to the detector energy resolution ΔE_d , which is assumed

to be constant for hydrogen and He over the energy range of interest in this work. However, significant energy deviation has been observed[32] for heavier particles. The various contributions can be added quadratically to obtain the total system energy resolution ΔE as

$$(\Delta E)^2 = (\Delta E_g)^2 + (\Delta E_s^i)^2 + (\Delta E_s^o)^2 + (\Delta E_{ms}^i)^2 + (\Delta E_{ms}^o)^2 + (\Delta E_n^f)^2 + (\Delta E_s^f)^2 + (\Delta E_d)^2. \quad (3.22)$$

In case of ERD, the kinematic broadening term arises due to the finite size of the detector aperture. This has a dominant contribution to the energy resolution when the effects of the sample roughness and the nonuniformity in the absorber foil thickness becomes negligible. The most commonly used and most simple aperture is a rectangular slit; although this may lead to the collection of some additional recoil atoms through its corners, with smaller energies[33]. However, the energy resolution is improved even by $\sim 50\%$ when the rectangular slit is replaced by a curved slit having the same area[34].

The necessity of an absorber foil plays an important role in ERDA depth resolution via energy straggling. It must be uniformly thick, free of pin-holes, and the thickness must be greater than or equal to the projectile range in the foil and less than the range of the recoils in it. To improve the depth resolution, usually absorber foils having low average nuclear charge are chosen (viz. Al or mylar) so that straggling is minimized. At lower energies, energy straggling and its correction in the absorber foil dominate at the surface and in depth therefore affecting the depth resolution. Pászti *et al.*[35] have shown that to achieve the same depth resolutions in the first 150 nm, for 1200 keV and 3000 keV He⁺, one would require approximately two times smaller α angles for the latter case. However, for a small α , the recoiling atoms have a longer path lengths which causes a tail on the lower energy side of the peak, because the probability of both multiple scattering and straggling increase. So far the recoil angle (θ_r) is concerned, for lower θ_r values the recoil energy increases (proportional to $\cos^2 \theta_r$) but the cross section (σ) decreases. In principle, with simultaneous decrement of α and θ_r , the depth resolution can be improved, however, the only limitation is the accomplishment of the measurements. It can be mentioned here that Pászti *et al.*[35] obtained the best depth resolution by changing the angle between the recoiling species and

the sample surface (β) such that $\alpha=\beta$. In this work a geometry has been chosen such that $\alpha=\beta=15^\circ$ and the recoil angle was 30° .

3.3.4 Depth of analysis

The depth of analysis in ERDA depends on the range of the projectile in the sample and the stopping of the scattered recoil in the absorber foil. The range of the projectile ions in a sample can be estimated using computer code, such as 'RSTOP' program of Ziegler[36], but the incident angle should be taken into account when determining the projected range, R_p (measured normal to the sample surface). However, the depth of analysis may be dominated by the stopping of the scattered recoil atoms in the sample and in the absorber foil. A practical limit to the analysis depth can be estimated from the minimum detectable energy which, for a surface barrier detector, is found to be ≈ 30 -40 keV. The higher incident energy results in an increase of the analyzable depth. In this work, energy values in the range of 1200 to 1700 keV have been utilized for different samples. Thus, typical depth of analysis of hydrogen in DLC films was observed to be ~ 4000 Å.

3.4 Analysis of H recoil spectra

The methodology of analyzing H recoil spectra has been demonstrated in the following subsections with the help of few examples. These include KDP, high- T_c $\text{YBa}_2\text{Cu}_3\text{O}_{7-x}$ (YBCO) (exposed to humid atmosphere), Si (implanted with hydrogen), and Al (implanted with both hydrogen and deuterium).

3.4.1 System calibration

The energy calibration, i.e., the width of an energy channel in an ERDA spectrum (in keV/channel) and the energy of the zeroth channel (in keV), requires at least two known energies and their respective channel numbers. This can be accomplished by (i) considering hydrogen and deuterium surface positions for a fixed He^+ energy, (ii) considering hydrogen surface positions for varying incident He^+ energy. Initially the calibration was checked using

Depth in mylar foil (\AA)	Hydrogen energy in mylar foil [E (keV)]	Stopping power of H in mylar foil at energy E (eV/ \AA)
0	720.0	4.4
5000	697.5	4.5
10000	674.6	4.6
15000	651.2	4.7
20000	627.3	4.9
25000	602.8	5.0
30000	577.6	5.1
35000	551.7	5.3
40000	525.1	5.5
45000	497.6	5.6
50000	469.2	5.9
55000	439.6	6.1
60000	408.3	

Table 3.2: Slab analysis to calculate stopping of hydrogen in a 6 μm mylar foil.

both the methods although in general the first method has been used for the present thesis work to obtain the energy calibration.

Fig.3.7 shows a typical H recoil spectrum obtained from a Si sample implanted with hydrogen. The spectrum is plotted as yield versus channel with the detected energy axis given along the top axis. In order to determine the E_d scale, the channel to energy conversion, δE_d , (in keV/channel) was determined from the channel corresponding to the surface of the hydrogen signal from Si:H. ($C_{\text{surface}} = 282$, marked H) and from the calculated surface scattering energy, $E_d(\text{H}_{\text{surface}}) = K_H E_0 - \Delta E_{\text{foil}}$. The energy loss in the absorber foil, ΔE_{foil} , is determined by “slab analysis”. In the example of Fig.3.7, the surface recoiled hydrogen passes through a 6 μm mylar foil which is approximated as a pure carbon layer with a density of 1.58 gm/cm³. (This effective density for carbon was derived experimentally[35] and differs from the actual density of mylar, 1.397 gm/cm³.) Table-3.2 shows the values for the hydrogen atom energy and stopping power as it passes through the mylar foil.

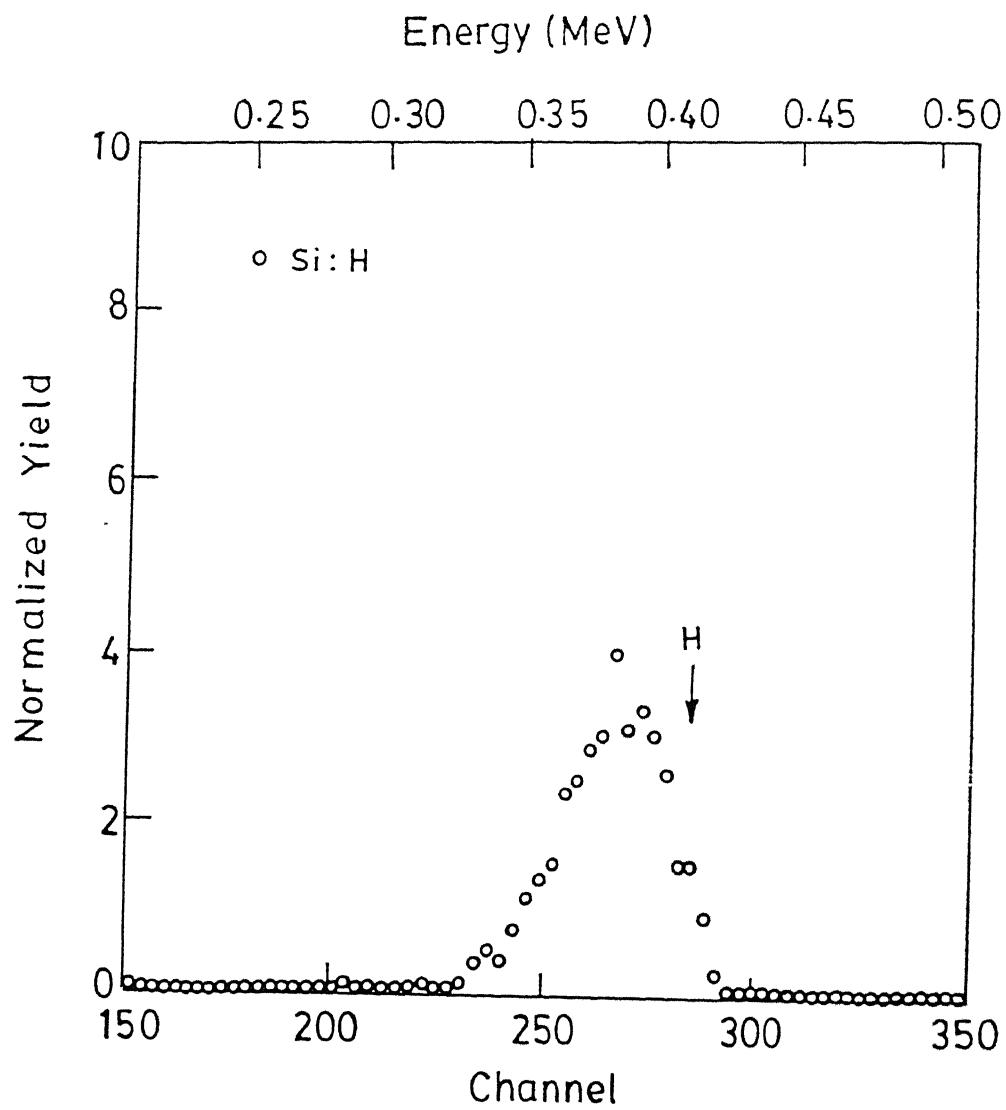


Figure 3.7: H recoil spectrum obtained from Si implanted with hydrogen.

Recoil hydrogen energy (keV)	Detected energy for single layer (keV)	Detected energy for slab analysis (keV)
450	146.4	36.4
500	216.3	133.7
600	347.8	301.9
700	471.6	442.8

Table 3.3: Comparison of hydrogen energy loss in a 5 μm mylar foil as calculated from single layer and slab analysis.

Initially, the surface hydrogen is recoiled (using 1500 keV $^4\text{He}^+$ projectile) with an energy $K_H E_0 = 720$ keV. The energy of the recoiled hydrogen shown for each depth layer increment in the mylar was determined from the energy in the previous layer minus the stopping power times the slab thickness (0.5 μm). The final detected energy is shown in the last line of *Table-3.2* as $E_d = 408.359$ keV, and therefore, ΔE_{foil} is 311.6 keV. An important point to be demonstrated in this table is that a complete slab analysis for the mylar range foil was needed to get an accurate ΔE_{foil} , because the hydrogen stopping power changes continuously (and in a non-linear fashion) throughout the mylar. If the mylar foil was taken as a single layer 6 μm thick and the stopping power as that for the energy incident on the mylar foil (0.224 keV/ \AA), then the final detected energy would be calculated as 450.516 keV rather than 408.3 keV. The magnitude of this error may be small for an energetic recoiled H (near the surface), but the error is extremely large for lower energy recoiled hydrogen atoms as observed from *Table-3.3*.

The channel to energy conversion factor is then given by $\delta E_d = E_d(H_{\text{surface}})/C_{\text{surface}} = 408.36 \text{ keV}/282 \text{ channel} = 1.45 \text{ keV/channel}$, assuming no non-linearities and off-sets in the energy scale have been introduced by the electronics of the detection system. However, very small non-linearity in the energy scale is always present for any practical system. The occurrence of a non-linear energy scale can be determined by measuring the surface channel position for more than one element. In this work, deuterium was chosen as the second species for calibrating the system where the same procedure of slab analysis was performed as mentioned above. Thus, the energy conversion factors become: 1.57 keV/channel and

26.43 keV where the second term is the zero channel energy arising from the non-linearity in the detection system.

3.4.2 Hydrogen quantification

Simulation

Using the analytical expressions for ERDA, the composition profiles from the experimental hydrogen recoil spectrum from a thick target can be obtained with the help of a simulation package. In general, in any simulation package, an iterative process is used in which the material composition and the layer thickness(es) are selected in order to make an initial guess for the stopping powers, energies, and recoil cross sections for each layer. This way an ERD spectrum is generated and compared to the experimental data. A concentration versus depth profile is determined by iteratively changing the layer thickness and composition, recalculating the simulated spectrum, and comparing to the experimental one. Several simulation codes, viz. RUMP (modified)[37], SENRAS[38], GISA3[39], RBX[40] are now available for quick and accurate data analysis. In this work the RUMP code has been used for simulating the hydrogen recoil spectra from different samples. It can be mentioned here that H(D) recoil cross section in RUMP works as a linear combination of two terms, viz. *XSECT* and *E2COF*. The values specified in *XSECT* are constants independent of energy and angle whereas, *E2COF* works in conjunction with *XSECT* to add a quadratic term to the cross sections[41]. The coefficients set by *E2COF* give the E^{-2} energy dependence of the cross section. The cross section must be specified in the rather peculiar internal units of RUMP, counts/ $\mu\text{C/msr}/10^{15}$ at./cm². The conversion factor corresponding to *XSECT* value of 1.0 is equal to 0.1602 barn. The unit for *E2COF* is same as *XSECT* with the energy measured in MeV. Thus, the cross section is determined by

$$\left(\frac{d\sigma}{d\Omega}\right) = XSECT + \frac{E2COF}{E^2} \quad (3.23)$$

To satisfy the above condition, linear fits to the experimental H and D recoil cross section data were obtained as described earlier (section 3.2.2). The respective *XSECT* and *E2COF* values for different recoil angles (θ_r) are thus fed to RUMP code to perform H(D) analysis.

Hand calculation

The analysis is much simpler for quantitative determination of the areal density of hydrogen in the surface layer of a sample. To compute the areal density of a thin H layer in the near-surface region, the following approach is a general one and can be extended to analyses of other layers which are not at the surface. The areal density (A) of hydrogen is the integrated concentration of hydrogen (N) over the layer thickness (τ) is obtained from Eqn. 3.20. Strictly speaking, for atoms which are present only on the surface, the summation over the peak shown in Eqn. 3.20 is a result of finite system-resolution as opposed to a summation over yield at different energies, but this equation shows the summation from channel $[E_d(0)]$ to channel $[E_d(x)]$ for generality to non-surface layers.

Examples

First, the example of RUMP simulation for a thick target will be demonstrated here. For this purpose, ERD analysis was performed on KDP samples. Using He^+ beam of 1.5 MeV incident at an angle of 15° with respect to the sample surface and for the recoil angle of 20° , H recoil spectra were collected from KDP and were analyzed by the RUMP code. Incidentally, results of the RUMP simulation were far from its actual H composition ($\text{H}=2$). In fact, it shows significant H-depletion at room temperature which was later on understood to be due to He^+ ion bombardment. The phenomenon of H-depletion will be dealt in detail in the next chapter. To overcome the problem of H-depletion, ERDA measurements were performed on KDP at 130 K which could reproduce the desired H composition, i.e., $\text{H}=2$ [42]. Fig.3.8 presents such a low temperature (130 K) ERDA spectrum obtained from KDP samples and its simulation. These measurements had enabled to standardize the present ERDA set-up.

Since, hydrogen can get incorporated in high- T_c superconductors via absorption of water vapour from the atmosphere, as prepared YBCO pellets were exposed to humid atmosphere and were later analyzed by ERDA. The depth distribution of hydrogen in the YBCO pellets exposed to humid atmosphere (3.5 h) is shown in Fig.3.9. The spectrum obtained from the as prepared pellet is also shown for comparison. RUMP analysis of the ERD spectrum obtained from the as prepared YBCO pellets shows very low ($\ll 0.1$ at.%). On the other hand, the exposed pellets show uniform hydrogen concentration of 3.1 at.% up to the accessible depth of 5000 Å[43].

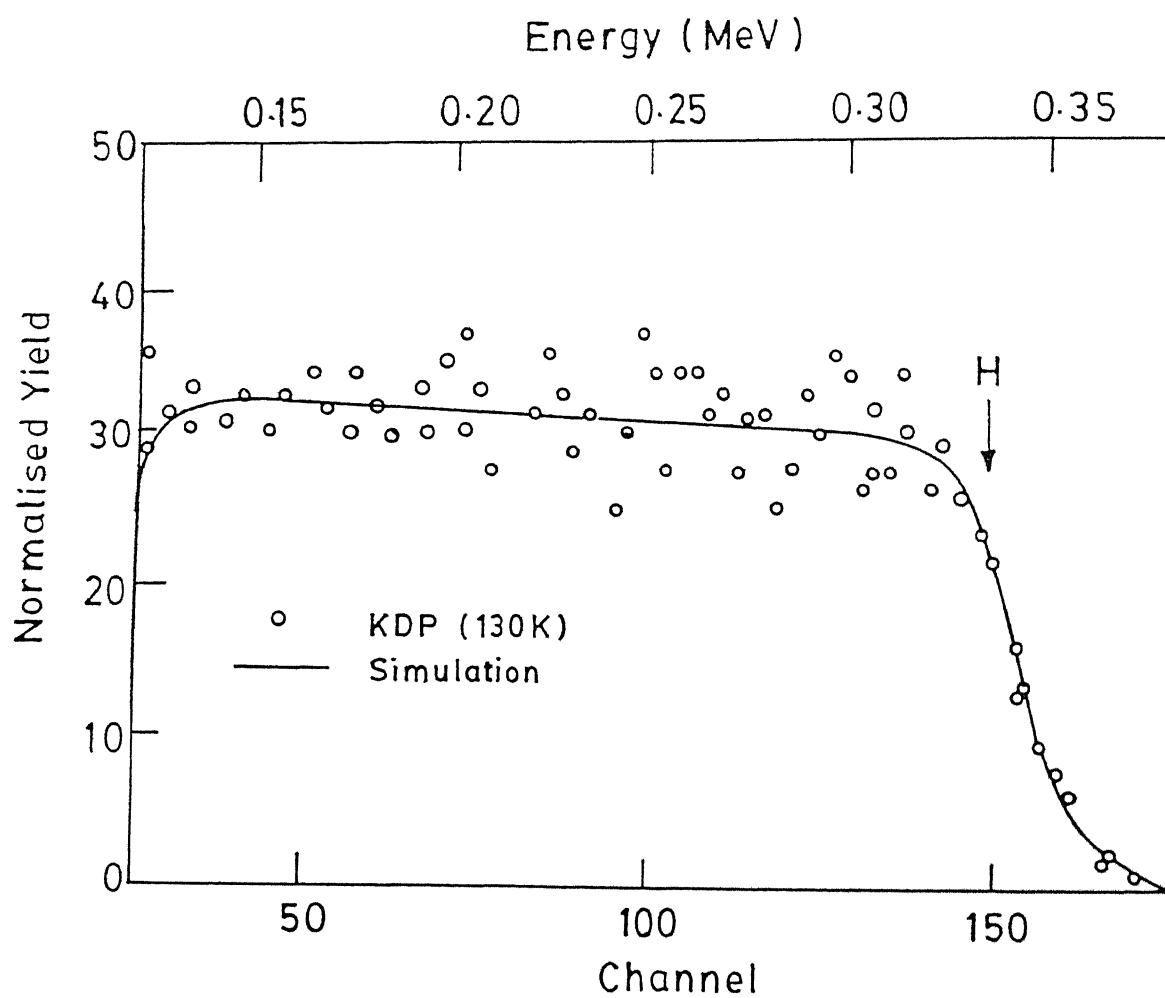


Figure 3.8: ERDA spectra obtained from KDP at 130 K : (o) experimental and (-) simulation.

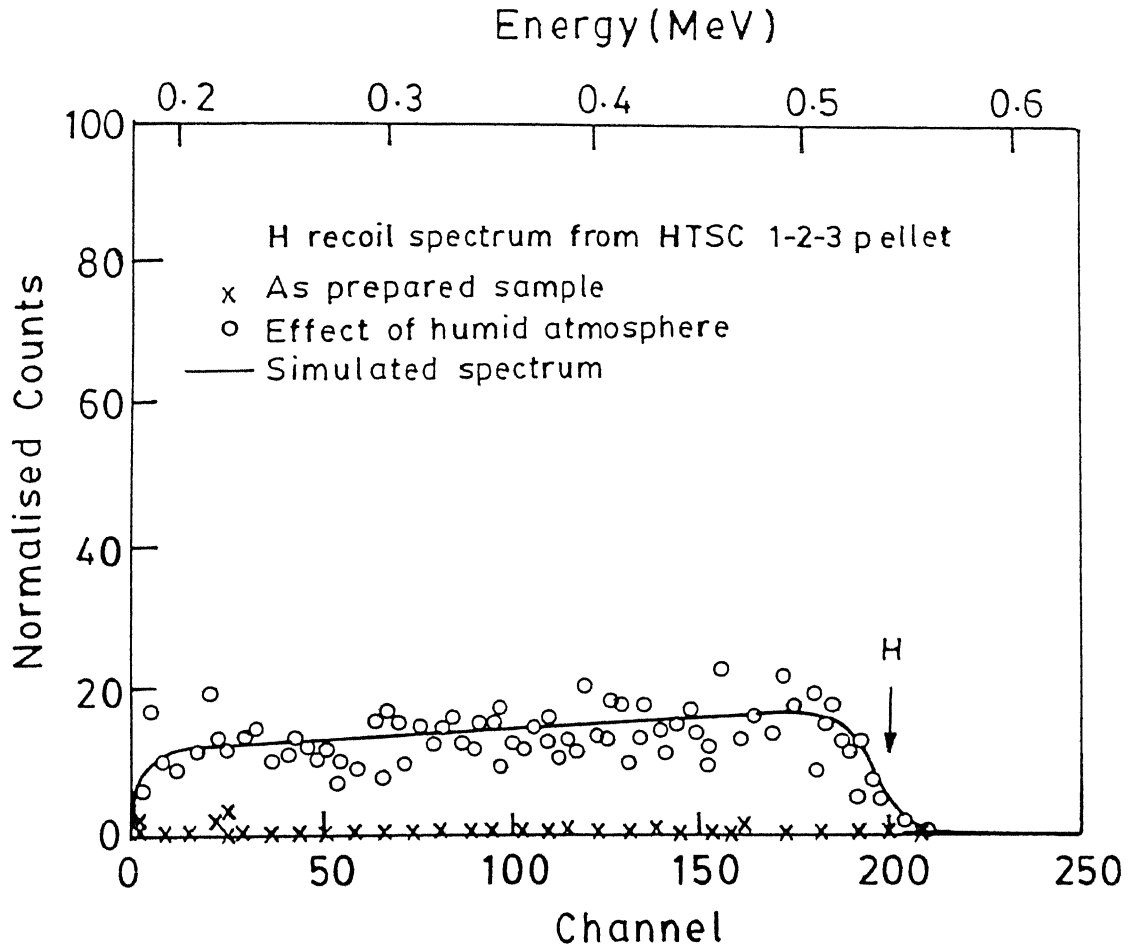


Figure 3.9: H recoil spectra from high- T_c YBCO pellets : before and after exposure to humid atmosphere. The experimental parameters are : $E_0 = 1.43$ Mev, $Q = 10 \mu\text{C}$, $\Omega = 0.865$ msr, and $\theta_r = 25^\circ$. The arrow indicates the surface position of recoiled hydrogen.

Now, the method of hand calculation for hydrogen analysis will be described with the example of thin implanted layer of hydrogen in *c*-Si. In the following example, Si was implanted using low energy hydrogen. The recoiled hydrogen spectrum is presented in Fig.3.7. In this case, 1.5 MeV He⁺ beam was incident at an angle (α) of 15° with respect to the sample surface. The recoiled H atoms were detected after getting scattered at an angle (θ_r) of 30° and travelling through a 6 μ m mylar foil. The R value corresponding to hydrogen was considered to be 1.35[28]. The total amount of charge collected from the incident beam was 10 μ C, giving a total of 6.25×10^{13} He atoms incident on the sample [6.25×10^{13} He = (10 μ C / 1.602×10^{-19} μ C/charge) / (1 charge/He)]. The number of integrated counts under the hydrogen signal was 180. Finally, taking the cross section value from corresponding to $E_0 = 1.5$ MeV and considering $\Omega = 0.865$ msr, the areal density of implanted H in the near-surface region of Si was calculated (following the method of hand calculation) to be 2.1×10^{16} cm⁻².

Before ending this chapter an example of simultaneous detection of H and D will be presented now using the same ERDA set-up. For this, Al samples were first implanted with 3 keV hydrogen and subsequently with deuteron of 3 keV. Typical H and D recoil spectra from as implanted Al:H:D sample is already presented in Fig.3.10. The H and D peaks are well separated in the spectrum which enables the analysis of both these species with a good accuracy. Following the same procedure (as mentioned in the last paragraph), the implanted areas under H and D signals were calculated to be of 1.1×10^{16} and 7.3×10^{16} at./cm², respectively.

3.5 Summary

In this chapter, the following things have been discussed:

- the importance of He⁺ induced low energy ERDA technique for analysis of hydrogen and its isotopes in materials,
- the basic concepts of ERDA and its formulism,
- the influence of system parameters on hydrogen analysis by ERDA and their optimization, and

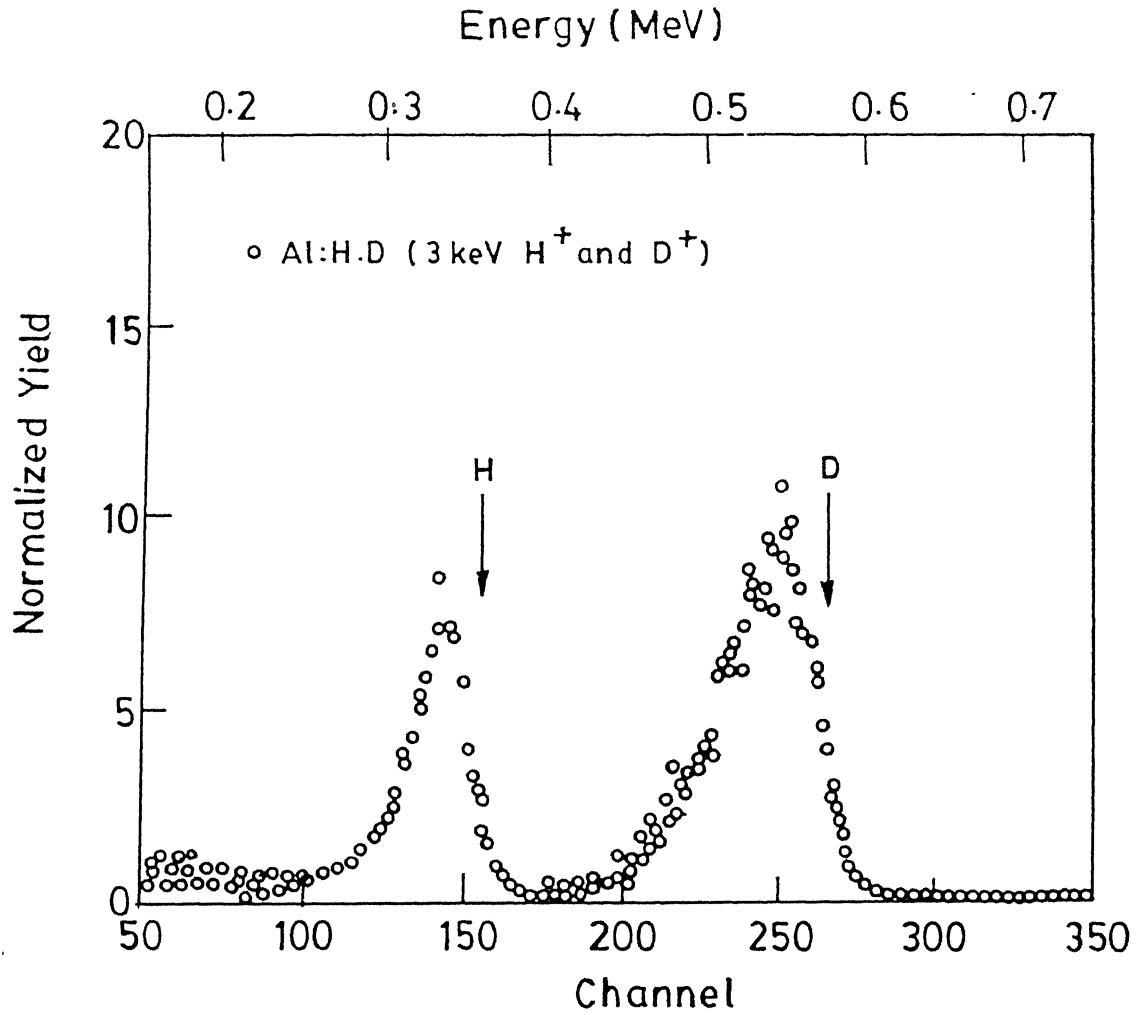


Figure 3.10: As implanted H and D recoil spectra (along with simulation) from Al:H:D sample. The experimental parameters are : $E_0 = 1.7$ Mev, $Q = 10 \mu C$, $\Omega = 0.468$ msr, and $\theta_r = 30^\circ$. The arrows indicate the sample the surface position of H and D.

- the methodology of analyzing hydrogen recoil spectra along with some examples.

Bibliography

- [1] L.C. Feldman and J.W. Mayer, “*Fundamentals of surface and Thin Film Analysis*” (North-Holland Publishing Co., Amsterdam, 1986).
- [2] J.B. Marion and F.C. Young, “*Nuclear Reaction Analysis*” (North-Holland Publishing Co., Amsterdam, 1968) p.142.
- [3] N. Bozoian, K.M. Hubbard and M. Nastasi, *Nucl. Instr. Meth. B*51 (1990) 311.
- [4] H.H. Andersen, F. Besenbacher, P. Loftager and W. Möller, *Phys. Rev. A*21 (1980) 1891.
- [5] V. Quillet, F. Abel and M. Schott, *Nucl. Instr. Meth. B*83 (1993) 47.
- [6] G. Freier, E. Lampi, W. Sleater and J.H. Williams, *Phys. Rev.* 75 (1949) 1345.
- [7] A.C.L. Barnard, C.M. Jones and J.L. Wiel, *Nucl. Phys.* 50 (1964) 604.
- [8] L. Kraus and I. Linck, *Nucl. Phys. A*224 (1974) 45.
- [9] S. Yamaguchi, Y. Fujino, S. Nagata, H. Kaneko, K. Hashimoto and M. Hirabayashi, *Nucl. Instr. Meth.* 218 (1983) 598.
- [10] D.C. Ingram, A.W. McCormik, P.P. Pronko, J.D. Carlson and W.A. Lanford, *Nucl. Instr. Meth. Nucl. Instr. Meth. B*6 (1985) 430.
- [11] S. Nagata, S. Yamaguchi, Y. Fujino, Y. Hori, N. Sugiyama and K. Kamada, *Nucl. Instr. Meth. B*6 (1985) 533.
- [12] F. Pászti, E. Kótai, G. Mezey, A. Manuaba, L. Pócs, D. Hildebrandt and H. Strusmy, *Nucl. Instr. Meth. B*15 (1986) 486.

- [13] W. Hong and Z.G. Qing, *Nucl. Instr. Meth. B34* (1988) 145.
- [14] Y. Wang, J. Chen, and F. Huang, *Nucl. Instr. Meth. B17* (1986) 11.
- [15] R.E. Beneson, L.S. Wielunski and W.A. Lanford. *Nucl. Instr. Meth. B15* (1986) 453.
- [16] E. Szilágyi, F. Pászti, A. Manuaba, C. Hajdu and E. Kótai, *Nucl. Instr. Meth. B43* (1989) 502.
- [17] J. Tirira, P. Trocellier, J.P. Frontier and P. Trouslan, *Nucl. Instr. Meth. B45* (1990) 203.
- [18] J.E.E. Baglin, A.J. Kellock, M.A. Crockett and A.H. Shih, *Nucl. Instr. Meth. B64* (1992) 469.
- [19] J.M. Blair, G. Freier, E. Lampi and W. Sleater, *Phys. Rev.* 75 (1949) 1678.
- [20] T. Lauritsen, T. Huus and G.G. Nilson, *Phys. Rev.* 92 (1953) 1501.
- [21] A. Galonsky, R.A. Douglass, W. Haeblerli, M.T. McEllistrem and H.T. Richards, *Phys. Rev.* 98 (1955) 586.
- [22] F. Besenbacher, I. Stensgaard and P. Vase, *Nucl. Instr. Meth. B15* (1986) 459.
- [23] T. Som, S. Dhar, N. Banerji, K. Ramakrishnan and V.N. Kulkarni, *Bull. Mater. Sci.* 19 (1996) 73.
- [24] J.F. Ziegler, "*The Stopping and Ranges of Ions in Matter*", Vols. 3-4 (Pergamon Press, New York, 1977).
- [25] W.-K. Chu, J.W. Mayer and M.-A. Nicolet, "*Backscattering Spectrometry*" (Academic Press, New York, 1978).
- [26] J.F. Ziegler, *Appl. Phys. Lett.* 31 (1977) 544.
- [27] H.H. Anderson and J.F. Ziegler, "*Hydrogen Stopping Powers and Ranges in All Elements*" (Pergamon Press, New York, 1977).
- [28] B.L. Doyle and P.S. Peercy, in "*Proc. workshop Summarizing Developing Techniques and formulating Requirements for the Future*" (Sandia National Laboratories, Albuquerque, New Mexico, 1979) p. 92-103.

- [29] W.-K. Chu, *Phys. Rev. A* 13 (1976) 2057.
- [30] J. L'Ecuyer, C. Brassard, C. Cardinal, J. Chhabal, L. L. Deschenes, J.P. Labrie, B. Terrault, J.G. Martel and R. St.-Jacques, *J. Appl. Phys.* 47 (1976) 881.
- [31] J.S. Williams and W. Möller, *Nucl. Instr. Meth.* 157 (1978) 213.
- [32] P. F. Hinrichsen, D.W. Hetherington, S.C. Gujrathi and L. Chiche, *Nucl. Instr. Meth. B* 45 (1990) 275.
- [33] “*Handbook of Modern Ion Beam Materials Analysis*”, Eds. J.R. Tesmer and M. Nastasi (Materials Research Society, Pittsburgh, PA, 1995).
- [34] B.L. Doyle and D.K. Brice, *Nucl. Instr. Meth. B* 45 (1990) 265.
- [35] F. Pászti, E. Szilágyi and E. Kótai, *Nucl. Instr. Meth. B* 54 (1991) 507.
- [36] J.F. Ziegler, J.P. Biersack and U. Littmark, “*The Stopping and Range of Ions in Solids*” (Pergamon Press, New York, 1985).
- [37] B. Blanpain, P. Révész, L.R. Doolittle, K.H. Purser and J.W. Mayer, *Nucl. Instr. Meth. B* 34 (1988) 459.
- [38] G. Vizkelethy, *Nucl. Instr. Meth. B* 45 (1990) 1.
- [39] J. Saarilahti and E. Rauhala, *Nucl. Instr. Meth. B* 64 (1992) 734.
- [40] E. Kótai, *Nucl. Instr. Meth. B* 85 (1994) 588.
- [41] “RUMP” Manual, *Computer Graphics Service*, p. 4p-49.
- [42] T. Som and V.N. Kulkarni, *Proc. Department of Atomic Energy Solid State Physics Symposium, India*, 40C (1997) 59.
- [43] T. Som, S. Dhar, S. Singh and V.N. kulkarni, in “*High Temperature Superconductivity - Ten Years After Its Discovery*”, Eds. K.B. Garg and S.M. Bose (Narosha, New Delhi, 1998) p. 285.

Chapter 4

Hydrogen depletion during ERDA: Experimental results and modelling

4.1 Introduction

The experimental details and formalism of ERDA have been presented in the previous chapters along with some illustrative examples to bring out the power and ease of the technique in the determination of concentration versus depth distribution of light elements, with special emphasis on H and D, in different kinds of materials. From this, although ERDA appears to be quite attractive for an accurate analysis of hydrogen and its isotopes in materials, it has to be noted that the phenomenon of desorption of hydrogen from the material subjected to energetic ion irradiation can lead to erroneous estimates with regard to the actual hydrogen contents since the depletion can occur due to the analyzing beam itself. Incidentally the phenomenon of desorption of hydrogen under irradiation was almost simultaneously reported during the years 1978-79 when L'Ecuyer *et al.* proposed for the first time the technique of ERDA for analysis of light elements. One of the early works on ion induced hydrogen desorption was reported by Bugeat and Ligeon in the case of silicon carbide[1]. Since then the energetic ion induced hydrogen desorption has been reported in variety of materials viz. polymers[2], amorphous hydrogenated carbon[3] and Si[4], hydrogen implanted beryllium

oxide[5], graphite[6], silicon nitride[7], silicon oxide[8], organic dye[9] etc. However, it may be noted that not all the materials show such desorption of hydrogen. For example, diamond films prepared under certain conditions, hydrogen implanted in certain materials (viz. Al, Si etc.) don't exhibit ion induced depletion of hydrogen. The study of ion induced hydrogen depletion phenomena becomes important on two accounts. Firstly, it affects the accuracy of the ERDA technique as mentioned in the beginning. Secondly, it becomes important in the context of nuclear fusion technology[10] and probably in semiconductor device technology where hydrogen is useful for passivation of defects.

In this chapter the results of He^+ induced depletion of hydrogen during ERDA measurements is presented for three different category of materials, viz. single crystalline potassium dihydrogen phosphate (KH_2PO_4 or KDP), diamondlike carbon (DLC) films deposited on Si under various conditions by dc glow discharge technique, and organic phospholipid (cardiolipin) thin films deposited on Si by spin coating technique. The importance of these materials and various experimental steps for sample preparation and hydrogen analysis have been described in the respective sections. The physico-chemical changes occurring in these materials due to hydrogen depletion were studied by FTIR and/or micro Raman spectroscopy are also described. Conclusions for each system are drawn at the end of the respective sections. While, in the later sections the ion depletion data from these different systems has been discussed together and a simple method has been followed (section 4.3) to determine the concentration of H at zero analyzing beam fluence, which is found to work satisfactorily for different types of materials. Subsequently, the hydrogen depletion curves for all the systems have been explained in the light of the existing phenomenological models[11, 12].

4.2 Ion induced hydrogen depletion

4.2.1 KDP system

In the recent years, MeV He^+ ion implantation (up to a dose of 10^{16} ions/cm²) has been used to produce optical waveguides[13] in a large number of materials like oxides (Al_2O_3 , SiO_2)[14–16], phosphate (KTiOPO_4)[17], titanate (BaTiO_3)[18], niobates[19, 20], etc. for use in the optoelectronic technology. The desired changes in optical properties are brought about

by several processes viz., changes in the stoichiometry, production of new phases, structural changes, defects produced by the electronic and nuclear energy loss, volume expansion in the nuclear damage region. stress effects etc. occurring during implantation.

There is a different class of nonlinear optical materials (dihydrogen phosphate crystals, viz., KDP (KH_2PO_4), ADP ($\text{NH}_4\text{H}_2\text{PO}_4$), etc.) which possess important optoelectronic properties[21] making them potential candidates for guided wave control. Recently, Benyacar et al. have studied damage induced by MeV D^+ and O^{6+} ions in these crystals[22]. However, to fabricate optical devices using these materials, a detailed and systematic study of ion induced stoichiometric and structural changes occurring in them is necessary. For example, hydrogen being the lightest element, ion irradiation would cause an easy displacement and migration through the material. In fact, this has been observed for many materials as mentioned above.

In this section, MeV He^+ induced stoichiometric changes in KDP crystals especially the changes occurring in its hydrogen content has been described. This has been followed by the study of effect of ion irradiation (under similar conditions) on KDP crystals which were coated with thin metallic layers of Au. Micro Raman spectroscopic measurements were employed to correlate the physico-chemical changes occurring in the samples as a consequence of hydrogen loss.

Experimental

Well polished, transparent, single crystalline KDP samples, procured from the Crystal Growth Centre, Anna University, Chennai, were used for He^+ irradiations at room temperature. 1.5 MeV He^+ beam was used for irradiation and *in situ* simultaneous measurement of hydrogen content of different samples was performed by ERD analysis.

Three different sample configurations, viz., (i) KDP crystals coated with 60 Å of Au film (KDP/Au(60 Å)), (ii) KDP deposited with 30 Å of Au film (KDP/Au(30 Å)) and (iii) bare KDP were used for He^+ irradiation. The irradiations were performed for a total of 8 μC integrated He^+ charge where the incident He^+ ions were impinging at a grazing angle of 15° with respect to the sample surface. This corresponds to a maximum ion dose of 2.4×10^{15} He^+/cm^2 . As a matter of fact, for each irradiation step the elastically recoiled hydrogen were detected by an ion implanted semiconductor detector kept at an angle of 30° with respect to the incident beam direction. These measurements had been complemented by studying

the bulk KDP composition by RBS using 1.5 MeV He^+ ions.

Results and discussion

A typical experimental RBS spectrum obtained from a KDP crystal deposited with 60 Å Au is shown in Fig.4.1. The spectrum was collected for an integrated charge of 2 μC . The surface positions for Au, K, P, O have been shown by arrows. Simulated spectrum (using RUMP code) has been obtained for a 2 μm thick layer having a composition of KH_2PO_4 with a top layer of Au of thickness 60 Å. Simulations performed using different H concentrations reveal that the theoretical spectrum does not depend much on the concentration of hydrogen. In fact, a change in the composition of hydrogen from H=2 to H=1 is reflected by an increase of $\sim 2\%$ in the spectrum height which is well within the statistical error of the data. Moreover, a change in H concentration should also get reflected in the energy to depth conversion due to change in the stopping power; but due to the use of thick samples, this effect is not visible in our experiments. The ERD spectra recorded for KDP/Au(60 Å), KDP/Au(30 Å) and bare KDP (i.e., without Au film) have been shown in Fig.4.2. All the spectra were normalized for an integrated He charge of 1 μC and a solid angle of 1 msr for direct comparison of the data. In all the cases, the surface position of hydrogen has been indicated by arrows. The reduction in the spectrum height (bulk) indicates enhanced hydrogen depletion from these samples. The experimental H composition obtained by simulating the spectra are plotted as a function of He^+ irradiation dose in Fig.4.3. This shows a rapid reduction in hydrogen concentration from bare KDP up to 1 μC of incident charge after which the rate of loss reduces and the H composition approaches an approximately constant value. At highest dose of $2.4 \times 10^{15} \text{ He}^+/\text{cm}^2$, the loss of hydrogen from bare KDP and KDP/Au(30 Å) sample is similar (72 and 69 % respectively). In case of KDP/Au(60 Å) sample the H-loss significantly reduces to 21%. The ERDA spectra of Fig.4.2 reveal that for KDP/Au(60 Å) sample, He^+ irradiations lead to the development of a well defined surface hydrogen peak. The area under this surface peak has been plotted in Fig.4.4 and is seen to increase linearly as a function of irradiation dose.

Fig.4.5 presents the infrared spectrum obtained from as obtained KDP sample. Assignment of different peaks has been shown in Table-4.1. The strong infrared band at around 885 cm^{-1} in KDP is assigned to the OH torsions[23]. It is to be noted here that since $\nu_1(\text{PO}_4)$ is observed with strong intensity at 924 cm^{-1} in the Raman spectrum (as seen in Fig.4.6)

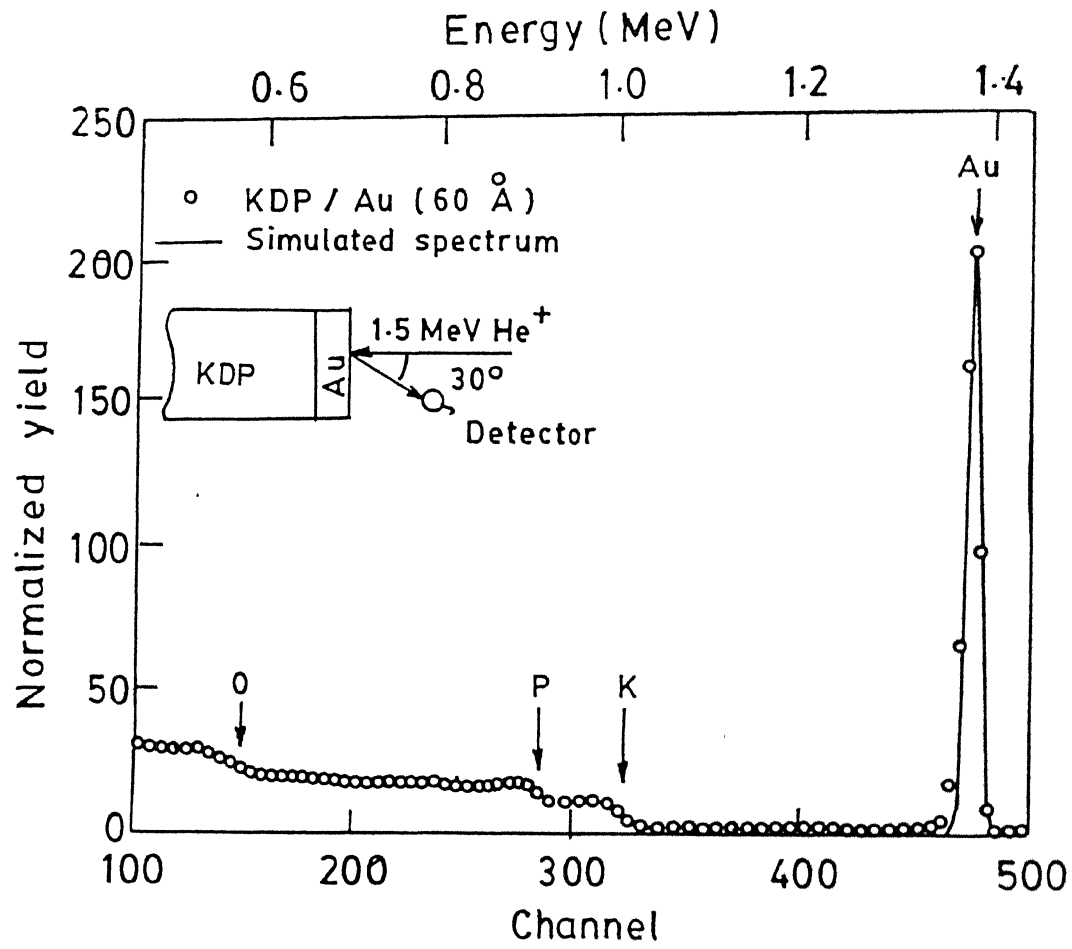


Figure 4.1: Experimental and simulated RBS spectra obtained from KDP/Au(60 Å) sample.

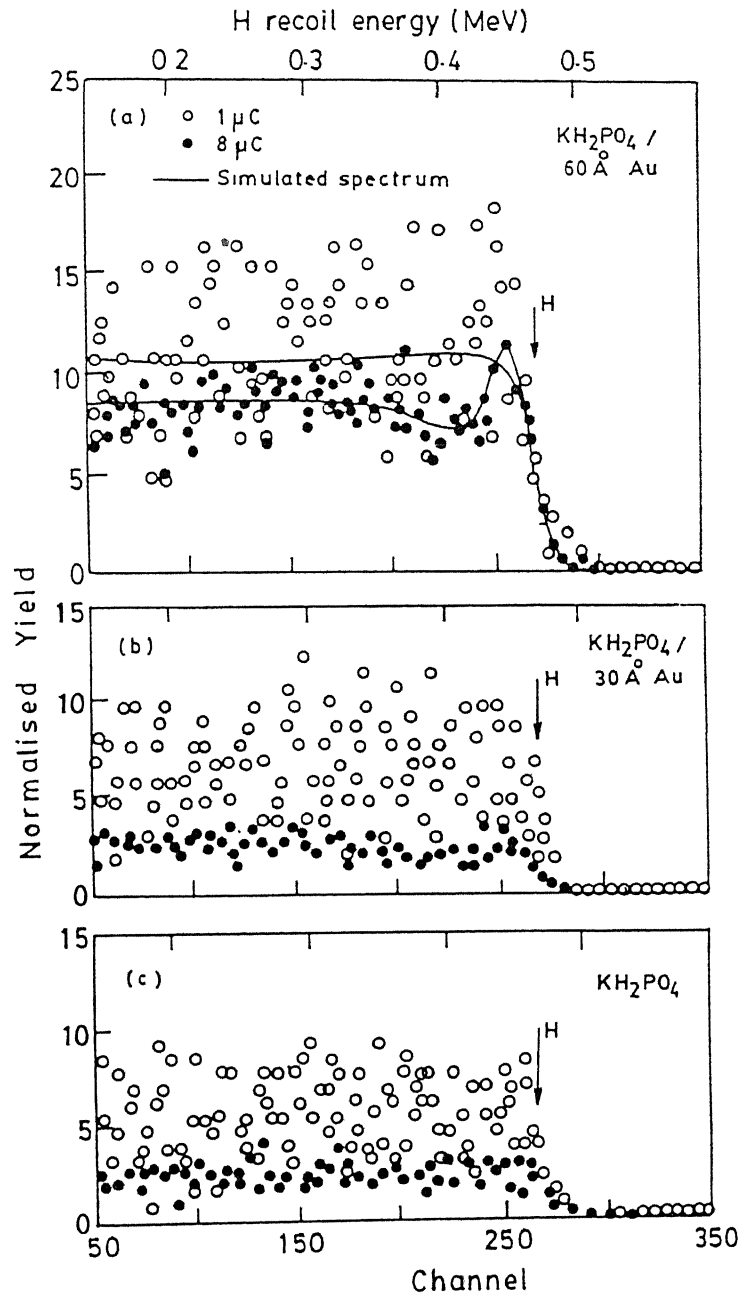


Figure 4.2: 1.5 MeV He^+ induced hydrogen recoil spectra obtained from different sample configurations: (a) $\text{KDP}/\text{Au}(60 \text{ \AA})$, (b) $\text{KDP}/\text{Au}(30 \text{ \AA})$ and (c) bare KDP samples.

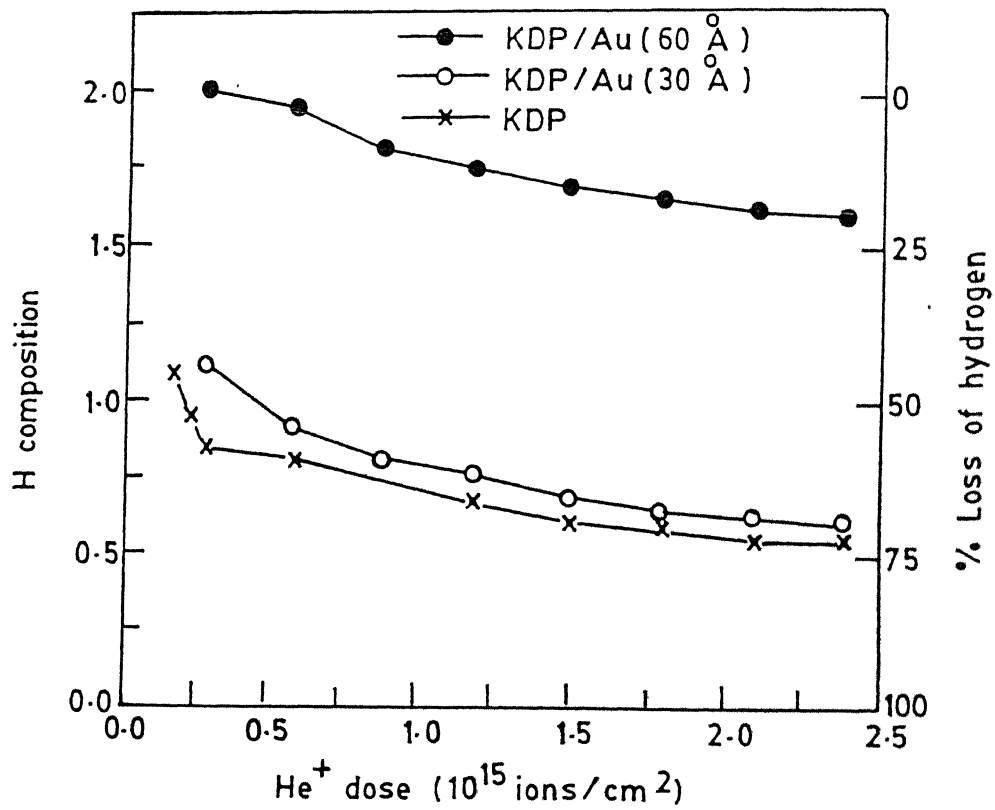


Figure 4.3: Variation in the hydrogen composition as a function of incident He⁺-dose obtained from different sample configurations.

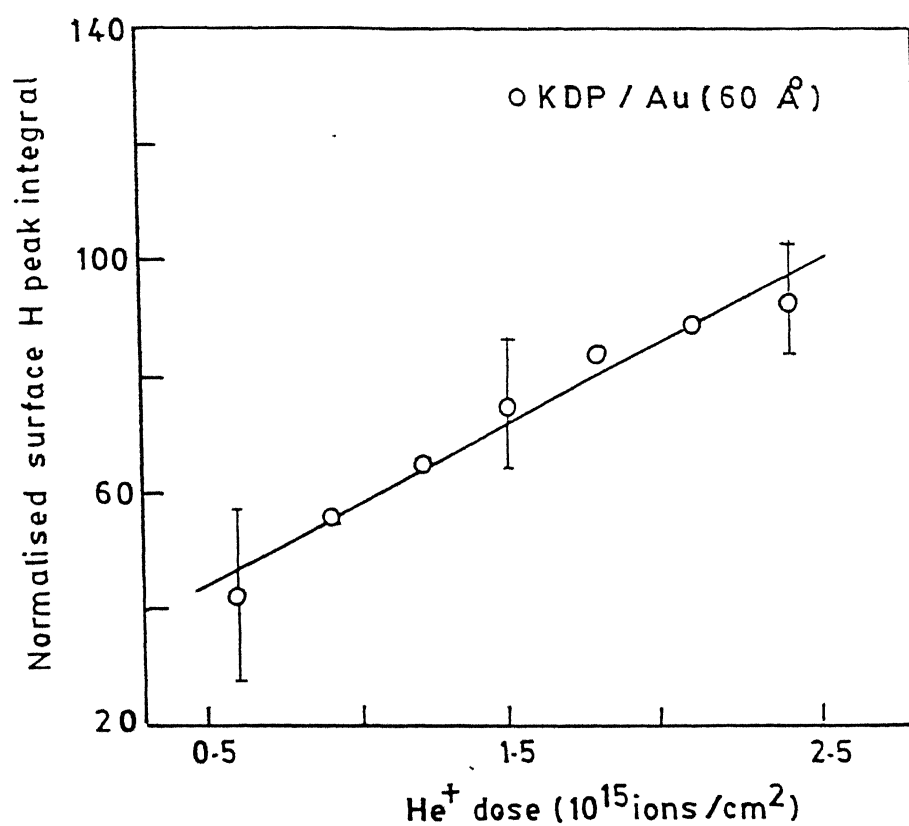


Figure 4.4: Growth of the surface hydrogen peak as a function of He⁺ irradiation dose. The solid line is a best fit to the experimentally obtained points. Each point represents the area under the surface H peak which has been obtained by subtracting the contribution of the flat portion of recoil spectra (see Fig.4.2).

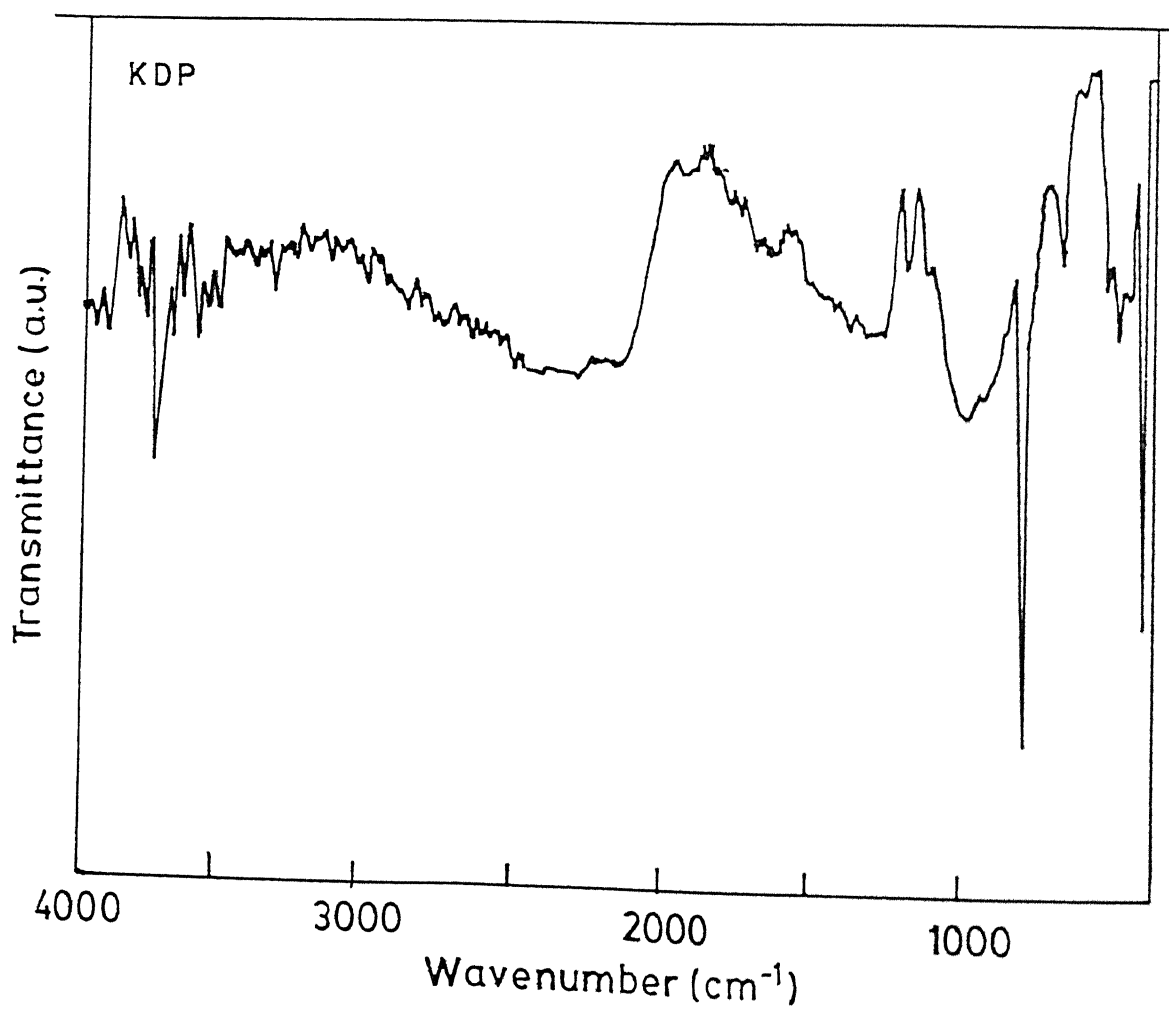


Figure 4.5: Infrared spectrum obtained from as obtained KDP.

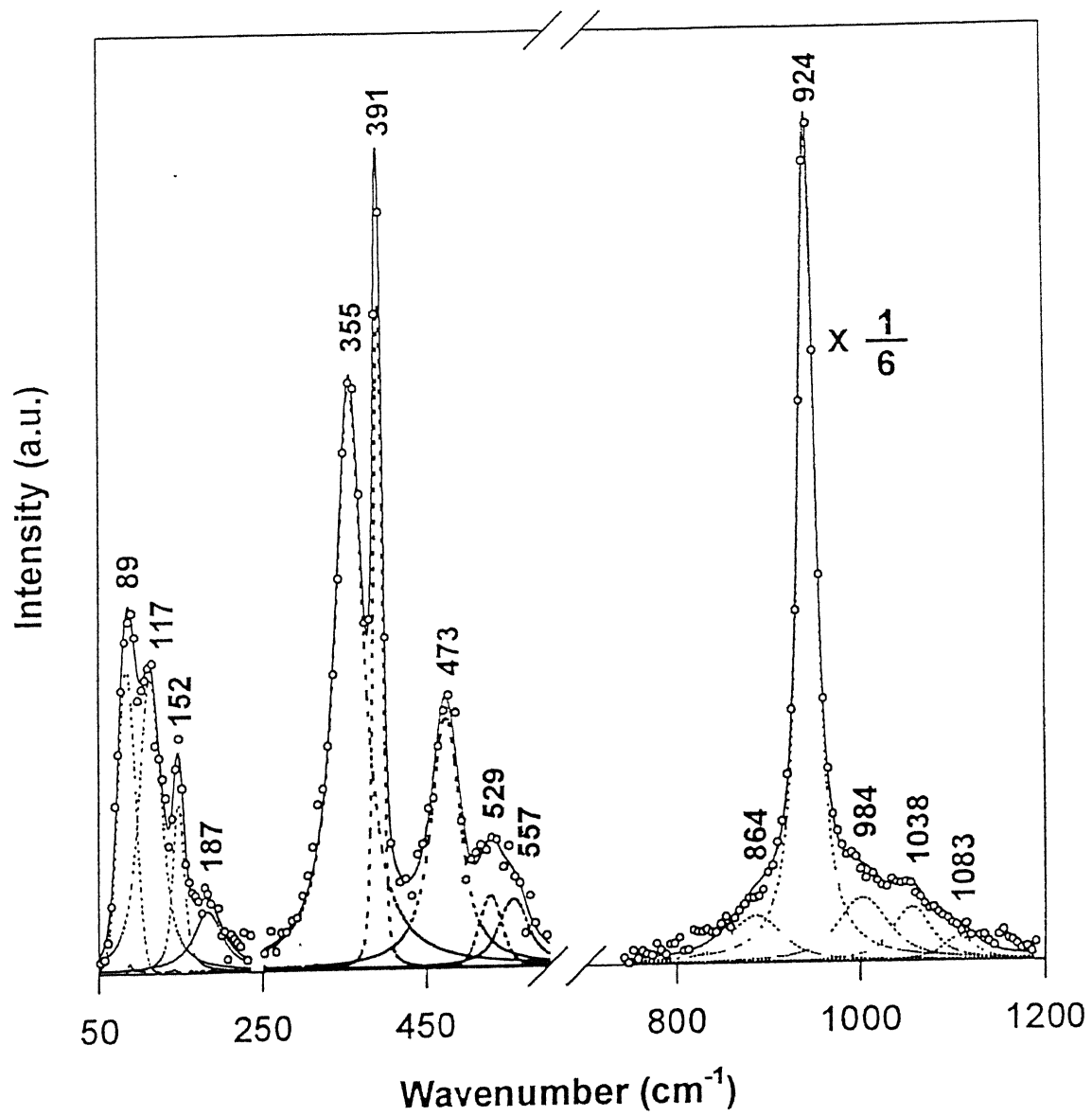


Figure 4.6: Deconvoluted micro Raman spectrum for as obtained KDP.

Observed peak (cm ⁻¹)	Assignment
472	$\nu_4(\text{PO}_4)$
506	$\nu_4(\text{PO}_4)$
532	$\nu_4(\text{PO}_4)$
886	O-H torsion
912	O-H torsion
971	$\nu_3(\text{PO}_4)$
1023	$\nu_3(\text{PO}_4)$
1092	$\nu_3(\text{PO}_4)$
1139	$\nu_3(\text{PO}_4)$
1277	P-O-H bending
1302	P-O-H bending
1660	out of plane O-H bending

Table 4.1: Observed infrared frequencies (400-2000 cm⁻¹) and their assignments for as obtained KDP at room temperature.

of the as obtained KDP sample, $\nu_3(\text{PO}_4)$ are expected to be higher in wavenumber than ν_1 . The three infrared bands at 971, 1023 and 1092 cm⁻¹ are reasonably assigned to the three splitted components of $\nu_3(\text{PO}_4)$ in KDP. Likewise, at the low frequency range three bands at 472, 506 and 532 cm⁻¹ have been attributed to the three frequencies of $\nu_4(\text{PO}_4)$ mode in KDP. The infrared spectra of the irradiated regions could not be taken due to the opacity developed on the surface of the crystal. As a matter of fact, the diffusion and scattering from the irradiated regions prevented transmission of IR radiation to record good spectra from the rather thick crystal.

The KDP crystal at room temperature may be considered as consisting of K⁺ and (PO₄H₂)⁻¹ ions belonging to the space group D_{2d} . The primitive cell for this model contains two K⁺ ions and two (PO₄H₂)⁻¹ ions. Fig.4.6 shows the deconvoluted Raman spectrum from the as obtained KDP crystal. Computer line shape analysis was performed using the PEAKFIT program. This spectrum corresponds well with those expected from D_{2d} symmetry. Both translational and rotational optical-phonon bands are expected in the lattice

vibrational spectra of the KDP-family crystals[24]. Using the assignments favoured by previous work on KDP-family crystals[25], the 91 cm^{-1} KDP band may be assigned to the transverse-optic phonons corresponding to K-PO_4 translatory vibrations along the c axis. The 187 cm^{-1} KDP band may be assigned to the PO_4 vibrational band. The broad bandwidth of the vibrational mode implies that the rotational optic phonons are susceptible to anharmonic phonon-phonon interactions. With two molecular units in the primitive unit cell and possible transverse-optic (TO) and longitudinal-optic (LO) splitting of the polar lattice modes several other lattice vibrational bands are expected, although some of them may be degenerate or very weak. The presence of a broad Rayleigh-wing band (not shown) may be attributed to the B_2 -symmetry soft mode or the Slater configurational mode. However, the Raman bands in the region from 320 to 1000 cm^{-1} show the internal modes of vibration of the PO_4 groups which are influenced by the site symmetries of the PO_4 group in the microcrystallites. The dominant band, due to the totally symmetric stretching model of PO_4 is observed at 924 cm^{-1} . In order to obtain information on the structural changes taking place in KDP due to ion irradiation, micro Raman spectroscopic studies were performed on various irradiated spots. *Table-4.2* presents the different peak assignments corresponding to room temperature micro Raman spectra recorded from as obtained and irradiated regions of KDP.

Fig.4.7 shows the overlapped Raman spectra obtained from different irradiated spots corresponding to varying He^+ fluences. From *Table-4.2* it becomes evident that the $\nu_1(\text{PO}_4)$ remains same leaving the $(\text{PO}_4)^-$ internal force field unaltered. In contrast, it is observed (from *Table-4.2*) that the $(\Delta\nu)_{1/2}$, I decrease with increasing He^+ ion fluence. This perturbation is attributed to the loss of hydrogen from the material and its amorphization with increasing He^+ ion fluence. Of course, from **Figs.4.8, 4.9, and 4.10** it becomes clear that the lattice translational mode and the asymmetric stretching mode of $\nu_3(\text{PO}_4)^-$ exhibit a monotonous increase in the frequencies corresponding to increasing ion fluences. This may result due to an increase in the external force field of $(\text{PO}_4)^-$ and can be termed as 'lattice hardening' caused as a consequence of continuous hydrogen depletion from KDP.

The depletion of hydrogen from the KDP sample in terms of the possible bond-breaking mechanism can be thought of as follows. As mentioned above, considering the structural unit as K^+ and $[\text{PO}_4\text{H}_2]^{-1}$ group, due to the beam interaction, $[\text{PO}_4\text{H}_2]^{-1}$ may lose its electron which moves to the conduction band leaving behind the free hole which can get self trapped

As obtained ($\nu, \Delta\nu_{1/2}, I$)	A ($\nu, \Delta\nu_{1/2}, I$)	B ($\nu, \Delta\nu_{1/2}, I$)	C ($\nu, \Delta\nu_{1/2}, I$)	Assignment
(89,24,2.5)	(91,26,2.6)	(94,29,3.0)	(98,42,4.0)	T (K-PO ₄)
(117,32,3.7)	(118,35,3.2)	(122,35,2.6)	(128,41, 1.8)	T (K-PO ₄)
(151,16,1.1)	(152,20,1.8)	(154,22,1.7)	(156,24,1.1)	ν (O-H...O)
(187,43,1.0)	(186,41,1.4)	(187,48,1.3)	(192,52,0.9)	L (K-PO ₄)
(355,41,10.7)	(356,48,11.8)	(355,46,7.5)	(355,37,8.7)	ν_2 (PO ₄)
(391,12,3.1)	(391,12,1.9)	(391,12,1.8)	(392,12,2.0)	ν_2 (PO ₄)
(473,44,4.7)	(470,48,6.9)	(471,46,4.4)	(469,57,6.4)	ν_4 (PO ₄)
(529,32,0.8)	(542,33,1.1)	(534,22,0.4)	(532,19,0.7)	ν_4 (PO ₄)
(557,42,1.1)	(565,25,0.4)	(562,24,0.4)	(562,36,0.9)	ν_4 (PO ₄)
(864,55,5.9)	(871,47,2.7)	(875,54,6.8)	(882,82,7.0)	O-H torsion
(924,46,58)	(924,24,49)	(924,25,42)	(924,24,41)	ν_1 (PO ₄)
(984,46,6.3)	(985,47,4.8)	(987,79,14.0)	(1002,82,10.2)	ν_3 (PO ₄)
(1038,55,7.9)	(1037,55,5.8)	(1050,45,5.3)	(1059,49,3.4)	ν_3 (PO ₄)
(1083,29,1.4)	(1093,38,2.1)	(1090,45,2.6)	(1109,57,1.4)	ν_3 (PO ₄)

Table 4.2: Different KDP Raman peak wavenumbers (ν in cm^{-1}), FWHM's ($\Delta\nu_{1/2}$ in cm^{-1}) and intensities (I in a.u.) along with respective peak assignments. A, B and C refer to the three different irradiated regions corresponding to fluences of 8.9×10^{14} , 1.78×10^{15} and 3.56×10^{15} He^+/cm^2 .

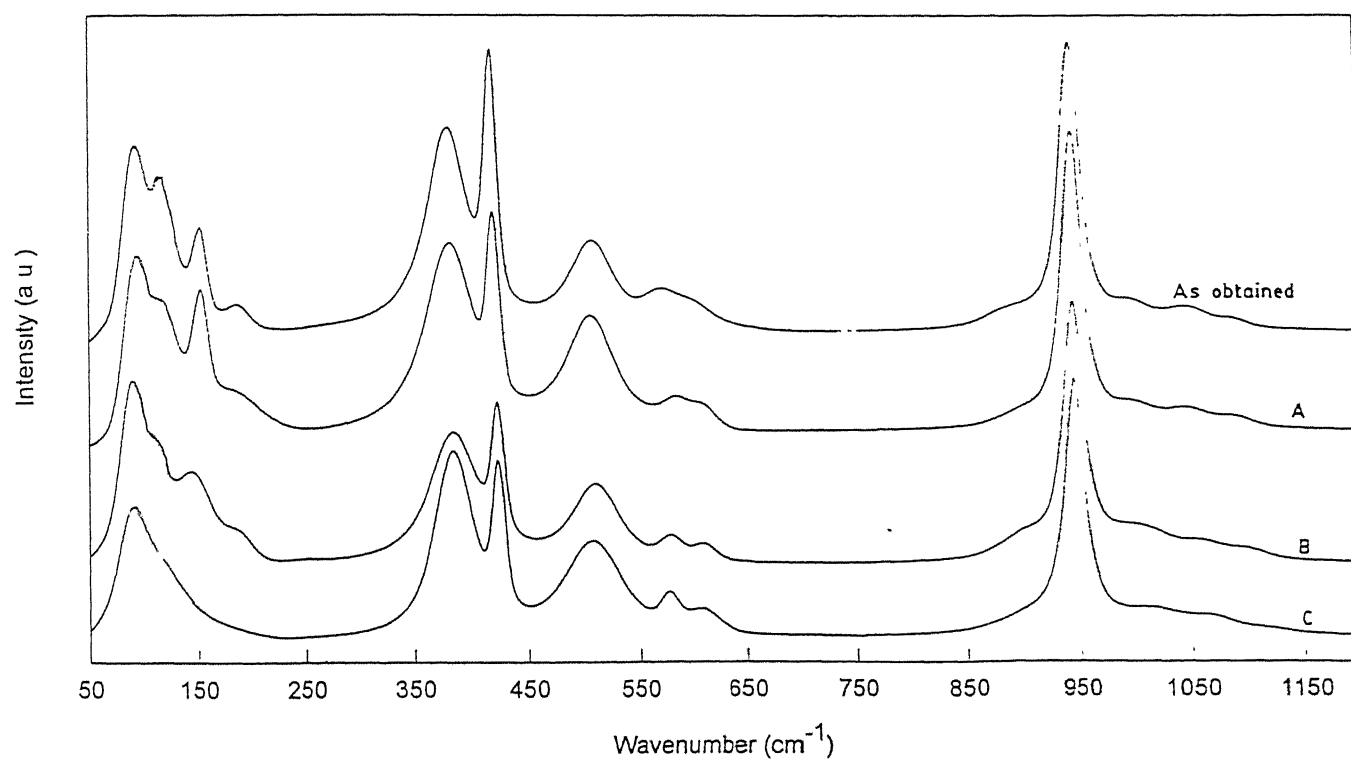


Figure 4.7: Overlapped Raman spectra from various irradiated regions of KDP. [Ref. Table 4.2]

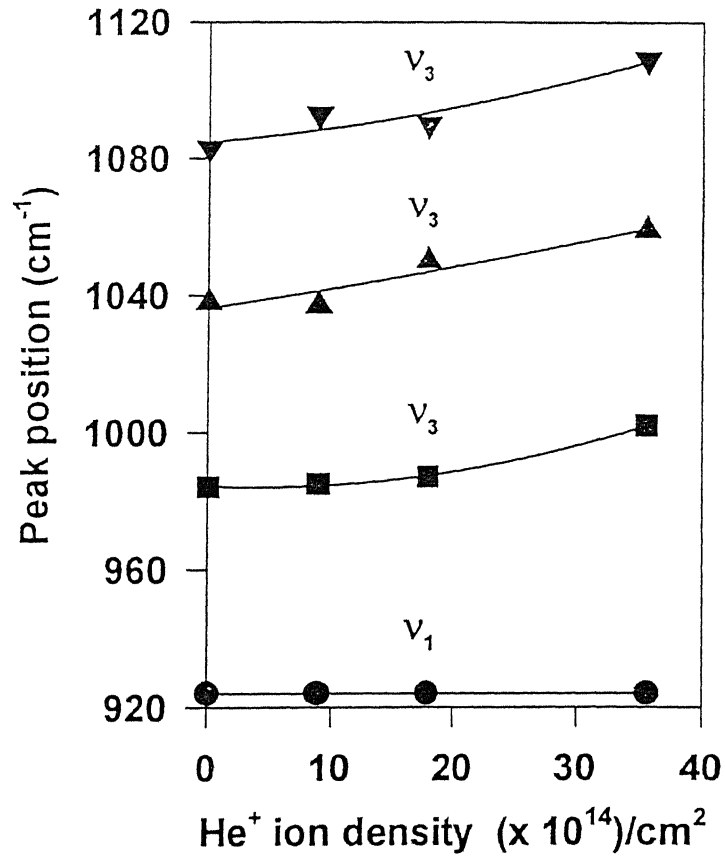


Figure 4.9: Variation in Raman peak shift corresponding to (a) $\nu_1(\text{PO}_4)$ and (b) $\nu_3(\text{PO}_4)$ modes as a function of He^+ ion fluence.

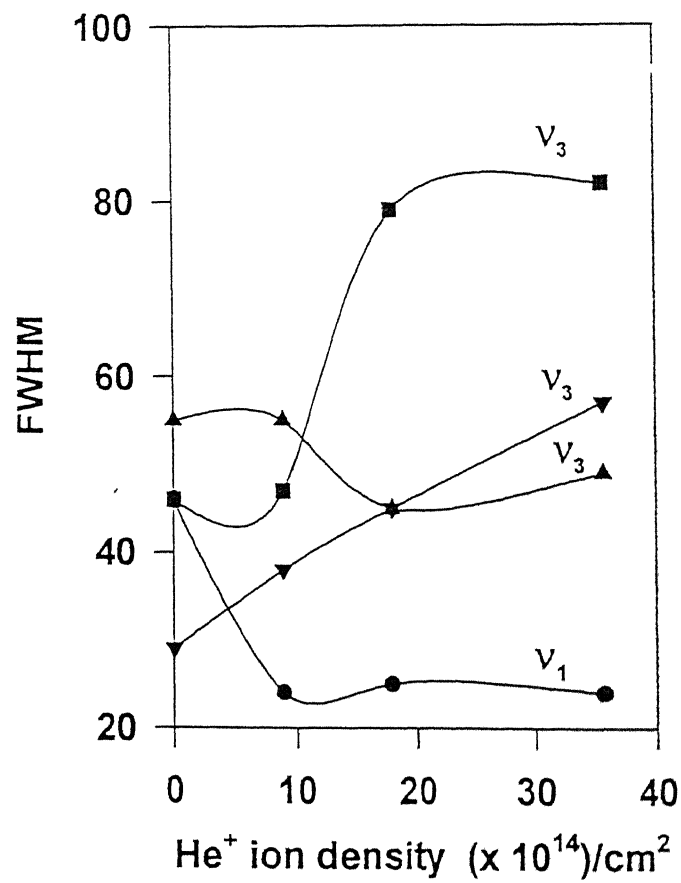


Figure 4.10: Variation in FWHM corresponding to (a) $\nu_1(\text{PO}_4)$ and (b) $\nu_3(\text{PO}_4)$ modes as a function of He⁺ ion fluence.

due to the configurational changes occurring in the neighbouring structural units. It has been proposed[22] that lattice relaxations involving atomic rearrangements do occur, thus creating a negatively charged hydrogen vacancy which can trap the positively charged hole. This process would give rise to a positively charged hydrogen which captures an electron and the resulting hydrogen atom can migrate towards the surface and eventually escapes from the sample. In case of KDP/Au(60 Å) samples, Au layer acts as a barrier, preventing hydrogen to escape from the sample and thus leading it to get accumulated at the surface (as seen in Fig.4.4).

Conclusions

Hydrogen concentration and its dependence on He^+ ion fluence has been studied in the optoelectronically important insulating KDP samples. The results indicate hydrogen depletion to take place from the samples under room temperature He^+ ion bombardment. The effect of Au of varying thickness as a top layer has also been studied which shows that a 60 Å Au layer on KDP acts as a barrier and considerably reduces the depletion of hydrogen from the samples. Hydrogen depletion from the KDP samples is followed by amorphization of KDP with increasing He^+ ion fluence as indicated by Micro Raman measurements on various irradiated spots.

4.2.2 DLC system

Thin films of polycrystalline diamondlike carbon (DLC) are of great interest due to their unique physical and chemical properties. Properties like extreme hardness, optical transparency, electrical resistivity, and chemical inertness make DLC films attractive as antireflection coatings for windows and optical components and as coatings for the reduction of wear and corrosion. These films are generally deposited from the decomposition of hydrocarbon gases and liquids[26]. As a consequence, they contain hydrogen in different amounts depending upon the process variables. Hydrogen may vary from a fraction of a percent in polycrystalline diamond films to about 50% in amorphous diamondlike carbon films[27]. Soft carbonised films may even have H/C ratio greater than one[28]. Further, this hydrogen may be bonded in sp , sp^2 or sp^3 configurations or it may be trapped in the samples in molecular form. It is, therefore, important to understand how the hydrogen incorpora-

tion, the film microstructure, and its optoelectronic properties are linked together. Post growth modification of the film properties by heat treatment and/or by energy deposition by external means can be a significant step in this direction. As a matter of fact, the possibility to modify the films in a controlled manner by energetic ion bombardment enables the researcher to follow gradual changes that the films undergo and to correlate them. In particular, hydrogen loss is observed to be a dominant phenomenon from DLC films during both thermal annealing[29, 30] and ion irradiation of various species over a wide energy range[31, 32]. Respective changes in C-C and C-H bonds have been characterized by Raman and IR spectroscopic measurements, respectively[33–36].

Moreover, hydrogen seems to control not only the sp^2 or sp^3 C ratio, but also the morphology of the deposit, which in turn determines most of the properties of these films[37]. It is now emerging that most of the plasma deposited DLC films consist of a mixture of strongly cross linked tetrahedrally bonded sp^3 C and three fold coordinated sp^2 C. Covalently bonded carbon atoms (sp^3 hybrids) constitute a three dimensional network leading to high hardness ta -C:H films (diamondlike properties). On the other hand, graphitic clusters (sp^2 hybrids) embedded in the network influence the electrical and optical properties of these films. Therefore, the measurement of absolute hydrogen content and the nature of its bonding in DLC films before and after their modification is expected to provide a feed back to modify suitably the process parameters. Although few reports exist on thermal and ion induced hydrogen depletion from DLC films as measured by ERDA[31, 32, 36, 38–43], systematic effort has not yet been put to understand the H-loss behaviour from a wide range of hydrogen containing DLC films and its correlation with the film microstructures.

This section describes He^+ ion irradiation induced H-depletion from a variety of hydrogen containing films having clearly distinguishable microstructural features. Corresponding physico-chemical changes occurring in some of the films were studied by FTIR and micro Raman spectroscopic measurements. Samples were also annealed in high vacuum in order to correlate the film microstructure and the growth process. For the purpose of comparison, polymeric as well as tetrahedrally bonded (ta -C:H) films were also studied.

Experimental

The DLC films were deposited on crystalline silicon substrates in a parallel plate dc glow discharge plasma reactor using pure as well as hydrogen diluted acetylene[44]. Table-4.3

Sample No.	Growth Parameters	Physical Properties
DLC 18	$p=4.0$ mbar, $T_s=250^\circ$ C, $V_b=V_f$, $C_2H_2/(C_2H_2+H_2)=1.0$	$E_g=2.2$ eV, $n=1.7$ Microhardness=soft
DLC 33/49	$p=0.6$ mbar, $T_s=375^\circ$ C, $V_b=V_f$, $C_2H_2/(C_2H_2+H_2)=1.0$	$E_g=1.8$ eV, $n=2.2$ Microhardness=1780 kgf/mm ²
DLC 40	$p=0.6$ mbar, $T_s=250^\circ$ C, $V_b=V_f$, $C_2H_2/(C_2H_2+H_2)=0.5$	$E_g=2.12$ eV, $n=2.1$ Microhardness=2100 kgf/mm ²
DLC 51	$p=0.6$ mbar, $T_s=250^\circ$ C, $V_b=-250$ V, $C_2H_2/(C_2H_2+H_2)=0.5$	$E_g=2.67$ eV, $n=2.15$ Microhardness=2420 kgf/mm ²

Table 4.3: Growth parameters and some of the physical properties of the samples on which hydrogen and microstructural analysis have been presented in this section[44].

shows the growth parameters and some physical properties of DLC films to be discussed in this section. The depth profiling of hydrogen from these films was performed by 1.5 MeV He⁺ induced ERDA. Spectra were simulated using the RUMP code. FTIR transmission measurements on selected samples were performed in the range of 400 to 4000 cm⁻¹ and micro Raman measurements were performed using a 514.5 nm Ar ion laser. For annealing experiments, the samples were heated up to 600° C at a heating rate of 20° C/min. Some of the treated samples were further heated up to 1000° C at the same heating rate. This type of thermally stimulated annealing effects are quite different from isothermal annealing at the same temperature (600° C) for extended periods[45]. Details of these set-ups have been described in Chapter 2.

Results and discussion

ERD analysis

Depth versus concentration profiles obtained for all the samples mentioned in *Table-4.3* have been presented in **Fig.4.11**. It is to be mentioned here that since most of the DLC films for e.g., DLC 33/DLC 49 and DLC 40 have hydrogen concentrations in the range of ~8-13 at.%, results of only one system, namely DLC 33 will be discussed below in detail as

a representative one. In addition, H-depletion from two more films, viz. DLC 18 and DLC 51 are described since they possess different microstructures (polymeric/*ta*-C:H).

ERDA spectra measured on DLC 33 are presented in **Fig.4.12**. The two hydrogen recoil spectra shown here are recorded for the fluences of 8.9×10^{14} and 6.2×10^{15} He^+/cm^2 , respectively at a target current of 2 nA over a sample area of 0.035 cm^2 . The recoiled hydrogen yield is normalized for an integrated He^+ charge of $1 \mu\text{C}$ and a solid angle of 1 msr for direct comparison of different ERDA spectra obtained from the same sample. Solid lines in **Fig.4.12** correspond to the simulated spectra and the surface position of hydrogen has been indicated by the arrow. Hydrogen depletion from the film is evident after continued He^+ bombardment which is followed by the growth of a surface hydrogen peak. The effect of He^+ ion fluence on the bulk hydrogen content has been demonstrated in the inset of **Fig.4.12**. Errors on the hydrogen concentration values are estimated to be $\sim 20\%$ for the spectra collected at low ion fluences, while the error is $\sim 10\%$ for higher fluences. These results were reproduced at different spots on the same sample using higher target currents up to 6 nA (not shown). Therefore, the enhanced concentration of hydrogen in the near-surface region of the film (up to a depth of 900 \AA), as compared to the bulk, is not an experimental artefact but is a reminiscence of the film growth. In fact, non-uniform depth profiles have been observed earlier also[36]. However, Boutard *et al.*[46] had found no measurable depletion of hydrogen from hard carbonized films under 2.6 MeV He^+ bombardment up to a dose of 2×10^{16} ions/ cm^2 . This indicates that hydrogen depth profiles are dependent on microstructure of the films and their thermal history.

To probe this dependence, ERDA experiments were carried out on several samples of known physical properties. **Figs.4.13** and **4.14** show the ERDA spectra obtained from two samples, DLC 51 and DLC 18, respectively. Significant changes are observed in the ion fluence dependence of hydrogen depth distributions obtained from the two films. In particular, DLC 51 shows a uniform hydrogen depth profile, which is typical of a compact film having a low hydrogen content. On the other hand, DLC 18 shows a larger hydrogen content towards the surface as compared to the bulk. In addition, with increasing ion fluence a surface hydrogen peak develops which is absent in case of the hard films. Results of ion fluence dependence on bulk hydrogen content have been presented in **Fig.4.15**. H-depletion data for DLC 40 is also included in the figure for comparison. A steep decrease in the bulk hydrogen content is observed from soft polymeric films like DLC 18.

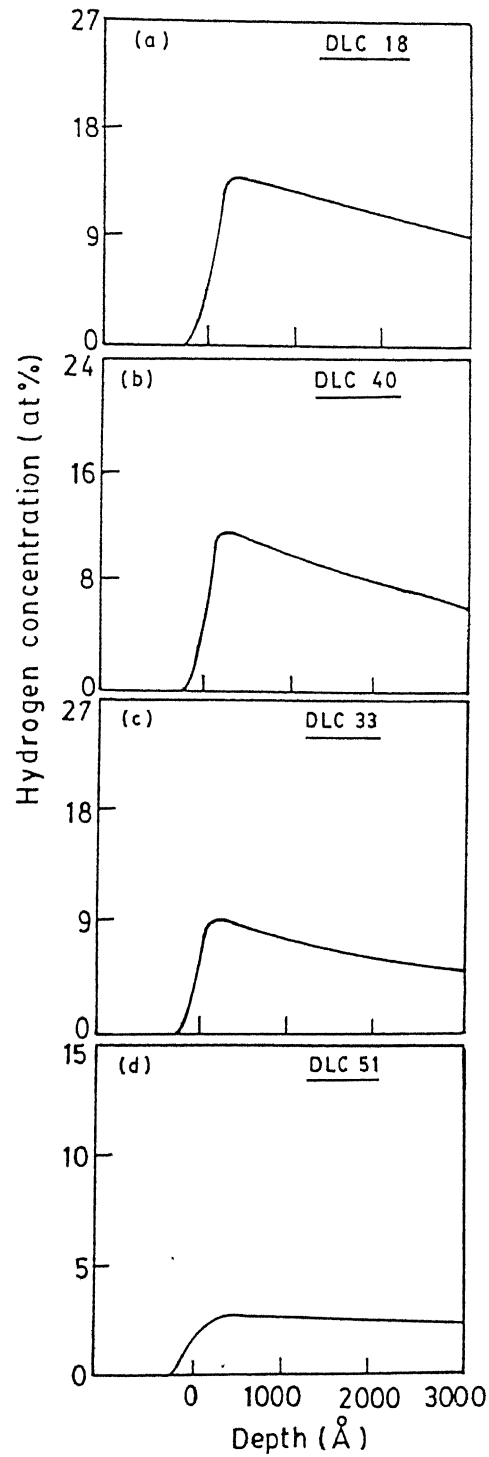


Figure 4.11: ERDA depth versus concentration profiles for various DLC samples studied in this work. All the spectra correspond to an integrated He^+ charge of $5 \mu\text{C}$.

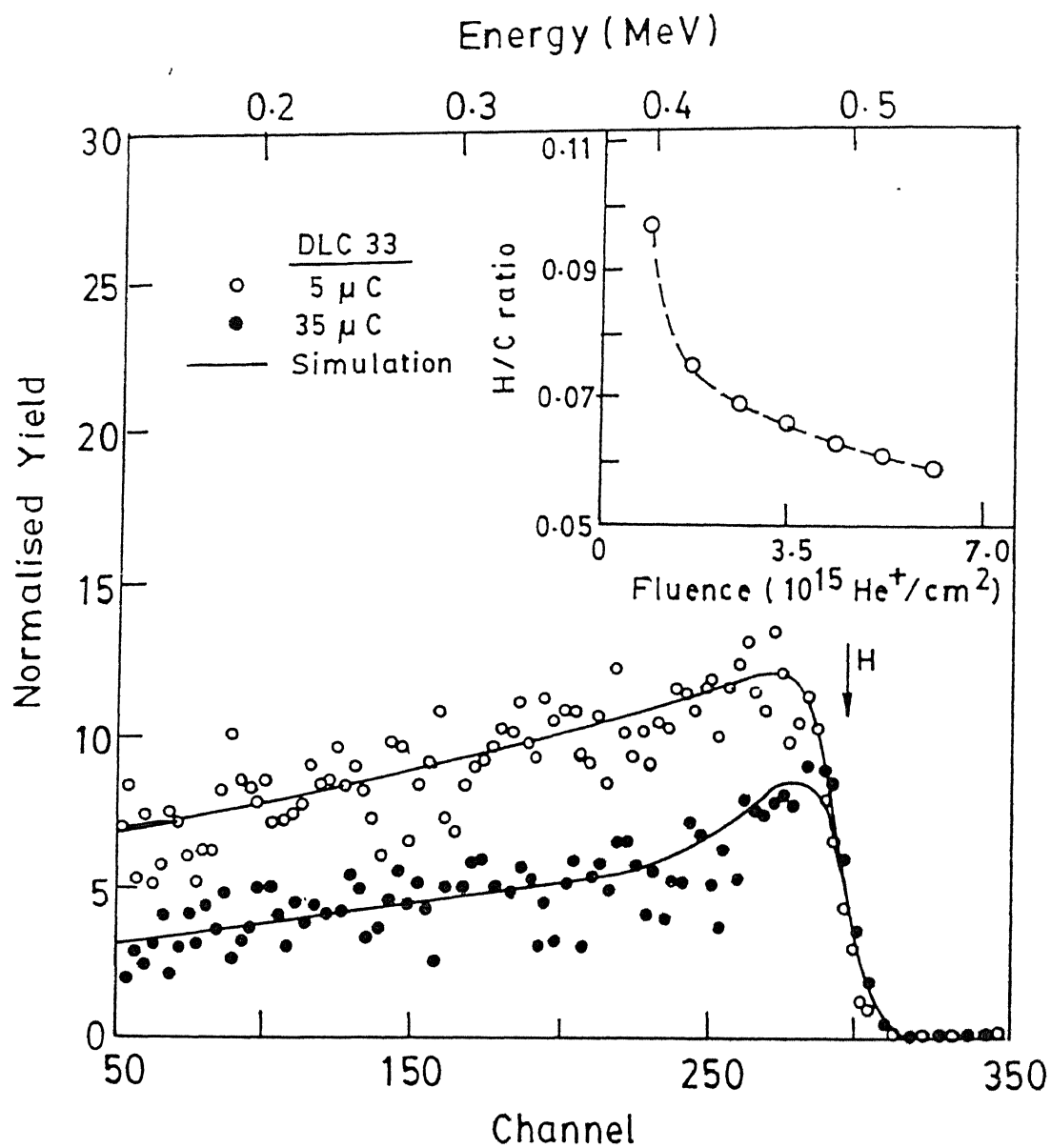


Figure 4.12: ERDA spectra obtained from DLC 33: (o) $8.9 \times 10^{14} \text{ He}^+/\text{cm}^2$, (•) $6.2 \times 10^{15} \text{ He}^+/\text{cm}^2$, (—) simulated spectra.

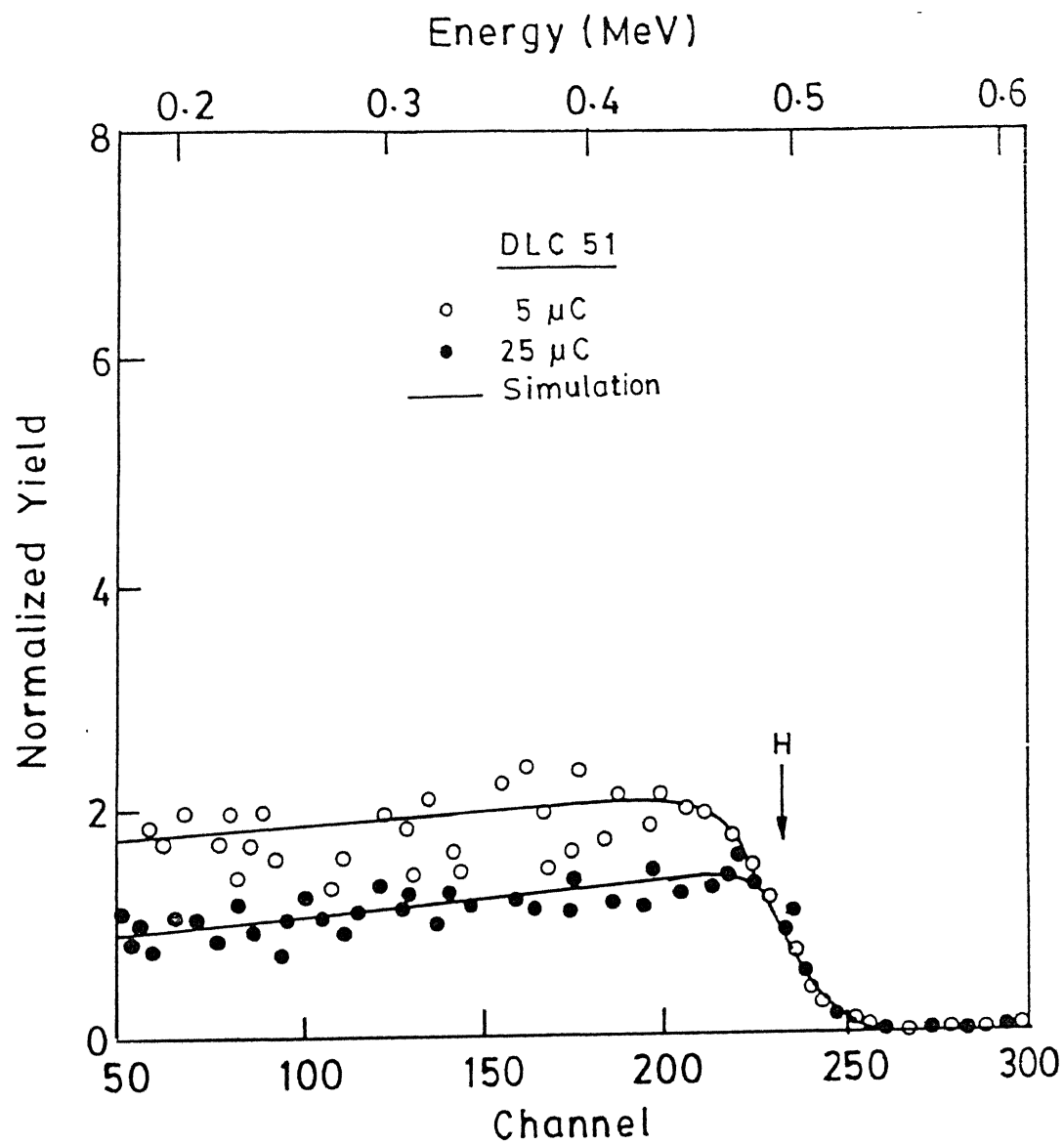


Figure 4.13: ERDA spectra obtained from DLC 51: (o) $1.8 \times 10^{14} \text{ He}^+/\text{cm}^2$, (•) $4.4 \times 10^{15} \text{ He}^+/\text{cm}^2$, (—) simulated spectra.

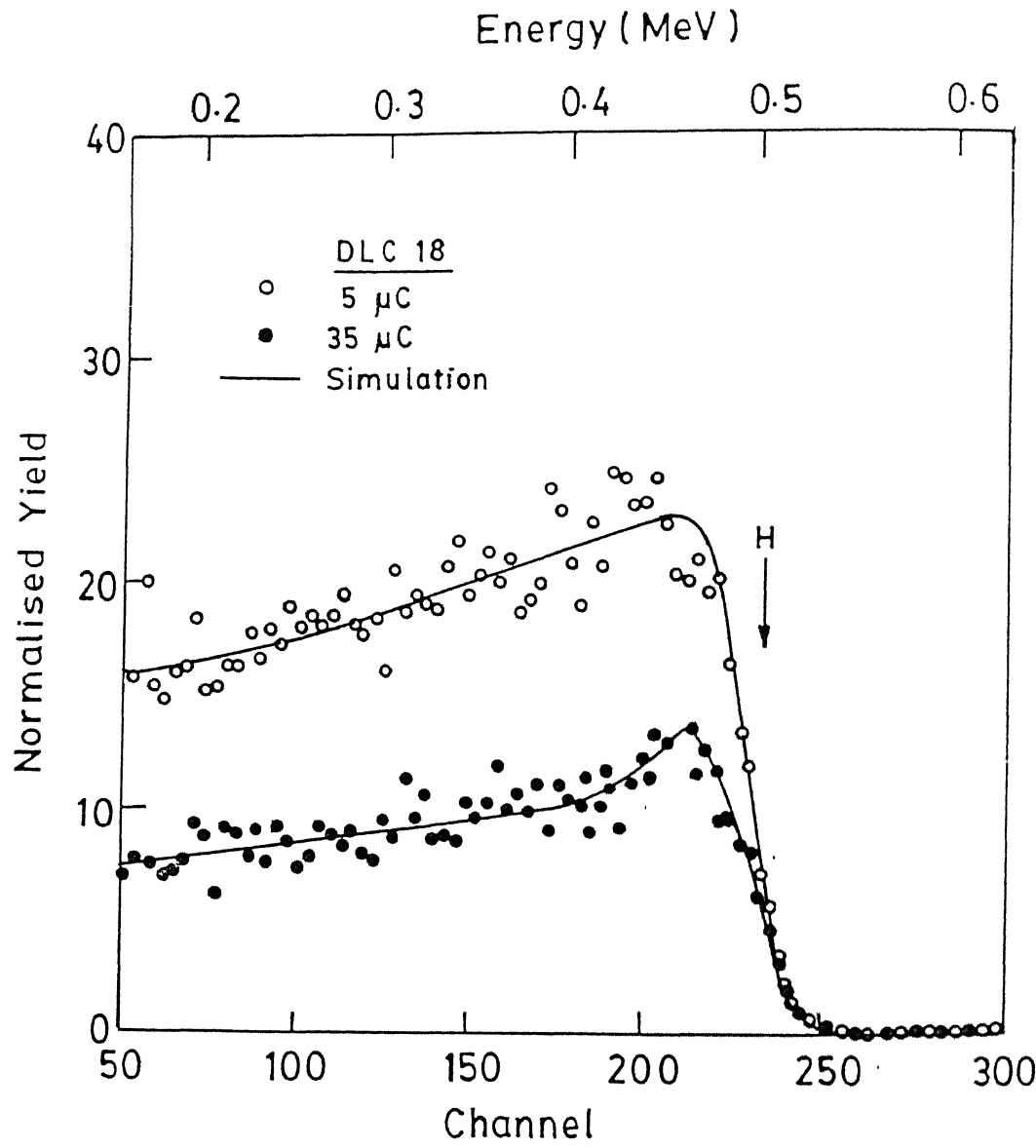


Figure 4.14: ERDA spectra obtained from DLC 18: (o) $1.8 \times 10^{14} \text{ He}^+/\text{cm}^2$, (•) $6.2 \times 10^{15} \text{ He}^+/\text{cm}^2$, (—) simulated spectra.

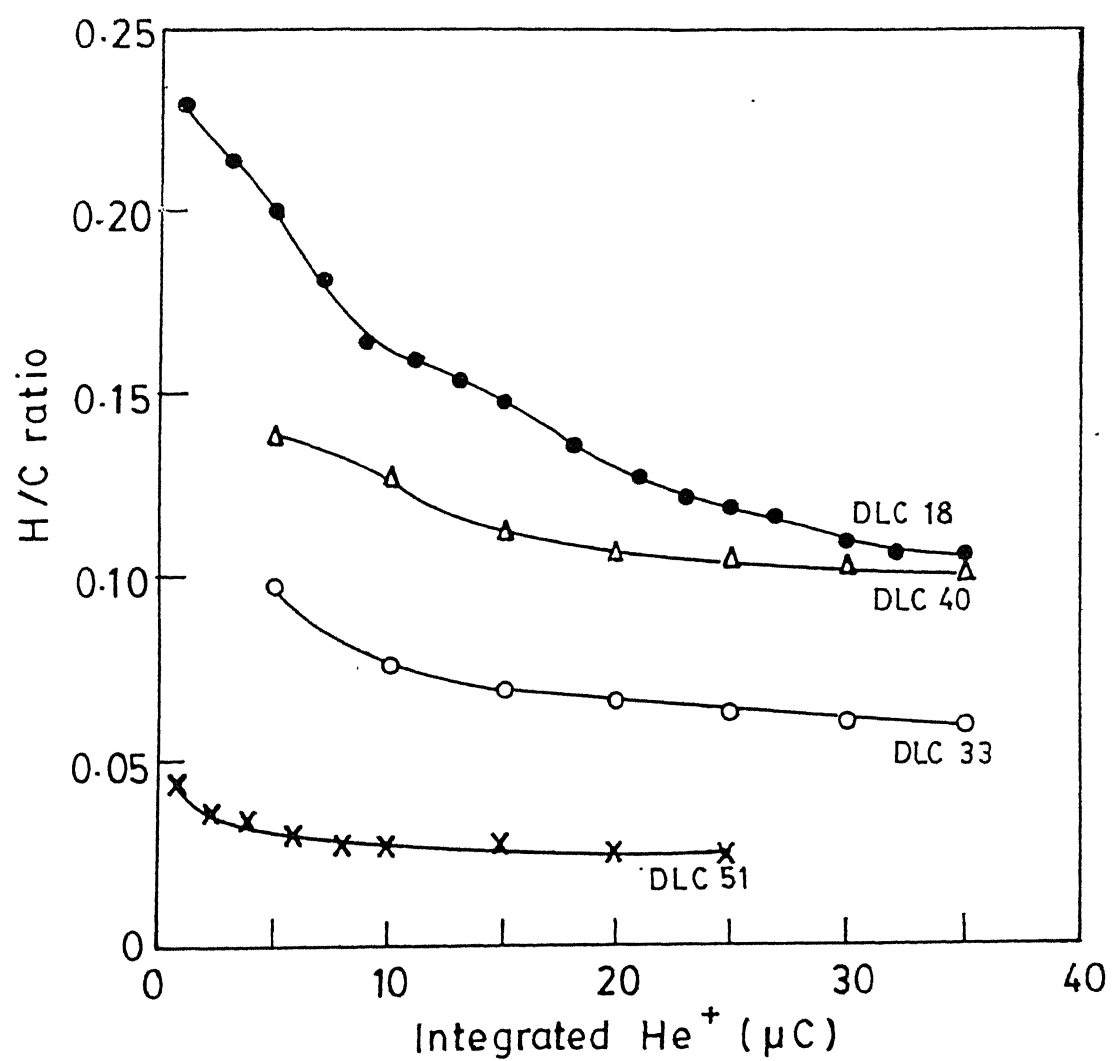


Figure 4.15: Dependence of bulk hydrogen content on analyzing ion fluence for various DLC samples studied in this work. Solid lines are guide to the eye.

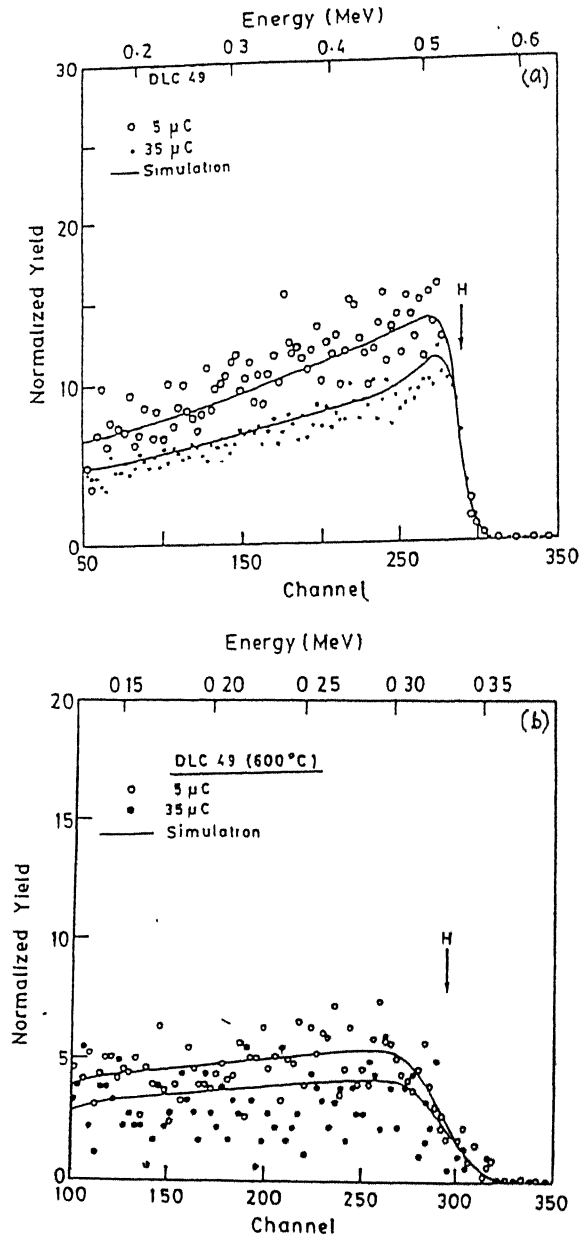


Figure 4.16: ERDA spectra obtained from DLC 49: (a) as deposited film: (o) $1.8 \times 10^{14} \text{ He}^+/\text{cm}^2$, (\bullet) $6.2 \times 10^{15} \text{ He}^+/\text{cm}^2$, (—) simulated spectra; (b) annealed film (600°C): (o) $1.8 \times 10^{14} \text{ He}^+/\text{cm}^2$, (\bullet) $6.2 \times 10^{15} \text{ He}^+/\text{cm}^2$, (—) simulated spectra.

In order to find out the correlation between film microstructure and the growth process, a few selected samples were thermally annealed. **Fig.4.16** compares the H recoil spectra obtained from DLC 49 before and after annealing at 600° C. It has been observed that hydrogen loss from the as deposited film is quite significant (~40%) due to prolonged irradiation. Simultaneously, a prominent surface hydrogen peak develops as a function of ion fluence. In contrast, no such surface peak is seen in case of the film annealed at 600° C. After reheating the sample up to 1000° C hydrogen is observed (spectrum not shown) to accumulate over a shallow region of 400 Å with a very small amount below this depth. This result is indicative of the possible decomposition of the film. A systematic study to understand this process could not be performed due to non-availability of similar type of films.

Infrared spectroscopy

IR spectroscopy was used to obtain information about the nature of hydrogen bonding and concentration in the films. **Fig.4.17** shows the IR transmission spectra in the range of 400-4000 cm^{-1} measured on three samples, viz. DLC 18, DLC 33, and DLC 51. Detailed analyses, as provided in *Table-4.4*, reveal that DLC 18 is a soft polymeric film, while the DLC 51 is a hard one of *ta*-C:H in nature.

Actually, the range between 2800-3100 cm^{-1} is of particular interest as this corresponds to the stretching vibrational modes of CH_x complexes[35]. **Fig.4.18** shows the FTIR spectra obtained from DLC 18 before and after He^+ ion irradiation corresponding to a dose of 6.2×10^{15} ions/ cm^2 . In case of the irradiated spot, peak positions centred around 2875, 2941, 2975, and 3011 cm^{-1} correspond to sp^3 CH_3 , sp^2 CH_2 , sp^3 CH_3 , and sp^2 CH bonds, respectively. It is observed that the intensities of the peak decrease slightly. This indicates that irradiation leads to decrease in the population of both sp^2 C-H bonds and sp^3 C-H bonds; although compared to the sp^3 C-H bonds, the decrease in the rate of sp^2 C-H bonds is less. Similar trend was observed in case of IR analyses performed on the irradiated spots from some other samples. It is seen that He^+ bombardment significantly modifies the structure of the films.

The IR spectra collected from DLC 49 before and after annealing at 600° C are presented in **Fig.4.19**. In case of the as deposited film, there are four absorption peaks centred around 2868, 2923, 2954, and 2966 cm^{-1} . These peaks are actually the absorption peaks of sp^3 CH_3 ,

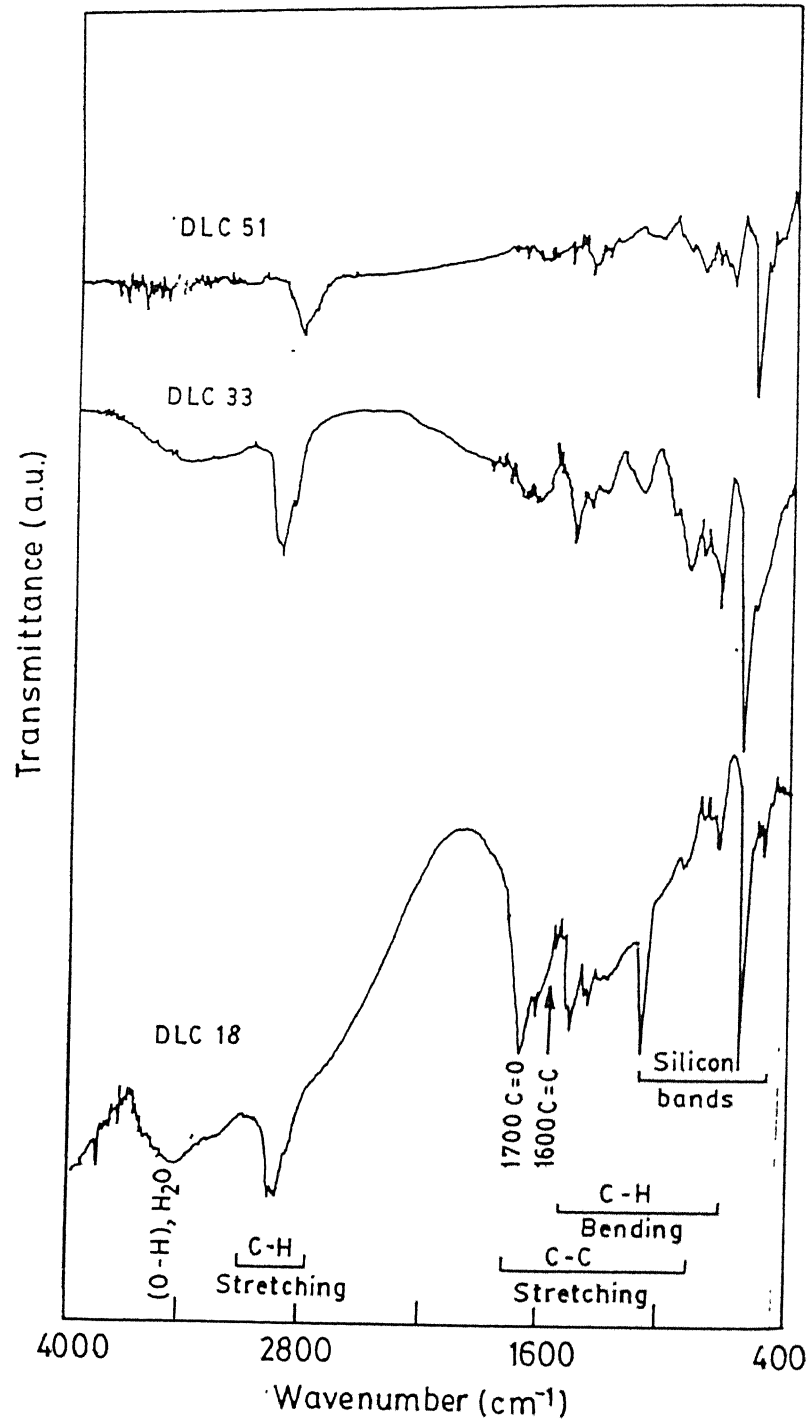


Figure 4.17: IR transmission spectra for three different DLC films, viz DLC 18, DLC 33 and DLC 51.

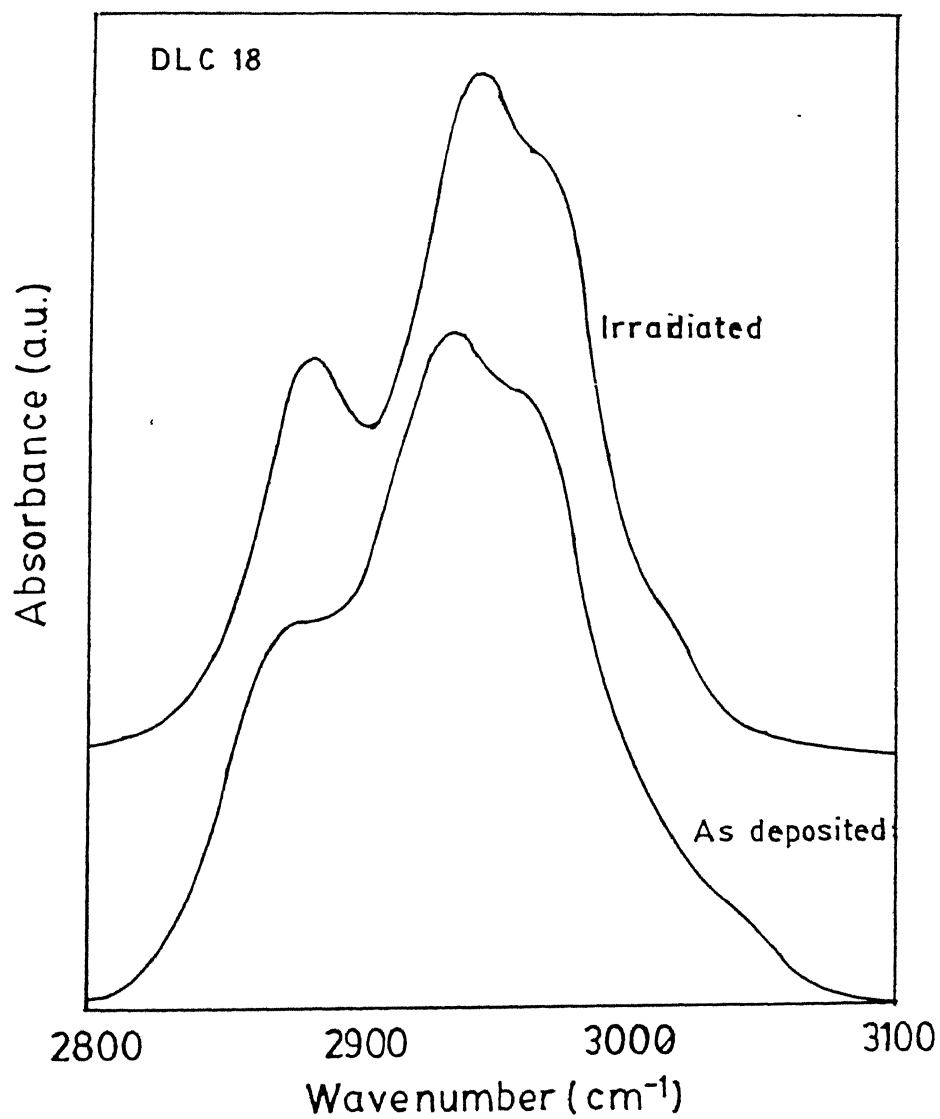


Figure 4.18: FTIR spectra obtained from DLC 18 before and after He⁺ irradiation corresponding to an ion fluence of 6.2×10^{15} ions/cm².

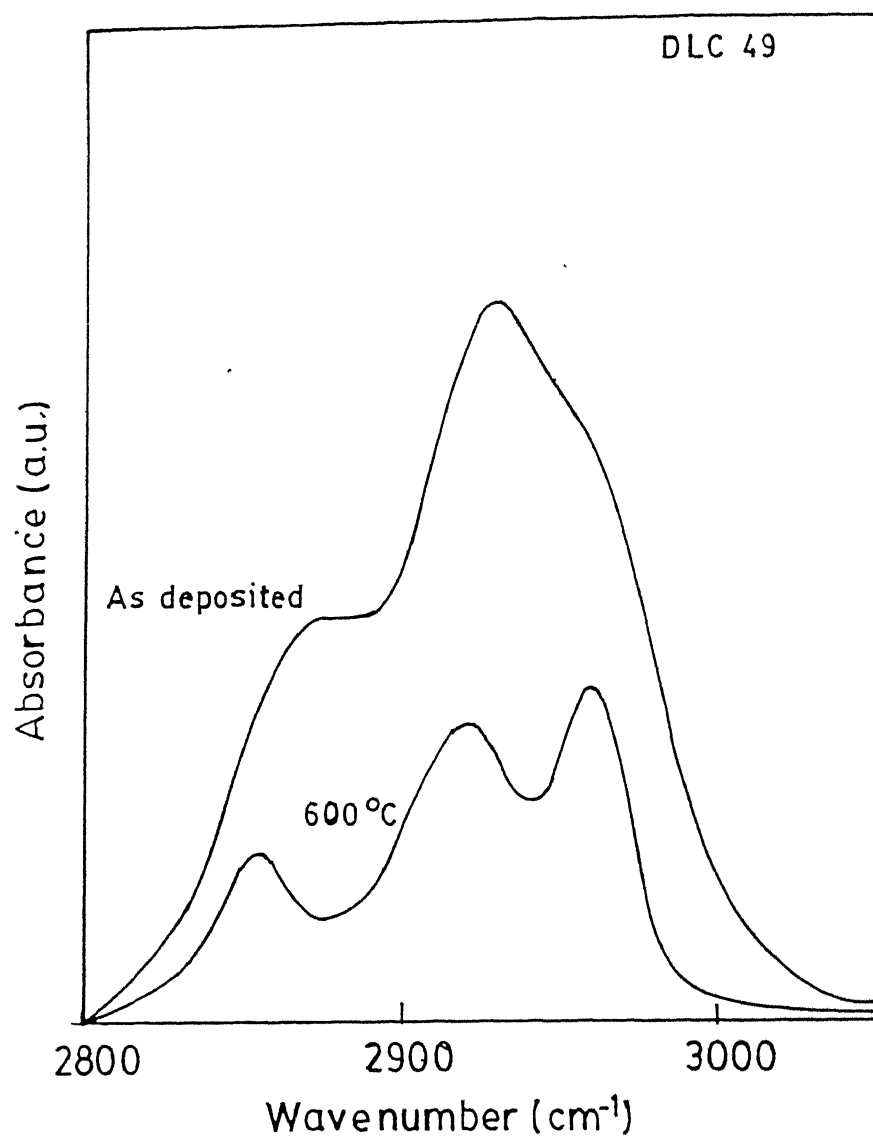


Figure 4.19: FTIR spectra obtained from DLC 49 before and after annealing at 600° C.

sp^3 CH₂, sp^2 CH₂, and sp^3 CH₃ bonds, respectively. On the other hand, deconvoluting the 600° C annealed spectrum, three prominent peaks were observed at 2853 cm⁻¹ (sp^3 CH₂), 2920 cm⁻¹ (sp^3 CH₂) and at 2961 cm⁻¹ (sp^3 CH₃). Reduction in hydrogen content is clear from decrease in area under the stretching vibration modes. Further, analysis shows that fraction of sp^2 hybridized C-C bonds increases from 0.27 to 0.66, while the fraction corresponding to sp^3 hybridization decreases from 0.54 to 0.28. The very fact that after annealing sp^3 CH₃ bonds decrease, while sp^2 CH₂ bonds increase is indicative of the presence of the methyl (CH₃) group in the as deposited film and its evolution with increasing temperature. In contrast, samples heated up to 1000° C did not show any vibrational modes due to hydrogen although a new absorption band at 3050 cm⁻¹ is observed due to aromatic ring groups consisting of three fold sp^2 bonded carbon.

Thermal effusion measurements

Fig.4.20 shows the thermal effusion spectra obtained from the same sample (DLC 49) during two separate heating cycles up to 1000° C. Figs.4.20(a) and (b) show the evolution of H₂ and CH₃ species during the two heating cycles. Absence of CH₃ and H₂ contributions below 600° C during reheating of the sample reveal that the effusion of these species are site dependent. Once these sites are exhausted and the film undergoes a structural transformation during the first annealing cycle, the above mentioned species do not reappear. This result is strong evidence that the methyl radicals in the effusion spectra is related to their presence in as deposited samples during growth itself. However, effusion spectra above 800° C is dominated by the decomposition of of this rather thin sample (~0.4 μm).

Micro Raman analysis

To investigate the He⁺ ion-beam induced structural changes taking place in the samples, micro Raman measurements were performed on selected DLC samples. Micro Raman is a very useful technique for characterizing C-C bonds in DLC films. It is known that[33] the Raman spectrum of small polycrystalline graphite (basal plane dimension ≤20 nm) exhibits a peak at about 1355 cm⁻¹ (peak *D*) and the large single-crystal graphite shows a peak at about 1580 cm⁻¹ (peak *G*). The Raman spectra of DLC films are composed of *D* and *G* peaks, but compared with those of small polycrystalline graphite and large single-crystalline graphite, both peaks are always broad and down-shifted to the low frequency

DLC 51	DLC 33	DLC 18	Assignment	Bonding
-	-	3400	3300-3500	O-H-O
-	3020	3023	3025	sp^2 CH ₂ (olef.)
3003	3000	3004	3000	sp^2 CH(olef.)
2960	2952	2961,2974	2970	sp^2 CH ₃ (asym.)
2936	2939	2951,2938	2945	sp^2 CH ₂ (arom.)
-	-	2938	2930	sp^3 CH ₃ (asym.)
2924,2921	-	2921	2925	sp^3 CH ₂ / sp^3 CH
2910	-	-	2915	sp^3 CH(asym.)
-	2868	2879	2870	sp^3 CH ₃ (sym.)
2851	-	-	2850	sp^3 CH ₂ (sym.)
-	1706	1700	1715	C=O
-	-	1600	1600	sp^2 C=C(olef.)
-	-	-	1580	sp^2 C=C(arom.)
-	1480	1480	1490	sp^2 CH ₃ (olef.)
-	1452	1450	1450	sp^3 CH ₃ / sp^2 CH ₂ (olef.)
1445	-	1440	1440	sp^3 CH ₂ (olef.)
1430	-	-	1435	sp^2 CH(arom.)
1370	1376	1380	1370	sp^3 CH
			1380	sp^3 CH ₃ (olef.)
-	1295	1280	1270	mixed sp^2/sp^3 C-C
			1280	sp^2 CH(olef.)
1110	1117	1100	1110	sp^2 CH ₂ (olef.)
970	978	975	970	sp^2 C-C(olef.)
895	888	885	885	sp^3 C-C
840			840	sp^2 C=C(arom.) & sp^3 C-H(olef.)
745	740	745	755	sp^2 C-H(arom.)
620	610	620	630	Si-H (wag)

Table 4.4: Observed infrared bands (in cm⁻¹) and their assignments (in cm⁻¹) for DLC 51, DLC 33, and DLC 18 films.

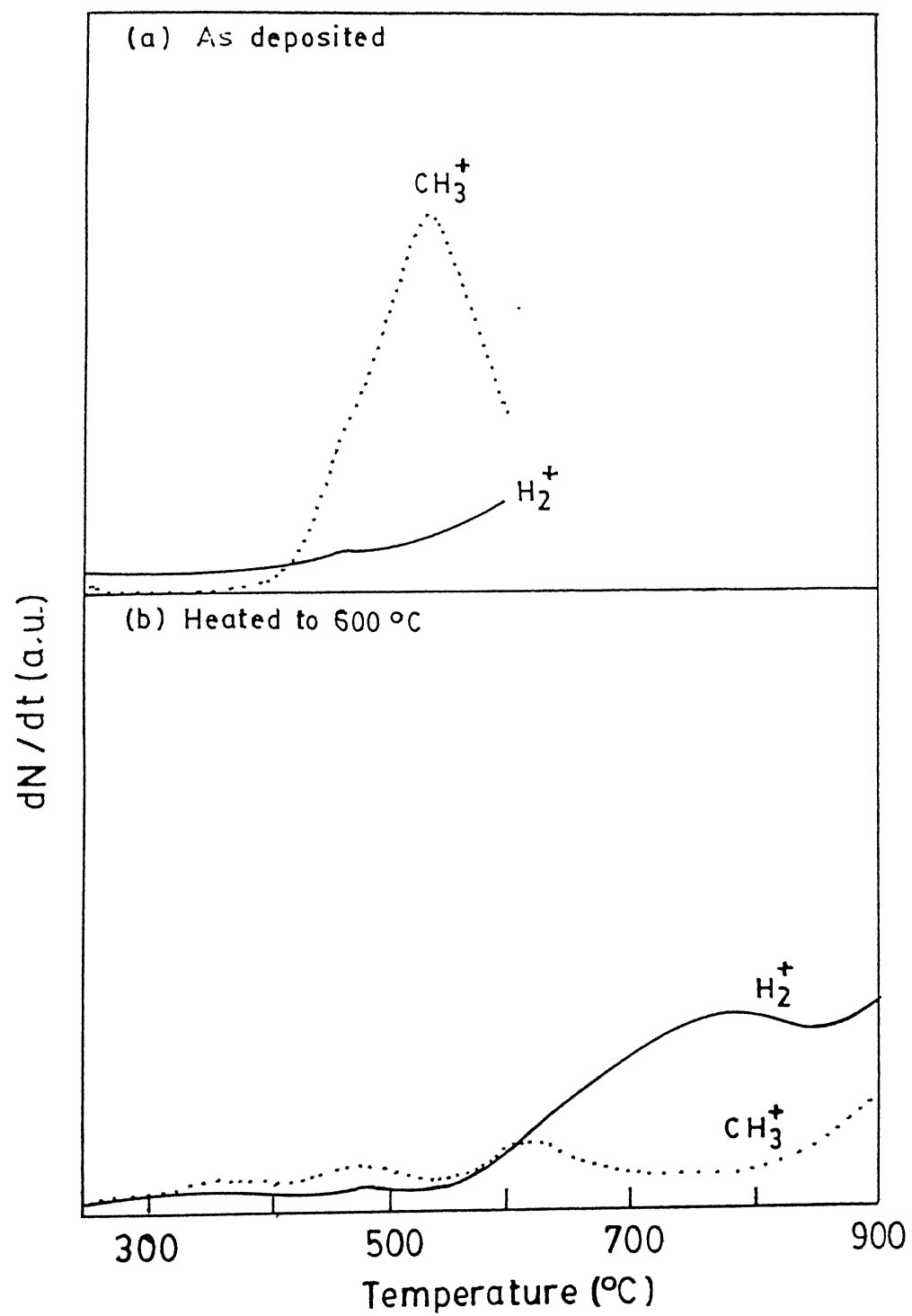


Figure 4.20: Thermal effusion spectra obtained from DLC 49: (a) 600 $^{\circ}$ C, (b) 1000 $^{\circ}$ C.

Sample	$\nu_D(\text{cm}^{-1})$	$\Delta\nu_D(\text{cm}^{-1})$	$\nu_G(\text{cm}^{-1})$	$\Delta\nu_G(\text{cm}^{-1})$	I_D/I_G
As deposited	1372	264	1583	183	0.45
Irradiated	1371	252	1590	87	0.82

Table 4.5: Results of micro Raman analysis obtained from a film DLC 33.

Annealing Temp.(°C)	$\nu_D(\text{cm}^{-1})$	$\Delta\nu_D(\text{cm}^{-1})$	$\nu_G(\text{cm}^{-1})$	$\Delta\nu_G(\text{cm}^{-1})$	I_D/I_G
600	1373	201	1605	113	0.74
1000	1372	197	1604	98	0.92

Table 4.6: Results of micro Raman analysis obtained from annealing of the sample DLC 49.

edge, which implies the presence of bond-angle disorder and the presence of some sp^3 C-C bonds[33]. **Fig.4.21** shows the micro Raman spectra recorded from DLC 33 before and after He^+ irradiation. The peak positions, full width at half maxima (FWHM) and diamond-to-graphitic-line intensity ratio (I_D/I_G) after a computer line shape analyses of these spectra are given in *Table-4.5*.

It can be seen that there is an upward shift in the G peak position and an increase in the (I_D/I_G) ratio takes place after irradiation. These two things indicate that graphitization of the film has occurred for an He^+ irradiation dose of 6.2×10^{15} ions/ cm^2 . Raman studies on several DLC films also showed similar trend. Irradiation induced decrease in the FWHM for the D (from 264 cm^{-1} to 256 cm^{-1}) and G lines (from 183 cm^{-1} to 87 cm^{-1}) is consistent with the removal of the bond-angle disorder and the increasing dominance of crystallites[33].

Raman spectra recorded on the 600°C and 1000°C heated sample (DLC 49) are shown in **Fig.4.22**. Two well resolved peaks are observed in both the spectra. The peak positions, their FWHMs, and the I_D/I_G ratios in these cases are provided in *Table-4.6*.

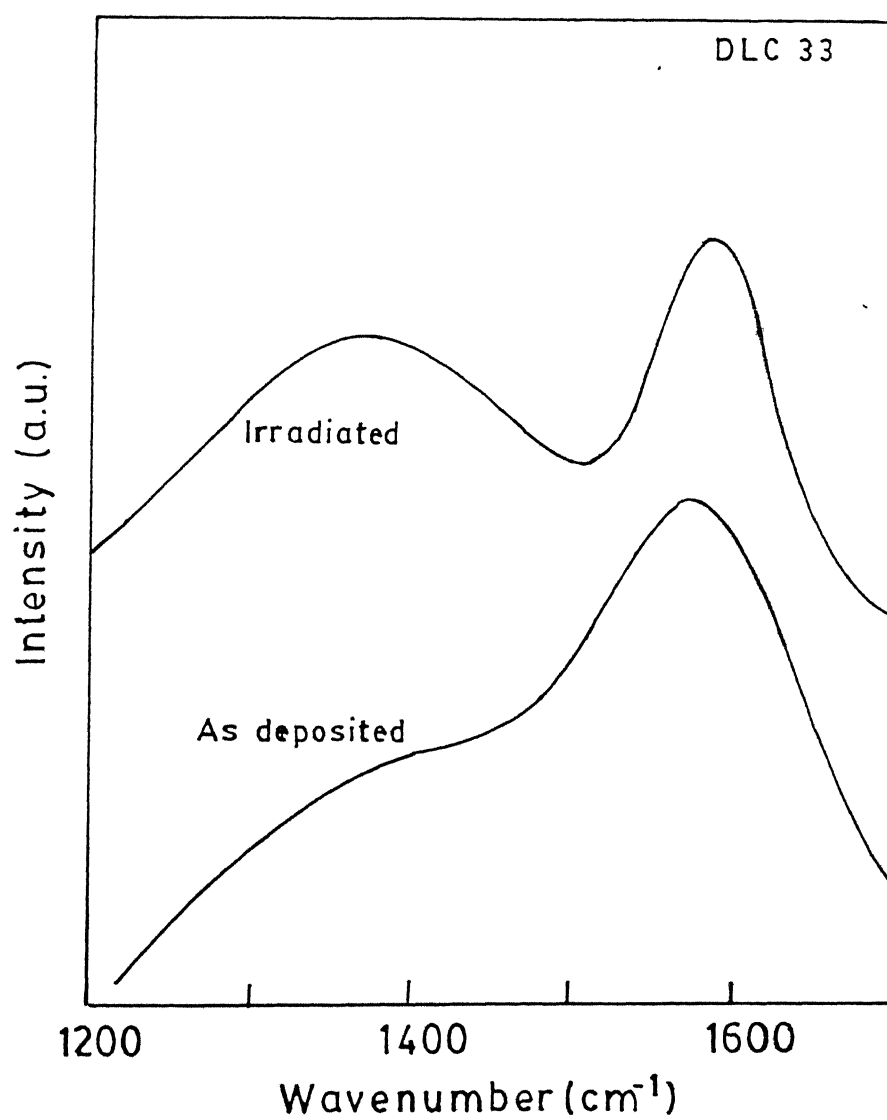


Figure 4.21: Micro Raman spectra recorded from DLC 33 before and after He⁺ irradiation corresponding to an ion fluence of 6.2×10^{15} ions/cm².

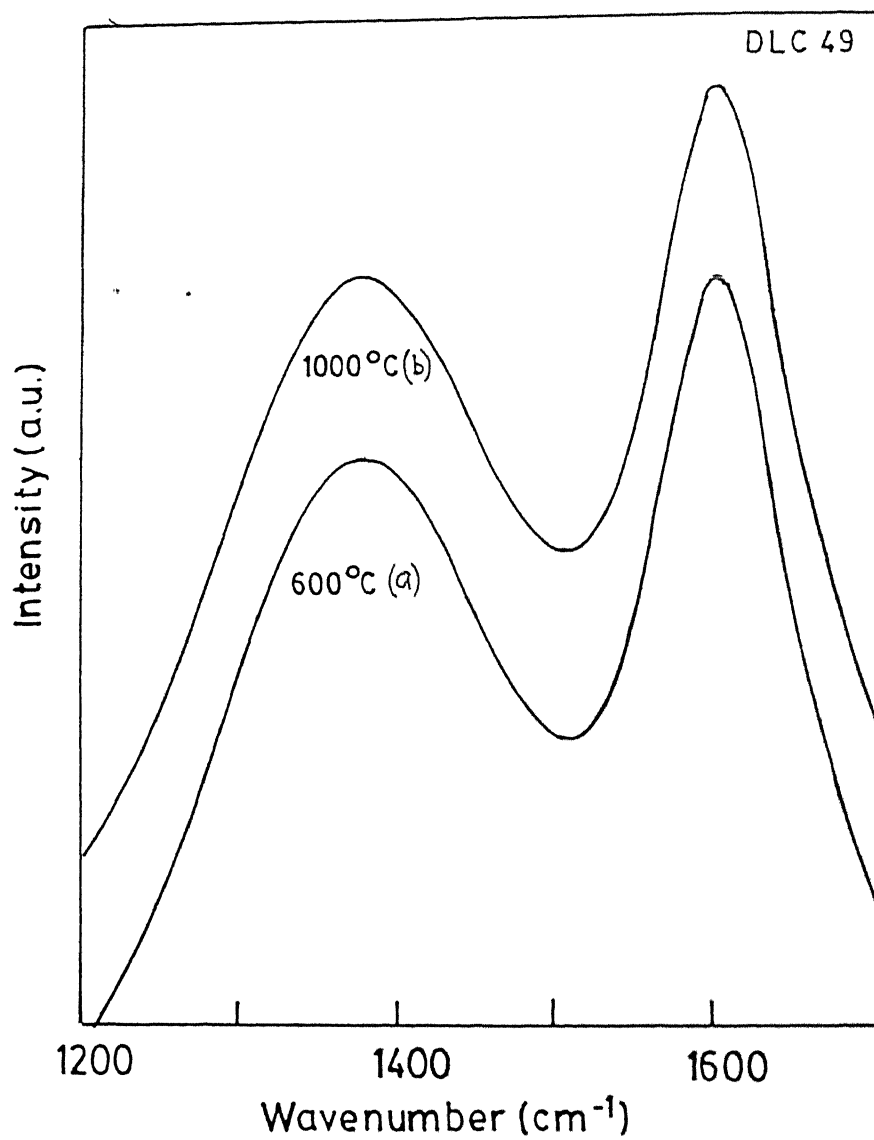


Figure 4.22: Micro Raman spectra recorded from DLC 49 after annealing at: (a) 600° C and (b) 1000° C.

Thus, upshift in the two peak positions (as compared to the literature reported values of D and G peaks), an increase in I_D/I_G , and a narrowing of G peak are observed after heating in vacuum. The upshift in the two peak positions towards the high frequency side indicates that the crystallites are dominated by sp^2 bonded C rather than sp^3 C bonds. The decrease in the FWHM of the G peak from $\sim 180 \text{ cm}^{-1}$ (spectrum not shown) in as deposited case to 113 cm^{-1} (600° C) to 98 cm^{-1} (1000° C) in the sample due to heating clearly indicates the removal of bond angle disorder and the dominance of graphite like crystallites. Further, the increase in I_D/I_G ratio suggests the growth in number or size of crystallites.

Combining ERDA results with that of IR spectroscopy, micro Raman, and thermal effusion data, comments can be made on the process of film growth itself. It appears that due to the plasma conditions leading to hard and dense films, a thin near-surface transitional layer (NSTL) is formed. In this NSTL, film growth precursors arrive and C is incorporated in the film, while H is removed. The growth region below this layer normally stabilizes and results in the uniform distribution of hydrogen. On the contrary, the process of H removal and C incorporation is inefficient in the plasma conditions leading to soft polymeric films where thickness of NSTL is rather large. Two extreme cases are expected. First is the growth of diamond films, where NSTL should be of the order of a monolayer. This indeed seems to be the case as high resolution ERDA result shows a sharp surface hydrogen peak in the microwave plasma deposited diamond films[47]. Other possibility is that of intermediate and high hydrogen containing films where practically no stabilized zone occurs and NSTL is of the order of film thickness. Higher hydrogen content and primary bonding in the form of CH_3 and CH_2 groups (indicated by IR analysis) are responsible for thermal effusion of hydrocarbons and high thermal erosion of material (amount of hydrocarbon evolved).

ERDA studies on such films show large nonuniformity in the hydrogen depth profiles (hydrogen rich at the surface). Also, this can be the possible reason for observing the growth of a surface peak in the near-surface region of several DLC films, viz. DLC 18, DLC 33/49, and DLC 40 during ERD analysis as mentioned below. In case of He^+ ion irradiation, the energy transfer from the bombarding ions leads to the removal of hydrogen resulting the sp^3 carbon configuration to become unstable and to break down into the C-C double bond sp^2 configuration. As the hydrogen removal continues, this configuration also becomes unstable and breaks into the sp^1 configuration (C-C triple bond). This in turn breaks finally into the sp^2 aromatic configuration[32]. Further, Micro Raman measurements also shows ion induced

decrease in the bond-angle disorder and a population increase in the sp^2 C-C bonds thus confirming the structural transformation. As a result of such ion-induced bond-breaking, lot of traps are created in the material. Consequently, atomic hydrogen that moves towards the surface during ion bombardment get trapped giving rise to the growth of a near-surface peak.

In case of DLC 49, significant loss of hydrogen and the growth of a surface hydrogen peak during ERDA was observed due to He^+ ion bombardment. Post irradiation annealing reveals that CH_3 and H_2 are the main effusing species during the heating cycle up to $1000^\circ C$. IR and Raman measurements also confirm the enhancement in sp^2 bonded C signals. Post annealing ERDA measurement shows no surface hydrogen peak. Hydrogen loss becomes negligible in this case and also the hydrogen profile becomes uniform which is more like a hard film having a compact microstructure (viz. DLC 51). Thus, the above argument in favour of the formation of NSTL during film growth is further fortified by these experiments

Conclusions

Four different type of DLC samples have been studied in this work which were prepared under different conditions and were having different hydrogen contents. These samples include very soft (polymeric) to very hard (tetrahedral symmetry) films having completely different microstructures. All these samples show hydrogen depletion while studied by ERDA technique for the determination of hydrogen depth versus concentration profiles. Subsequent physico-chemical changes occurring in these films were studied by FTIR and micro Raman spectroscopies. The infrared results indicate that the films get rich in sp^2 CH_2 bonds as sp^3 CH_3 bonds decrease followed by hydrogen depletion due to energetic ion bombardment. Micro Raman studies also indicate ion induced removal of bond-angle disorder and increasing dominance of graphite like crystallites.

4.2.3 Phospholipid system

The emerging possibilities of developing novel biosensors for solid state electrochemistry and molecular bioelectronics applications (e.g., fabrication of immunochemically sensitive field-effect transistor) have made thin films of phospholipids important. Interfaces of lipid films with Si, Au and other inorganic substances form the basis of many electronic and

biotechnological applications[48]. These molecular assemblies are also very useful in molecular pattern recognition, actuation and information processing due to their unique structural and functional stability[48]. The lipid surfaces are ideal substrates for deposition of proteins, which are primary chemical sensors. As a specific case, thin films of cardiolipin, a highly charged anionic phospholipid, have been demonstrated to have potential applications in molecular electronics to fabricate lipid based electrical devices[49]. Usually, phospholipid films are characterized by techniques such as atomic force microscopy[50], scanning probe microscopy[51], and infra-red analysis[52]. However, for the successful development of such bioelectronic devices it is necessary to have information about their thickness, stoichiometry and their response to high vacuum and ion-beam processing.

ERDA and RBS have emerged as powerful tools for characterizing thin films of variety of materials. The potential of these techniques to characterize organic films is not fully explored[53, 54]. The main issues, concerning the applicability of ion-beam analysis techniques for characterizing organic layers, are the accuracy of the quantitative estimation of the light elements and the probable degradation of the material due to ion impact. In view of these and the fact that several commonly used characterization techniques namely, electron microscopy, secondary ion mass spectrometry employ energetic charged particles, it was felt worthwhile to explore the efficacy of ion-beam techniques, ERDA and RBS to characterize thin films of cardiolipin.

This section describes the preparation of thin films of phospholipid and its characterization by ERDA, RBS and channeling techniques. In particular, ERD and RBS techniques were employed to determine the stoichiometry and thickness of thin cardiolipin films deposited on (100) oriented *c*-Si. On the other hand, RBS-channeling technique was utilized to reduce the background signal arising from Si substrate in order to improve the sensitivity of detection of the film constituents. The changes occurring in the hydrogen content of these films during ERD analysis and the effect of ion irradiation on its structural and bonding configuration were also studied by micro Raman spectroscopy and FTIR spectroscopy, respectively.

Experimental

Diphosphatidyl glycerol (*cardiolipin*) (see Fig.4.23)[55] was isolated from bovine heart. The method of extraction is a combination of different aspects of the several published

methods[56–58] and incorporation of suitable modifications as suggested by Hallen[59]. Extracted cardiolipin was purified by column chromatography. Purity of extracted lipid was checked by a single spot on silica gel thin layer chromatography developed by a solution of chloroform, methanol, and water (65:25:4) or chloroform, methanol, and ammonia (70:30:4). Prior to film deposition, Si substrates were ultrasonically cleaned in trichloroethylene, ethyl alcohol, acetone, and distilled water. Thin films of cardiolipin were deposited by spin coating technique using a centrifuge at a speed of 10.000 r.p.m.

Since the ion-beam based measurements are carried out under high vacuum, first some preliminary measurements were performed to investigate the stability of the cardiolipin films against weight loss by evaporation under high vacuum. Weight loss measurements of the as-prepared phospholipid films kept under high vacuum for long durations revealed that the films did not evaporate in vacuum indicating very low vapour pressure of cardiolipin. These experiments clearly indicated the possibility of studying such films in high vacuum.

Thin films of cardiolipin were analyzed by RBS and ERDA, under high vacuum condition (2×10^{-6} mbar) at room temperature, using 1.23 MeV $^4\text{He}^+$ ions. For RBS-channeling experiments, a three-axes goniometer was utilized for orienting the samples in different positions with respect to the incident He^+ beam and an ion implanted semiconductor detector was kept at an angle of 150° with respect to the incident beam direction. On the other hand, for ERDA measurements, $^4\text{He}^+$ beam was allowed to impinge at an angle of 15° with respect to the sample surface and a similar detector was placed at an angle of 30° with respect to the incident beam. Various regions of the film were analyzed to study the lateral film uniformity. Several films of different thicknesses prepared under similar conditions were studied. The changes occurring in the film stoichiometry and the residual hydrogen in the films were studied as a function of the $^4\text{He}^+$ fluence up to $3.33 \times 10^{16} \text{ He}^+ \text{ ions/cm}^2$.

Results and discussion

RBS

A typical RBS spectrum obtained from a thin phospholipid film deposited on Si (100) substrate is shown in Fig.4.24(a). The arrows indicate the surface positions of C, O, P (constituents of *cardiolipin*) and Si (substrate). The simulated spectrum has been shown by the continuous curve. Fig.4.24(b) presents the RBS-channeling spectrum obtained from the same sample. Comparison shows that C, O and P signals are more clearly visible in case of

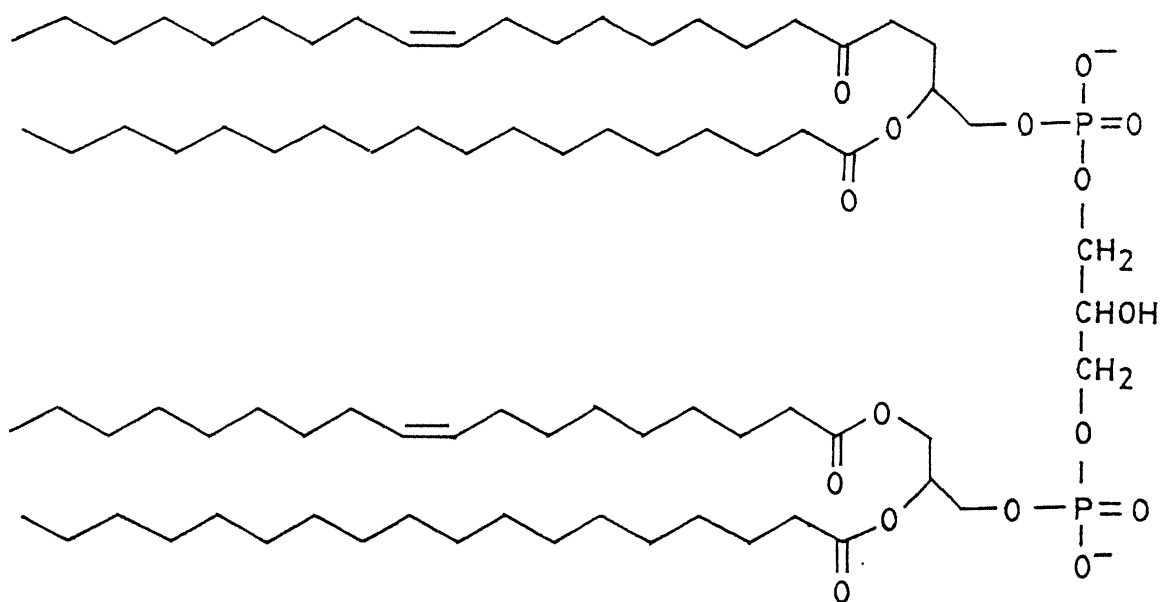


Figure 4.23: Structure of *cardiolipin*.

the aligned spectrum. The spectra have been collected for a He^+ charge of $10 \mu\text{C}$ and it has been tested that they match well with the subsequent RBS spectra collected for cumulated He^+ charge of $40 \mu\text{C}$. This indicates that the concentrations of C, O and P in *cardiolipin* films remain unaltered under He^+ ion irradiation. The density of *cardiolipin* has been determined to be 1.05 gm/cm^3 [60]. However, in the present study, the areal density, which is a natural unit of thickness in RBS analysis, has been utilized as a measure of thickness of these films. From the RBS spectrum of the *cardiolipin* films (Fig.4.24(a)), areas under C, O, and P are evaluated by subtracting the background arising due to Si substrate. On the other hand, a polynomial fitting has been done for the Si portion of the aligned spectrum which is shown as a smooth line in Fig.4.24(b). The RBS signals from C, and O ride over this smoothed line which forms the background. The area under the RBS signals of C, O, and P are then obtained by subtracting this background. The areal densities of these species are calculated from

$$(Nt)_i = A_i / Q\sigma\Omega \quad (4.1)$$

where $(Nt)_i$'s are the individual areal density of C, O, and P; A_i 's are the area under the C, O, and P peaks; Q is the amount of He^+ charge collected, σ is the scattering cross section and Ω is the solid angle subtended by the detector ($=2.57 \text{ msr}$).

A comparison of the C, O, and P contents obtained from the RUMP simulation of the random spectrum (Fig.4.24(a)) and those obtained by hand calculations using the aligned spectrum (Fig.4.24(b)) are given in Table-4.7 (accuracy $\pm 5\%$). The thickness/areal densities mentioned pertain to the RBS analyzing spot on the film and not the entire film. During the analysis, the areal densities of C, O, and P do not show any variation. In other words, no variation in the local thickness has been observed. However, RBS measurements on several different regions of the same film reveal that the lateral non-uniformity in film thickness/total areal density is about 30% over a film area of $1 \text{ cm} \times 1 \text{ cm}$. The analysis of RBS spectra obtained from different films also shows the same C:O:P ratio. It is to be noted that RBS-channeling analysis provides C, O, P contents of the films quite accurately which matches well with the nominal composition of *cardiolipin* ($\text{C}_{81}\text{O}_{17}\text{P}_2\text{H}_{152}$).

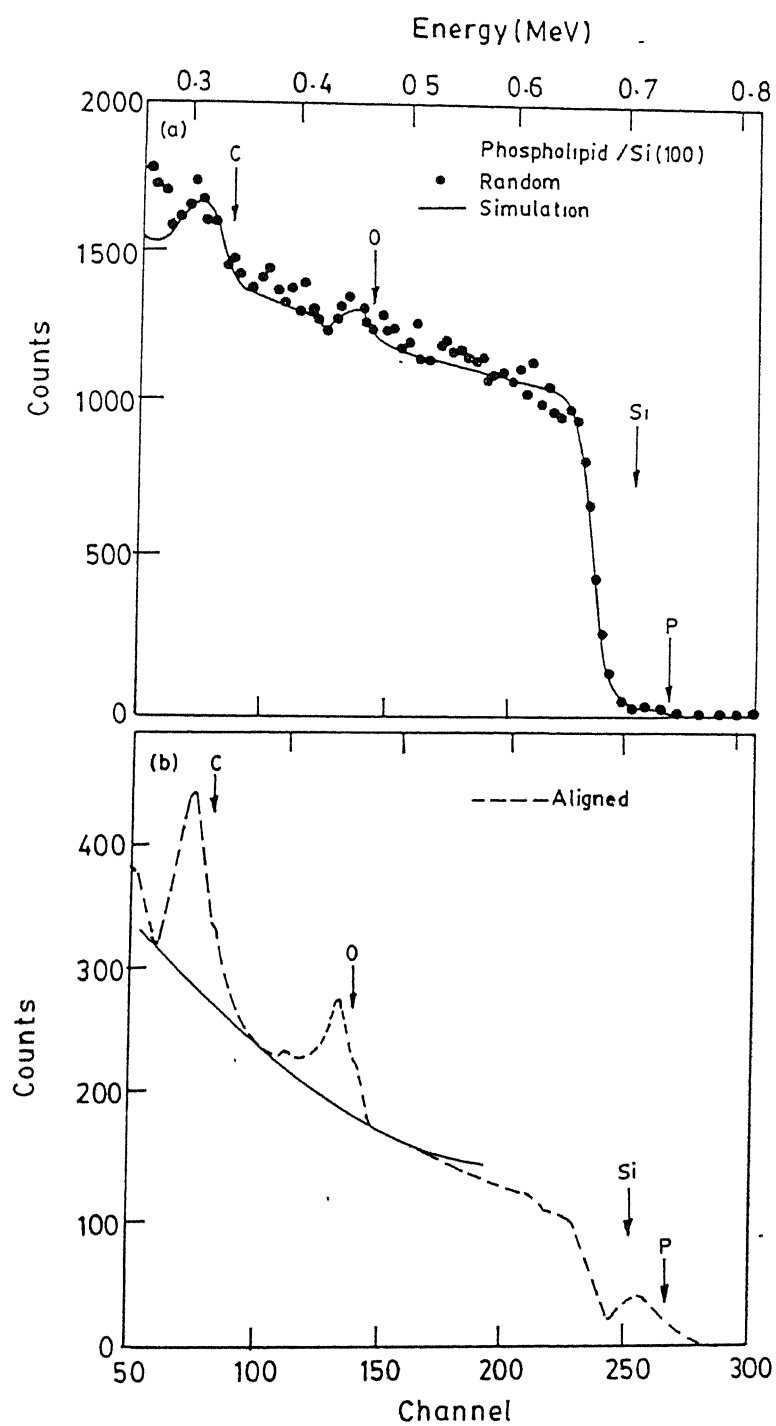


Figure 4.24: (a) Random and (b) aligned RBS spectra of a *cardiolipin* film (#TK-2), collected after He^+ cumulated charge of $40 \mu\text{C}$.

Method of evaluation	Reference Spectrum	Partial areal density		
		C (at./cm ²)	O (at./cm ²)	P (at./cm ²)
RUMP simulation	Fig.4.24(a)	4.7×10^{17}	9.9×10^{16}	1.1×10^{16}
Hand calculation	Fig.4.24(b)	1.4×10^{17}	3.0×10^{16}	4.5×10^{15}

Table 4.7: Comparison of carbon, oxygen and phosphorous contents of cardiolipin film ($\#TK - 2$), as obtained from RBS.

ERDA

Fig.4.25 shows normalized ERDA spectra recorded after He^+ ion fluences of 8.33×10^{14} and 3.33×10^{16} ions/cm² corresponding to He^+ integrated charge of 1 μC and 40 μC respectively. Spectra were also recorded for other He^+ incident charges from 2 to 39 μC in steps of 1 μC but are not shown in the figure for clarity. It has been observed that for all the films, total area under the H recoil peak continuously decreases as a function of incident He^+ ion fluence. The variation in peak integral of recoiled hydrogen with He^+ ion fluence has been shown in the inset of Fig.4.25. This shows a steep reduction in total hydrogen from these films which approaches a constant value at high doses. Evaluation of film thickness and composition has been done by means of RUMP simulation package. The film thickness and its composition used for simulation corresponding to different ion fluences are given in Table-4.8. It is to be noted that the errors in the values of H content are estimated to be $\sim 10\%$ by taking into account various uncertainties such as helium and hydrogen stopping powers in the phospholipid films and other parameters used in the simulation. It is important to study the hydrogen loss behaviour at much lower fluences so that extrapolation to zero fluence acts as a more precise measure of the film stoichiometry. However, measurements at very low fluences are restricted by poor statistics.

RBS-channeling

In general, when any such films are deposited on Si, the detection sensitivity of C and O by RBS gets reduced because of the background signal arising from the thick Si substrate. RBS-channeling technique enables one to reduce this background by a significant amount. During channeling, an energetic ion-beam is channelled through the atomic planes of the substrate and thus reducing the number of scattering centres. As a result, the backscat-

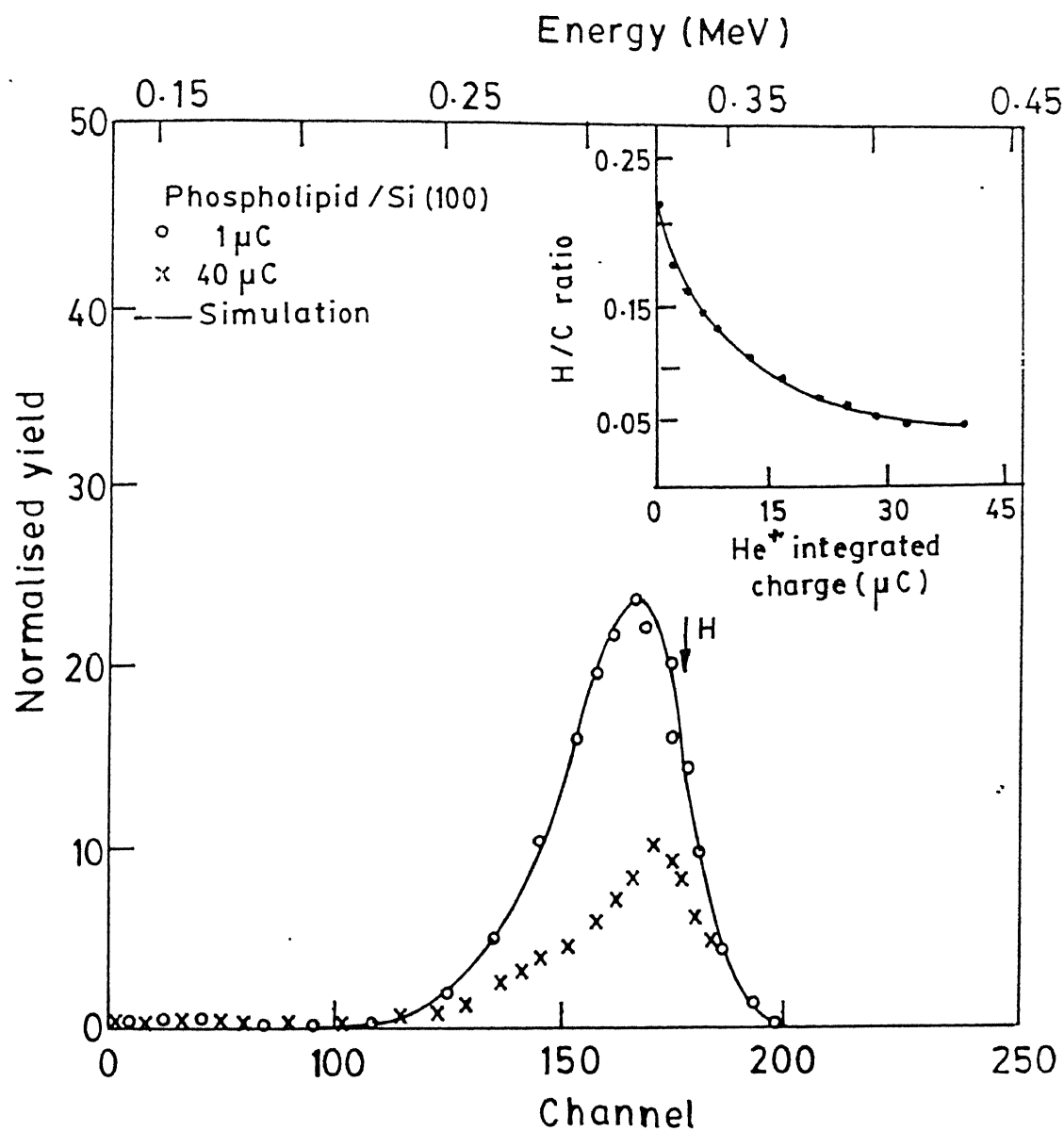


Figure 4.25: ERDA spectra of a *cardiolipin* film (#TK-2), collected after cumulated He⁺ charge collection of $1 \mu\text{C}$ and $40 \mu\text{C}$. The arrow indicates the surface position of H. The inset depicts ion-induced desorption of hydrogen from phospholipid films as a function of the cumulated dose during irradiation by He⁺ ions of 1.23 MeV, used for ERDA. The solid line is a guide to the eye.

He ⁺ integrated charge (μC)	Areal density (at./cm ²)	Partial areal density			
		H (at./cm ²)	C (at./cm ²)	O (at./cm ²)	P (at./cm ²)
1	9.6×10^{17}	8.9×10^{16}	3.3×10^{17}	6.9×10^{16}	7.8×10^{15}
40	8.5×10^{17}	3.2×10^{16}	3.3×10^{17}	6.9×10^{16}	7.8×10^{15}

Table 4.8: Comparison of thickness and composition of *cardiolipin* film (#TK-2) for two different He⁺ ion fluences, as obtained from ERDA.

tering yield from the substrate is largely reduced and signals arising from the constituent elements of the thin-film material becomes prominent. This advantage has been utilized of RBS-channeling technique to identify the C, O, and P signals of the *cardiolipin* films more distinctly as compared to the random RBS signal (see Fig.4.24(b)). The experimental χ_{min} value for Si was found out to be 9.3% which is higher as compared to the virgin Si because of the dechanneling occurring in the *cardiolipin* films. Detailed analysis indicates that C, O, and P contents of the films remain almost same (within $\pm 5\%$) even after an integrated He⁺ charge collection of 40 μC , while the H population of the films is affected significantly.

IR analysis

IR transmission spectra were recorded from the as deposited and He⁺ irradiated phospholipid films in the range of 400-4000 cm^{-1} using the same set-up as described earlier. IR spectrum obtained from the as deposited phospholipid films has been shown in Fig.4.26. The peak positions obtained from as deposited as well as He⁺ irradiated regions (spectrum not shown) and the corresponding bonding configurations have been provided in Table-4.9.

It is observed that in case of the as deposited film, there are three absorption peaks centred around 2867, 2941, and 2971 cm^{-1} . These peaks are actually the absorption peaks of sp^3 CH₃, sp^2 CH₂, and sp^3 CH₃ bonds, respectively. On the other hand, deconvolution of the IR spectrum obtained from the irradiated regions reveals three prominent peaks appearing at 2843 cm^{-1} (sp^3 CH₂), 2932 cm^{-1} (sp^3 CH) and at 2941 cm^{-1} (sp^2 CH₂). Reduction in hydrogen content due to ion irradiation is followed from the decrease in area under the stretching vibration modes. The very fact that sp^3 C-H bonds decrease, while sp^2 C-H bonds increase indicates significant structural changes to take place due to He⁺ ion irradiation

As deposited (cm ⁻¹)	Irradiated (cm ⁻¹)	Bonding configuration
734	740	sp^2 C-H (arom.) O-P-O O-P=O
890	895	sp^3 C-C (olef.)
970	963	sp^2 C-C (olef.)
1109	1109	Phosphodiester stretch
1384	1388	sp^3 CH ₃
1474	1468	sp^2 CH ₂ (olef.)
1574	1570	sp^2 C=C (arom.)
1734	1734	C=O ester stretch
2867	2843	sp^3 CH ₃ (sym.) sp^3 CH ₂ (sym.) respectively
2941	2900	sp^2 CH ₂ (arom.) sp^3 CH (asym.) respectively
2971	2941	sp^3 CH ₃ (asym.) sp^2 CH ₂ (arom.) respectively

Table 4.9: Peak positions and various bonding configurations observed in infrared spectra of phospholipid films.

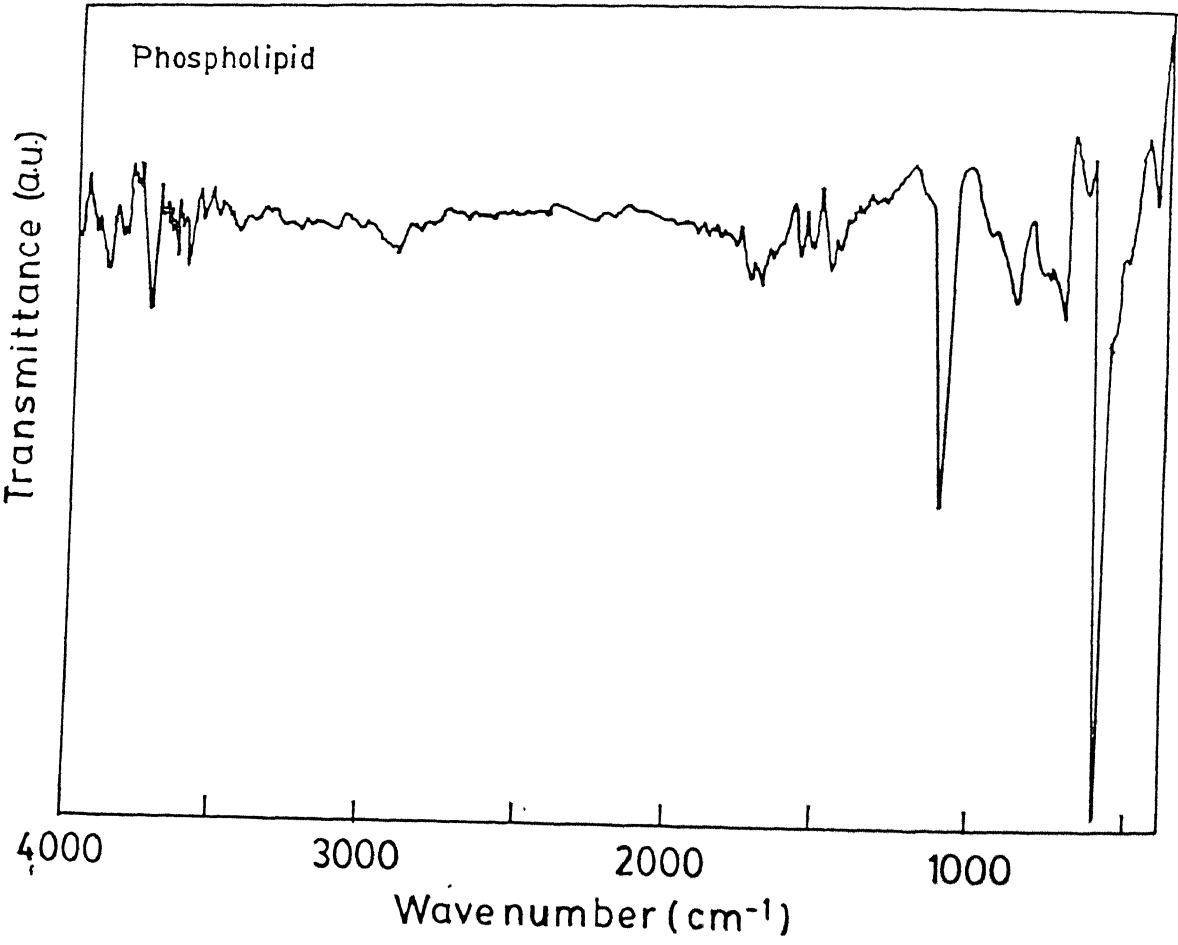


Figure 4.26: IR spectrum of as deposited phospholipid film on Si (100) substrate.

Sample	$\nu_1(\text{cm}^{-1})$	$\Delta\nu_1(\text{cm}^{-1})$	$\nu_2(\text{cm}^{-1})$	$\Delta\nu_2(\text{cm}^{-1})$	$\nu_3(\text{cm}^{-1})$	$\Delta\nu_3(\text{cm}^{-1})$
As deposited	1393	163	1588	42	1704	92
Irradiated	1387	122	1528	136	1601	85

Table 4.10: Raman peak positions and respective FWHMs obtained from phospholipid samples.

followed by H-depletion from the lipid films.

Micro Raman analysis

To investigate the changes occurring in the phospholipid films, during He^+ ion-beam induced elemental analysis, micro Raman measurements were performed on the as deposited films and the irradiated spots. Such micro Raman spectra have been presented in Fig.4.27. The results of computer line-shape analysis by PEAKFIT program has been provided in Table-4.10. From the Raman spectrum of the as deposited lipid films (Fig.4.27(a)), three clear peaks are observed. However, after irradiation, all the peaks corresponding to 1393 cm^{-1} , 1588 cm^{-1} , and 1704 cm^{-1} get shifted towards the lower wavenumbers (as indicated in Fig.4.27(b)).

The two extreme peaks become narrower, while the middle one becomes very broad to be hardly identified separately. Irradiation induced narrowing of the two major peaks indicate the dominance of crystallites. Peak shift towards the lower wavenumber region may be indicative of the formation of $\alpha\text{-C:H}$ network with high disorder being created due to ion bombardment and subsequent loss of hydrogen. This is because of the fact that the Raman spectrum of $\alpha\text{-C:H}$ films typically comprises of standard D and G lines as mentioned in the case of DLC films. Therefore, irradiation leads to the graphitization (sp^2 bonded C) of the phospholipid films. At the same time, the intensity ratio of the two extreme peaks drastically reduces which can be due to the growth in crystal dimensions.

The probable hydrogen depletion mechanism associated to the hydrogen depletion during ERDA measurements can be discussed as follows. The possibility of decomposition of lipid films due to rise in temperature is ruled out because the expected temperature rise of these films is only few degrees. It is more likely then that depletion occurs due to the energy deposited by the analyzing beam by electronic excitations in the films which leads to the

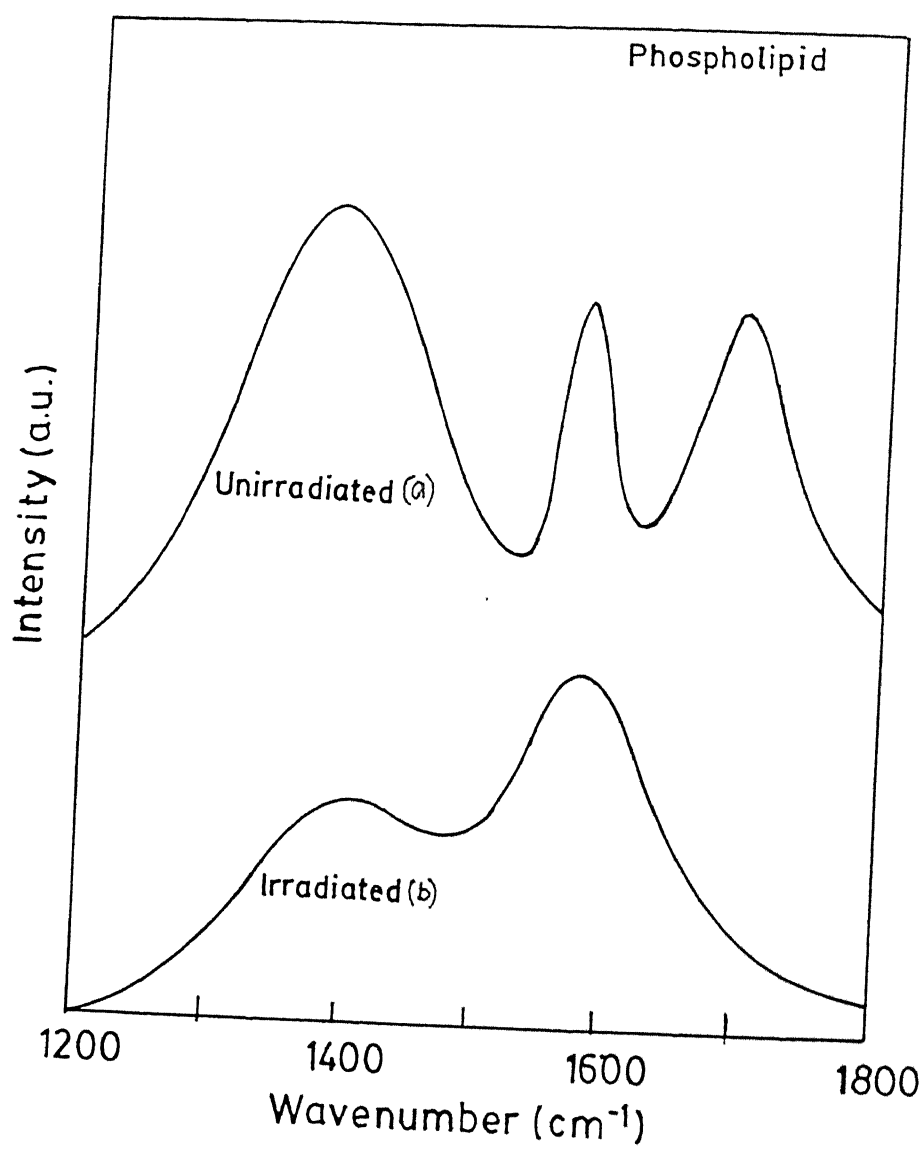


Figure 4.27: Raman spectra of phospholipid film obtained from: (a) as deposited and (b) He⁺ irradiated spot.

breaking of the C-H bonds, whose content is high in cardiolipin films (**Fig.4.23**). The high probability of such adjacent bond-breaking leads to the release of hydrogen which is followed by substantial structural changes as revealed by the IR and micro Raman analysis. If two such liberated H atoms recombine within a characteristic distance, the formation of molecular hydrogen takes place which can easily diffuse through the lipid films. Since no prominent H accumulation takes place near the surface side of the film (**Fig.4.25**), it appears that the liberated hydrogen leaves the films. The residual value of H may correspond to the fraction of unbroken bonds which are too distant from another similar bond thus restricting further recombination of hydrogen.

Conclusions

The feasibility of studying thin phospholipid films (viz. cardiolipin) on crystalline Si substrates in high vacuum condition using energetic ion-beams has been demonstrated. Stability of these films under high vacuum has been tested by the weight loss measurements. Thin films of cardiolipin have been characterized using ion-beam analysis techniques like RBS-channeling and ERDA. The composition of C, O, and P in the cardiolipin films has been determined quite accurately and it remains unaltered under He^+ irradiation during analysis. However, hydrogen depletion takes place from the films under ion bombardment. This has been explained by He^+ ion induced bond-breaking which leads to chemical reconstruction process. Infrared and micro Raman measurements show that hydrogen depletion from the lipid films is followed by reduction in sp^3 bonded carbon and enhancement in the quantity of sp^2 bonded carbon indicating the formation of an $\alpha\text{-C:H}$ network.

4.3 Determination of initial hydrogen concentration

The results of He^+ induced depletion of hydrogen during ERDA in different materials presented in the foregoing sections raise an important issue regarding the ability of ERDA to measure the true or initial concentration in such materials. It is clear that ERDA would not yield the original hydrogen distribution in these materials even if a very low analyzing fluences ($<10^{12}$ ions/cm²) is employed. Of course, as the ion fluence is reduced the measured H concentration will certainly approach a value nearer to the true concentration. At

Sample name	Measured H/C ratio at the lowest fluence	Initial H/C ratio
DLC 51	0.047	0.049
DLC 33	0.097	0.111
DLC 40	0.138	0.154
DLC 18	0.230	0.238

Table 4.11: Initial H/C ratios for different DLC films obtained from the method of extrapolation proposed in this work.

to preferential evaporation of some hydrogen-rich species in vacuum (which was beyond the detection limit of the weight loss measurements performed in this work). Therefore, it may not be very practical to use the procedure for this type of liquid films to get the high initial hydrogen concentration.

The procedure has been used for all the DLC samples studied in this work (Fig.4.31) to determine the *unknown* initial hydrogen concentration. The extrapolated concentrations are expected to be within 5% of the initial concentration in these films. The results are presented in Table-4.11.

In the following section the ion induced hydrogen depletion has been discussed on the basis of different phenomenological models proposed in the literature after giving a brief review of these models.

4.4 Phenomenological/empirical models

4.4.1 Review of the existing models

In the literature two types of model have been proposed to explain the hydrogen desorption phenomenon. In the first category, the observed desorption curve is fitted using a single or multiple-term inverse exponential fitting. For example, Behrisch *et al.*[61] have chosen a simple exponential function for fitting the H-desorption from *a*-C:H layers induced by high energy (>100 MeV) I ions:

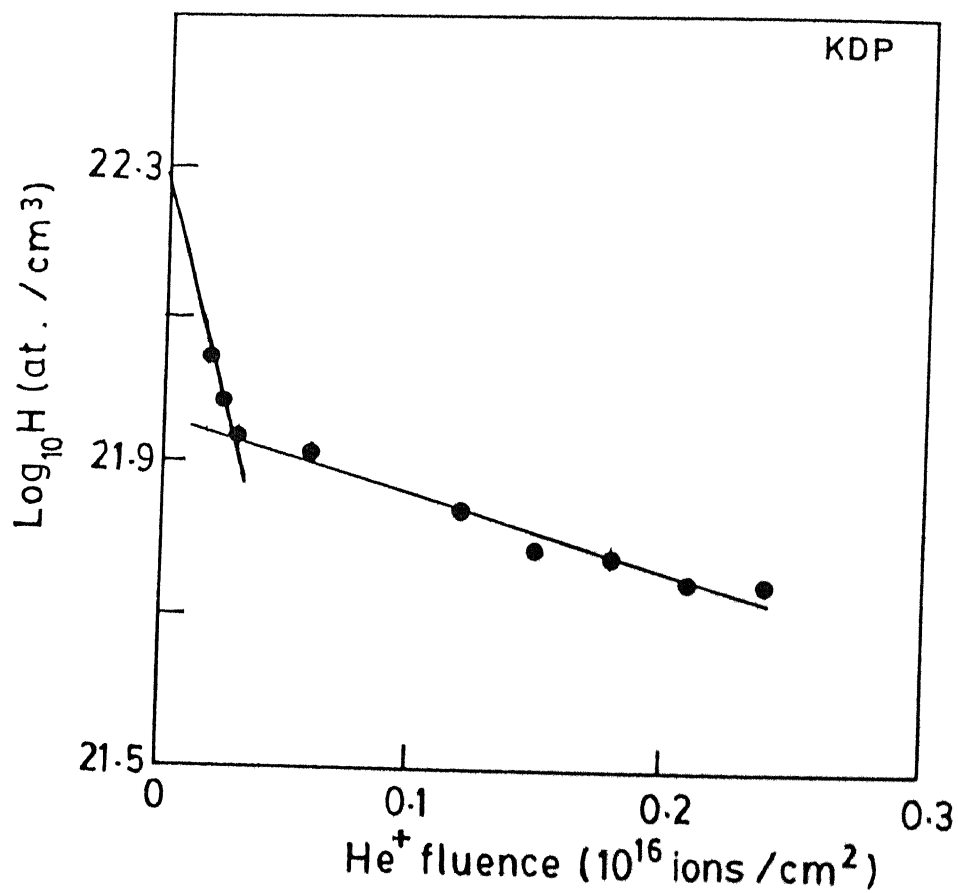


Figure 4.28: Determination of initial hydrogen concentration of KDP by extrapolation method. Experimental data points (•) have been best fitted as indicated by the solid lines.

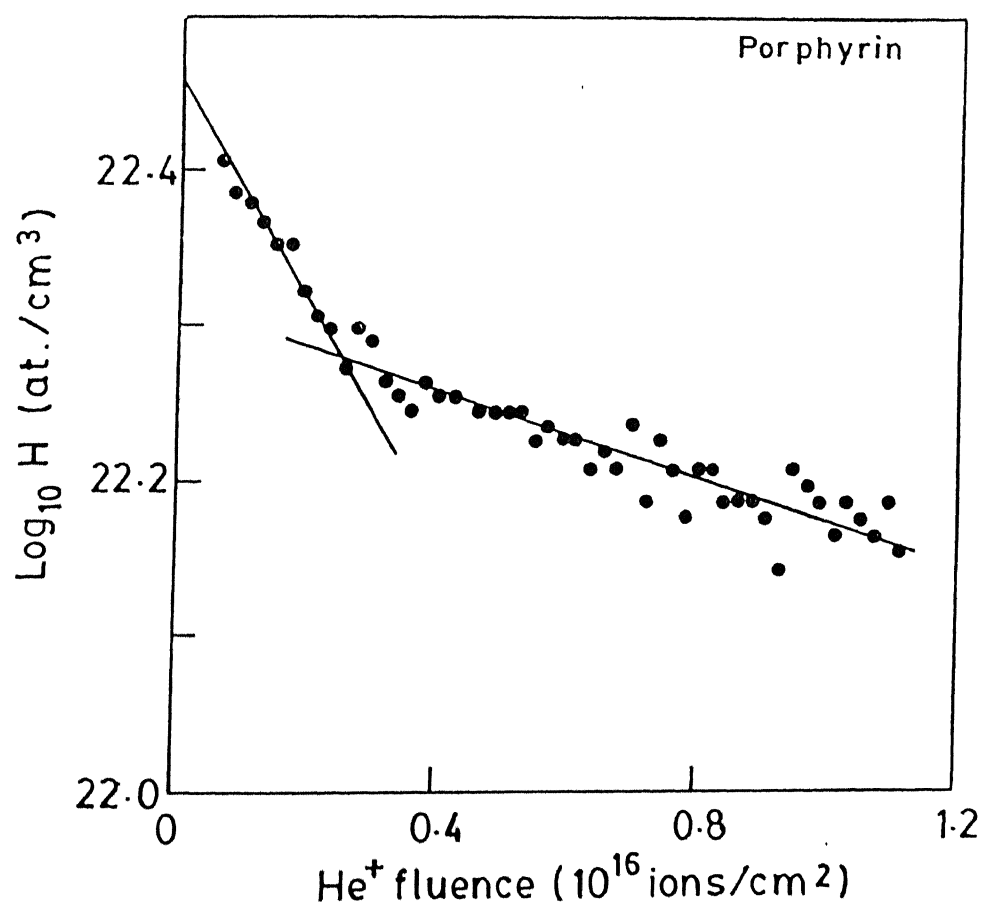


Figure 4.29: Determination of initial hydrogen concentration of porphyrin by extrapolation method. Experimental data points (•) have been best fitted as indicated by the solid lines. It may be noted here that initial three data points of the actual depletion curve has not been considered here for extrapolation.

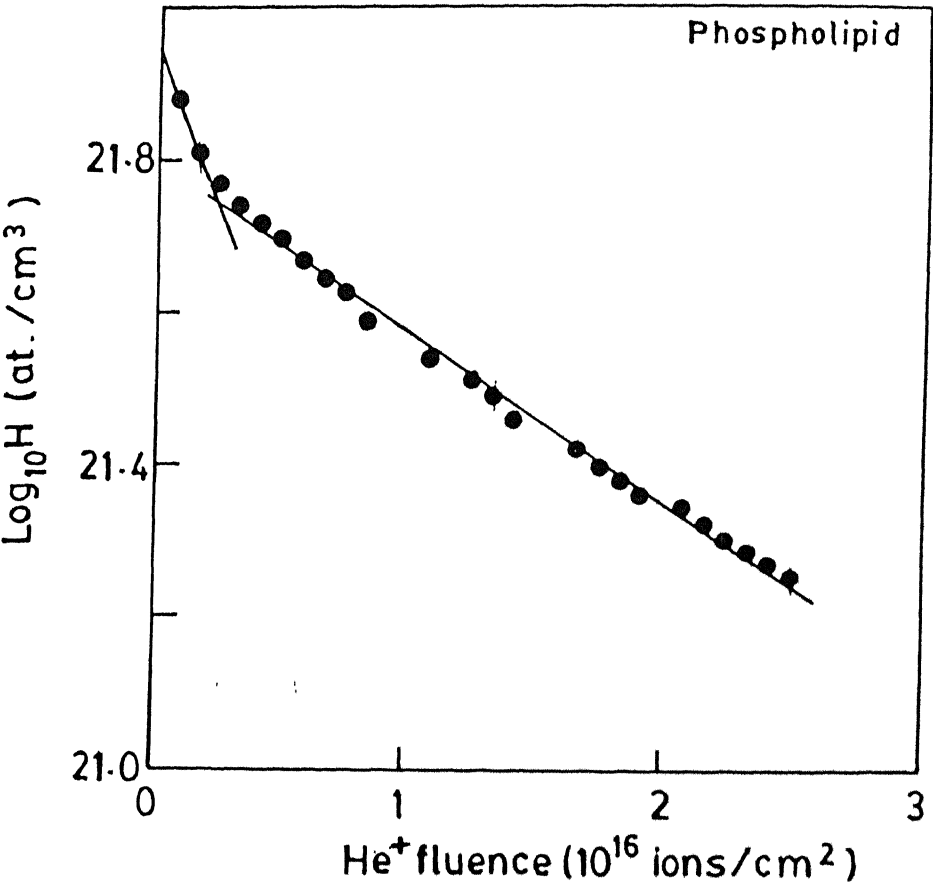


Figure 4.30: Determination of initial hydrogen concentration of phospholipid by extrapolation method. Experimental data points (•) have been best fitted as indicated by the solid lines.

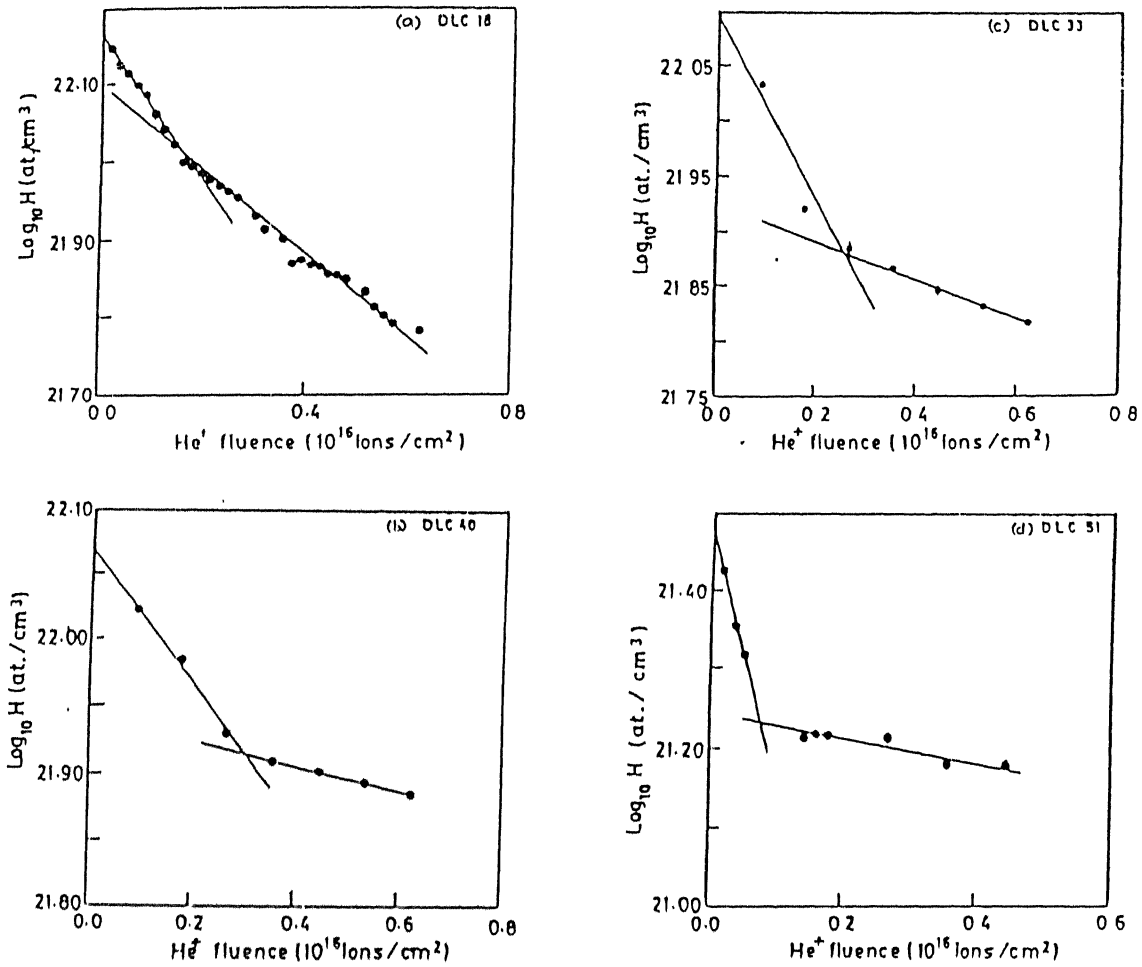


Figure 4.31: Determination of initial hydrogen concentration of DLC films: (a) DLC 18, (b) DLC 40, (c) DLC 33 and (d) DLC 51 by the method of extrapolation. Experimental data points (●) in all four cases have been best fitted as indicated by the solid lines.

$$n(\varphi) = n_0 \exp(-\sigma \varphi), \quad (4.2)$$

where n_0 is the initial hydrogen concentration, σ is the hydrogen desorption rate and φ is the ion fluence.

On the other hand several authors have used a two-term inverse exponential equation also to fit their experimental desorption curves[3-7]. The retained amount of hydrogen is given by

$$n(\varphi) = n_1 \exp(-\sigma_1 \varphi) + n_2 \exp(-\sigma_2 \varphi), \quad (4.3)$$

where σ_1 , σ_2 are parameters for fitting, $(n_1 + n_2)$ is the initial hydrogen concentration of the sample. In fact these two terms describe the extreme details of the experimental evolution: n_1 and σ_1 denote the initial behaviour during bombardment; and n_2 and σ_2 are assigned to the final decrease when the fluence of incident ions become large and the H content rather low.

More recently, Mareé *et al.*[54] have proposed the following relationship to describe the amount of retained hydrogen and the total amount of incident particles:

$$H(\varphi) = H(0) \{a_\alpha e^{-(\sigma_\alpha \varphi)} + a_\beta e^{-(\sigma_\beta \varphi)} + a_h\}, \quad (4.4)$$

with $a_\alpha + a_\beta + a_h = 1$.

In this equation, the degradation is characterized by two (dose-independent) degradation cross-sections, σ_α and σ_β . From the measurement of the degradation curve, extrapolation to the amount of hydrogen at zero dose, $H(0)$ is feasible, using the recoil cross-section of hydrogen[62]. However, the accuracy of this extrapolation is determined by the swift depletion of hydrogen at low dose, which is mainly characterized by the cross-section σ_α , since σ_β is about seven times lower and a_α , a_β are of the same magnitude.

Baumann *et al.*[63] used a three-term inverse exponentials, to fit their hydrogen desorption data from α -C:H system. Recently, Turgeon and Paynter[64] have used an infinite number of terms in the fitting equation for the perfect fitting of any experimental hydrogen desorption curve. However, it has been argued that although multiplication of terms and of fitting parameters (two per term) add to the sensitivity on each individual data point, this kind of expression may not have adequate physical relevance. In this regard, Schrezer *et al.*[6] had argued that multiple first-order release processes would indicate multiple fractions of H (D) in different binding states which should be independent of primary ion energy.

The second category of the models on hydrogen desorption data is based on physical arguments of ion-matter interaction. Adel *et al.*[11] developed a phenomenological relationship which could satisfactorily explain the hydrogen depletion data from a -C:H films. More recently, de Jong *et al.* had suggested an improved understanding to explain the hydrogen depletion data obtained from organic thin films of porphyrin[12]. The essence of the models proposed by Adel *et al.* and de Jong *et al.* is given in the next section followed by the analysis of the data obtained in this work and its comparison with other data in the literature.

4.4.2 Model of Adel *et al.*

Based on the experimental evidence for molecular effusion[65], Adel *et al.*[11] presented a description of ion induced H-depletion from a -C:H films. Their model is statistical in nature and is based on a second-order kinetic process, namely the recombination of atomic to molecular hydrogen, and assumes that all hydrogen is equally bonded. The model is in agreement with many published data, including their own.

According to this model, due to the passage of a single energetic ion, if two hydrogen atoms are liberated and recombine in the bulk to form H_2 then this molecular hydrogen diffuses out of the material. For this event to occur, two C-H bonds must be broken within a short characteristic distance from each other and within a time short compared to the lifetime of free hydrogen atoms in the damaged material. In this model, suggested by Adel *et al.* it is assumed that (a) the time scale of all ion-matter interactions is sufficiently small such that at relevant current densities each ion interacts independently with the target, and (b) once a H_2 molecule has been formed in the bulk, it diffuses out of the material without further interactions.

In this case, a characteristic volume V is considered within which the formation of a H_2 molecule takes place. When only a single hydrogen atom is left in this volume, the hydrogen release must cease (i.e., $V = \rho_f^{-1}$ where ρ_f is the final volume density of hydrogen at which the H content reaches its constant minimum value). Assuming V to be of cylindrical geometry of cross section A and D the ion dose per unit area, Adel *et al.* had derived the relationship between the hydrogen content as a function of ion fluence given by Eqn. 4.2. The irradiation dose dependence of the hydrogen concentration as described by the above model was fitted to several available experimental data[63, 66, 67] by varying the parameter

K . In all the cases where ion-induced H release from α -C:H was analyzed, V was considered to be 140 \AA^3 . Adel *et al.* had tried to correlate the effective molecular release cross section (K) and the electronic stopping powers $(dE/dx)_e$ for several H-depletion data mentioned above. In spite of producing very good fits for H-depletion data from several α -C:H films, the model assumes a fixed final volume hydrogen concentration which fails in predicting the final hydrogen concentration in case of all the H-depletion data mentioned in this work. Also, it fails to predict about the bond-breaking probability which is important in the determination of the hydrogen molecular release cross section.

Abel *et al.* also showed that fitting with Adel's model is clearly inconsistent to their experimental data[68]. They concluded that $(dE/dx)_e$ is not the only pertinent parameter. Instead, they proposed that one should consider the deposited energy density per unit volume inside the ion track. This makes the determination of the track radius to be important and hence the nature of the incident ions. As mentioned above more recently, de Jong *et al.*[12] have modelled the hydrogen loss from organic thin layers of porphyrins ($\text{PdC}_{44}\text{H}_{28}\text{N}_4\text{O}_4$), following a different formalism than Adel *et al.* They have compared their experimental data by fitting with Adel's model and have shown its limitation to predict a suitable final hydrogen concentration.

4.4.3 de Jong *et al.*'s model

de Jong *et al.* considered the primary step in the hydrogen-release process to be the cleavage of molecular bonds due to electronic energy deposition by the incident ions. Excitation or bond cleavage can either be induced by the passing ion itself or, by the secondary electrons which are emitted along the track. These secondary electrons (δ -rays) distribute their kinetic energy to a cylindrical region surrounding the ion's path, which is called the 'ion track'. The width of the cylinder depends on the range of the δ -rays[69] which is empirically related to the initial kinetic energy w of the secondary electrons[70]. As a matter of fact, considering the effective radius of the ion track to be r_{eff} , H radicals are produced through molecular bond cleavage with a probability (ξ) that depends on the total number of emitted δ -rays per unit path length N_δ . This reveals the importance of secondary electrons with respect to energy deposition and hence the creation of damage. A schematic diagram of the ion track has been presented in Fig.4.32.

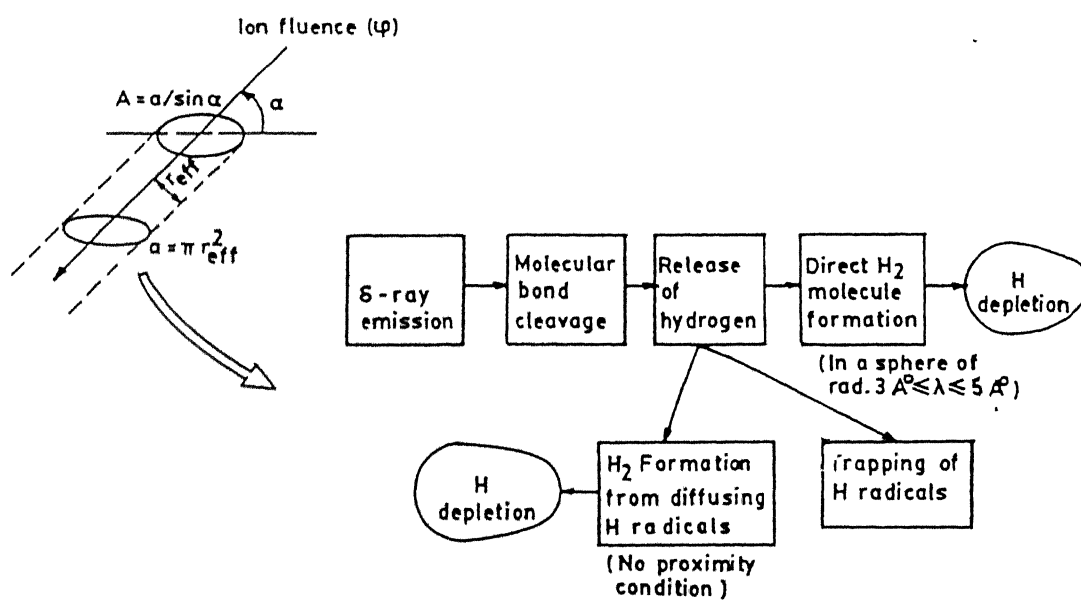


Figure 4.32: Schematic diagram of an ion track and possible mechanism of H_2 molecule formation on it.

Hydrogen release

In the model proposed by de Jong *et al.* it is assumed that if two hydrogen radicals are liberated within a very close distance, they will recombine to form a hydrogen molecule along the track of an impinging ion. It is further assumed that such direct recombination will be possible only if both the hydrogen atoms are created within a spherical volume, $V = (4/3)\pi\lambda^3$, where λ is the characteristic recombination distance.

There exists another possibility to form a hydrogen molecule by recombination of two free H radicals after diffusion through the material. In this case, however, no proximity condition for the recombination needs to be satisfied. The recombination process then competes with the trapping of free hydrogen radicals and depends on the concentration of radicals and traps.

1. Direct recombination of hydrogen radicals

Considering the hydrogen density in the material to be ρ , an average number of $N = \rho V$ bound hydrogen atoms are present within the spherical recombination volume and the average number of H_2 molecules that will be formed out of these N atoms is given by

$$N_{mol} = \xi^2 \left(\frac{1}{2}\right) \rho V (\rho V - 1). \quad (4.5)$$

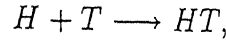
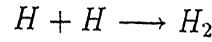
Therefore, the decrease of the bonded H-atom density in the track, $d\rho$, per impinging ion, di , due to direct recombination $(d\rho/di)_{dir}$, is given by

$$\left(\frac{d\rho}{di}\right)_{dir} = - \left(\frac{2 N_{mol}}{V}\right) = -\xi^2 \rho (\rho V - 1). \quad (4.6)$$

The process of direct recombination ceases when on an average only one atom remains within V , in analogy with Adel's model[11]. However, the diffusing radicals will still be able to combine to form H_2 regardless of the hydrogen density in the material, as will be subsequently discussed.

2. Hydrogen molecules formed by diffusing radicals

When a free hydrogen radical cannot instantly form a molecule with another liberated radical, it will diffuse through the material until it is either trapped or it reacts with a second diffusing material. This process can be described by two competing chemical reactions along the track:



where T represents a "hydrogen trap" and HT a trapped H atom. According to standard reaction kinetics, the reaction-rate equations are given by

$$\left(\frac{d[H_2]}{dt} \right) = k_1 [H]^2 \quad (4.7)$$

$$\left(\frac{d[HT]}{dt} \right) = \kappa_2 [H][T] \approx k_2 [H] \text{ with } k_2 = \kappa_2 [T] \quad (4.8)$$

where $[..]$ denotes a concentration (at./cm³) and k_1 and κ_2 are reaction constants. The time t in Eqns. 4.7 and 4.8 correspond to the time during which the reactions take place, starting from the passage of the impinging ion.

Thus, considering $(d\rho/di)_{dif}$ to be the decrease in the density of hydrogen as a result of the recombination of diffusing radicals per ion passing through the track region and assuming ξ to be very small,

$$\left(\frac{d\rho}{di} \right)_{dif} = - \left[\xi \rho - \left(\frac{k_2}{2k_1} \right) \ln \left(1 + \xi \rho \frac{2k_1}{k_2} \right) \right] \approx - \frac{k_1}{k_2} \xi^2 \rho^2. \quad (4.9)$$

3. Hydrogen content as a function of ion fluence

Adding the two contributions $(d\rho/di)_{dir}$ (Eqn. 4.6) and $(d\rho/di)_{dif}$ (Eqn. 4.9), and assuming that the total number of ions I incident on the track region with effective radius r_{eff} can be expressed in terms of the ion fluence φ : $I = A\varphi$ with $A = \pi r_{eff}^2 / \sin \alpha$ (α is the angle between the projectile and the sample surface), de Jong *et al.* obtained the relation between the hydrogen content and the ion fluence to be given by

$$\rho(\varphi) = \left[\frac{1}{\left(V + \frac{k_1}{k_2} \right) + \left[\frac{1}{\rho(0)} - \left(V + \frac{k_1}{k_2} \right) \right] \exp(-\xi^2 A \varphi)} \right] \rho V > 1, \quad (4.10)$$

where $\rho(0)$ is the initial H concentration.

The free parameters in Eqn. 4.10 are the recombination volume V , the ratio of the reaction constants (k_1/k_2) , and the parameter $A\xi^2$ which is the product of the effective

track area and the bond-breaking probability squared. The only parameter that depends on the beam energy is $A\xi^2$. Therefore, mean values for V and (k_1/k_2) are calculated from the three parameter fits and the curves are fitted again with $A\xi^2$ as the only free parameter.

4.4.4 Comparison with experimental results

We now go on to explain the experimental data presented in this chapter on the basis of de Jong's model (i.e., utilization of Eqn. 4.10 to fit the depletion curves). Apart from the measured hydrogen concentration versus fluence data one needs to know the initial hydrogen concentration $\rho(0)$. In case of KDP and phospholipid the values have been calculated from the chemical formula and the densities. In case of DLC films the values obtained the extrapolation to zero fluence (section 4.3) have been used. The fitted H-depletion curves (each of which includes the zero fluence point) for KDP, DLC's and phospholipid samples have been shown in Figs.4.33, 4.34 and 4.35, respectively. In each case the least square errors has been used based on different statistical information theoretic criteria[71]. To understand the hydrogen depletion in terms of the above model, values of various important fitting parameters have been provided in Table-4.12. This table also includes similar parameters for He induced hydrogen depletion data reported in the literature.

Although many of these materials belong to completely different class, an attempt has been made to compare the various fitting parameters to achieve a more general view of the hydrogen depletion phenomenon from these materials. It will enrich the understanding of ion induced H-depletion phenomenon and a general picture would emerge in terms of various physical parameters. For example, $A\xi^2$ is an important parameter which determines the shape of a H-depletion curve and involves the bond-breaking probability in an ion track of radius, r_{eff} . While comparing the amount of energy deposited along the track volume, it is evident that the bond-breaking probability ξ should be small and it should be representative of the microstructure of the materials. To show this dependence, $A\xi^2$ has been plotted against the electronic energy loss, $(\frac{dE}{dx})_e$ (Fig.4.36). This plot includes all the samples studied in this work. It also includes data points obtained by fitting the experimental ion induced H-depletion data reported in the literature. The fitting was performed using the procedure mentioned above. Interestingly, it is observed that the different data points can be grouped into two categories. One is the low-mass (up to He) projectile regime and the other

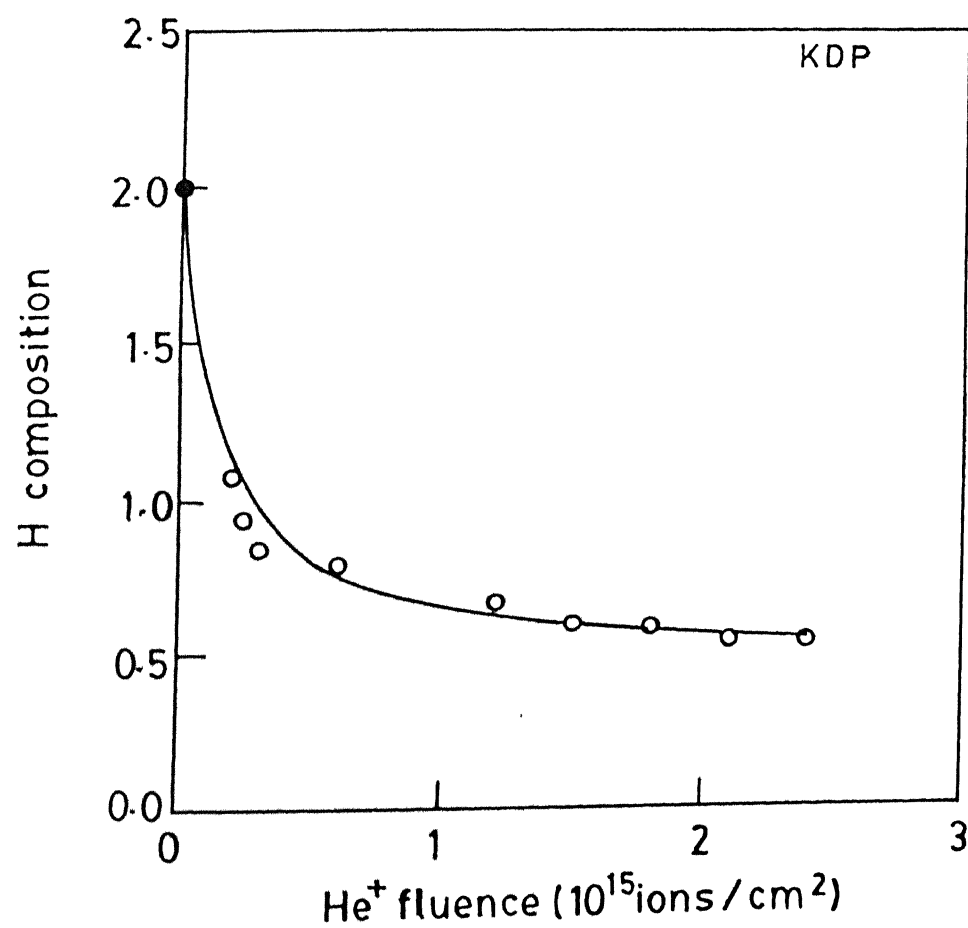


Figure 4.33: Fitted H-depletion curve for KDP: (●) extrapolated H composition at zero analyzing fluence, (○) experimental data points, (—) fitted curve using Eqn. 4.10.

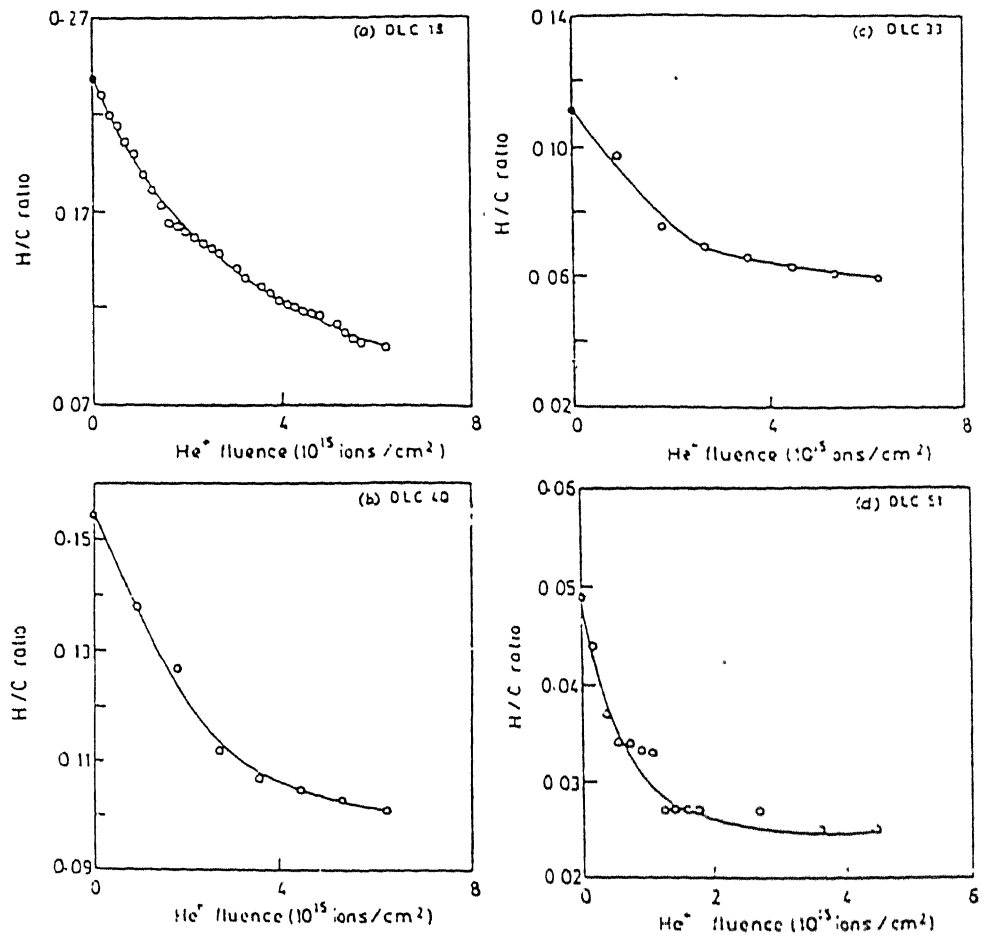


Figure 4.34: Fitted H-depletion curve for different DLC films: (a) DLC 18, (b) DLC 40, (c) DLC 33 and (d) DLC 51. The experimental data points (o) have been fitted (–) curve using Eqn. 4.10. [In all the four cases extrapolated H/C ratio at zero analyzing fluence (●) has also been included.]

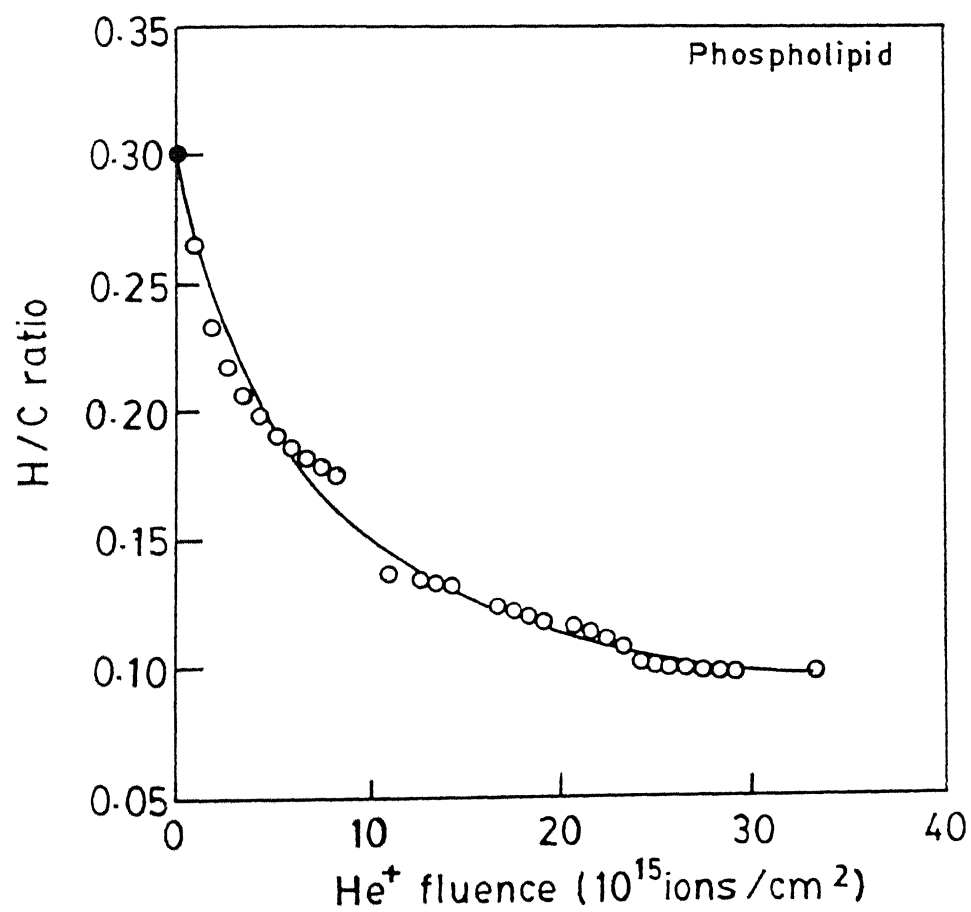


Figure 4.35: Fitted H-depletion curve for phospholipid: (•) extrapolated H/C ratio at zero analyzing fluence, (o) experimental data points, (—) fitted curve using Eqn. 4.10.

Sample	E_0 (MeV)	$A\xi^2$ (\AA^2)	A (nm^2)	ξ	N_δ (nm^{-1})	ξ/N_δ (a.u.)	$(dE/dx)_e$ ($\text{eV}/\text{\AA}$)	Reference
KDP	1.5	5.6	5.6	0.099	7.0	1.41	32.45	This work
DLC 18	1.4	0.41	14.9	0.016	4.7	0.34	24.20	This work
DLC 40	1.5	2.75	8.5	0.056	4.9	1.16	31.30	This work
DLC 33	1.5	3.61	6.3	0.075	6.7	1.13	35.97	This work
DLC 51	1.4	9.56	3.9	0.156	10.2	1.53	41.50	This work
Phospholipid	1.2	0.07	24.8	0.005	4.38	0.11	22.81	This work
Porphyrin	2.0	2.39	21.0	0.033	3.2	1.03	18.63	[4.12]
$\text{Si}_x\text{O}_y\text{H}_z$	3.0	0.44	12.4	0.019	3.3	0.57	23.00	[4.8]

Table 4.12: Explanation of the quantities in the table: E_0 is the beam energy used in the experiment, $A\xi^2$ is extracted from the fitting of H-depletion data, A is the effective ion track area, ξ is the bond-breaking probablity in the ion track, and N_δ is the number of secondary electrons emitted per unit length.

one is the heavy-mass (beyond N) projectile regime. However, this plot demonstrates the common feature that samples containing higher amount of hydrogen have lower values of $A\xi^2$ (and ξ) in comparison to the cases where the materials contain lesser amount of hydrogen. This becomes even clear when the α -C:H (DLC) samples are considered. It is observed from Table-4.12 that as the DLC samples become harder, ξ becomes higher indicating a compact microstructure. Precisely speaking, the more compact a sample becomes, its density increases and hence within a small track radius, the ion encounters more number of atoms which results in the enhancement of ξ . Further, ξ is expected to be approximately proportional to the total number of secondary electrons emitted per unit length, N_δ , as observed from Table-4.12. However, for samples having very high hydrogen concentration, ξ/N_δ is found to have very low values which is attributed to very low densities of these materials.

The other way to realize the microstructure dependence of hydrogen depletion is to consider the values of the other parameters (viz. V and k_1/k_2) obtained from the fitting of the desorption curves. It can be recalled that V is the recombination volume (i.e., when the direct H_2 molecular recombination process ceases due to the presence of only one hydrogen atom

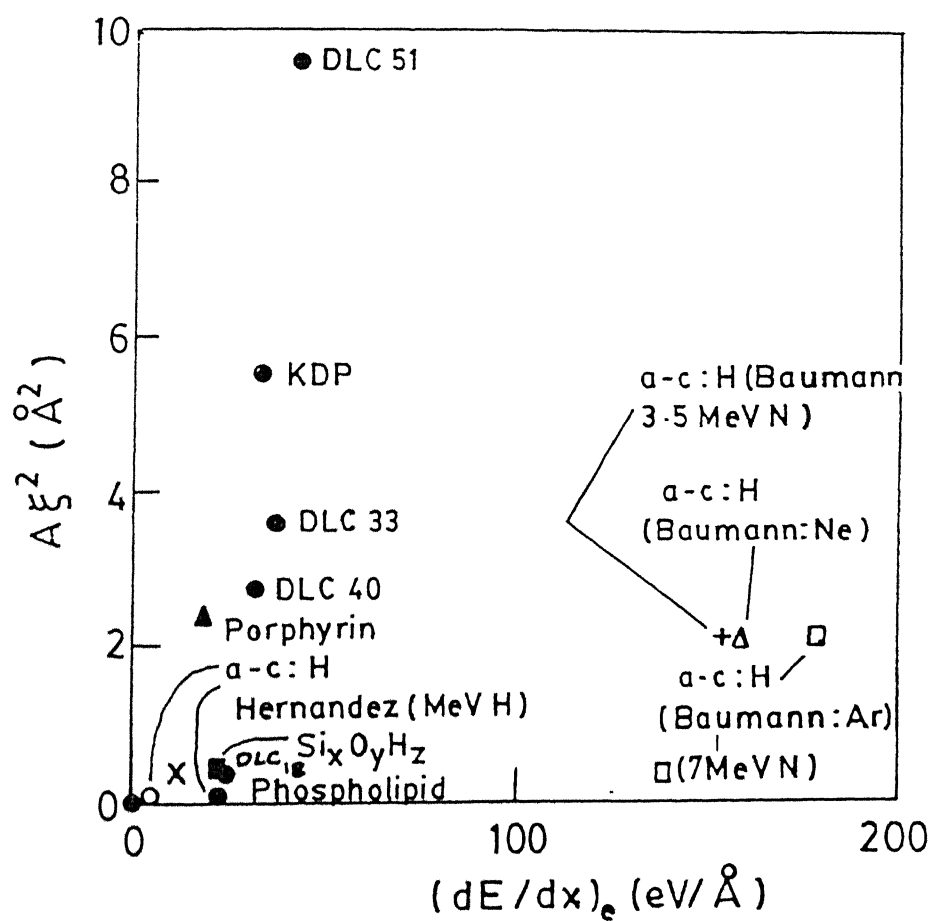


Figure 4.36: $A\xi^2$ versus electronic energy loss $\left[\left(\frac{dE}{dx}\right)_e\right]$ plot for all the samples studied in this work alongwith literature repored data. Reported data were fitted using Eqn. 4.10 in order to extract the $A\xi^2$ values.

Sample	V (\AA^3)	k_1/k_2 (\AA^3)
KDP	174.9	2.5
DLC 18	114.7	1.3
DLC 40	134.7	6.6
DLC 33	158.8	8.0
DLC 51	516.1	11.9
Phospholipid	458.2	1.0

Table 4.13: Comparison of recombination volume (V) and ratio of reaction rates (k_1/k_2) for all the samples studied in this work.

within this characteristic spherical volume) related to the range of the molecular potential of a hydrogen molecule. On the other hand, k_1/k_2 is the ratio of the reaction constants for two possible mechanisms (as mentioned in section 4.4.3) of H_2 molecule formation within an ion track where k_2 contains the density of traps. *Table-4.13* provides the fitted values of V and k_1/k_2 obtained for various cases undertaken in this thesis work.

Comparison of the fitted values for the DLC samples shows that for the very soft films, viz. DLC 18, V and k_1/k_2 both have the lowest values. As the films become more and more hard and compact, both these values keep on increasing and for the hardest films (DLC 51), both of these parameters have their highest values. This clearly indicates that for films having a dense and compact microstructure, the recombination volume become high as they contain less hydrogen. At the same time, density of traps, i.e., number of π electrons also get reduced, therefore the value of k_1/k_2 increases. In contrast, for softer films, hydrogen concentration is quite high and the number of traps get enhanced to bring down the k_1/k_2 ratio. This clearly indicates that hydrogen depletion phenomenon is very much dependent on the microstructure of these materials and their hydrogen concentrations.

Further improvements of the model are possible by considering the continuous modifications in the molecular structure induced by the ion bombardment. The material will gradually evolve to an amorphous network, which will certainly have impact on the diffusion and trapping of free radicals. The assumption of a constant material density and/or concentration of traps is not very realistic, and the creation/annihilation of traps will have

to be incorporated into the model to achieve an even accurate description of the hydrogen desorption process.

4.5 Summary

The results of He^+ ion induced hydrogen depletion and the physico chemical changes (as studied by FTIR and micro Raman techniques) occurring in the properties of different materials viz. KH_2PO_4 (KDP), DLC films and thin films of phospholipid, a biological fluid, were presented in this chapter. All these films exhibit exponential decrease of the hydrogen concentration as a function of the analyzing He^+ ion fluence.

In case of KDP, the effect of Au of varying thickness has been shown to act as a barrier to considerably reduce the depletion of hydrogen from the samples. Hydrogen depletion from the KDP samples is also followed by significant structural changes as indicated by Micro Raman measurements on various irradiated spots.

For the DLC films, the infrared results indicate that the films get rich in sp^2 CH_2 bonds as sp^3 CH_3 bonds decrease followed by hydrogen depletion due to energetic ion bombardment. Micro Raman studies also indicate ion induced removal of bond-angle disorder and increasing dominance of graphite like crystallites.

Probably, it is for the first time that the thin films of biological fluid have been investigated using energetic ion-beam. Thin films of cardiolipin have been characterized using analysis RBS-channeling and ERDA. The ^{concentration} of C, O, and P in the cardiolipin films has been determined quite accurately and it remains unaltered under He^+ irradiation during analysis. Infrared and micro Raman measurements show that hydrogen depletion from the lipid films is followed by reduction in sp^3 bonded carbon and enhancement in the quantity of sp^2 bonded carbon indicating the formation of an α -C:H network in these films.

The depletion data in all the cases exhibit two regimes of exponential decay: the steep descend in the H concentration at low fluences ($\sim 10^{14}$ ions/cm²) as well as the slow but still continuing H loss at high fluences ($\sim 10^{16}$ ions/cm²). The extrapolation to the zero analyzing fluence of the initial fastest depletion regime is shown to yield the initial hydrogen concentration in KDP and porphyrin (materials with known initial hydrogen concentration) quite satisfactorily. This procedure of identification of the fastest depletion regime and its extrapolation to zero fluence has been used to determine the initial hydrogen concentration

in DLC films. However, in case of the films of biological fluid, i.e., phospholipid, the extrapolated value was found to be lower than the actual one almost by an order of magnitude.

The hydrogen depletion from these different materials have been explained on the basis of a model proposed by de Jong *et al.* This model considers the physical arguments of bond-breaking due to the secondary electron emission along the ion track and subsequent formation of H_2 molecule (within a small recombination volume) and its escape along with the trapping of the H radicals in the material.

The fitting of the depletion curves for these different materials yields the values of i) bond-breaking probability, ξ , ii) recombination volume, V , iii) the ratio of the respective rate constants for hydrogen molecule formation and trapping. These parameters have been shown to have a systematic dependence on the microstructure in case of the DLC films. The values of $A\xi^2$ (where A is the area of the ion track) shows systematic increase as a function of the electronic energy loss of the incident ion. Further, the comparison of the results of H-depletion induced by light and heavy ions shows two distinct regions with the common feature that samples containing higher amount of hydrogen have lower values of $A\xi^2$ in comparison to the cases where the materials contain less amount of hydrogen.

Further improvements of the model are possible by considering the continuous modifications in the molecular structure induced by the ion bombardment. The assumption of a constant material density and/or concentration of traps is not very realistic and the creation/annihilation of traps should be incorporated in the model to achieve a better understanding of the mechanism of hydrogen depletion. Also, there exists a scope of incorporating the exo-diffusion of hydrogen by correlating the diffusion coefficient of hydrogen with the respective rate constants of hydrogen molecule formation and trapping of hydrogen radicals.

Bibliography

- [1] J.P. Bugeat and E. Ligeon, *Nuch. Instr. Meth.* 159 (1979) 117.
- [2] T. Venkatesan, S.R. Forrest, M.L. Kaplan, P.H. Schmidt, C.A. Murray, W.L. Brown, B.J. Wilkens, R.F. Roberts, L. Rupp, Jr. and H. Schonhorn, *J. Appl. Phys.* 56 (1984) 2778.
- [3] D. Boutard, B.M.U. Scherzer and W. Möller, *J. Appl. Phys.* 65 (1989) 3833.
- [4] J.P. Thomas, M. Fallavier and J. Tousset, *Nucl. Instr. Meth.* 187 (1981) 573.
- [5] B.M.U. Scherzer, R.S. Blewer, R. Behrisch, R. Schultz, J. Roth, J. Borders and R. Langley, *J. Nucl. Mater.* 85/86 (1979) 1025.
- [6] B.M.U. Scherzer, M. Weilunski, W. Möller, A. Turos and J. Roth, *Nucl. Instr. Meth.* B33 (1988) 714.
- [7] G.G. Ross and I. Richard, *Nucl. Instr. Meth.* B64 (1992) 603.
- [8] C. Godet, R. Etemadi and C. Clerc, *Appl. Phys. Lett.* 69 (1996) 3845.
- [9] C.H.M. Marée, A. Kleinpenning, A.M. Vredenberg, F.H.P.M. Habraken, *Nucl. Instr. Meth.* B118 (1996) 301.
- [10] J. Pillath and J. winter, *J. Nucl. Mater.* 176/177 (1990) 319.
- [11] M.E. Adel, O. Amir, R. Kalish and L.C. Feldman, *J. Appl. Phys.* 66 (1989) 3248.
- [12] M.P. de Jong, A.J.H. Mass, L.J. van Ijzendoorn, S.S. Klein and M.J.A. de Voigt, *J. Appl. Phys.* 82 (1997) 1058.

- [13] P.D. Townsend, P.J. Chandler and L. Zhang, *Optical effects of Ion Implantation* (Cambridge University Press, Cambridge, 1994).
- [14] M.L. Dalal, M. Rahmani and P.D. Townsend, *Nucl. Instr. Meth. B*32, 61 (1988).
- [15] C.W. Pitt, J.D. Skinner and P.D. Townsend, *Elect. Lett.* 20 (1984) 4.
- [16] L. Zhang, P.J. Chandler, P.D. Townsend and F.L. Lama. *NATO ASI Series E* 170 (1989) 371.
- [17] L. Zhang, P.J. Chandler, P.D. Townsend, Z.T. Alwahabi, S.L. Pityana and A.J. McCaffery, *J. Appl. Phys.* 73 (1993) 2695.
- [18] K. E. Youden, S.W. James, R.W. Eason. P.J. Chandler, L. Zhang and P.D. Townsend, *Opt. Lett.* 17 (1992) 1592.
- [19] G.L. Destefanis, P.D. Townsend and J.P. Gailliard, *Appl. Phys. Lett.* 32 (1978) 293.
- [20] F.A. Strohkendl, D. Fluck, Ch. Buchal, R. Irmscher and P. Gunter, *Appl. Phys. Lett.* 59 (1991) 3354.
- [21] M. Vallade, *Phys. Rev. B*12, (1975) 3755.
- [22] M.A.R. de Benyacar, A. Carabelli and H. Lanza, *Radiat. Eff. Defects in Solids* 128 (1994) 357.
- [23] H. Ratajczak, *J. Mol. Struct.* 3 (1969) 27.
- [24] J.J. Kim and W.F. Sherman, *Phys. Rev. B*36 (1987) 5651.
- [25] R.P. Lowndes, N.E. Tornberg and R.C. Leung, *Phys. Rev. B*10 (1974) 911.
- [26] J.C. Angus and C.C. Haymann, *Science* 241 (1988) 913 .
- [27] P. Koidl, Ch. Wild, B. Dischler, J. Wagner, and M. Ramsteiner, *Mat. Sci. Forum* 52&53 (1989) 41 .
- [28] D. Boutard, B.M.U. Scherzer and W. Möller, *J. Appl. Phys.* 65 (1989) 3833 .
- [29] Ch. Wild and P. Koidl, *Appl. Phys. Lett.* 51 (1987) 1506.

- [30] M. Malhotra and S. Kumar, *Diam. Relat. Mater.* 6 (1997) 1830.
- [31] D.C. Ingram and A.W. McCormick, *Nucl. Instr. Meth. B34* (1988) 68.
- [32] M.J. Paterson, K.G. Orrman-Rossiter, S. Bhargava, and A. Hoffman, *J. Appl. Phys.* 75 (1994) 792.
- [33] R.O. Dillon, J.A. Woollam, and V. Katkanant, *Phys. Rev. B* 29 (1986) 3482.
- [34] T.M. Wang, W.J. Wang, and C. Jing, *Diam. Relat. Mater.* 5 (1996) 1418.
- [35] B. Dischler, A. Bubenzer, and P. Koidl, *Solid State Commun.* 48 (1983) 105.
- [36] Y. Bounouh, M.L. Thèye, A. Dehbi-Alaoui, A. Matthews, and J.P. Stoquert, *Phys. Rev. B* 51 (1994) 9597.
- [37] F.W. Smith, *J. Appl. Phys.* 55 (1984) 764.
- [38] D. Boutard, B.M.U. Scherzer, and W. Möller, *J. Appl. Phys.* 65 (1989) 3833.
- [39] R.L.C. Wu, *Surface Coating Technol.* 51 (1992) 258..
- [40] F.L. Freire Jr., C.A. achete, D.F. Franceschini, C. Gatts, and G. Mariotto, *Nucl. Instr. Meth. B* 80/81 (1993) 1464.
- [41] W.J. Wang, T.M. Wang, and B.L. Chen, *Nucl. Instr. Meth. B* 117 (1996) 140.
- [42] J. González-Hernández, R. Asomoza, A. Reyes-Mena, J. Rickards C., S.S. Chao, and D. Pawlik, *J. Vac. Sci. Technol. A* 6 (1991) 1796.
- [43] N. Matsunami, *Nucl. Instr. Meth. B* 64 (1992) 800.
- [44] M. Malhotra, *Ph.D. thesis*, Indian Institute of Technology, Kanpur, 1996.
- [45] J.L. Akkerman, H. Efstathiadis, and F.W. Smith, *J. Appl. Phys.* 80 (1996) 3068.
- [46] D. Boutard, B.M.U. Schrezer, and W. Möller, *Phys. Rev. B* 38 (1988) 2988.
- [47] T. Sharda and D.S. Mishra, *Solid State Commun.* 98 (1996) 879.
- [48] C. Nicolini, and F. Nazza, *Thin Solid Films* 284 (1996) 1.

- [49] M. Aizawa, S. Kato, and S. Suzuki, *J. Membrane Sci.* 2 (1977) 125.
- [50] Y. Chunbo, W. Ying, Y. Xiaomin, L. Zuhong, and L. Juzheng, *Appl. Surf. Sci.* 103 (1996) 531.
- [51] L.K. Tamm, C. Böhm, J. Yang, Z. Shao, J. Hwang, M. Edidin, and E. Betzig, *Thin Solid Films* 284-285 (1996) 813.
- [52] S. M. Stephens and R.A. Dluhy, *Thin Solid Films* 284-285 (1996) 381.
- [53] L. Calcagno, G. Compagnini and G. Foti, *Nucl. Instr. Meth. B* 65 (1992) 413.
- [54] C.H.M. Marée, A. Kleinpenning, A.M. Vredenberg and F.H.P.M. Habraken, *Nucl. Instr. Meth. B* 118 (1996) 301.
- [55] R.B. Gennis, *Biomembranes Molecular Structure and Function* (Springer-Verlag, New York, 1989) p. 25.
- [56] J. Folch, M. Lee, and H. Sloan-Stanley, *J. Biol. Chem.* 226 (1957) 497.
- [57] J. Eichberg, and J.D. Bwinham, *J. Lipid Res.* 11 (1970) 386.
- [58] G.M. Gray, and M.G. Macfarlane, *Biochem. J.* 70 (1958) 409.
- [59] R.M. Hallen, *Ph. D. Thesis*, Indian Institute of Technology, Kanpur, 1981.
- [60] T.K. Khan, *Ph. D. Thesis*, Indian Institute of Technology, Kanpur, 1997.
- [61] R. Behrisch, V.M. Prozesky, H. Huber and W. Assmann, *Nucl. Instr. Meth. B* 118 (1996) 262.
- [62] J.E.E. Baglin, A.J. Kellock, M.A. Crockett and A.H. Shih, *Nucl. Instr. Meth. B* 56 (1993) 859.
- [63] H. Baumann, T. Rupp, K. Bethge, P. Koidl and Ch. Wild, *European Mater. Res. Soc. Conf. Proc.* 17 (1987) 343.
- [64] S. Turgeon and R.W. Paynter, *Nucl. Instr. Meth. B* 118 (1996) 322.
- [65] Ch. Wild and P. Koidl, *Appl. Phys. Lett.* 51 (1987) 1506.

- [66] S. Prawer, R. Kalish, M. Adel, and V. Richter, *J. Appl. Phys.* 61 (1987) 4492.
- [67] J. Gonzalez-Hernandez, R. Asomaza, A. Reyes-Mena, J. Rickards C., S.S. Chao, and D. Pawlik, *J. Vac. Sci. Technol. A* 6 (1988) 1798.
- [68] F. Abel, V. Quillet, and M. Schott, *Nucl. Instr. Meth. B* 105 (1995) 86.
- [69] L.C. Feldman and J.W. Mayer in *Fundamentals of Surface and Thin Film Analysis* (Elsevier Science, Amsterdam, 1986).
- [70] M.P.R. Waligórsky, R.N. Hamm, and R. Katz, *Nucl. Tracks Radiat. Meas.* 11 (1986) 309.
- [71] D. Kundu and A. Mitra, *J. Plann. and Inf.* (in press).

Chapter 5

Role of hydrogen to study ion induced delamination of CVD diamond

5.1 Introduction

In the last chapter, results of ERD analysis of hydrogen in different materials like KDP, DLC and phospholipid systems were described. All these materials exhibited H-depletion which was understood in the light of a general phenomenological model. This chapter presents the results of ERDA measurements performed on yet another important material, namely thin films of diamond.

Diamond is one of the hardest known wear-resistant materials. Natural diamond is impervious to chemical etch even at high temperatures. Usually, most of its properties are retained to a large extent in the thin films of diamond. In recent years, the intense efforts in growing large area diamond films by chemical vapour deposition (CVD) on various substrates and buffer layers have opened several avenues for their promising applications in diverse fields such as superhard protective coatings, microelectronic devices[1, 2], etc. These

applications stem from the unique combination of different physical properties of these diamond films. For example, their exceptionally high thermal conductivity, low dielectric constant and large band gap make them useful for fabrication of several passive electronic devices, while the superior charge-carrier transport properties make them important in fabricating active electronic devices. It is now well established that diamond-based devices offer many significant advantages compared with Si- and GaAs-based devices. For example, diamond based devices have higher breakdown voltages, higher operation speed, superior power handling capabilities etc. Also, these devices would be most suitable for high temperature operations[3, 4]. In general, the films have to be tailored for specific needs. For example, fabrication of microelectronic devices requires special capabilities and novel techniques for isolation and patterning of diamond films. In recent years, selective modification of the surface regions of materials has extensively been studied in silicon device processing using ion-beams of both light and heavy elements[5]. However, ion-beam induced modifications in case of polycrystalline diamond films and diamond based device applications remain mostly unexplored[6–8].

It can be mentioned here that, most of the applications mentioned here and in the literature depend on the properties of the diamond films which are influenced by the film processing parameters. To illustrate, CVD technique utilizes hydrocarbons such as methane, acetylene, etc. for producing diamond films. Although the growth mechanism of these CVD films is yet to be understood completely, it is quite clear that the gas mixture which contains hydrogen in requisite proportion (in excess of 98% by volume) plays a crucial role[1, 9] in the growth process. The presence of hydrogen selectively etches out the non-diamond bonded material thereby reducing the incorporation of graphitic component in the films[1] but at the same time, hydrogen in a small quantity becomes an obvious impurity in CVD diamond films. Further, hydrogen being the lightest element, it can migrate very fast and might alter the diamond-based device characteristics significantly. Therefore, it is important and necessary to undertake the studies concerning the quantification of residual hydrogen present in diamond films and its migration. In this regard, ERDA can be very useful for depth profiling of hydrogen in CVD diamond films[10].

This chapter describes the effect of He^+ ion irradiation and *in-situ* simultaneous detection of hydrogen depth distribution from CVD diamond films grown on Si. The diamond films (prepared under certain condition) are observed to get delaminated under He^+ ion

bombardment. The films contain a very small amount of hydrogen but at the same time the interface is very rich with hydrogen. This interfacial hydrogen plays the important role of a *marker* during ERD measurements, revealing the threshold ion fluence at which the delamination takes place.

5.2 Experimental

Hot filament chemically vapour deposited diamond films on crystalline Si substrates were used for the present study. The silicon substrates were precoated with a thin layer of SiO_2 . The selective nucleation was achieved by using photoresist mixed with fine diamond powder patterned by standard photo-lithographic process followed by etching in buffered hydrofluoric acid (BHF)[11]. Rutherford backscattering measurements were performed in a high vacuum of 2×10^{-6} Torr using 1.5 MeV He^+ ions incident normal to the sample surface to determine the thickness of the diamond films. X-ray diffraction (XRD) experiments using a $\text{Cu-K}\alpha$ radiation ($\lambda=1.5418 \text{ \AA}$) were performed to study the cubic diamond phase in the as deposited films. The surface morphologies of the as-deposited and the irradiated films were studied by scanning electron microscopy (SEM). The diamond films were irradiated with 1.5 MeV He^+ ions at room temperature using a geometry such that the beam was made to impinge at an oblique angle of 75° to the surface normal. This geometry allowed the *in-situ* simultaneous detection of hydrogen by ERDA[12]. An ion implanted semiconductor detector was placed, at an angle of 30° with respect to the incident beam, to detect the recoiled hydrogen signal. Micro Raman spectroscopy was employed to measure the film stresses at several points before and after He^+ ion irradiation. Description of XRD, SEM and micro Raman set-ups have been provided in Chapter 2.

5.3 Results and discussion

5.3.1 RBS

The thickness of the as deposited film was $0.95 \mu\text{m}$, as evaluated from the shift in the edge of Si signal in the RBS spectra. The XRD pattern of the as grown sample in **Fig.5.1** shows the

presence of (111), (220) and (311) cubic diamond phase in the sample. The SEM micrograph of the as deposited film is presented in **Fig.5.2** which shows good quality diamond film with uniformly distributed grains of $\sim 1 \mu\text{m}$ in size. The triangular shape of most of the crystalline facets are typical of the (111) film orientation.

Projected range of 1.5 MeV He^+ ions in diamond film is $2.5 \mu\text{m}$ with a range straggling of $0.09 \mu\text{m}$. Thus for an oblique incidence of 75° with respect to the surface normal, the ions traverse through the diamond films and come to rest at a depth of about $0.64 \mu\text{m}$, i.e., most of the ions are stopped well within the diamond films. The irradiation experiments were performed under a high vacuum of 2×10^{-6} mbar and the hydrocarbon contamination was minimized by using liquid nitrogen traps.

5.3.2 SEM

Fig.5.3(a) shows a low magnification SEM micrograph of the film taken after irradiation with 1.5 MeV He^+ ions. The three spots from left to right correspond to irradiations performed using He^+ incident current densities of $0.66 \mu\text{A}/\text{cm}^2$ (channel-A), $0.33 \mu\text{A}/\text{cm}^2$ (channel-B) and $1 \mu\text{A}/\text{cm}^2$ (channel-C) respectively. Each spot corresponds to a total He^+ ion fluence of 3.6×10^{16} ions/ cm^2 . The cracking of the film and its exfoliation is visible at each irradiated spot. In **Fig.5.3(b)** the propagation of ion induced cracks is clearly visible while **Fig.5.3(c)** shows the magnified view of the nature of the exfoliated region where the debris of the exfoliated film are also visible. Higher magnification pictures of the central region of the delaminated spot did not reveal any signature of diamond crystallites (see **Fig.5.4**). These results indicate that there might be a possibility of making ion-beam induced channels in diamond films for device applications.

5.3.3 Irradiation and ERDA

CVD diamond films are known to contain small amounts of hydrogen. ERDA was effectively used to monitor this hydrogen during irradiation. *In-situ* ERDA spectra recorded after different He^+ fluences are presented in **Fig.5.5**. These spectra have been normalized for direct comparison and are analyzed using the RUMP code. The spectrum corresponding to He^+ irradiation fluence of 5.2×10^{15} ions/ cm^2 (solid circles in **Fig.5.5**) shows hydrogen content

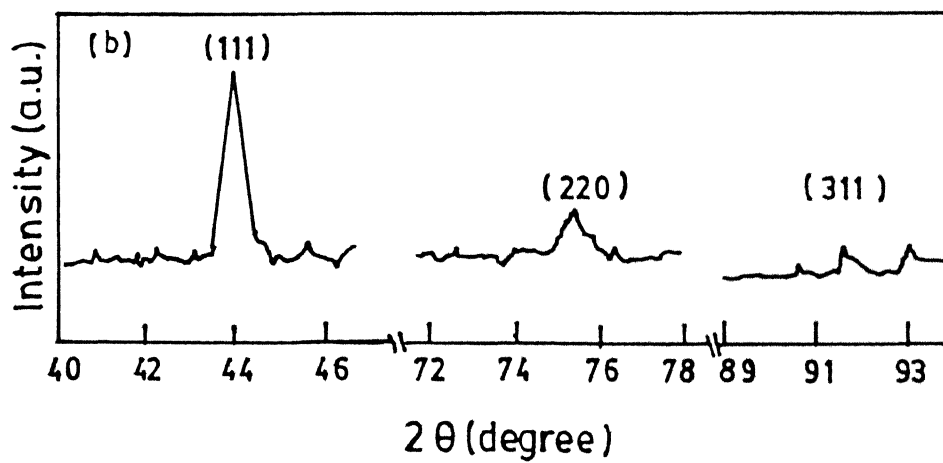


Figure 5.1: X-ray diffractogram of an as-deposited CVD diamond film grown on Si.

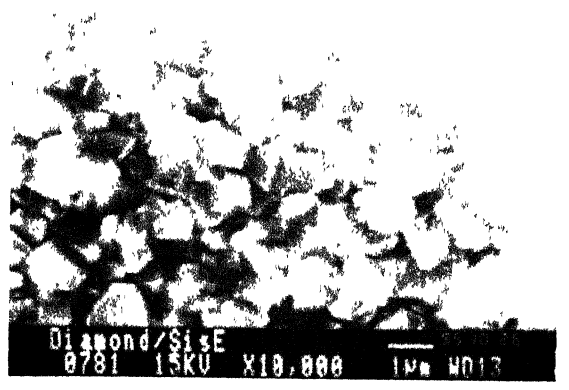


Figure 5.2: SEM micrograph of the as-deposited diamond film on crystalline Si.

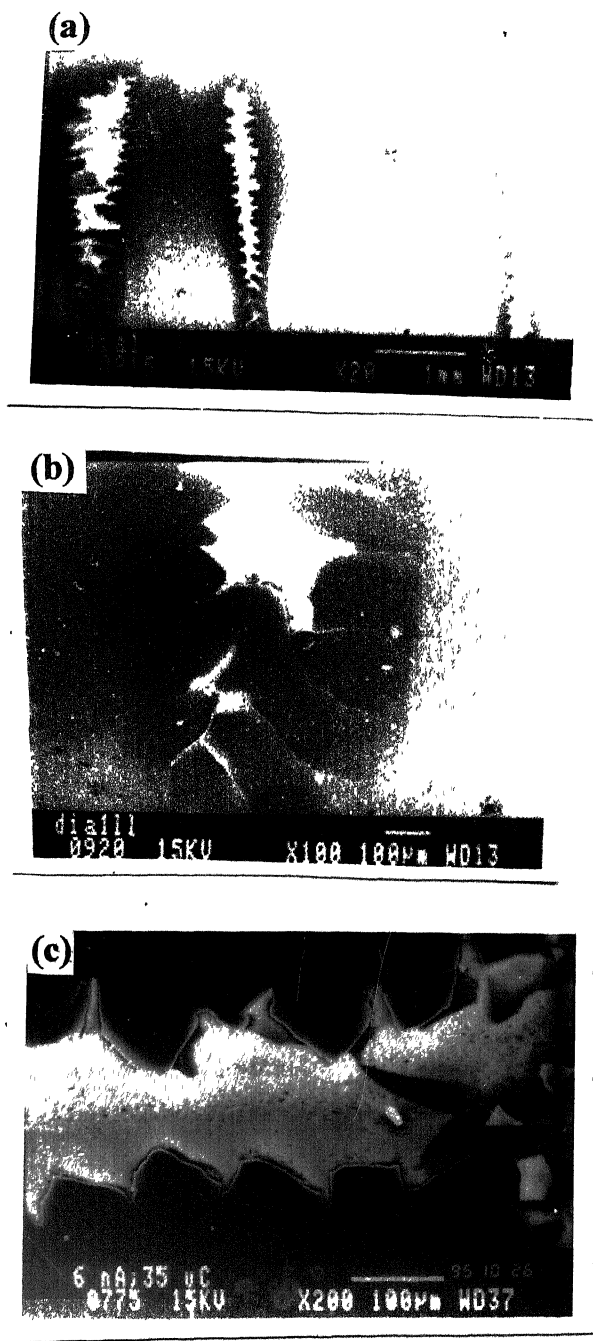


Figure 5.3: SEM photographs of He^+ ion irradiated diamond film: (a) three different ion irradiated regions on the film corresponding to three different target current densities; (b) propagation of the ion induced cracking of diamond film; and (c) close view of a delaminated spot on the diamond film corresponding to a target current density of $1 \mu\text{A}/\text{cm}^2$.

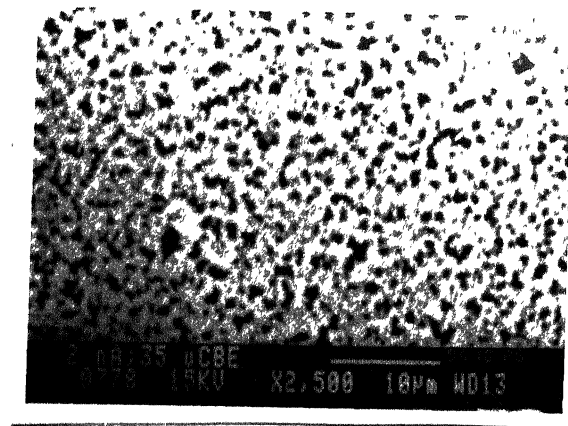


Figure 5.4: SEM micrograph obtained from one of the delaminated spots.

~ 0.8 at.% which is in accordance with the reported level of hydrogen in good quality diamond films. Quantitative determination of hydrogen from such films using ERDA is estimated to be accurate within $\pm 10\%$ in the present geometry. As the bombardment continues, a sudden increase in the hydrogen signal is observed at the fluence of about 1.0×10^{16} He^+/cm^2 . It is also observed that the amount of hydrogen remains constant beyond this fluence. It may be noted that this enhancement in hydrogen content can not be due to ion induced cracking of hydrocarbons since the experiments were performed in clean and high vacuum environment. Also, the enhancement of hydrogen due to such hydrocarbon cracking would be continuous and would not show a threshold behaviour.

It is argued that the enhancement in the quantity of hydrogen is observed for higher ion fluences ($\geq 1.0 \times 10^{16}$ He^+/cm^2) as *now* the Si substrate is directly exposed to the incident He^+ ions after delamination of the diamond film. The enhanced hydrogen signal from the Si substrate is expected as this surface is rich in hydrogen due to the processing history of these films as described earlier[11]. Further, for easy comprehension of ERDA spectra, the depth scale (just above the hydrogen recoil spectra) and hydrogen content (on the right y-axis) are also provided in **Fig.5.5**. In case of delaminated film (spectra corresponding to ion fluences $\geq 1.0 \times 10^{16}$ He^+/cm^2), zero of the depth scale corresponds to the exposed Si surface. It may be pointed out that it is not possible to extract an accurate hydrogen depth profile from the ERDA spectra on delaminated regions as the incident He^+ beam now falls on the exposed Si substrate as well as partly on the diamond films. However, the sudden increase in hydrogen signal in the present case is effectively used as an *in-situ* marker to observe the onset of the delamination process. The threshold nature of peak hydrogen content versus fluence plot has been shown in the inset of **Fig.5.5**. Similar threshold behaviour is observed for other current densities at different spots. It is therefore inferred that there is a critical fluence associated with the delamination of diamond films which has been effectively determined by ERDA.

5.3.4 Effects of irradiation

Role of temperature

In order to understand the removal of diamond films from Si substrate, the effects of ion bombardment need to be considered. Assuming i) the thermal dissipation of ion beam energy

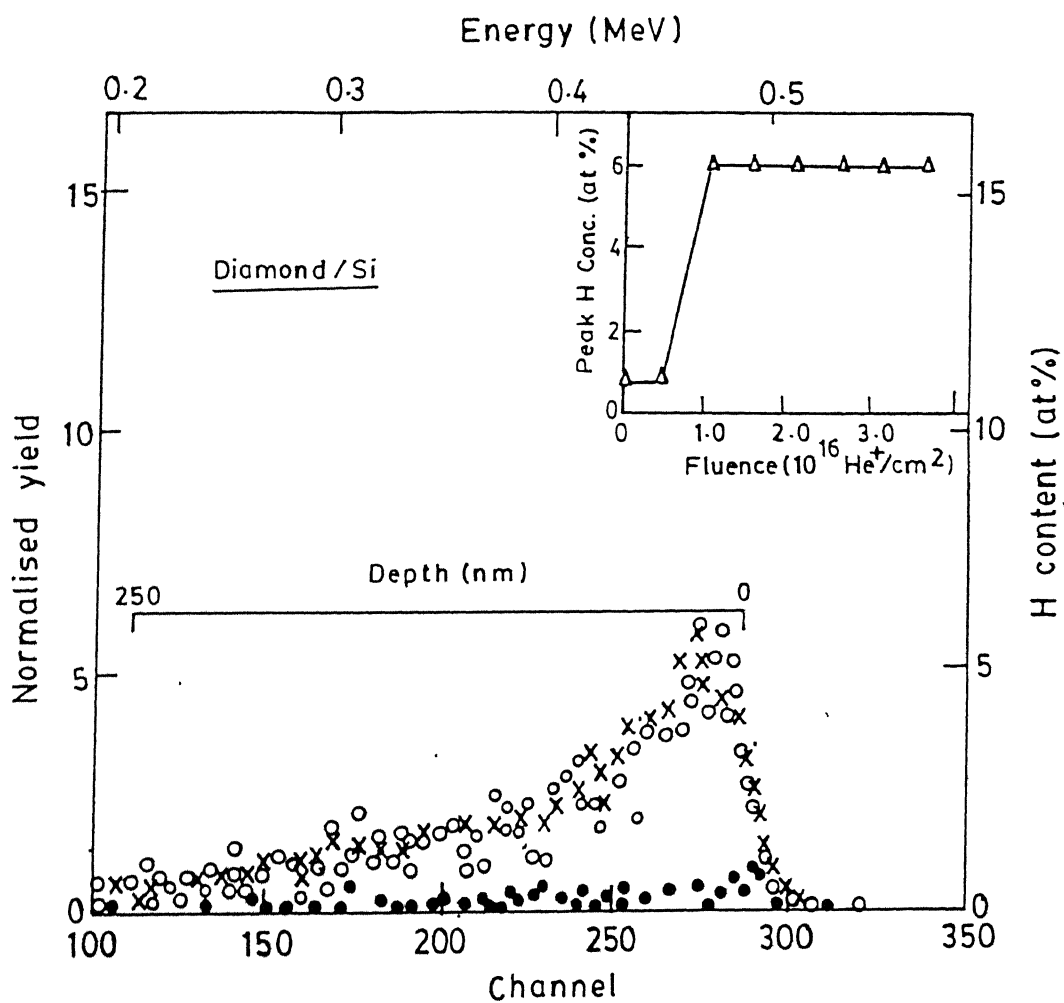


Figure 5.5: 1.5 MeV He^+ induced ERDA spectra corresponding to different ion fluences: 5.2×10^{15} ions/cm² (●), 1.0×10^{16} ions/cm² (○), and 3.6×10^{16} ions/cm² (×). The inset depicts the variation in surface H content (at.%) with He^+ ion fluence.

is just equal to the radiative heat loss of the diamond film and, ii) the interfacial SiO_2 layer is poor heat conductor, one may find the rate of temperature rise from the following equation[13]:

$$C \rho V \left(\frac{dT}{dt} \right) = P(t) - \epsilon \sigma A [T^4 - T_0^4] \quad (5.1)$$

where C is the specific heat (0.52 J/gm-K), ρ is the density (3.515 gm/cm^3), V is the volume of the diamond film under the irradiated spot ($\sim 10^{-7} \text{ cm}^3$), and T is the final temperature. The first term on the right-hand side of the above equation is the power input due to the ion beam (Watt) while the second term corresponds to the radiative cooling of the whole sample [ϵ is the effective emissivity of the irradiated system, A is the total radiating area (cm^2), σ is the Stefan-Boltzmann constant ($5.7 \times 10^{-5} \text{ erg/cm}^2\text{-deg}^4\text{-sec}$) and T_0 is the temperature of the surroundings ($T_0 = 300 \text{ K}$)]. The solution of this equation for different beam powers show that irradiated region can reach a maximum temperature of 325 K during bombardment. Therefore, the delamination cannot be explained on the basis of sample heating during irradiation.

Role of film stress

It is interesting and important to note that the features of the delaminated regions appear quite similar to those of the exfoliated blisters formed on materials surfaces by ion bombardment at very high fluences[14]. In order to explain exfoliation in blistering, two types of mechanism have been reported in the literature. First is build up of gas pressure at high ion doses[15] and the second one is the stress enhancement and its release[16]. In the present case, ion fluence is in the intermediate range of 1.0×10^{15} to $1.0 \times 10^{16} \text{ He}^+/\text{cm}^2$ which corresponds to <0.01 He per diamond atom. The gas pressure[17] for this range of ion fluence is given by

$$p = 4.83 \times 10^7 \exp(5.15 \times 10^{-29} n_{\text{He}}) [\text{N/m}^{-2}], \quad (5.2)$$

where n_{He} is He at./m^3 . In the present case p turns out to be 0.048 GPa which is very small for blistering and exfoliation to occur.

An alternative mechanism invokes build up of lateral stresses integrated over the thickness of the implanted layer during ion bombardment[18]. These stresses show saturation effect and they concentrate at the lattice imperfections to cause plastic deformation of the surface layer which finally leads to the relief of integrated lateral stress. In case of metals, these stresses reach saturation for fluences of 10^{17} to 10^{18} ions/cm². However, for semiconductors and insulators, stresses built by ion bombardment are proportional to the lattice structural damage caused by energy deposited into atomic collisions and/or ionization processes. The effects are very large for these materials and lower fluences of $\sim 10^{15}$ ions/cm² are sufficient to reach saturation of the stress effect[19]. In the present case, the as deposited diamond films contain considerable stress which is incorporated during their growth[20]. This residual stress gets enhanced during He⁺ ion bombardment. Thus ion bombardment quickly (at low doses) leads to stress saturation condition and since diamond films are brittle, it causes exfoliation of the films bypassing the intermediate stage of blistering. It is difficult to directly measure the film stresses during ion bombardment. The bending cantilever plate technique was used in the past for *in-situ* measurements of the lateral stresses in ion bombarded semiconductors and insulators[21, 22]. In this work, micro Raman spectroscopy has been utilized for stress measurements to investigate its role in delamination of ion irradiated regions of the CVD diamond films.

5.3.5 Micro Raman spectroscopy

Fig.5.6 shows the Raman spectra obtained from the diamond films using a 514.5 nm Ar⁺ laser excitation. The upshifted Raman line at 1333.1 cm^{-1} suggests the presence of high compressive stress in the films[19]. Leaving the doublet phonon shifts, singlet phonon wave number calculations for different planes of polycrystalline diamond films yield the variation of average value of biaxial stress(τ) as[23]

$$\tau = -1.08(\nu_s - \nu_0) [\text{GPa}] \quad (5.3)$$

where $\nu_0 = 1332 \text{ cm}^{-1}$ is the peak wave number of natural diamond and ν_s is that of singlet cubic diamond. The biaxial stress in the film was estimated from Raman shift to be 1.19 GPa, which is much higher than the estimated thermal stress of 0.25 GPa[20]. In contrast,

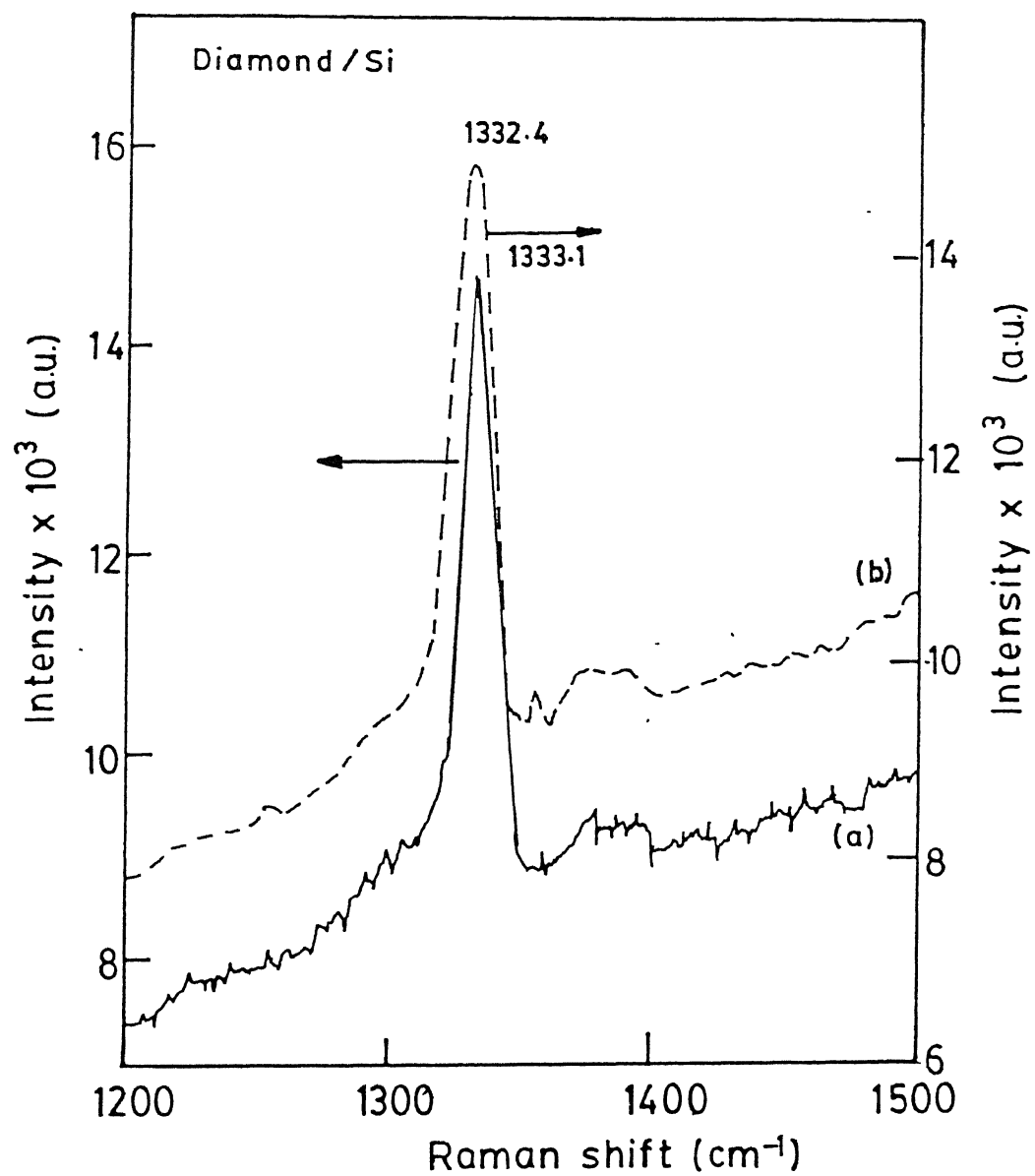


Figure 5.6: Micro Raman spectra of diamond films on Si from: (a) as deposited region and (b) periphery of the delaminated region.

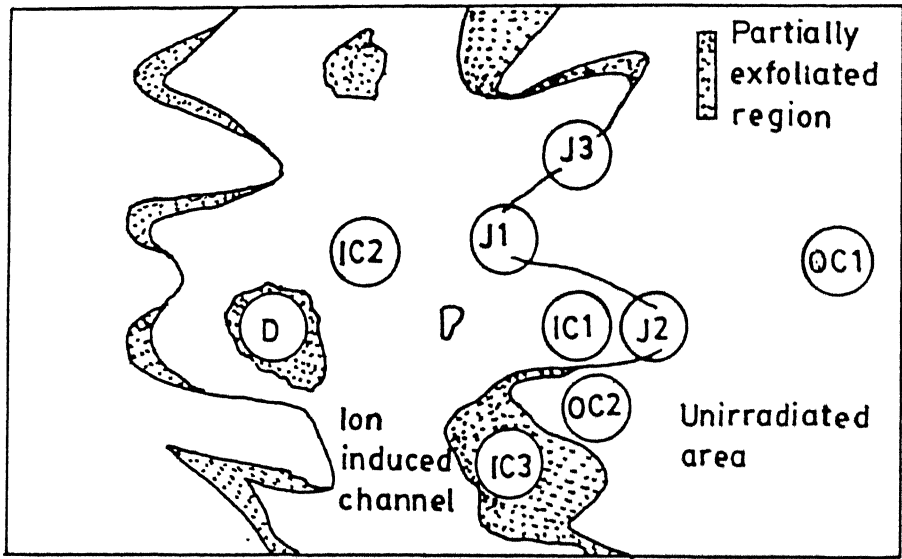


Figure 5.7: The trace of an ion beam induced channel taken from TV screen assisted with Raman microprobe and a video camera. OC's, IC's and J's are different spots where Raman spectra were excited. The circle around each spot shows the apparent size ($2\text{ }\mu\text{m}$) of focused laser beam.

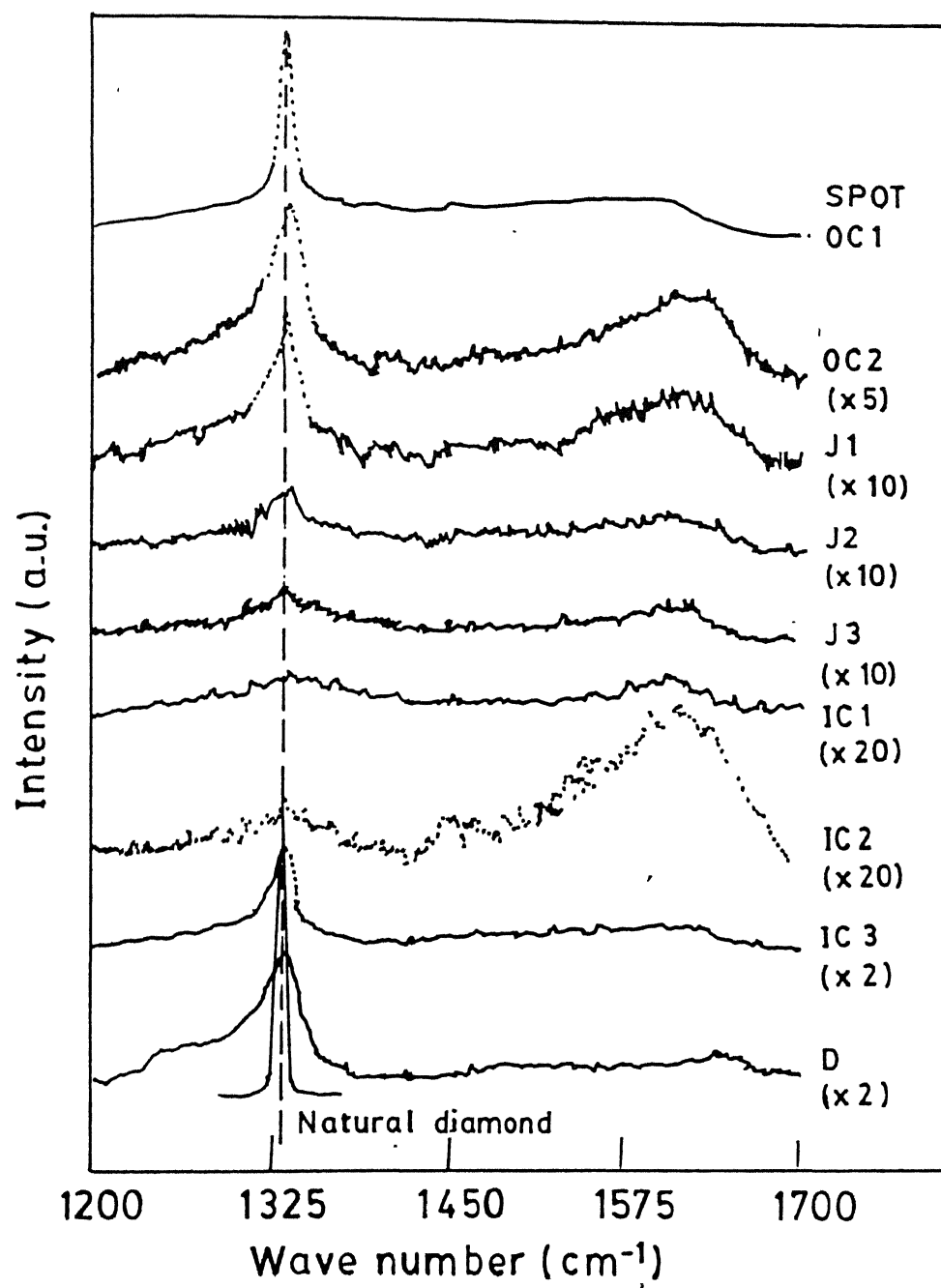


Figure 5.8: Room temperature Raman spectra recorded from natural diamond and from various spots in and around Channel-A under 514.5 nm excitation.

The Raman intensity depends on the volume probed, limited by the spot size and the penetration depth of incident radiation. Due to the experimental limitations, it was difficult to keep the unirradiated film area the same under each excitation around the periphery of a channel. Additionally, the junction layers under such an excitation are not at the same height. Therefore, a difference in the peak intensity is expected from spots J1, J2 and J3. The Raman spectra were best fitted to different diamond components after a linear background subtraction. Figs.5.9 shows the curve fitted spectra from selected spots (OC1, OC2, IC1 and IC2) of channel A, in that order.

The stress increases as one moves towards the channel from unirradiated region (OC1 \rightarrow OC2). In each channel stress was found maximum at the channel boundary near curvatures. This may be due to the random termination of diamond lattice and build-up strain caused by implantation. The maximum stress induced by ion irradiation at the channel boundary (J2) varies according to the target current. In this study, total implant (charge accumulated) in the films was kept constant at different target currents. The lowest target current density takes longer time to cause exfoliation of the film and vice versa i.e., the time rate of removal of different surface layer varies with target current. This might lead to a stress gradient near the channel boundary. However, higher target currents result in instantaneous exfoliation of the film. This may be the reason for the change of stress at spots J2 at different target currents (3.35 GPa in channel-A, 4.75 GPa in channel-B and 5.83 GPa in Channel-C, respectively).

The debris also show a considerable stress (maximum of 3.46 GPa in Channel-C), which is however, less than the maximum stress observed at J2. Similar stress distribution was observed around each channel studied. Raman study of CVD diamond films grown on a Ti-alloy reveals that the film can accommodate residual stress up to 2.4 times that of as deposited film, before its delamination occurs[23]. The findings from the as deposited films and at channel boundaries are in agreement with this observation. Therefore, the maximum stress at J2 may be considered as the threshold value necessary to cause exfoliation process in these films.

5.4 Conclusions

In summary, it was shown that CVD diamond films deposited on Si substrates get delaminated during 1.5 MeV He⁺ irradiation performed at room temperature. *In-situ* monitoring of

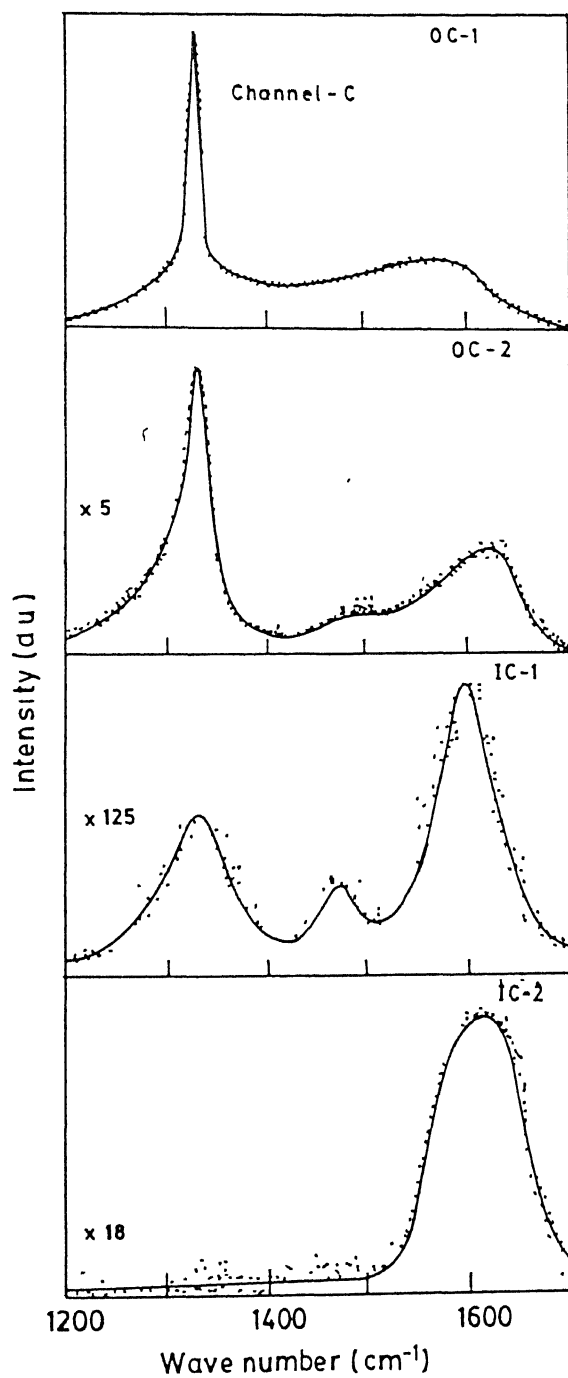


Figure 5.9: 514.5 nm excited room temperature Raman spectra from the spots OC1, OC2, IC1, and IC2 of Channel-C.

hydrogen, during irradiation, using ERDA has effectively been used to estimate the threshold ion fluence for exfoliation to occur. The exfoliation has been explained on the basis of the enhancement of the residual stress during He^+ ion bombardment leading to stress saturation condition of the brittle diamond films. The variation of stress at various spots around the two dimensional channels formed by ion irradiation at different target currents was found to be similar. These results lead to the possibility of isolation of devices using MeV ions in diamond films by judicious choice of film/substrate combination. It also reveals that diamond films under stress are fragile under MeV ion bombardment.

Bibliography

- [1] *Diamond: Electronic Properties and Applications*, Eds. L.S. Pan and D.R. Kania (Kluwer Academic Publishers, Massachusetts, 1995).
- [2] J. Narayan, V.P. Godbole, G. Matera, and R.K. Singh *J. Appl. Phys.* 71 (1992) 966.
- [3] K.V. Ravi, *Mat. Sci. Eng. B*19 (1993) 203.
- [4] K.V. Ravi and M.I. Landstrass, *Proc. Fourth Int. High Frequency Power Conservation Conf. '89, Intertec Communications*, (Ventura, CA, 1989) p. 103.
- [5] C.S. Kalbitzer, *Nucl. Instr. Meth. B*63 (1992) 1.
- [6] P. Gonon, S. Prawer, K.W. Nugent, and D.N. Jamieson *J. Appl. Phys.* 80 (1996) 5006.
- [7] S. Han, S.G. Prussin, J.W. Ager III, L.S. Pan, D.R. Kania, S.M. Lane, and R.S. Wagner, *Nucl. Instr. Meth. B*80/81 (1993) 1446.
- [8] S. Han, R.S. Wagner, J. Joseph, M.A. Plano, and M. Dale Moyer, *Rev. Sci. Instrum.* 66 (1995) 5516.
- [9] J.C. Angus, A. Argoitia, R. Gat, Z. Li, M. Sunkara, L. Wang and Y. Wang, *Phil. Trans. R. Soc. Lond. A*342 (1993) 195.
- [10] T. Sharda, D.S. Mishra, D.K. Avasthi and G.K. Mehta, *Solid State Commun.* 98 (1996) 879.
- [11] A. Masood, M. Aslam, M.A. Tamor, and T.J. Potter, *J. Electrochem. Soc.* 138 (1991) L67.

- [12] T. Som, S. Dhar, N. Banerji, K. Ramakrishnan, and V.N. Kulkarni, *Bull. Mater. Sci.* 19 (1996) 73.
- [13] L.M. Gratton, A. Miotello and C. Tosello, *Appl. Phys.* A36 (1985) 139.
- [14] B.M.U. Scherzer in “*Sputtering By Particle Bombardment II*”, Ed. R. Behrisch (Springer Publishing Co., Topics in Applied Physics, Vol. 52, 1987), p. 271.
- [15] J.H. Evans, *J. Nucl. Mater.* 68 (1977) 129.
- [16] R. Behrisch, J. Bottiger, W. Eckstein, U. Littmark, J. Roth, and B.M.U. Scherzer, *Appl. Phys. Lett.* 27 (1975) 199.
- [17] J.S. Rowlinson, *Mol. Phys.* 7 (1963/64) 349.
- [18] E.P. EerNisse and S.T. Picraux, *J. Appl. Phys.* 48 (1977) 14.
- [19] S. Bhargava, *Ph. D. Thesis*, Indian Institute of Technology, Kanpur, 1996.
- [20] H. Windischmann, G. Epps, Y. Cong, and R.W. Collins, *J. Appl. Phys.* 69 (1991) 2231.
- [21] E.P. EerNisse, *J. Appl. Phys.* 45 (1974) 167.
- [22] E.P. EerNisse and S.T. Picraux, *J. Appl. Phys.* 48 (1977) 9.
- [23] J.W. Ager, III and M.D. Drory, *Phys. Rev. B* 48 (1993) 2601.

Chapter 6

Out-diffusion of H from Si and GaAs

6.1 Introduction

During the period of the middle and late 1980's, enormous amount of work was performed on the properties of hydrogen in crystalline semiconductors such as silicon, GaAs and related materials. This was followed by the discovery that hydrogen could passivate the electrical activity of both shallow acceptors[1–4] and shallow donor dopants[5, 6]. This discovery was preceded by the ability of atomic hydrogen to neutralize deep level defects[7, 8] in crystalline semiconductors. Thus, hydrogen is seen to serve as an all purpose impurity or defect passivant. Usually deep-level passivation is thermally more stable than shallow-level passivation, and is thought to have more practical applications. The subsequent voluminous literature on the subject has revealed a rich detail of the microscopic properties of hydrogen-dopant complexes. On the other hand, the microscopic nature of number of deep levels not being clear, the mechanisms of deep-level passivation are at a preliminary stage.

Further, with the present trend in down-scaling of semiconductor devices to less than 1000 Å, and doping profiles to less than 50 Å, it is becoming obvious that intensified studies of hydrogen behaviour in the very near-surface region (<1000 Å) are needed[9]. As a matter of fact, there are evidences that dopants may trap multiple-hydrogen atoms in their vicinity, reducing the effective hydrogen diffusivity and leading to build up of this element in the near-surface region. The effective diffusivity of hydrogen under a particular set of experimental

condition is determined by the material conductivity type and resistivity, total amount of hydrogen incorporated, and the method of hydrogen insertion. Therefore, it is important that the details of the diffusion profiles must be studied for a good understanding of the hydrogen diffusion and the mechanism for the introduction of hydrogen into semiconducting materials. In this regard, ERDA provides a powerful way for quantifying hydrogen and for studying its diffusion behaviour in the near-surface region of these materials.

This chapter starts with a brief review of various methods for incorporating hydrogen in semiconductors, the charge states and microscopic forms that hydrogen assumes in the lattice, nature of dopant-hydrogen complexes, and configuration of hydrogen in semiconductors. It also describes the development of a low energy (1-10 keV) dc plasma source ion implantation set-up for implanting hydrogen in the near-surface region of materials. This set-up has been used to perform low energy hydrogen implantation in crystalline silicon (*c*-Si) and gallium arsenide (*c*-GaAs) for the present work. As a matter of fact, the main aim of this chapter is to show the efficacy of plasma source ion implantation technique for implanting hydrogen in different crystalline semiconductors and to study its migration. With this intention some preliminary studies have been performed as described in the later sections.

Depth profiling of H was done by ERDA. Migration and outdiffusion of hydrogen has been studied in the temperature range of 100-700° C. From the retained amount of hydrogen present in the Si samples, activation energy associated with hydrogen removal was obtained.

6.2 Techniques for hydrogen incorporation in semiconductors

Incorporation of hydrogen in semiconductors can occur in variety of ways. These can be classified into two groups – processes in which hydrogen is introduced in an intentional and controlled manner, such as exposure to plasma or by direct ion implantation, and those processes in which hydrogen gets injected into the semiconductors in an uncontrolled and often unintentional way. Examples of the latter include crystal growth, sample cleaning and fabrication processes such as boiling in water[10], wafer polishing[11] in the presence of hydrogen containing reagents and heat treatment in molecular hydrogen[12, 13]. It can

be mentioned here that it is the atomic hydrogen which is the active species for defect and impurity passivation, and therefore a sufficient concentration needs to be incorporated into the semiconductor to observe significant changes in the electrical properties.

6.2.1 Hydrogen plasma exposure

The commonly used hydrogenation systems generally consist of a quartz tube to which molecular hydrogen is pumped at a reduced pressure (0.1-0.3 Torr, typical flow rate $\sim 10^3$ cm⁴/min). The plasma is excited by capacitively or inductively coupled low frequency (~ 30 kHz) or radio-frequency (13.56 MHz) power via a high frequency oscillator[14]. It is of course, possible to use commercially available plasma assisted deposition reactors, where hydrogen is introduced at reduced pressure into the system and ionized by a dc voltage.

The energy distribution and composition of most hydrogen plasmas used to insert hydrogen into semiconductors is, in general, not well known. The neutral flux incident upon a sample at 0.1 Torr is $\sim 10^{16}$ particles cm⁻²/sec, with an ion flux also of 10^{16} particles cm⁻²/sec. These ions produced at the plasma edge have energies in the range of 100-1000 eV which are much higher than the threshold value of energy for atomic displacement (~ 15 eV). This causes introduction of near-surface damage into the sample during the plasma exposure.

6.2.2 Broad beam ion implantation

An alternative method for incorporating hydrogen into semiconductors is implantation of low energy monoenergetic hydrogen ions. Typical ion energies are 400-1500 eV at a current density of 0.5-1.5 A/cm² for time long enough to achieve total doses of $\sim 10^{17}$ H⁺ ions/cm². This broad beam, multi aperture ion sources are commonly known as Kaufman ion sources. They have a number of advantages for hydrogenation, including close control of H⁺ ion energy, dose and much shorter exposure times (\sim several minutes), rather than at least 30 min. with plasmas. The major disadvantage, of course, is the extensive damage created in the near-surface (1000 Å) region by the high level of hydrogen bombardment. The damage can be annealed but this can destroy the beneficial effects of hydrogen in passivating defects, that is, the hydrogen attaches to the vacancies it has created in collisions with silicon atoms.

6.2.3 Plasma source ion implantation

In 1986 Conrad and Castagna[15] developed a new cost-effective implantation technique known as plasma source ion implantation (PSII)[16-21]. This is a non-line-of-sight process where any arbitrary shaped sample is immersed in a low pressure (10^{-5} - 10^{-2} Torr) steady-state plasma ambient and is pulsed biased to a high negative potential. As a result a plasma sheath is formed (a region of strong electric field) and the ions of a particular gaseous species follow the electric field lines and get implanted into the target depending on the energy they gain from the electric field. This technique has distinct advantages over the conventional ion implantation technique. Some of these advantages can be listed as follows:

- (i) elimination of need for target manipulation and beam restoring,
- (ii) elimination of need for target masking,
- (iii) greater production throughput, especially for large targets.
- (iv) readily scaled to large and/or heavy targets of arbitrary shape,
- (v) smaller, less expensive, simpler to maintain and operate and more compatible to "in-house" operation. However, understanding the depth profiles resulting from PSII is more complex in connection to collisional and diffusional aspects.

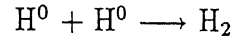
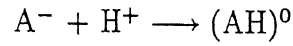
6.3 Shallow impurity passivation by hydrogen

The acceptor passivation can be removed by annealing at temperatures which depend strongly on the acceptor concentration and geometry. For example, in case of implanted samples, passivated B is reactivated at $\geq 160^\circ \text{C}$, while Ga is reactivated at $\sim 200^\circ \text{C}$. Evidence of In-H complex to be stable $\sim 350^\circ \text{C}$ was also reported. Reactivation mechanism is simply dissociation of the acceptor-hydrogen complexes with diffusion of hydrogen away from the dopant. Retrapping of hydrogen is highly probable in heavily doped samples. Molecule formation is also another possible intermediate reaction. pathway prior to evolution of $\text{H} \geq 500^\circ \text{C}$. Reactivation energies[22] measured in lightly doped samples (fabricated into Schottky diodes) show values ~ 1.3 - 1.4 eV for B, Al, Ga, In-H complexes. Dissociation of acceptor-hydrogen complexes for $T \geq 150^\circ \text{C}$. Donor passivation is a more elusive effect than acceptor passivation. For $n^+ \text{Si}$, $>95\%$ donor passivation may take place[23] with retarded indiffusion of hydrogen. Reactivation energies for few donors like Si, Ge, Sn etc. are mostly in the range

of 2.04 to 2.13 eV corresponding to the temperature range of ~ 375 to 400°C [24]. This indicates that acceptor passivation is less stable than that for the donors.

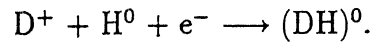
Hydrogen is an amphoteric species, with both an acceptor (A) and a donor (D) state in the gap of Si and probably in other semiconductors also. In p-type material, the hydrogen is therefore in a positive charge state (H^+) or neutral (H^0), while in n-type material it can be in a negative charge state (H^-) or neutral (H^0). In doped materials therefore the hydrogen motion can be influenced by internal or external electric fields.

In p-type Si hydrogen occupies the bond-centred (BC) site leaving the acceptor three-fold coordinated. Thus, trapping of injected electrons by the proton would lead to the formation of neutral H^0 and subsequent association of these atoms to form H_2 molecules:

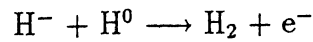
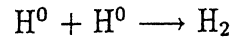


When located at the BC site, the H^+ is neutralized by the lattice. It can't therefore be considered as a bare proton, since the charge is somewhat delocalized with charge exchange occurring with the Si lattice[25]. It is emphasized that direct compensation is not the cause of acceptor deactivation, but rather the formation of neutral complexes.

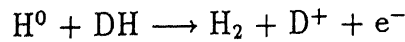
In n-type Si, hydrogen occupies the antibonding (AB) site. If it is present in the form of H^- then $\text{D}^+ + \text{H}^- \longrightarrow (\text{DH})^0$ is formed, while for hydrogen being present as H^0 , formation of $(\text{DH})^0$ takes place by the following route[26]:



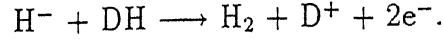
Molecule formation could occur through the reactions given by



as well as pick-off reactions of the form[27]



and



The hydrogen is calculated to be at an AB site in a ‘-ve’ charge state[28].

It has been suggested that molecules would occupy tetrahedral interstitial sites (T_d), although another type of H_2 complex (H_2^*) might have one hydrogen at a BC site and the other at the AB site[29]. From the calculated binding energies (hydrogen-dopant)[30] in n-Si and p-Si it has been observed that H-B pair is more stable than H_2 for hydrogen in either BC or AB site, while in n-Si only the T_d site is more stable than molecule formation.

6.4 Hydrogen diffusion

The diffusion of hydrogen in Si is complex due to the presence of hydrogen in different charge states and the fact that hydrogen is present in a number of different forms, viz. atomic, molecular (or larger clusters) or bound to a defect or impurity. The probability for formation of these different forms is dependent on the defect or impurity concentration as well as the hydrogen concentration itself. The apparent diffusivity is function of the sample conductivity and type, and the method of hydrogen insertion. In case of low hydrogen concentration such as acid etching or boiling in water, hydrogen diffuses very fast as opposed to the case of high hydrogen concentrations, such as plasma exposure[31, 32].

6.5 Experimental

6.5.1 PSII set-up and H implantation

A low energy PSII facility has been developed for implantation of low energy (1-10 keV) H, D, N etc. in materials. The implantation chamber has a diameter of 22 cm and is 20 cm long. It is vertically mounted on a turbomolecular pump and has two viewports as well as two approach ports. The base pressure of the chamber is $\sim 10^{-7}$ Torr. Inside the chamber, there are two cylindrical electrodes of diameter 2.5 cm. One of the electrodes is grounded and

the other one is used for mounting the target to be implanted. The latter one is electrically isolated from the chamber wall and is connected to the output of the high voltage power supply, as shown in Fig.6.1.

When the base pressure is achieved, a flow of the gaseous species to be implanted is established in the chamber to provide a final equilibrium gas pressure of 10^{-2} to 10^{-3} Torr. The plasma is generated by ionizing the gas with the help of applied bias. As the sheath containing an electric field is formed, it shields the surrounding plasma from the applied potential. As a result, ions within and at the edge of the sheath are accelerated by the electric field and get implanted into the target.

Wafers of Si and GaAs were procured in well polished condition and standard cleaning procedure was used for these samples. Hydrogen implantation was performed at room temperature using the above mentioned PSII set-up. For the work described here, 1-3 keV hydrogen implantations were achieved in Si and GaAs. Implantations were carried out for time duration of 10-30 min. The flux of particles impinging on the samples was also monitored by measuring the cathode current. The set-up gives typical cathode current of $15\ \mu\text{A}$ over the cathode area. Thus, 30 min. plasma implantation should result an implantation dose of 5×10^{16} at./cm².

Annealing of the H implanted samples was done for 10 to 60 min. in the temperature range of 100 to 700° C in a clean vacuum of 3×10^{-6} Torr.

6.5.2 ERDA measurements

Hydrogen areal densities of the as implanted as well as vacuum annealed samples were estimated by ERDA measurements using He⁺ ions of 1.2 to 1.4 MeV energy. Incident ions were impinged on the hydrogen implanted samples making an angle of 15° with respect to the sample surface. The recoiled hydrogen signals were recorded using an ion implanted semiconductor detector kept at an angle of 30° with respect to the transmitted beam direction. A 5 μm mylar foil was employed as an absorber foil to restrict the scattered projectiles from reaching the detector. The details of the ERDA set-up has been described in Chapter 2. From these data the remaining fraction of hydrogen in the Si and GaAs samples were calculated.

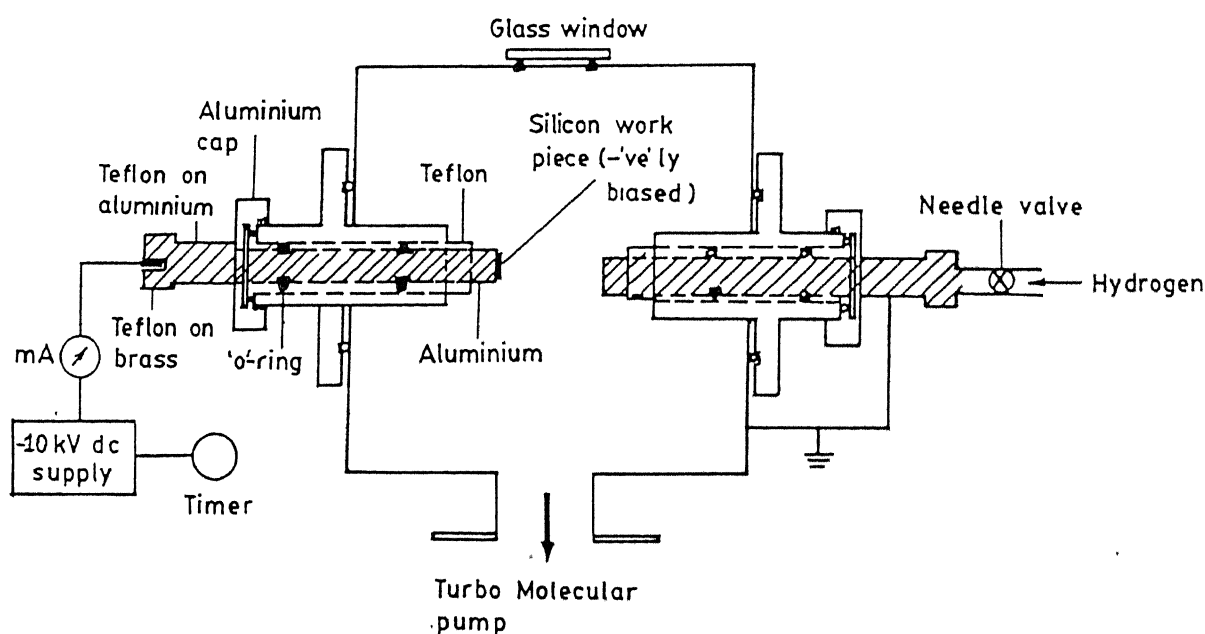


Figure 6.1: Schematic diagram of dc plasma source ion implantation set-up.

6.6 Results and discussion

6.6.1 Si:H system

A typical ERDA spectrum obtained from the as implanted Si (010) has been presented in Fig.6.2. The solid line indicates the simulated spectrum obtained from RUMP simulation package. In this case, the simulation yields a hydrogen concentration of 4.7×10^{16} at./cm², with the peak of Gaussian distribution (FWHM=400 Å) located at a depth, x (=120 Å) from the surface. Similarly, ERDA spectra recorded from all the thermally annealed samples were simulated in order to determine the amount of retained hydrogen in the Si samples. This was performed by normalizing the individual hydrogen concentration (after each annealing step) with respect to the as implanted one. These results have been presented in Fig.6.3 where the amount of retained hydrogen in Si has been plotted as a function of annealing time.

Fig.6.3 shows that the amount of implanted hydrogen does not change at all up to a temperature of 350° C. However, annealing at 400° C results in the decrease in the amount of retained hydrogen. This reduction continues till 60 min. after which no further decrease is observed. The reduction in the total amount of hydrogen indicates the hydrogen out-diffusion from Si. Further the rate of H loss is higher till 15 min. after which it reduces. Similar trend is observed for all other desorption curves obtained for annealing at higher temperatures up to 600° C as (seen from Fig.6.3) although at lower temperatures (for e.g., $T=400^\circ$ C) the decay is much slower.

The decay curves have been fitted by the following equation:

$$N_H(t) = N_0 \exp[-t/\tau(T)] \quad (6.1)$$

where $N_H(t)$ is the hydrogen concentration at any time t , N_0 is the initial hydrogen concentration, τ is the time constant for hydrogen evolution, and T is the temperature. The time constant for the hydrogen evolution was determined from the least-square fitting of the slope of the straight lines in Fig.6.3. It can be mentioned here that the time constant τ can be related to the activation energy E_a by the following relationship[33]:

$$\tau(T) = \tau_0 \exp(E_a/T) \quad (6.2)$$

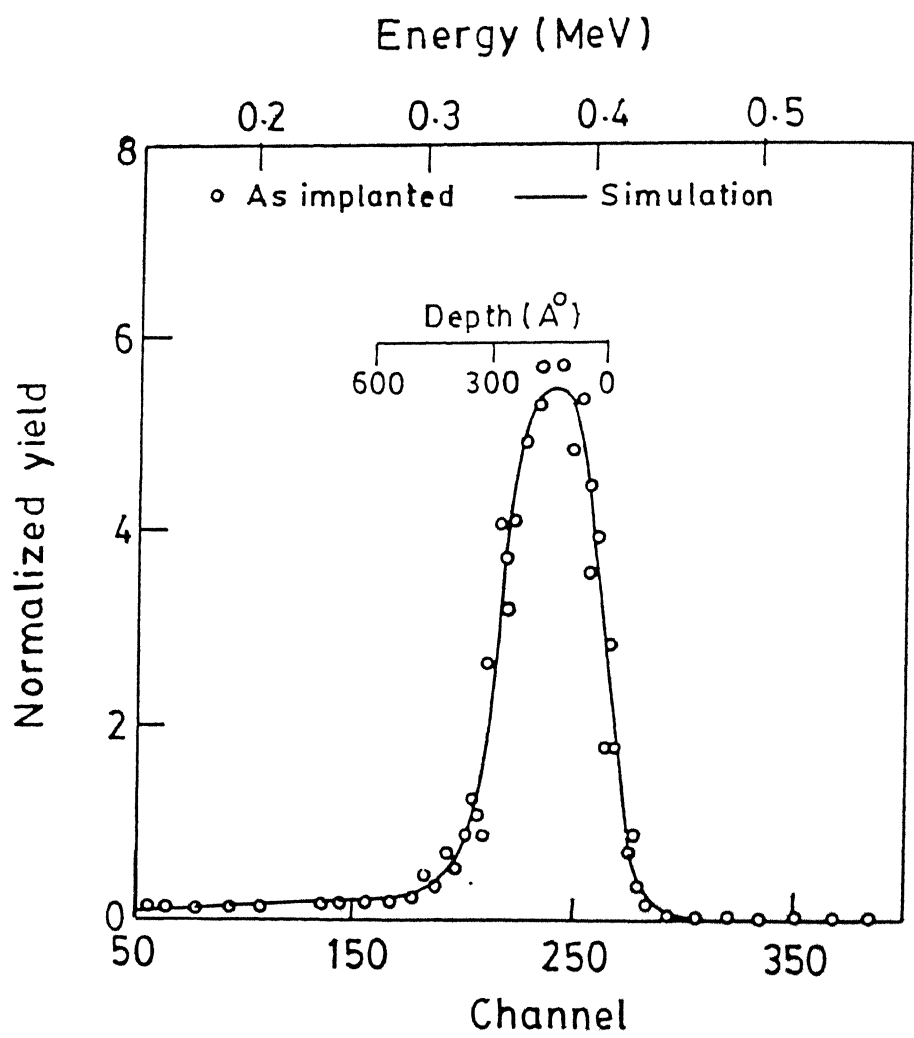


Figure 6.2: H recoil spectrum obtained from as implanted Si.

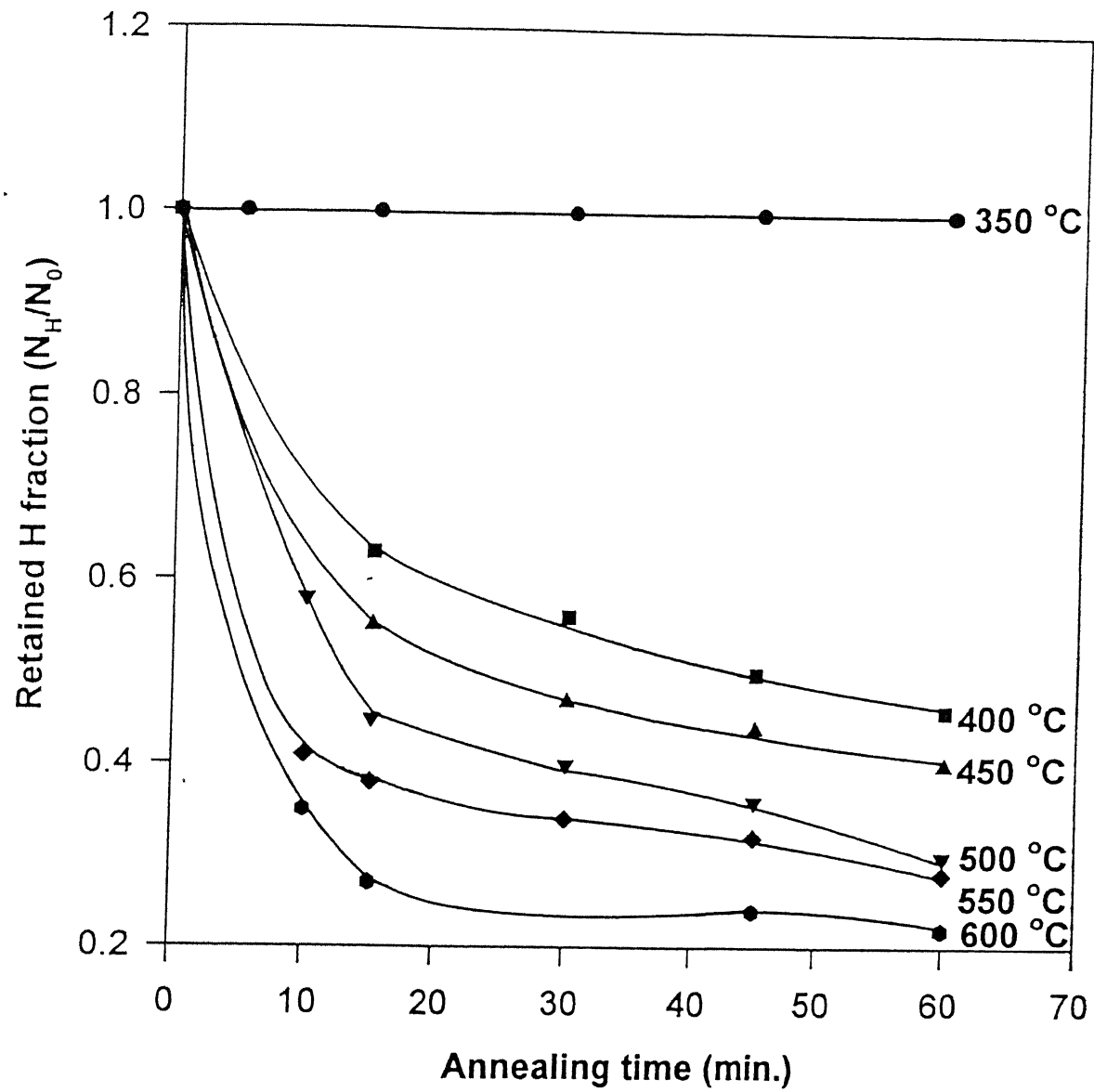


Figure 6.3: Variation in the retained hydrogen fraction in Si after vacuum anneal at different temperatures. Solid lines are guide to the eye.

The values of τ as a function of the inverse annealing temperature have been plotted in Fig.6.4. This Arrhenius plot allows one to obtain the apparent activation energy (E_a), associated with hydrogen out-diffusion from Si upon vacuum annealing. This gives an activation energy for hydrogen out-diffusion to be 0.21 eV for temperatures $\geq 400^\circ\text{C}$. The apparent activation energy of hydrogen out-diffusion from Si (010) obtained in this case is close to the theoretical value (0.3 eV)[34, 35]. Such detrapping energy (0.31 eV) was also observed for 4 keV H^+ implanted Si(100)[36]. It has been discussed earlier (section 6.3) that hydrogen may be present in different states in crystalline Si and each configuration results in different activation energies. Further, H may passivate dangling bonds and/or form complex with implantation induced defects created in the near-surface region of Si. As the temperature increases, the rate of depassivation becomes high which causes hydrogen out-diffusion.

6.6.2 GaAs:H system

Fig.6.5 shows ERDA spectra of n^+ -GaAs(Si) samples in the as implanted condition and after isochronal annealing performed at 300 and 400°C respectively. For the as implanted case simulation gives a total hydrogen content of $5.6 \times 10^{16}\text{ at./cm}^2$, with the peak located at $\sim 100\text{ \AA}$ from the surface. An interesting change in the profile is observed at 400°C . The concentration under the tail reduces significantly and the surface peak becomes sharper as compared to the as-implanted peak, but the total hydrogen content remains almost same (Fig.6.6). This phenomenon may be attributed to the migration of hydrogen from the bulk to the near-surface defect sites caused during implantation or to the possible reactivation of Si donors as reported in the literature[37]. A net loss of hydrogen, indicating hydrogen out-diffusion is seen above 400°C .

Next we go on to describe the results of the changes occurring in the concentration versus depth profiles of hydrogen in undoped semi-insulating (SI) GaAs (100) crystals. Plasma ion implanted SI-GaAs samples (LEC grown) were isochronally annealed in vacuum in the range of $100\text{--}350^\circ\text{C}$. Fig.6.7 shows the overlapped experimental and simulated ERDA spectra obtained from two different set of samples, viz. as implanted and after annealing at 350°C . The arrow indicates the surface position of hydrogen. Simulated spectra in the figure have been indicated by solid lines. As implanted samples show a total hydrogen concentration

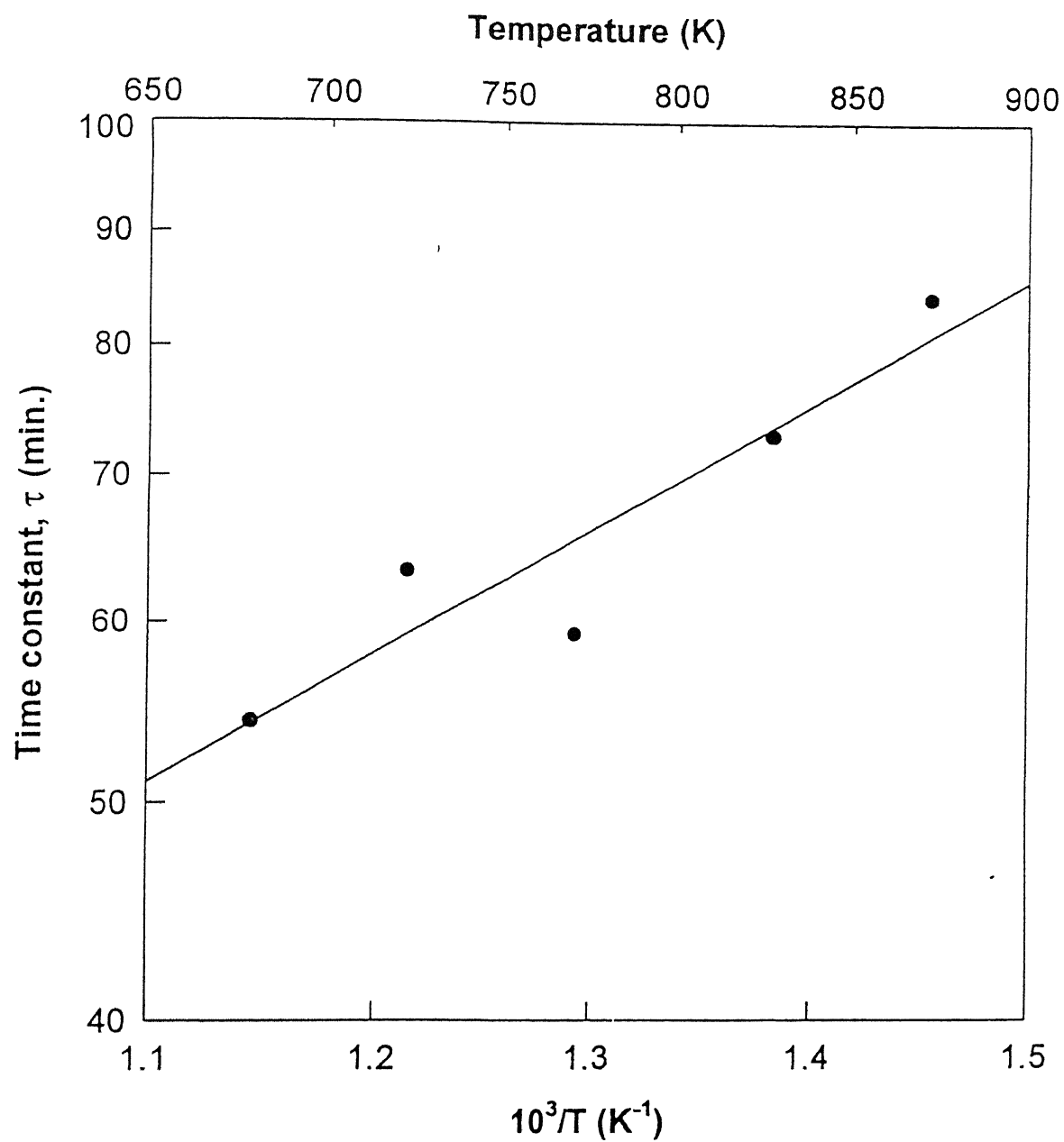


Figure 6.4: Time constant for hydrogen evolution (τ) from Si as a function of inverse temperature.

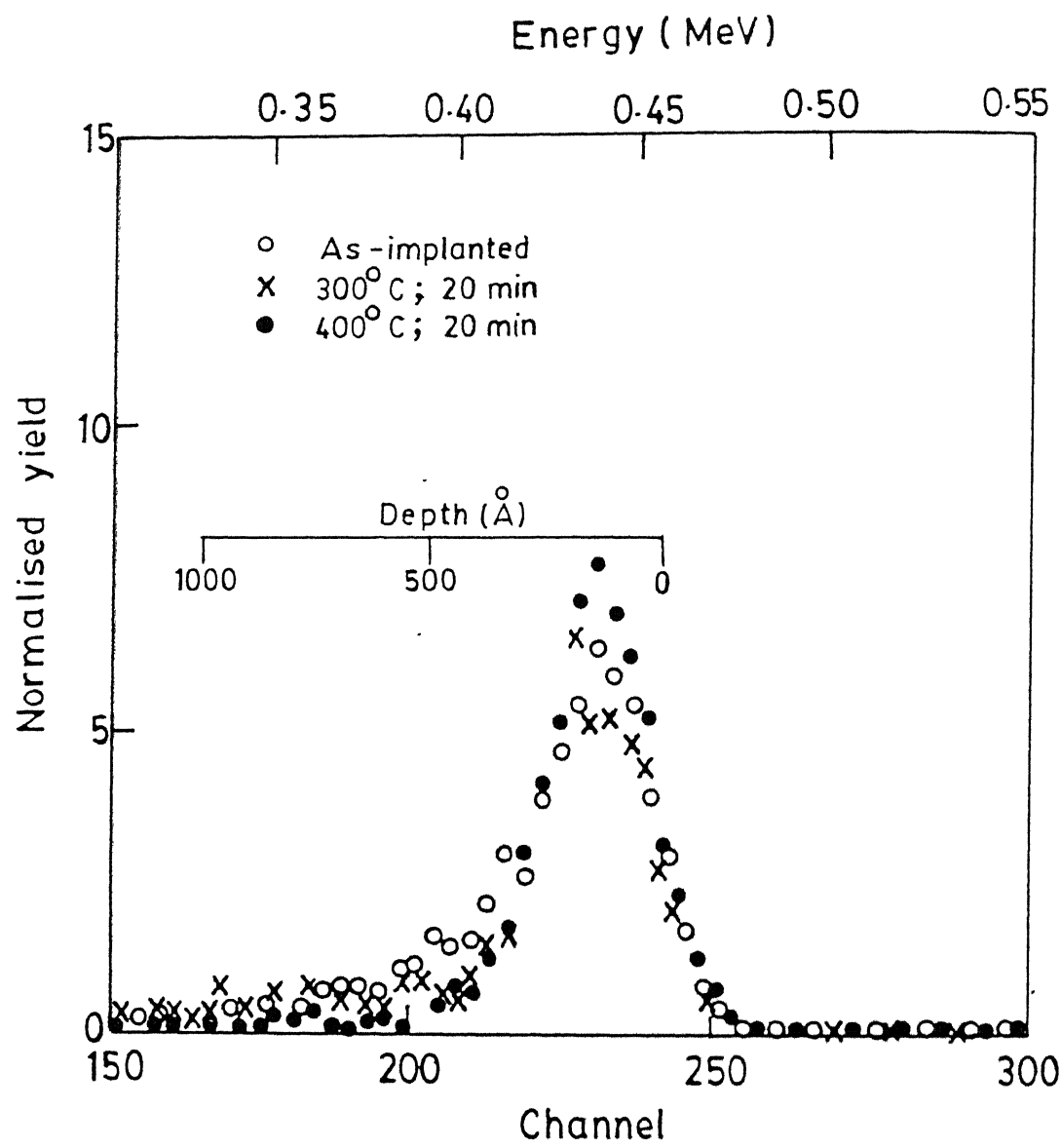


Figure 6.5: 1.38 MeV ERDA spectra of n^+ -GaAs(Si):H samples.

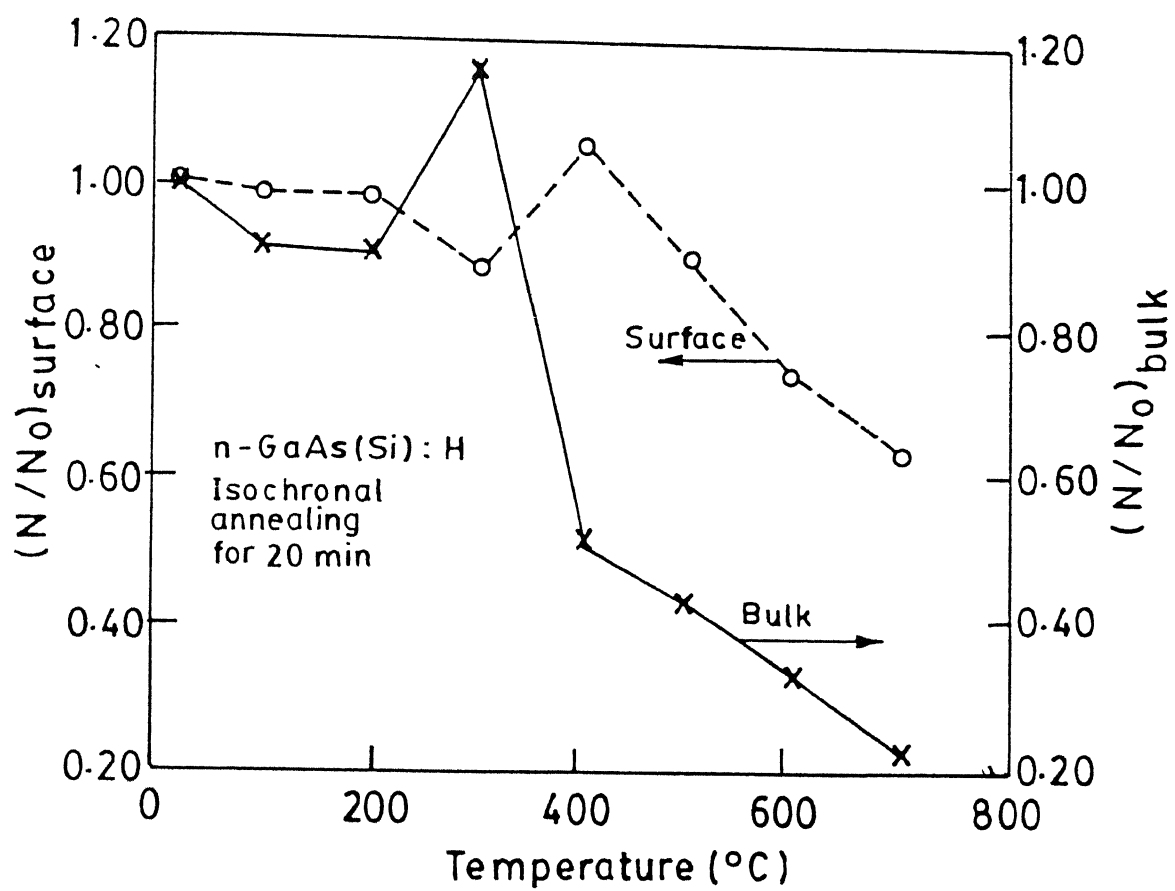


Figure 6.6: Variation in integrated fraction of remaining H, (N/N_0) .

Sample Description	x (Å)	FWHM (Å)	Peak Concentration(at.%)
As implanted	140	370	13.8
100° C; 10 min.	120	380	13.8
200° C; 10 min.	100	300	15.9
300° C; 10 min.	80	200	25.9
350° C; 10 min.	76	130	38.2

Table 6.1: Results of RUMP simulation.

of 2.8×10^{16} at./cm² with the peak of Gaussian distribution (FWHM=370 Å) located at a depth, x (=140 Å) from the surface. Fig.6.8 presents the variation of the peak width of hydrogen distribution as a function of annealing temperature. Similar analysis has been done for other samples also and all the results have been presented below in Table-6.1.

Interestingly, hydrogen concentration in the near-surface region of the SI-GaAs:H samples is observed to increase after isochronal annealing at different temperatures, although total hydrogen concentration remains same over the total analyzable depth. This is followed by the hydrogen peak narrowing as shown in Fig.6.8, where a sharp decrease in the peak width takes place above 100° C. This increase in hydrogen concentration in the near-surface region of SI-GaAs samples can occur due to the migration of hydrogen towards the surface which is rich with defects produced due to exposure of the samples to hydrogen plasma or due to the formation and increase in size of stable H agglomerates like H-filled voids etc., as a function of annealing temperature[38].

6.7 Summary and conclusions

In summary, hydrogen implantation in p-Si (010) samples was performed using dc plasma ion implantation set-up. Hydrogen depth profiling was performed by ERDA technique. Vacuum annealing in the temperature range of 300-600° C reveals that hydrogen out-diffusion takes place >350° C. The decay curves follow an exponential nature from which the time constants for H-evolution have been calculated. These data have been utilized to determine the activation energy for hydrogen. Hydrogen out-diffusion has been attributed to the

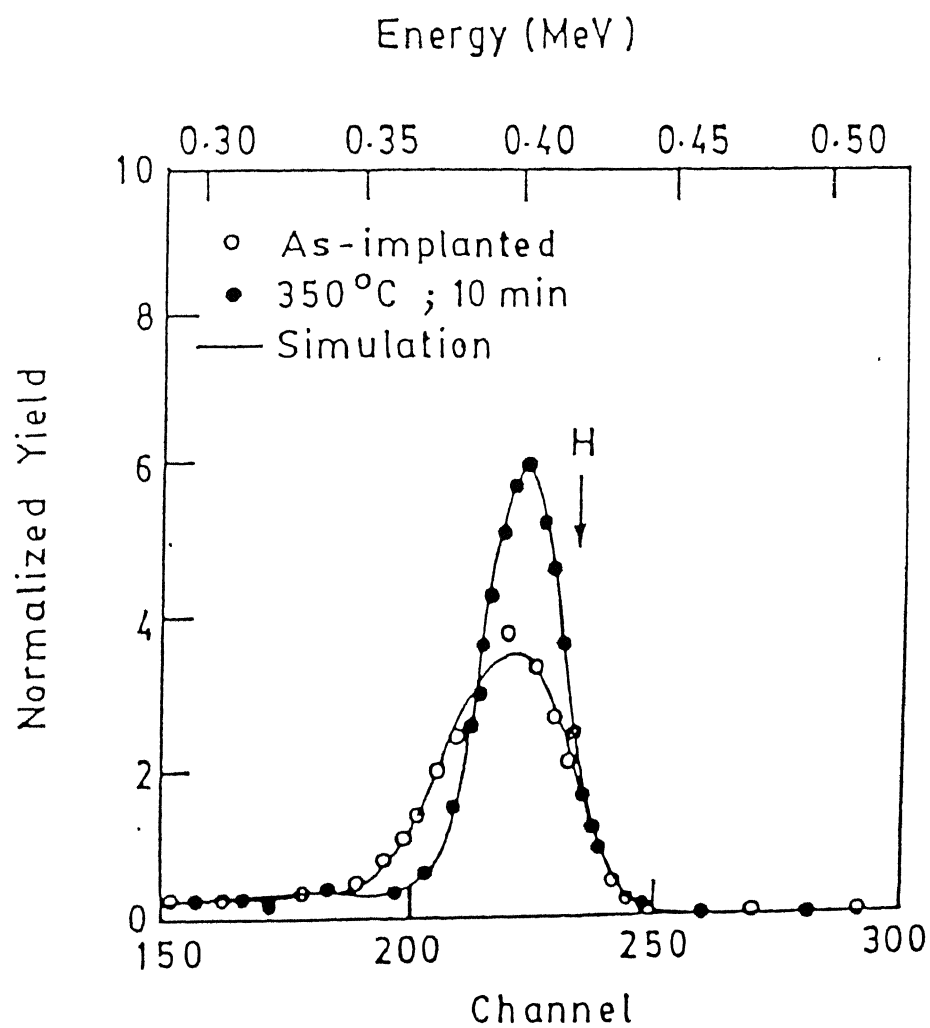


Figure 6.7: ERDA spectra and their simulations for SI-GaAs:H samples.

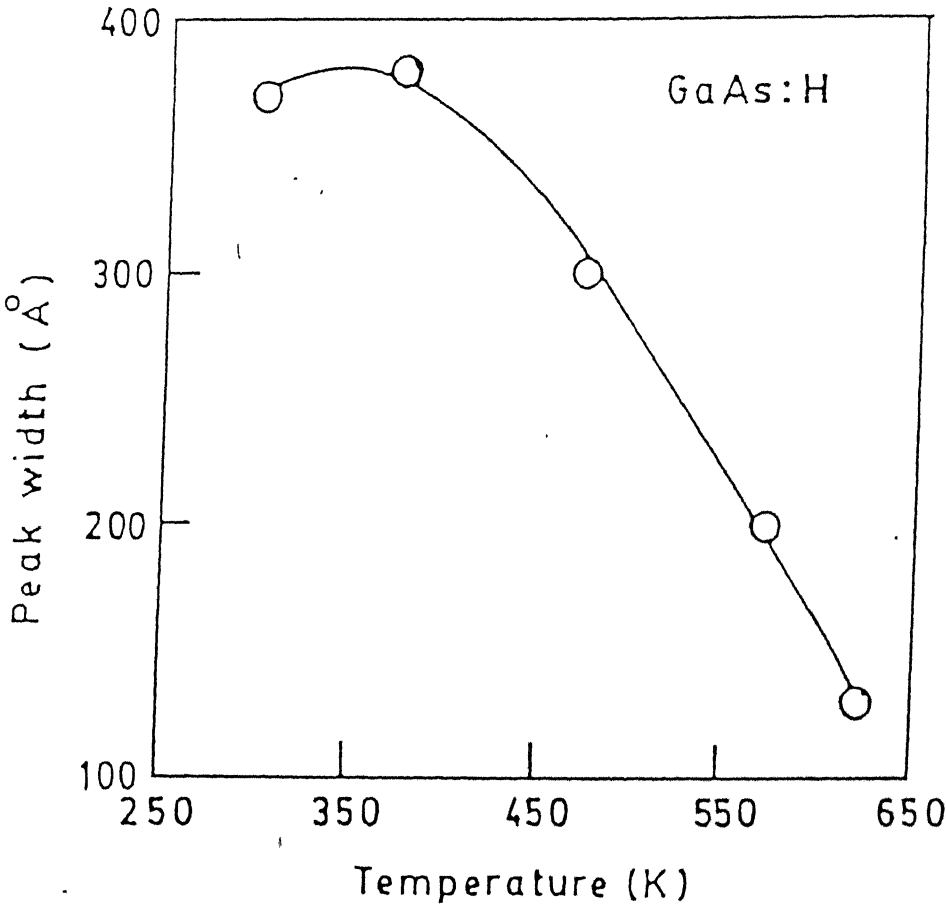


Figure 6.8: Variation of the peak width of hydrogen distribution in SI-GaAs as a function of temperature.

depassivation of plasma implantation induced defects/dangling bonds in Si.

Isochronal vacuum annealing of n^+ -GaAs(Si) samples implanted with low energy hydrogen ions shows narrowing of the peak at 400° C followed by its out-diffusion from the sample at higher temperatures. On the other hand, isochronal vacuum annealing in the temperature range of 100-350° C shows an increase in hydrogen concentration in the near-surface region of low energy hydrogen implanted SI-GaAs. This redistribution of implanted hydrogen has been explained by the migration of hydrogen towards the near-surface region which is decorated with plasma ion implantation induced defects.

Bibliography

- [1] C.T. Sah, J.Y.C. Sun and J.J. Tzou, *J. Appl. Phys.* 54 (1983) 5864.
- [2] J.I. Pankove, R.O. Wance and J.E. Berkyheiser, *Appl. Phys. Lett.* 45 (1984) 1100.
- [3] C.T. Sah, J.Y.C. Tsun and J.J. Tzou, *Appl. Phys. Lett.* 43 (1983) 204; *Appl. Phys. Lett.* 43 (1983) 962.
- [4] J.I. Pankove, D.E. Carlson, J.E. Berkyheiser, and R.O. Wance, *Phys. Rev. Lett.* 51 (1983) 2224.
- [5] N.M. Johnson, C. Herring and D.J. Chadi, *Phys. Rev. Lett.* 56 (1986) 269.
- [6] K. Bergman, M. Stavola, S.J. Pearton, and J. Lopata, *Phys. Rev. B* 37 (1988) 2770; *Mat. Res. Soc. Symp. Proc.* 104 (1988) 291.
- [7] S.J. Pearton, in *Hydrogen in Semiconductors*, Eds. J.Pankove and N. Johnson, (Academic, New York, 1991), Ch.3.
- [8] S.J. Pearton, J.W. Corbett and T.S. Shi, *Appl. Phys.* A43 (1987) 153.
- [9] A.E. Jaworowski, *Surf. Interface Anal.* 14 (1989) 27.
- [10] A.J. Tavendale, A.A. Williams and S.J. Pearton, *Appl. Phys. Lett.* 48 (1986) 590.
- [11] S.J. pearton, J.W. Corbett and M. Stavola, *Adv.Mater.* 4 (1992) 332.
- [12] I. A. Veloarisoa, D.M. Kozuch, R.E. Peale, M. Stavola, and G.D. Watkins, *Bull. Am. Phys. Soc.* 36 (1991) 945.
- [13] S.A. McQuaid, R.C. Newman, J.H. Tucker, E.C. Lightowlers, R. Kubaik, and M. Goulding, *Appl. Phys. Lett.* 58 (1991) 2934.

- [14] J.I. Pankove, in *Semiconductors and Semimetals*, Vol. 21D (Academic, New York, 1984) Ch. 14, p. 261.
- [15] J.R. Conrad and T. Castagna, *Bull. Am. Phys. Soc.* 31 (1986) 1479.
- [16] J.R. Conrad, J.L. Radtke, R.A. Dodd, F.J. Worzala, and N. Tran, *J. Appl. Phys.* 62 (1987) 4391.
- [17] J. Tendys, I.J. Donnelly, M.J. Kenny, and J.T.A. Pollock, *Appl. Phys. Lett.* 53 (1988) 2143.
- [18] A. Chen, J.T. Scheur, C. Ritter, R.B. Alexander, and J.R. Conrad, *J. Appl. Phys.* 70 (1991) 6757.
- [19] L. Zhang, J.L. Shohet, D. Dallmann, J.H. Booske, R.R. Speth, K. Shenai, M.J. Goeckner, J.B. Kruger, P. Rissman, J.E. Turner, E. Perez-Albuerne, S. Lee, and N. Meyyappan, *Appl. Phys. Lett.* 65 (1994) 962.
- [20] S. Qin, J.D. Bernstein, Z. Zhao, C. Chan, J. Shao, and S. Denholm, *Nucl. Instr. Meth. B* 106 (1996) 636.
- [21] W. Ensinger, *Nucl. Instr. Meth. B* 120 (1996) 270.
- [22] T. Zundel and J. Weber, *Phys. Rev. B* 39 (1989) 13459.
- [23] S.J. Pearton, M. Stavola and J.W. Corbett, *Mat. Sci. Forum* 38-41 (1989) 25.
- [24] S.J. Pearton, W.C. Dautremont-Smith, J. Chevallier, C.W. Tu, and K.D. Cummings, *J. Appl. Phys.* 59 (1986) 2821.
- [25] C.G. Van de Walle, J. Bar-Yam and S.T. Pantellides, *Phys. Rev. Lett.* 60 (1988) 2761.
- [26] S.T. Pantellides, *Appl. Phys. Lett.* 50 (1987) 995.
- [27] S.J. Pearton, J.W. Corbett and M. Stavola, in *Hydrogen in Crystalline Semiconductors* (Springer-Verlag, Heidelberg, 1992).
- [28] N.M. Johnson, C. Herring and D.J. Chadi, *Phys. Rev. Lett.* 56 (1986) 269.
- [29] P. Deak, L.C. Snyder and J.W. Corbett, *Phys. Rev. B* 37 (1988) 6887.

- [30] K.J. Chang and D.J. Chadi, *Phys. Rev. Lett.* 60 (1988) 1422; *Phys. Rev. Lett.* 62 (1989) 937.
- [31] D. Mathiot, *Phys. Rev. B* 40 (1989) 5867.
- [32] S.J. Pearton, J.W. Corbett and J.T. Bernstein, *Physica B* 170 (1991) 85.
- [33] I.J.R. Baumvol, E.P. Gusev, F.C. Stedile, F.L. Freire, Jr., M.L. Green and D. Brasen, *Appl. Phys. Lett.* 72 (1998) 450.
- [34] M. Capizzi and A. Mittiga, *Appl. Phys. Lett.* 50 (1987) 882.
- [35] J.W. Corbett, S.N. Sahu and T.S. Shi, *Phys. Lett.* 93A (1983) 303.
- [36] K. Umezawa, J. Yamane, T. Kuroi, F. Shioji, K. Oura and T. Hanawa, *Nucl. Instr. Meth. B* 33 (1988) 638.
- [37] J. Chevallier, W.C. Dautremont-Smith, C.W. Tu and S.J. Pearton, *Appl. Phys. Lett.* 47 (1985) 108.
- [38] J. Keinonen, E. Rauhala, J. Räsänen, K. Saarinen, P. Hautojärvi and C. Corbel, *Physica B* 170 (1991) 235.

Chapter 7

Summary and conclusions

The presence of hydrogen affects the physical, chemical, mechanical and electrical properties of many materials like metals, semiconductors, insulators, superconductors, etc. Therefore, detection and analysis of hydrogen play an important role in many scientific and technical problems, and hydrogen-material system has emerged as an important area of research. In many cases the study the of hydrogen in the near-surface region (up to 1 μm) is important.

In the past two decades, several techniques have emerged for probing hydrogen in materials. Especially, the nuclear techniques offer an advantage of quantifying hydrogen in a direct manner among which the elastic recoil detection analysis (ERDA) allows simultaneous depth profiling of all the three isotopes of hydrogen in a non-destructive fashion. This technique was first demonstrated by L'Ecuyer *et al.* (1976) by using a ^{35}Cl beam at 30 MeV. Subsequently Doyle and Peercy showed (1979) the successful use of ERDA technique for measuring ^1H depth distributions using a ^4He beam from a 2.5 MeV Van de Graaff accelerator. These findings triggered a great interest in the application of ERDA in diverse research field of hydrogen-material systems.

The present thesis work dealt with the detection of hydrogen and its depth profiling by ERDA using (MeV $^4\text{He}^+$ ions) in different materials, viz. potassium dihydrogen phosphate (KH_2PO_4 or KDP), diamondlike carbon (DLC) and diamond films, thin films of a biological fluid - phospholipid, and semiconductors like Si and GaAs.

The present work was undertaken with the objectives of setting up of ERDA facility around the 2 MeV Van de Graaff accelerator at IIT Kanpur, to study the ion induced

and/or thermal effects on the hydrogen in the near-surface region, and to study the physico chemical changes using FTIR and micro Raman techniques. Since, at these energies recoil cross sections are non-Rutherford, the experimental hydrogen recoil cross section data of Quillet *et al.* were utilized to obtain a semiempirical relationship useful for the RUMP simulation package used for the simulation of ERDA spectra. With this the ERDA set-up was standardized by performing experiments on KH_2PO_4 crystals at 130 K.

Subsequently, the results of He^+ ion induced hydrogen depletion and the physico chemical changes (as studied by FTIR and micro Raman techniques) occurring in the properties of different materials viz. KH_2PO_4 (KDP), DLC films and thin films of phospholipid, a biological fluid, were presented. All these films exhibit exponential decrease of the hydrogen concentration as a function of the analyzing He^+ ion fluence.

In case of KDP, the effect of Au of varying thickness was shown to act as a barrier to considerably reduce the depletion of hydrogen from the samples. Hydrogen depletion from the KDP samples was followed by amorphization with increasing He^+ ion fluence as indicated by Micro Raman measurements on various irradiated spots.

For the DLC films, the infrared results indicated that the films get rich in sp^2 CH_2 bonds as sp^3 CH_3 bonds decrease followed by hydrogen depletion due to energetic ion bombardment. Micro Raman studies also indicated ion induced removal of bond-angle disorder and increasing dominance of graphitelike crystallites.

To the best of the author's knowledge, it is for the first time that the thin films of biological fluid were investigated using energetic ion-beam. Thin films of cardiolipin have been characterized using analysis RBS-channeling and ERDA. The composition of C, O, and P in the cardiolipin films were determined quite accurately and it remained unaltered under He^+ irradiation during analysis. Infrared and micro Raman measurements showed that hydrogen depletion from the lipid films was followed by reduction in sp^3 bonded carbon and enhancement in the quantity of sp^2 bonded carbon indicating the formation of an α -C:H network in these films.

The depletion data in all the cases exhibited two regimes of exponential decay: the steep descend in the H concentration at low fluences ($\sim 10^{14}$ ions/ cm^2) followed by a slow depletion at high fluences ($\sim 10^{16}$ ions/ cm^2). The extrapolation to the zero analyzing fluence of the initial fastest depletion regime is shown to yield the initial hydrogen concentration in KDP and porphyrin (materials with known initial hydrogen concentration) quite satisfactorily.

This procedure of identification of the fastest depletion regime and its extrapolation to zero fluence was used to determine the initial hydrogen concentration in DLC films and were expected to be accurate within 5%. However, in case of the films of biological fluid, i.e., phospholipid, the extrapolated value yields a hydrogen concentration of 8.89×10^{21} at./cm³ which was quite low as compared to the actual hydrogen concentration of 7.27×10^{22} at./cm³. This discrepancy was attributed either due to lack of identification of the fastest depletion region (which may be occurring at even lower fluence $\ll 10^{11}$ ions/cm²) or due to formation of non-stoichiometry in the near-surface region of the films as a result of preferential evaporation of some hydrogen-rich species in vacuum (which was beyond the detection limit of the weight loss measurements performed in this work). It was inferred that it may not be very practical to use the procedure for this type of liquid films to get the high initial hydrogen concentration.

The hydrogen depletion from these different materials was explained on the basis of a model proposed by de Jong *et al.* This model considers the physical arguments of bond-breaking due to the secondary electron emission along the ion track and subsequent formation of H₂ molecule (within a small recombination volume) and its escape along with the trapping of the H radicals in the material.

The fitting of the depletion curves for these different materials yielded the values of i) bond-breaking probability, ξ , ii) recombination volume, V , iii) the ratio of the respective rate constants for hydrogen molecule formation and trapping. These parameters were shown to have a systematic dependence on the microstructure in case of the DLC films. The values of $A\xi^2$ (where A is the area of the ion track) showed systematic increase as a function of the electronic energy loss of the incident ion. Further, the comparison of the results of H-depletion induced by light and heavy ions showed two distinct regions with the common feature that samples containing higher amount of hydrogen had lower values of $A\xi^2$ in comparison to the cases where the materials contain less amount of hydrogen.

One of the interesting findings of this work was the delamination of CVD diamond films deposited on Si substrates during 1.5 MeV He⁺ irradiation performed at room temperature. Since diamond films contain very less amount of hydrogen, hydrogen depth distribution from the film and film/substrate interface had played a crucial role as that of a 'marker' to determine the threshold fluence (of 1.0×10^{16} He⁺/cm²) at which the delamination occurred. The nature of as deposited and delaminated diamond films was investigated using scanning electron microscopy (SEM). On the basis of these observations and micro Raman spectro-

scopic measurements, it was proposed that the residual film stress gets enhanced under He^- ion bombardment leading to stress saturation condition which caused the delamination of diamond films. These results lead to the possibility of isolation of devices using MeV ions in diamond films by judicious choice of film/substrate combination. It also revealed that diamond films under stress are fragile under MeV ion bombardment.

The importance of hydrogen in crystalline semiconductors and its various methods of incorporation in these materials was described. It also described the importance of the PSII technique and the development of such a low energy dc PSII set-up for studying migration of hydrogen in crystalline semiconductors, viz. Si and GaAs. Using this set-up, hydrogen implantation was performed in p-Si (010) samples. Hydrogen depth profiling was performed by ERDA technique. Vacuum annealing in the temperature range of 300-600° C revealed that hydrogen out-diffusion takes place >350° C. The decay curves followed an exponential nature from which the time constants for H-evolution were calculated which resulted an activation energy of hydrogen. These data were utilized to determine the activation energy for hydrogen which was found to be 0.21 eV for temperatures $\geq 400^\circ \text{C}$ which is in reasonable agreement with the literature reported value of 0.31eV. Hydrogen out-diffusion was attributed to the depassivation of plasma implantation induced defects/dangling bonds in Si.

In case of vacuum annealing of n^+ -GaAs(Si) samples implanted with low energy hydrogen ions narrowing of the H peak at 400° C followed by its out-diffusion from the samples at higher temperatures was noted. On the other hand, isochronal vacuum annealing in the temperature range of 100- 350° C showed an increase in hydrogen concentration in the near-surface region of low energy hydrogen implanted SI-GaAs. This redistribution of implanted hydrogen was explained by the migration of hydrogen towards the near-surface region which was decorated with plasma ion implantation induced defects.

Scope of future work

The observation of ion induced delamination of diamond films can be further explored and studied using diamond films prepared under different conditions. It appears that this novel phenomenon can be successfully used to create microchannels (using microsize ion beam) in diamond films which might be important in certain applications.

The temperature dependence of ion induced hydrogen depletion from optoelectronic materials can be undertaken along with the studies of changes occurring in the refractive index in these materials.

In case of the biological samples, the author feels that there is a vast scope of studying ion induced modification in these materials since certain structures like Si/phospholipid bilayers/protein are used as biosensors. Ion beam provides an efficient way of direct writing of patterns at any desired spot on such structures.

So far ion induced hydrogen depletion from various materials is concerned, temperature dependent studies will be desired to determine the more suitable experimental conditions. In all three cases it is expected that *in-situ* mass spectroscopic studies will provide direct information about the evolution of various hydrogenous species during ion bombardment. Finally with regard to the understanding of the depletion mechanism, there is a scope of further improvement of the phenomenological model by correlating the diffusion coefficient of hydrogen with the respective rate constants of hydrogen molecule formation and trapping of hydrogen radicals.